



UNIVERSITÀ DEGLI STUDI DI MILANO

Scuola di Dottorato in Fisica, Astrofisica e Fisica Applicata

Dipartimento di Fisica

Corso di Dottorato in Fisica, Astrofisica e Fisica Applicata

Ciclo XXXV

**Deep Learning Applications to Particle Physics:
from Monte Carlo simulation acceleration
to ProtoDUNE reconstruction**

Settore Scientifico Disciplinare FIS/02

Supervisore: Professor Stefano Carrazza

Coordinatore: Professor Matteo Paris

Tesi di Dottorato di:

Marco Rossi

Anno Accademico 2022/2023

Commission of the final examination:

External Member:

Prof. Stefano Giagu, Sapienza Università di Roma

External Member:

Prof. Pietro Govoni, Università degli Studi di Milano-Bicocca

Internal Member:

Prof. Raoul Rontsch, Università degli Studi di Milano

External Referee:

Dr. Giuliano Panico, Università di Firenze

External Referee:

Dr. David Rousseau, University of Paris-Saclay

Final examination:

Date 6 February 2023

Università degli Studi di Milano, Dipartimento di Fisica, Milano, Italy

To Chiara and Livia

MIUR subjects:

FIS/02

PACS:

07.05.Mh, 02.70.Uu

Abstract

The thesis arises in the context of deep learning applications to particle physics. The dissertation follows two main parallel streams: the development of hardware-accelerated tools for event simulation in high-energy collider physics, and the optimization of deep learning models for reconstruction algorithms at neutrino detectors. These two topics are anticipated by a review of the literature concerning the recent advancements of artificial intelligence models in particle physics.

Event generation is a central concept in high-energy physics phenomenology studies. The state-of-the-art software dedicated to Monte Carlo simulation is often written for general-purpose computing architectures (CPUs), which allow great flexibility but are not compatible with specialized accelerating devices, such as Graphics Processing Units (GPUs).

The original tools presented in the thesis, PDFFlow and MadFlow, manage to combine these two aspects in Python and require no prior knowledge of specific programming languages for hardware accelerators. The former product, PDFFlow, is a Parton Distribution Functions (PDFs) interpolator, the latter, MadFlow, aims at building a complete tool suite to accelerate the whole event generation framework.

The reconstruction pipeline at neutrino detectors is comprised of many different algorithms that work in synergy to extract a high-level representation of detector data. All the most important experiments in neutrino physics are developing software to automatically process and extract this information. This work describes the implementation of deep learning techniques to improve neutrino reconstruction efficiency at the ProtoDUNE-SP detector.

Two original contributions are presented concerning raw data denoising and a hit-clustering procedure named "slicing". Both denoising and slicing involve the implementation and the training of novel neural network architectures, based on state-of-the-art models in machine learning, such as feed-forward, convolutional and graph neural networks. They represent a proof of concept that these models are indeed capable of providing an important impact on signal reconstruction at neutrino detectors.

Contents

Contents	vii
List of Figures	ix
List of Tables	xv
Introduction	xvii
Motivation	xvii
Thesis overview	xviii
 Part I : Physics and computer science background	 3
1 Physics background	3
1.1 The standard model of particle physics	3
1.2 Neutrino physics	5
1.3 Monte Carlo techniques	16
2 Introduction to deep learning and its physics applications	33
2.1 Fundamental definitions and techniques of machine learning	33
2.2 Review of AI applications in particle physics	47
 Part II : Monte Carlo event generators on hardware accelerators	 65
3 Interpolating parton distribution functions	65
3.1 Parton Distribution Functions	65
3.2 LHAPDF: the Les Houches Accord PDF	66
3.3 PDFFlow : interpolating PDFs on GPUs	68
4 MadFlow : a Monte Carlo event generator on GPUs	79
4.1 The MadFlow design	80
4.2 Physics examples	85
4.3 Conclusion and outlook	89

Part III : Deep learning models for neutrino physics	93
5 Denoising ProtoDUNE-SP Raw Data with deep learning	93
5.1 The ProtoDUNE Single Phase design	93
5.2 Signal processing and deconvolution method in LArTPCs	100
5.3 Deep learning strategies for ProtoDUNE raw data denoising	102
6 Clustering at ProtoDUNE-SP with supervised learning	115
6.1 The Pandora framework	115
6.2 The Cluster Merging Network	121
Future directions	127
Bibliography	129
List of Publications	147
Acknowledgments	149

List of Figures

1.1	The standard model of particle physics. The figure is taken from [8].	5
1.2	The inverse transform method for sampling random numbers according to some probability distribution function $p(x)$.	25
1.3	The acceptance-rejection method for sampling random numbers according to some probability distribution function $p(x)$.	26
2.1	Three limit cases. <i>Left panel</i> , the linear output model has not captured the curvature present in the data. Training errors are high: underfitting. <i>Central panel</i> , the model fits well all the data: good generalization. <i>Right panel</i> , the model interpolates the samples with a complicated function with low training error, but high validation error: overfitting. The figure source code is inspired from the Scikit-learn [42] package documentation.	36
2.2	Typical trends of training and generalization (over the validation set) errors during training. Eventually, the training curve flattens (orange points and red curve), while the validation loss starts increasing. This behavior signals overfitting and the black line marks the best moment to stop the optimization algorithm, namely, as soon as the generalization gap starts increasing.	37
2.3	An artificial neuron.	39
2.4	A Feed-Forward or dense layer.	39
2.5	Images, both grayscale and RGB, are represented by rank 3 tensors. Convolution is the state-of-the-art operation in ML for image processing.	39
2.6	Sparse interactions vs full connectivity. Grey shaded circles the central node receptive field. <i>Left</i> : convolutional layer with kernel size equal to three, stride one and same padding. <i>Right</i> : fully connected layer. Each neuron in the output is linked to every neuron in the input. Even with this simple model, we have a large number of edges in the graph.	41
2.7	The attention mechanism.	42
2.8	The Transformer model.	42

- 2.9 Different learning rate behaviors: one-dimensional problem with a quadratic loss function. This example is meaningful since every function can be approximated by a quadratic polynomial if we sit sufficiently close to a minimum. 45
- 2.10 Optimization of an elliptical loss function with different optimization algorithms. The red point is the loss function global minimum. Gradients give great contributions in the vertical direction, presenting in an oscillating pattern and leading to slow convergence of SGD. RMSProp and Adam algorithms solve this issue through momentum. 46
- 2.11 The data structure timeline of physics jets: only engineered features were used as input to neural networks before 2014; after [77], several encoding structures have been investigated to efficiently represent jets. The descriptive pictures in the chart are taken, in order of appearance, from: [76, 84, 92, 97, 100, 103]. 53
- 2.12 Monte Carlo simulation of signal ($0\nu\beta\beta$ decay of ^{136}Xe) and background (single electron of energy equal to the Q value of ^{136}Xe) events in gaseous xenon at 15 bar. The picture shows the energy deposition heatmap colored from blue (low deposition) to red (large deposition). The signal consists of two electrons emitted from a common vertex, resulting in a region (blob) of intense deposition at both track ends. Conversely, the background shows one blob only, leading to cut-off-based discrimination, if the two blobs are properly reconstructed. 57
- 2.13 The cyan pixel highlights the current convolution pixel. The normal convolution kernel operates on all pixels within the kernel window, while the sparse one acts on non-zero neighboring pixels only. 58
- 2.14 A sample event from the simulated TrackML dataset. The left panel shows a collision event with the TrackML detector picture and the right image is a schematic representation of the upper half of the detector projected on the r - z plane. The figure is taken from [178]. 61
- 3.1 Scheme of the LHAPDF algorithm for PDF values access. The grid knots spacing is uniform for convenience only, real PDF grids are not uniform in the $(\log x, \log Q)$ plane. 68
- 3.2 Matrix multiplication functions code snippet. The `@tf.function` decorator requires to define the shape of the input tensors, where `None` signal a variable length dimension. 71
- 3.3 Time comparison of different matrix multiplication implementations. 71
- 3.4 `PDFFlow` flowchart. Blocks are color-coded as follows: red for the tool, violet for classes, green for functions and class methods, and white for interpolation algorithms. 71

3.5	PDFFlow vs LHAPDF relative difference for the NNPDF3.1 NLO central PDF. In both the sub-figures, the first column refers to differences in a grid of x points for fixed Q values, while the second column shows differences in a grid of Q values for fixed x .	73
3.6	PDFFlow vs LHAPDF relative difference for $\alpha_s(Q)$ interpolation. The left and right panels refer to NNPDF3.1 NLO and MMHT14 NLO sets, respectively.	74
3.7	PDFFlow vs LHAPDF running time comparison. Top and bottom rows plot respectively the absolute and relative execution time as functions of the input size.	74
3.8	Single top quark production. Top row: Feynman diagram. Bottom row: comparison of the execution time between PDFFlow and VegasFlow code against MG5_AMC@NLO .	75
3.9	Quark initiated VBF Higgs production. Top row: Born Feynman diagram. Bottom row: comparison of the execution time between PDFFlow and VegasFlow code against NNLOJET plus LHAPDF.	75
3.10	The examples figures	75
3.11	Relative difference between PDFFlow and LHAPDF (same as 3.5) for the MMHT2014 NLO set for all flavors.	77
4.1	The MadFlow tool-suite includes all the needed ingredients for MC event generation on hardware accelerators: on top of the VegasFlow MC integrator, the GPU phase space generator constructs physical points to be fed in the computation of the luminosity factor done with PDFFlow and the evaluation of the partonic cross section $\hat{\sigma}$ through the ME computation. The final results are presented as unweighted events.	80
4.2	The MadFlow design. The MG5_AMC@NLO plugin exports the code for the ME evaluation and connects the various MadFlow components to perform the parallel MC integration. Eventually, unweighted events are produced along with the MC estimation for the cross-section.	81
4.3	The diagrams contributing to the $pp \rightarrow t\bar{t}$ process.	84
4.4	Leading order differential cross sections for $gg \rightarrow t\bar{t}$ process at $\sqrt{s} = 13$ TeV. In both panels, the top row shows the histogram distributions output by MadFlow and MG5_AMC@NLO , while the bottom one represents the ratio of the two to highlight the statistical agreement.	86
4.5	MadFlow integration timings for different processes: $gg \rightarrow t\bar{t}$ (top left), $pp \rightarrow t\bar{t}$ (top right), $pp \rightarrow t\bar{t}g$ (bottom left), $pp \rightarrow t\bar{t}gg$ (bottom right). Comparison of the results for consumer and professional-grade CPUs (red bars) and GPUs (blue bars) hardware. The plots report the available memory alongside each related device name. We note a systematic performance improvements for GPU cards.	87
4.6	$pp \rightarrow t\bar{t}ggg$ process MadFlow timings.	88

5.1	Sketch of the ProtoDUNE-SP detector. Only one drift chamber is depicted, the other extends to the left of the CPA.	94
5.2	Wires wrapping around a ProtoDUNE-SP APA plane: U, V and W planes in green, magenta and blue, respectively.	94
5.3	The electron path drift and weighting potential in the Garfield simulation from [227]. The equipotential lines are labeled by numbers from 1 to 60 indicating the percentage with respect to V_w^{\max} , namely the electric potential on the considered wire.	98
5.4	The waveforms due to single electron drift in the Garfield simulation by [227]. The solid waveforms refer to an electron starting position directly in front of the considered wires (center path). The dashed waveforms consider the shifted electron path starting from the boundary of the simulation volume. This shows that drifting particles influence the measured current also on distant wires.	99
5.5	The MicroBooNE electronics response to an impulse signal located at $t = 0$: left panel plots the pre-amplifier response function for 4.7 mV/fC. Both diagrams are taken from the study in [227].	100
5.6	The signal processing flowchart is currently implemented by neutrino experiments such as MicroBooNE and DUNE. The figure is taken from [227].	103
5.7	The GCONV layer. The input vector \mathbf{H}_i^l is updated to \mathbf{H}_i^{l+1} by means of NLA and 2D convolution operations. NLA relies on a previously computed KNN graph.	104
5.8	The GCNN neural network architecture. Input and output are batches of noisy \mathbf{x} and denoised \mathbf{x}_{DN} images, respectively. The network is organized as low-pass (LPF) and high-pass (HPF) filters as in [239]. As explained in section 5.3.2 we concatenate an ROI block, pre-trained on background vs signal binary segmentation, with multi-scale preprocessing layers.	105
5.9	The USCG-Net architecture. The adaptive pooling layer has a two-fold utility: in the left branch it downscales the input, while in the right one, it provides upsampling. We employ the first 4 blocks of a pre-trained ResNeXt-50 in the shallowest layers of the network. The blocks respectively contain 9, 12, 18 and 9 convolutional layers. The horizontal dashed lines represent residual connections with a 1×1 convolution for enhanced expressivity and are employed to match the number of image channels between the left and right branches. The SCG layer builds the adjacency matrix \mathbf{A} and the vectors of node features $\hat{\mathbf{Z}}$ to be passed into a GCN layer to output the final representation of the nodes $\hat{\mathbf{Z}}'$.	106
5.10	Example taken from <code>dunetpc v08_24_00</code> dataset. The horizontal orange dashed line in the first panel marks the channel to extract the waveforms from.	108
5.11	Example taken from <code>dunetpc v09_10_00</code> dataset. The horizontal orange dashed line in the first panel marks the channel to extract the waveforms from.	108

- 5.12 Detail of a raw waveform from `dunetpc v08_24_00` dataset: label, traditional algorithm and neural network outputs. The version, `v08` or `v09`, next to the model name in the legend refers to which dataset the corresponding model was trained on. 113
- 5.13 Detail of a raw waveform from `dunetpc v09_10_00` dataset: label, traditional algorithm and neural network outputs. The version, `v08` or `v09`, next to the model name in the legend refers to which dataset the corresponding model was trained on. 113

- 6.1 Scheme of the Pandora reconstruction workflow for a ProtoDUNE-SP event. The red blobs refer to data structures that serve as inputs for the Pandora algorithms or their products. White boxes identify high-level reconstruction step and are gathered into two main pipelines: `PandoraCosmic` and `PandoraTestBeam`. In the middle, the slicing algorithm aims at isolating the Test Beam related CaloHits. The CR muon tagging algorithm, labeled by a dashed box, is taken from the LArSoft implementation. 118
- 6.2 Cosmics rays and test beam event: U plane view. Hits with the same color belong to the same main Monte Carlo simulated particle. 120
- 6.3 U plane view: 2D initial clusters with more than 5 hits computed by Pandora. 120
- 6.4 2D initial clusters purity. The histogram is peaked towards high purity values. 122
- 6.5 The CM-Net network architecture: given a feature vector of the cluster pair, outputs the probability that the cluster pair should be merged. 122
- 6.6 Test beam benchmark flowchart: marks each plane view as correct, split or lost. The threshold is $t = 90\%$. 125
- 6.7 Reconstructing MC TB slices: green bars for CM-Net, red bars for Pandora. Dashed lines represent the overall TB energy score. Rows from top to bottom represent correct, lost and bottom percentages. 125

List of Tables

1.1	The number of mixing angles and phases needed to parametrize the general unitary $N \times N$ PMNS matrix both in the case of Dirac and Majorana neutrino fields.	8
1.2	The list of experiments that are sensitive to certain neutrino mass difference ranges: characteristic values for L and E and relative ranges of $ \Delta m_{ij}^2 $. The experiments are categorized as Very Short Baseline (VBSL), Short Baseline (SBL), Medium Baseline (MBL) and Long Baseline (LBL) depending on the neutrino source-detection distance. All the numbers neglect matter effects on the oscillation probability equation. The table is taken from [24].	11
1.3	Global fits for the 3ν parameters. The two mass-ordering schemes are presented separately. The excess in the χ^2 by the IO is given by the $\Delta\chi^2$ quantity for each analysis. All the results include the contribution by the Super-Kamiokande experiment [25], which provided only the tabulated χ^2 test values for their measurements. The table is taken from [24].	12
1.4	The hierarchical approach to sample weighted n -body phase space configurations.	29
2.1	List of the most common activation functions. The parameter α in ReLU and ELU is an input positive constant. The Soft-Max activation is typical of multi-class problems: $\varphi_m(x_k)$ is the probability to obtain the k -th category out of a total of m classes.	38
2.2	Summary of the proposed architectures for jet classification. The table is inspired from [104].	53
2.3	Review of the deep learning for neutrino physics publications. The first column identifies which detector the publication focuses on. PilarNet [159] is a general-purpose open dataset for LArTPCs data. Note: [152] was published before the PilarNet [159] dataset but deals with similar data and objectives. The citations are color-coded based on the neural network type implemented in the relative work: FFNNs, CNNs, GNNs, Hexagonal CNNs, Sparse CNNs, Quantum CNNs .	59

3.1	Description of the system used for the matrix multiplication benchmark: hardware and software information.	69
3.2	Description of the systems in which the different codes have been run.	72
3.3	Time required to evaluate all 11 flavours from N_{rep} members of NNPDF3.1 NLO in a grid of 2415 points in x , using the P1 system.	76
4.1	Description of the software used for the different MadFlow experiments. The last two lines regard the software compiled for Radeon/AMD architectures.	86
4.2	Comparison of event computation time for MadFlow and MG5_AMC@NLO on Intel i9-9980XE system with 18 cores and 128 GB of RAM for CPU simulation and Nvidia Titan V 12 GB for GPU simulation.	88
5.1	Datasets for training and testing. The two samples differ in producer package version, size and event beam energies. The second dataset contains 10 events for each p energy specified.	107
5.2	Test metrics for denoising on <code>v08_24_00</code> dataset. Results for collection plane and 2 GeV beam energy only. <code>v08</code> or <code>v09</code> in the first column refer to which dataset the corresponding model was trained on.	112
5.3	Test metrics for denoising on <code>v09_10_00</code> dataset. Results for collection plane and 2 GeV beam energy only. <code>v08</code> or <code>v09</code> in the first column refer to which dataset the corresponding model was trained on.	112
6.1	List of the extracted intra and inter-cluster features. The first column groups the features into categories: the number in parentheses highlights how many components of the final feature vector the specific category gathers.	123

Introduction

Motivation

The present thesis arises in the context of particle physics and aims to investigate novel deep learning solutions in the event simulation and reconstruction pipeline. The key idea is that machine learning provides performance and accuracy speed-ups which the physics community cannot waive to. We identify two main areas of interest for our research: hardware acceleration for Monte Carlo simulation and the implementation of new deep learning-based software for reconstruction algorithms at neutrino detectors.

Hardware acceleration is defined as the process by which an application offloads certain computing tasks onto specialized hardware components accessible by the computing system, enabling greater software efficiency than would be possible when running on a general-purpose CPU alone. Our techniques leverage mainly on Graphics Processing Units (GPUs), but, in principle, other hardware might be worth testing in the future, such as Tensor Processing Units (TPUs) and, perhaps, Field Programmable Gate Arrays (FPGAs).

Monte Carlo event simulators are software tools that play a central role in HEP phenomenology. They exploit MC techniques to compute differential cross-sections of particle physics processes and provide samples of weighted and unweighted events. Simulation, indeed, is the first step into the production chain of events at hadron colliders, followed by detector simulation and reconstruction. The quantity of computational resources employed for running these tools is huge. Specifically, it has been estimated [1, 2] that the two major LHC experiments, namely ATLAS and CMS, collect an order of $\mathcal{O}(10^{10})$ events for every year of data taking and, correspondingly, they further generate a factor of 3 more simulated events. Moreover, the quantity of data is bounded to grow in the future during the High-Luminosity LHC phase, which will start towards the end of 2027. In this context, one of the ideas to successfully face this challenge is to optimize existing software to fully leverage modern hardware architectures, such as Graphics Processing Units (GPUs).

Experimental setups in High Energy Physics (HEP), therefore, produce large datasets, containing huge amounts of information. As described in section 2.2,

there have been high interest and numerous published results about applying artificial intelligence (AI) models to particle physics. The final goal is to be able to provide end-to-end data processing solutions. The hope is that AI strategies and deep learning in particular will eventually manage to scan the physics details hidden inside experimental data. Although we do not know yet whether this will happen and, further, data processing is often an obscure step towards obtaining the results, we cannot leave without the automation and the speed at which these methods manipulate data. Experiments, indeed, aim to build larger and more complex machines, which put computing facilities under extreme stress.

We dedicate a considerable part of the present thesis to investigate deep learning applications to the reconstruction workflow in the context of the Deep Underground Neutrino Experiment (DUNE). In particular, we discuss two algorithms and their solution employing neural network techniques.

Thesis overview

Main results

Interpolating Parton Distribution Functions on GPUs: `PDFFlow` is the first Parton Distribution Functions access tool able to run on Graphics Processing Units. We demonstrated the possibility to implement software that can exploit hardware acceleration while maintaining the same level of accuracy as the state-of-the-art methods in the field. The usage of the software does not require specific knowledge or experience in low-level programming languages dedicated to hardware accelerators. Coupling `PDFFlow` with the existent `VegasFlow` program, we delivered the first particle physics phenomenology calculation at next-to-leading order accuracy in perturbation theory on GPU.

Automated Monte Carlo event generator on GPU: The `MadFlow` tool-suite encapsulates the implementations of `VegasFlow` and `PDFFlow` in a single software, that automates the computation particle physics processes on hardware accelerators at leading order. The program takes advantage of the `MG5_AMC@NLO` meta-programming capabilities to automatically produce code for GPU matrix element calculations and phase space sampling for user-requested particle physics processes. We fully test the performance and accuracy results of `MadFlow` for different physical processes, proving that the tool is able to handle complex computations involving a high number of Feynman diagrams even despite complying with the memory constraints of modern GPUs.

ProtoDUNE-SP raw data denoising with Graph Neural Networks: We investigate different strategies for denoising raw data at the ProtoDUNE-SP experiment designing two novel Graph Neural Networks architectures. The work addresses the first step of reconstruction for Liquid Argon Time Projecting Chamber detectors. We train and test our neural networks on simulated datasets generated with the `LArSoft` framework. We prove that our models' performance is competitive and, in fact, outperforms the traditional methods currently employed for denoising raw data by the latest neutrino experiments.

Slicing algorithm at ProtoDUNE-SP with deep neural networks: In the context of the neutrino event reconstruction, the slicing method aims to cluster the detector hits into sets named slices, where all the hits in each group belong to the same main interaction that happened within the detector. We implement a neural network model to process the detector hits, to replace the traditional slicing method included in the Pandora reconstruction framework based on topological algorithms. We train our architecture on simulated data and design a first test to compare the clustering performance of our model against the state-of-the-art one at separate detector hits between test beam and cosmic ray interactions. We discover that our approach outperforms the traditional one implemented in Pandora.

Organizational note

The present thesis consists of three Parts, for a total of six Chapters. Each part is devoted to the study of an application of deep learning in the context of particle physics. The three parts split the discussion into an introduction of physical and computer science background, a presentation of our novel contributions to simulation and a discussion of the techniques implemented for detector reconstruction. Part I is composed of chapters 1 and 2 and give an overview of the physics and computer science background, respectively. We discuss the Standard Model of particle physics and give a more detailed insight into neutrino physics and Monte Carlo techniques. On the computer science side, we introduce the fundamental concepts of artificial intelligence and machine learning, providing also an overview of the main state-of-the-art AI applications in the particle physics research field. Part II comprehends chapters 3 and 4 and presents the construction and characterization of efficient automated computation methods for parton distribution functions interpolation and Monte Carlo simulation of particle physics processes on hardware accelerators. Part III encompasses chapter 5 and 6 describing the implementation of novel deep learning-based algorithms for event reconstruction at the ProtoDUNE-SP detector. We discuss different strategies designed for experimental raw data denoising and a clustering approach for detector hits named slicing. Parts II and III have appeared in peer-reviewed publications in scientific journals and international conference proceedings. Some variations have been made in the presentation of previously published results, to maintain consistency of style and content structure throughout the manuscript.

Chapter 1: Physics background We give a high-level overview of the Standard Model of particle physics, describing the model's particle content with a focus on the fermion sector. We introduce the Higgs mechanism, the main technique used to include mass terms for particle fields without explicitly breaking gauge symmetry. We discuss the leptonic sector with a focus on neutrinos, investigating the neutrino oscillation phenomenon and how to extend the Standard Model to include neutrino masses both from a theoretical and experimental point of view. The last section of the chapter is devoted to a presentation of numerical integration and Monte Carlo techniques. We also describe the most

widely used methods for sample generation following given probability density functions: in this context, we focus also on the physical phase space sampling techniques for collider events introducing both a hierarchical and a democratic (RAMBO) approach.

Chapter 2. Introduction to deep learning and its physics applications This chapter includes a review of the machine learning and deep learning algorithms and a review of the most important applications of these techniques to the particle physics research field available in the literature. We define the concept of learning algorithms and neural networks, giving examples of the main operations exploited in this field such as matrix multiplications, image convolutions and the attention mechanism. We finally present a study on stochastic optimization methods, used to train neural networks. The last part of the chapter summarizes the main applications of such techniques in particle physics, highlighting their great success and spread in many fields, specifically we concentrate on reconstruction at colliders (jet physics and particle tracking) and neutrino physics. Other applications, like fast event simulation and detection of new physics, are mentioned in passing only.

Chapter 3. Interpolating parton distribution functions Our first novel contribution is in the field of parton distribution functions (PDF): we design the `PDFFlow` software that can exploit hardware acceleration to provide PDF values access. In this chapter, we briefly set the stage by introducing the concept of PDFs and giving a detailed description of the state-of-the-art tool for PDF access, namely LHAPDF6. We present the LHAPDF framework concept from the historical point of view and its interpolating algorithm. We leverage the TensorFlow library to demonstrate the performance gain of our software with respect to the LHAPDF6 implementation while matching their output accuracy. Finally, we benchmark our setup on particle physics experiments both at leading and next to leading order in perturbation theory.

Chapter 4. MadFlow: a Monte Carlo event generator on GPUs The work on hardware accelerators continues with the implementation of a full tool suite able to port a complete Monte Carlo event generator for particle physics processes on Graphics Processing Units (GPUs). We exploit the same concepts of `PDFFlow` to design a matrix element generator and a phase space sampler that is compatible with GPUs. Further, we provide an algorithm to store the generated events asynchronously to preserve the performance speed-up delivered by our framework when coupled to hardware accelerators. As in the `PDFFlow` chapter, the benchmarks are supported by particle physics processes examples.

Chapter 5. Denoising ProtoDUNE-SP Raw Data with deep learning This chapter starts the discussion about reconstruction algorithms for neutrino LArTPC detectors, in particular, ProtoDUNE-SP. We introduce first the design of the ProtoDUNE-SP detector and how Liquid Argon Time Projecting Chambers record information about physics events. Our work focuses on the first stage of the signal-processing pipeline:

raw data denoising, that is taking the detector signal and automatically mitigating the noise inherently introduced by the electronics. The state-of-the-art technique that tackles this problem is deconvolution. Instead, we investigate different deep learning approaches based on graph neural networks.

Chapter 6. Clustering at ProtoDUNE-SP with supervised learning

The final chapter of this thesis is devoted to the slicing algorithm. Slicing is a step in the reconstruction chain at LArTPC detectors and is currently managed by the Pandora framework. Thus, we first describe the Pandora concept and how it implements event reconstruction. We present, then, our deep learning-based approach to the slicing algorithm along with a benchmark comparison of our method against the Pandora one.

Part I

Physics and computer science background

Physics background

Contents

1.1	The standard model of particle physics	3
1.2	Neutrino physics	5
1.2.1	SM neutrino	5
1.2.2	Neutrino oscillation	7
1.2.3	Neutrino masses	12
1.3	Monte Carlo techniques	16
1.3.1	Numerical Integration	16
1.3.2	Monte Carlo Integration	19
1.3.3	Adaptive Monte Carlo: VEGAS algorithm	23
1.3.4	Sample generation	24
1.3.5	Phase space generation from particle collisions	27

In this chapter, we introduce the physics topics which the present thesis is based upon. We discuss the Standard Model (SM) of particle physics, describing the model's particle content and highlighting its gauge symmetries. Then, we restrict our attention to the physics of neutrinos, given the central role of such particles in part 4.3. In particular, we focus on the neutrino oscillation mechanism, which implies a non-zero mass of such particles and requires extending the SM to include lagrangian mass terms for neutrinos. We give both theoretical and experimental insights into this research field.

We conclude the chapter with a dissertation on Monte Carlo (MC) techniques, the fundamental tools for phenomenology studies. We present the mathematical formalism behind these methods to show how MC methods are suited to sample from high-dimensional probability distributions to generate events for particle physics processes.

1.1 The standard model of particle physics

In this section, we set the stage by giving a brief introduction of the standard model [3] of particle physics. The SM describes our current understanding of three out of four fundamental interactions in nature: the strong, weak and electromagnetic forces. The last fundamental force, gravity, is not included in the theory, given that its mathematical properties, e.g. non-renormalizability, make it incompatible with the model. The SM lagrangian, containing only 19

free parameters, effectively yields accurate predictions of physical processes validated by many experimental results [4]. Despite its success, the model still contains open questions [5], such as the lack of a consistent description of neutrinos, whose discussion will be presented in section 1.2. Here, we present a descriptive overview of the SM, leaving the interested reader to the detailed dissertation of specialized quantum field theory (QFT) books, such as [6].

Formally, the SM is a Yang Mills theory with $SU(3)_C \times SU(2)_L \times U(1)_Y$ gauge symmetry group, where the subscripts C , L and Y stand respectively for the color group of Quantum Chromodynamics (QCD), the fact that the weak force couples only to left chiral components of fermion fields and the hypercharge. In such theories, there is always a one-to-one correspondence between the generators of the symmetry group and the bosonic fields representing force carriers. The physical fields for the gluons correspond to the 8 generators of $SU(3)_C$. The $3 + 1$ generators of $SU(2)_L \times U(1)_Y$, instead, are linked with the electroweak physical bosons, namely $W^\pm/Z/\gamma$, through a spontaneous symmetry breaking (SSB) mechanism [7]. In QFT, including a mass term for gauge bosons in the lagrangian would explicitly break the local symmetry. Instead, the SSB is a process that allows gauge bosons to acquire mass coupling with a scalar field, which gains a non-zero vacuum expectation value (VEV). In the SM, this scalar field is called the Higgs boson ϕ and it is realized as a doublet of fields:

$$\phi = \begin{pmatrix} \phi^+ \\ \phi^0 \end{pmatrix} \quad \langle \phi \rangle = \begin{pmatrix} 0 \\ \frac{v}{\sqrt{2}} \end{pmatrix} \quad (1.1)$$

where upper and lower components of ϕ are two complex scalar fields and the angular parentheses represent the VEV operator. When ϕ^0 acquires a non-zero VEV $v\sqrt{2}$, it is responsible to give mass to the SM particles.

The fermionic sector of the SM is organized in three families, containing quark doublets with one up (u/c/t) and one down (d/s/b) quark type each and the leptons, gathering the charged leptons (e/ μ / τ) and their associated neutrinos ($\nu_e/\nu_\mu/\nu_\tau$). Leptons interact with the electroweak force only. In particular, the SM neutrinos are massless and carry no electromagnetic charge and, therefore, cannot be easily experimentally revealed. Figure 1.1 schematically shows the elementary particles predicted by the SM. In particular, quarks in the SM lagrangian acquire masses through Yukawa interactions with the Higgs boson fields. The lagrangian terms for such interactions are:

$$-\mathcal{L}_{Y,\text{quark}} = Y_{ij}^d \bar{Q}_L^i \phi d_R^j + Y_{ij}^u \bar{Q}_L^i \epsilon \phi^* u_R^j + \text{h.c.} \quad (1.2)$$

where the $Y^{u,d}$ are complex 3×3 matrices, i, j are the generation labels (u, c, t in the case of up-type quarks), ϵ is the 2×2 anti-symmetric tensor. Q_L^i , d_R^j and u_R^j are the quark fields in the weak eigenstate basis, namely Q_L^i are left-handed quark doublets and the others represent the quark right-handed singlets.

When the Higgs field ϕ acquires a non-zero VEV, the equation 1.2 can be expanded around that value, yielding the explicit quark mass terms. However, the physical states are obtained by diagonalizing the $Y^{u,d}$ matrices by the following bi-unitary transformations:

$$Y^f \rightarrow M_{\text{diag}}^f = V_L^f Y^f V_R^{f\dagger} \quad (1.3)$$

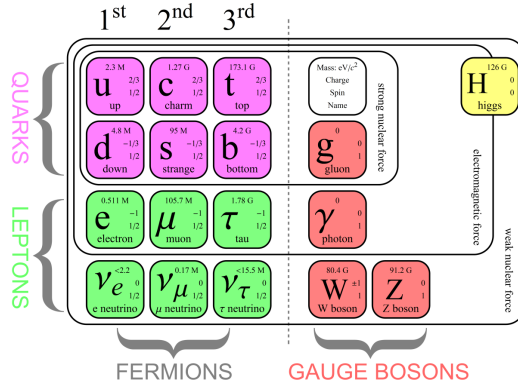


Figure 1.1: The standard model of particle physics. The figure is taken from [8].

for $f = u, d$ and all the V are unitary matrices. This is possible of course only if the quark fields transform accordingly. In this new basis, i.e. the mass basis, the equation 1.2 is properly diagonalized, while the charged current weak interactions W^\pm are modified as:

$$\frac{-g}{\sqrt{2}} (\bar{u}_L, \bar{c}_L, \bar{t}_L) \gamma^\mu W_\mu^+ V_{\text{CKM}} \begin{pmatrix} d_L \\ s_L \\ b_L \end{pmatrix} + \text{h.c.}, \quad V_{\text{CKM}} = V_L^\dagger V_L^u = \begin{pmatrix} V_{ud} & V_{us} & V_{ub} \\ V_{cd} & V_{cs} & V_{cb} \\ V_{td} & V_{ts} & V_{tb} \end{pmatrix} \quad (1.4)$$

The V_{CKM} is the Cabibbo-Kobayashi-Maskawa (CKM) matrix [9], which mixes the weak-flavor eigenstates to obtain the mass ones. The standard parametrization of the CKM matrix [10] involves three angles ($\theta_{12}, \theta_{13}, \theta_{23}$) and a CP-violating phase δ [11]:

$$V_{\text{CKM}} = \begin{pmatrix} 1 & 0 & 0 \\ 0 & c_{23} & s_{23} \\ 0 & -s_{23} & c_{23} \end{pmatrix} \begin{pmatrix} c_{13} & 0 & s_{13}e^{-i\delta} \\ 0 & 1 & 0 \\ -s_{13}e^{i\delta} & 0 & c_{13} \end{pmatrix} \begin{pmatrix} c_{12} & s_{12} & 0 \\ -s_{12} & c_{12} & 0 \\ 0 & 0 & 1 \end{pmatrix} \quad (1.5)$$

where $s_{ij} = \sin \theta_{ij}$ and $c_{ij} = \cos \theta_{ij}$. A review on the latest experimental measures of the values of the CKM matrix can be found at [12].

1.2 Neutrino physics

1.2.1 SM neutrino

The standard model neutrinos are part of the lepton doublets of $SU(2)_L$:

$$L_{L\alpha} = \begin{pmatrix} \nu_\alpha \\ l_\alpha \end{pmatrix}_L \quad (1.6)$$

where the subscripts α and L indicate the α -th lepton family the left-handed projection of the fields obtained acting with the projector $P_L = \frac{1}{2}(1 - \gamma_5)$. We note that within the SM the right-handed charged leptons are singlets of weak interactions and no right-handed neutrinos exist. Further, neutrinos do

not carry any strong or electromagnetic charge, but are subject to the following charged-current (CC) and neutral-current (NC) weak interactions:

$$-\mathcal{L}_{CC} = \frac{g}{\sqrt{2}} \sum_{\alpha} \bar{\nu}_{L\alpha} \gamma^{\mu} l_{L\alpha}^{-} W_{\mu}^{+} + \text{h.c.} \quad (1.7)$$

$$-\mathcal{L}_{NC} = \frac{g}{2 \cos \theta_W} \sum_{\alpha} \bar{\nu}_{L\alpha} \gamma^{\mu} \nu_{L\alpha} Z_{\mu}^0 \quad (1.8)$$

where g is the weak coupling constant and $\cos \theta_W$ is the Weinberg angle. In particular, the NC interaction influences the decay width of the Z^0 boson in the SM, which, in turn, is related to the number of measured active light neutrinos N_{ν} .

In general, the SM neutrinos are dubbed active neutrinos since they couple with the SM interactions as seen above. There exist, however, Beyond Standard Model (BSM) theories that include the possibility to have other neutrinos that are singlets of the SM gauge group and therefore are called sterile. Both light (with mass $m_{\nu} \leq M_Z/2$) and heavy sterile neutrino hypotheses are present in BSM theories. Experiments at LEP on the measurement of the decay width of the Z^0 boson constrained the N_{ν} number [13]:

$$N_{\nu} = \frac{\Gamma_Z^{\text{invisible}}}{\Gamma(Z \rightarrow \nu \bar{\nu})_{\text{SM}}} = 2.9840 \pm 0.0082 \quad (1.9)$$

This measurement excluded the fourth active light neutrino option.

A neutrino mass term cannot be included in the SM because it would break the symmetries of the model. In fact, the SM exhibits an accidental global symmetry besides the gauge $SU(3)_C \times SU(2)_L \times U(1)_Y$ one:

$$G_{\text{SM}}^{\text{global}} = U(1)_B \times U(1)_{L_e} \times U(1)_{L_{\mu}} \times U(1)_{L_{\tau}} \quad (1.10)$$

which reflects the conservation of the baryon number B and the leptonic flavor numbers $L_{e,\mu,\tau}$. Moreover, also the total lepton number $L = L_e + L_{\mu} + L_{\tau}$ is conserved, being the quantum number associated with the sub-group of $G_{\text{SM}}^{\text{global}}$. We show that these symmetries forbid any neutrino mass term in the SM.

The SSB mechanism allows all the SM fermions to acquire a mass coupling with the Higgs boson field like in equation 1.2. Charged leptons admit a similar contribution:

$$-\mathcal{L}_{Y,\text{lep}} = Y_{\alpha\beta}^l \bar{L}_{L\alpha} \phi E_{R\beta} + \text{h.c.} \quad (1.11)$$

where E_{Ri} are the right-handed singlets leptons of $SU(2)_L$ and ϕ is the Higgs boson field. The $Y_{\alpha\beta}^l$ is the 3×3 Yukawa matrix for leptons analogous to the quark one. Expanding the Higgs field around its VEV v one obtains terms such as $Y_{\alpha\beta}^l \frac{v}{\sqrt{2}} l_{L\alpha} l_{R\beta}$, yielding mass $m_{\alpha\beta}^l = Y_{\alpha\beta}^l \frac{v}{\sqrt{2}}$ to the leptons. Such a lagrangian term cannot be written for neutrinos, since the right-handed field is not available.

In principle, a mass term like $\bar{L}_L L_L^c$ might arise at loop level in the SM, where $L^c = C \bar{L}^T$ is the charge conjugated field and C is the charge conjugation matrix satisfying $C \gamma_{\mu} C^{-1} = -\gamma_{\mu}^T$. However, this would break the

total lepton number conservation accidental symmetry of the model, since the term would produce interactions with $|\Delta L| = 2$. In light of these considerations, the SM neutrinos are, in fact, massless, opening the problem of consistently describing the neutrino oscillation mechanism (see the next section 1.2.2) while preserving gauge invariance and renormalizability of the theory.

1.2.2 Neutrino oscillation

The first intuition of the neutrino oscillation dates back to 1957 by Pontecorvo [14, 15], which advocated a mechanism similar to the kaon anti-kaon mixing for the mesonium (μ^+e^-) and anti-mesonium (μ^-e^+) oscillation. This matter-antimatter oscillation was possible only by violating the leptonic number conservation. Some years later, the first quantitative neutrino mixing model was proposed in [16] and further refined in [17, 18].

The idea is that the left-handed flavor $\nu_{(e,\mu,\tau)L}$ and mass $\nu_{(1,2,3)L}$ eigenstates of the active neutrinos are linked by a unitary transformation, represented by the so-called Pontecorvo-Maki-Nakagawa-Sakata (PMNS) matrix U :

$$\begin{pmatrix} \nu_e \\ \nu_\mu \\ \nu_\tau \end{pmatrix}_L = \begin{pmatrix} U_{e1} & U_{e2} & U_{e3} \\ U_{\mu 1} & U_{\mu 2} & U_{\mu 3} \\ U_{\tau 1} & U_{\tau 2} & U_{\tau 3} \end{pmatrix} \begin{pmatrix} \nu_1 \\ \nu_2 \\ \nu_3 \end{pmatrix}_L \quad (1.12)$$

Employing greek indices for the flavor states and latin ones for the mass states, the equation above can be written in short form:

$$\nu_{\alpha L}(x) = \sum_i U_{\alpha i} \nu_{iL}(x) \quad (1.13)$$

The matrix U satisfies the unitary conditions:

$$(UU^\dagger)_{\alpha\beta} = \sum_i U_{\alpha i} U_{\beta i}^* = \delta_{\alpha\beta}, \quad (U^\dagger U)_{ij} = \sum_\alpha U_{\alpha i}^* U_{\alpha j} = \delta_{ij}, \quad (1.14)$$

A 3×3 unitary matrix can be parametrized by 3 angles and 6 phases. However, it is possible to transform the neutrino and charged lepton fields with an unobservable global phase to absorb 5 out of the 6 PMNS phases. The aforementioned transformation can be made manifest considering the lagrangian term of the CC interaction, equation 1.7, which is left invariant by the following:

$$l_\alpha(x) \rightarrow e^{i\phi_\alpha} l_\alpha(x), \quad \nu_i(x) \rightarrow e^{i\phi_i} \nu_i(x), \quad U_{\alpha i} \rightarrow e^{i\phi_{\alpha i}} U_{\alpha i} \quad (1.15)$$

where $\phi_{\alpha i} = \phi_\alpha - \phi_i$. There exist indeed only 5 independent phase differences $\phi_{e1}, \phi_{e2}, \phi_{e3}, \phi_{\mu 1}, \phi_{\tau 1}$ among the 9 possible ones.

This is only true when the neutrinos are described by Dirac fields, while it is not the case if neutrinos are Majorana. Indeed the phase transformation introduced by equation 1.15 would yield a complex mass for the Majorana fields:

$$\frac{1}{2} m_i \nu_{iL}^T C \nu_{iL} \rightarrow \frac{1}{2} m_i e^{2i\phi_i} \nu_{iL}^T C \nu_{iL} \quad (1.16)$$

Therefore, in this case, it is not possible to redefine the ν_i fields to absorb the phases and we have, in fact, 3 phases left to describe the PMNS matrix.

Count	Majorana	Dirac
Rescalable fields	N	$2N - 1$
Angles θ_i	$\frac{1}{2}N(N - 1)$	$\frac{1}{2}N(N - 1)$
Phases δ_i	$\frac{1}{2}N(N - 1)$	$\frac{1}{2}(N - 1)(N - 1)$
Total free parameters	$N(N - 1)$	$(N - 1)^2$

Table 1.1: The number of mixing angles and phases needed to parametrize the general unitary $N \times N$ PMNS matrix both in the case of Dirac and Majorana neutrino fields.

We report a summary of the number of independent parameters needed to describe the PMNS matrix for the general case of N lepton flavors in table 1.1.

The standard parametrization of the PMNS matrix for 3 flavor neutrinos is similar to the CKM one, see equation 1.5, except for the presence of an extra $U(1)$ matrix P in the Majorana case:

$$U = \begin{pmatrix} 1 & 0 & 0 \\ 0 & c_{23} & s_{23} \\ 0 & -s_{23} & c_{23} \end{pmatrix} \begin{pmatrix} c_{13} & 0 & s_{13}e^{-i\delta_{CP}} \\ 0 & 1 & 0 \\ -s_{13}e^{i\delta_{CP}} & 0 & c_{13} \end{pmatrix} \begin{pmatrix} c_{12} & s_{12} & 0 \\ -s_{12} & c_{12} & 0 \\ 0 & 0 & 1 \end{pmatrix} P \quad (1.17)$$

where $c_{ij} = \cos \theta_{ij}$, $s_{ij} = \sin \theta_{ij}$ with the mixing angles θ_{ij} lying in the first quadrant $[0, \pi/2]$ and $\delta_{CP} \in [0, 2\pi)$ is the Dirac phase responsible for the violation of the CP symmetry. Multiple representations of the P matrix are present in the literature and all depend on two Majorana phases, which can be taken in the interval $[0, \pi)$:

$$P = \begin{pmatrix} e^{i\alpha_1} & 0 & 0 \\ 0 & e^{i\alpha_2} & 0 \\ 0 & 0 & 1 \end{pmatrix}, \quad \begin{pmatrix} 1 & 0 & 0 \\ 0 & e^{i\phi_2} & 0 \\ 0 & 0 & e^{i(\phi_3 + \delta_{CP})} \end{pmatrix}, \quad \begin{pmatrix} e^{i\rho} & 0 & 0 \\ 0 & 1 & 0 \\ 0 & 0 & e^{i\sigma} \end{pmatrix} \quad (1.18)$$

Majorana masses do not have any influence on the neutrino oscillation process we are going to discuss, but enter in the calculation of lepton violating processes such as the neutrinoless double beta decay $0\nu\beta\beta$ [19, 20].

In the following, we introduce the description of the neutrino oscillation phenomenon, which will be described by the transition probability $P(\nu_\alpha \rightarrow \nu_\beta)$ of a certain neutrino with flavor α to become a neutrino with flavor β . We will show that the oscillation mechanism requires massive neutrinos to be observed. Therefore we will consider these particles to have a small mass m_i for $i = 1, 2, 3$ and always move at ultra-relativistic speed as it happens in all realistic experimental conditions. We will present the main techniques to design neutrino mass terms for BSM lagrangians in the next section 1.2.3.

The ideal neutrino oscillation experiment in vacuum involves a three-step process: the production of a neutrino of pure flavor state α , the propagation of the particle along a distance L and the detection of the final flavor β at the end of the apparatus setup. Let us consider, then, an initial state produced by some CC process, (e.g charged pion decay $\pi^+ \rightarrow \mu^+ \nu_\mu$):

$$|\nu(t=0)\rangle = |\nu_\alpha\rangle = \sum_i U_{\alpha i}^* |\nu_i\rangle \quad (1.19)$$

The propagation through the vacuum is described by the evolution operator obtained by the exponentiation of the Hamiltonian and leads to the following

state at time t :

$$|v(t)\rangle = \sum_i U_{\alpha i}^* e^{-iE_i t} |v_i\rangle = \sum_i U_{\alpha i}^* e^{-iE_i t} \sum_{\beta} U_{\beta i} |v_{\beta}\rangle \quad (1.20)$$

The final probability amplitude is obtained by acting with the state $\langle v_{\beta}|$ and the corresponding probability by applying the modulus square to the bra-ket notation:

$$P(\nu_{\alpha} \rightarrow \nu_{\beta}) = |\langle v_{\beta} | v(t) \rangle|^2 = \left| \sum_i U_{\beta i} U_{\alpha i}^* e^{-iE_i t} \right|^2 = \sum_{ij} (J_{\alpha\beta})_{ij} e^{-i(E_i - E_j)t} \quad (1.21)$$

where we have defined the self-adjoint matrix $(J_{\alpha\beta})_{ij} = U_{\alpha i} U_{\beta i}^* U_{\alpha j}^* U_{\beta j}$. It is clear from this definition that the $J_{\alpha\beta}$ matrices do not depend on the Majorana phases, since the P factor of equation 1.17 cancel out in the product.

The energy eigenvalues E_i in the ultra-relativistic limit are dominated by the particle kinetic energy and can be expanded for $m_i^2/p^2 \ll 1$:

$$E_i = \sqrt{\mathbf{p}^2 + m_i^2} = |\mathbf{p}| + \frac{m_i^2}{2E}, \quad \text{with } E \simeq |\mathbf{p}| \quad (1.22)$$

Inserting this approximation into equation 1.21 yields:

$$P(\nu_{\alpha} \rightarrow \nu_{\beta}) = \sum_{ij} (J_{\alpha\beta})_{ij} \exp\left(i \frac{\Delta m_{ji}^2 L}{2E}\right) \quad (1.23)$$

where $L = ct$ and $\Delta m_{ji}^2 = m_j^2 - m_i^2$ is the squared mass difference between the neutrino mass eigenstates. After some algebraic manipulations, we obtain:

$$P(\nu_{\alpha} \rightarrow \nu_{\beta}) = \delta_{\alpha\beta} - 4 \sum_{i < j} \Re(J_{\alpha\beta})_{ij} \sin^2\left(\frac{\Delta m_{ij}^2 L}{4E}\right) + 2 \sum_{i < j} \Im(J_{\alpha\beta})_{ij} \sin\left(\frac{\Delta m_{ij}^2 L}{2E}\right) \quad (1.24)$$

This result makes evident that in order to have neutrino oscillation, we should not have a degenerate mass spectrum and a trivial flavor mixing matrix, namely $\Delta m_{ij}^2 \neq 0$ and $U \neq \mathbb{I}$, respectively. The oscillation probability $P(\nu_{\alpha} \rightarrow \nu_{\beta})$ depends on the four parameters of the PMNS matrix (θ_{12} , θ_{13} , θ_{23} and δ_{CP}) and the two independent squared mass differences (Δm_{21}^2 , Δm_{31}^2).

The violation of the CP symmetry is given by the fact that the probabilities for the particles are not the same as for the anti-particles. We define the CP asymmetry parameter as¹:

$$\Delta P_{\alpha\beta} = P(\nu_{\alpha} \rightarrow \nu_{\beta}) - P(\bar{\nu}_{\alpha} \rightarrow \bar{\nu}_{\beta}) \quad (1.25)$$

¹The C, P, T discrete symmetries transform the $P(\nu_{\alpha} \rightarrow \nu_{\beta})$ as follows:

$$\begin{aligned} P(\nu_{\alpha} \rightarrow \nu_{\beta}) &\xrightarrow{CP} P(\bar{\nu}_{\alpha} \rightarrow \bar{\nu}_{\beta}) \\ P(\nu_{\alpha} \rightarrow \nu_{\beta}) &\xrightarrow{T} P(\nu_{\beta} \rightarrow \nu_{\alpha}) \\ P(\nu_{\alpha} \rightarrow \nu_{\beta}) &\xrightarrow{CPT} P(\bar{\nu}_{\beta} \rightarrow \bar{\nu}_{\alpha}) \end{aligned}$$

Note that the exchange from neutrinos to anti-neutrinos is achieved by CP rather than C, because the latter would transform $\nu_L \rightarrow \bar{\nu}_L$ which, in fact, do not exist in the SM.

As a consequence of equation 1.24, the investigation of the CP violation should be done in the appearance channels ($\beta \neq \alpha$), rather than in disappearance ones ($\beta = \alpha$). The latter case, indeed, yields the same probability for neutrino and anti-neutrinos since the PMNS matrix appear in the formula only in the combination $|U_{\alpha i} U_{\alpha i}^*|$, which is real. Constraints on the CP violation in neutrino oscillation can be derived expressing the asymmetry parameter in the following form [21, 22]:

$$\Delta P_{\alpha\beta} = \pm 16J \sin\left(\frac{\Delta m_{21}^2 L}{4E}\right) \sin\left(\frac{\Delta m_{31}^2 L}{4E}\right) \sin\left(\frac{\Delta m_{32}^2 L}{4E}\right) \quad (1.26)$$

where the sign of the right-hand side is + for even permutations of (e, μ, τ) , – for the odd ones instead, and the quantity J is called the Jarlskog invariant and equals to:

$$J = \Im(J_{e\mu})_{12} = \frac{1}{8} \cos \theta_{13} \sin 2\theta_{12} \sin 2\theta_{13} \sin 2\theta_{23} \sin \delta_{\text{CP}} \quad (1.27)$$

Interestingly, the form of the asymmetry parameter tells that it is universal and do not depend on the particular observation channel: $\Delta P_{e\mu} = \Delta P_{\tau e} = \Delta P_{\mu\tau}$. The asymmetry parameter product is non-zero only if all of its factors are non-zero. Therefore, to observe CP violation, the mass spectrum should be non-degenerate (as it should have been to observe the oscillation) and, further, the parameters of the PMNS matrix should obey:

$$\theta_{ij} \neq 0, \quad \delta_{\text{CP}} \neq 0, \pi \quad (1.28)$$

Equation 1.24 is valid in general for all numbers of neutrino flavors N . In fact, in many situations, such as in the oscillation of solar and atmospheric neutrinos, it is possible to neglect subleading terms and CP violation effects and consider just a two-flavor approximation. In these cases, the PMNS matrix reduces to a 2×2 rotation by an angle θ and there is just one squared mass difference Δm^2 to take into account. The appearance probability becomes:

$$P(\nu_\alpha \rightarrow \nu_\beta) = P(\bar{\nu}_\alpha \rightarrow \bar{\nu}_\beta) = \sin^2 \theta \sin^2\left(\frac{\Delta m_{ij}^2 L}{4E}\right) \quad (1.29)$$

The oscillation probability for neutrino appearance, equation 1.24, describes the probability that a neutrino ν_α produced by some source A is revealed after propagation in the vacuum for a distance L by a detector B as ν_β . This ideal scheme, however, represents only an approximation of the real case. First, source A never produces a beam of monoenergetic neutrinos, but rather a flux of particles with an energy spectrum $\Phi(E)$. Second, the propagation over long distances does not happen in vacuum, therefore, especially in the case of layers of matter with high density, a proper description of the propagation should be implemented (see [23, 24] for a detailed description of this topic). Third, detector B does not have infinite energy resolution but rather presents an efficiency $\epsilon(E)$ to reveal a certain process with cross-section $\sigma(E)$.

In this context, the final result for the appearance probability, given in equation 1.24, is an expected value given by the convolution of the theoretical

Experiment	Baseline	$L(\text{m})$	$E(\text{MeV})$	$ \Delta m_{ij}^2 (\text{eV})$
Solar		10^{10}	1	10^{-10}
Atmospheric		$10^4 - 10^7$	$10^2 - 10^5$	$10^{-1} - 10^{-4}$
Reactor	VSBL-SBL-MBL	$10 - 10^3$	1	$1 - 10^{-3}$
	LBL	$10^4 - 10^5$		$10^{-4} - 10^{-3}$
Accelerator	SBL	10^2	$10^3 - 10^4$	> 0.1
	LBL	$10^5 - 10^6$		$10^{-2} - 10^{-3}$

Table 1.2: The list of experiments that are sensitive to certain neutrino mass difference ranges: characteristic values for L and E and relative ranges of $|\Delta m_{ij}^2|$. The experiments are categorized as Very Short Baseline (VSBL), Short Baseline (SBL), Medium Baseline (MBL) and Long Baseline (LBL) depending on the neutrino source-detection distance. All the numbers neglect matter effects on the oscillation probability equation. The table is taken from [24].

probability $P_{\alpha\beta}(E)$ with the detection ingredients named above:

$$\begin{aligned}
\langle P_{\alpha\beta} \rangle &= \frac{\int d\Phi(E) \sigma(E) P_{\alpha\beta}(E) \epsilon(E)}{\int d\Phi(E) \sigma_{\text{tot}}(E) \epsilon(E)} \\
&= \delta_{\alpha\beta} - 4 \sum_{i < j} \Re(J_{\alpha\beta})_{ij} \langle \sin^2 X_{ij} \rangle + 2 \sum_{i < j} \Im(J_{\alpha\beta})_{ij} \langle \sin(2) X_{ij} \rangle
\end{aligned} \tag{1.30}$$

where the X_{ij} quantity can be expressed by restoring the SI units of measure:

$$X_{ij} = \frac{\Delta m_{ij}^2 L}{4E} = 1.267 \frac{\Delta m_{ij}^2}{\text{eV}^2} \frac{L/E}{\text{m/MeV}} \tag{1.31}$$

The above equations highlight that the probability oscillates along the distance traveled by the neutrinos with period: $4\pi E / |\Delta m_{ij}^2|$. Also, the sin functions are averaged, which brings two alternative behaviors discriminated by the value of the ratio between energy and distance: if $(E/L) \ll |\Delta m_{ij}^2|$, the argument of the oscillating functions is small and the probability goes to zero, instead if $(E/L) \geq |\Delta m_{ij}^2|$, the function is rapidly oscillating and it gets averaged out to $\langle \sin^2 X_{ij} \rangle = 1/2$. As a consequence, the experiments looking for measuring the neutrino mass difference will be only sensible to some mass intervals based on their experimental setup. Table 1.2 collects the neutrino energy and the baseline distance parameters for the experiments in neutrino oscillation. Each of these kinds of experiments will be sensible to just a portion of the whole mass difference spectrum.

So far, most of the PMNS matrix 1.17 parameters have been measured at 3σ precision by several analyses. The better-known parameters are, indeed, θ_{12} and θ_{13} , while the remaining θ_{23} and the CP violating phase δ_{CP} involve major uncertainties. In particular, the octant of the θ_{23} angle has yet to be discovered with enough statistical precision, namely greater than 3σ . Furthermore, CP conservation is still a possible scenario, given that the hypothesis $\delta_{\text{CP}} = \pi$ is discouraged, but cannot be completely rejected with a high enough confidence level.

Regarding the other parameters governing the neutrino oscillation, the square mass difference Δm_{21}^2 is known and is positive, yielding $m_2 > m_1$. On the other hand, the known precision measurement of the Δm_{32}^2 quantity

Table 1.3: Global fits for the 3ν parameters. The two mass-ordering schemes are presented separately. The excess in the χ^2 by the IO is given by the $\Delta\chi^2$ quantity for each analysis. All the results include the contribution by the Super-Kamiokande experiment [25], which provided only the tabulated χ^2 test values for their measurements. The table is taken from [24].

Param	Ref [26]		Ref [27]		Ref [28]	
	bfp $\pm 1\sigma$	3σ range	bfp $\pm 1\sigma$	3σ range	bfp $\pm 1\sigma$	3σ range
NO	Best Fit Ordering		Best Fit Ordering		Best Fit Ordering	
$\frac{\sin^2\theta_{12}}{10^{-1}}$	$3.10^{+0.13}_{-0.12}$	$2.75 \rightarrow 3.50$	$3.04^{+0.14}_{-0.13}$	$2.65 \rightarrow 3.46$	$3.20^{+0.20}_{-0.16}$	$2.73 \rightarrow 3.79$
$\theta_{12}/^\circ$	$33.82^{+0.78}_{-0.76}$	$31.61 \rightarrow 36.27$	$33.46^{+0.87}_{-0.88}$	$30.98 \rightarrow 36.03$	$34.5^{+1.2}_{-1.0}$	$31.5 \rightarrow 38.0$
$\frac{\sin^2\theta_{23}}{10^{-1}}$	$5.63^{+0.18}_{-0.24}$	$4.33 \rightarrow 6.09$	$5.51^{+0.19}_{-0.80}$	$4.30 \rightarrow 6.02$	$5.47^{+0.20}_{-0.30}$	$4.45 \rightarrow 5.99$
$\theta_{23}/^\circ$	$48.6^{+1.0}_{-1.4}$	$41.1 \rightarrow 51.3$	$47.9^{+1.1}_{-4.0}$	$41.0 \rightarrow 50.9$	$47.7^{+1.2}_{-1.7}$	$41.8 \rightarrow 50.7$
$\frac{\sin^2\theta_{13}}{10^{-2}}$	$2.237^{+0.066}_{-0.065}$	$2.044 \rightarrow 2.435$	$2.14^{+0.09}_{-0.07}$	$1.90 \rightarrow 2.39$	$2.160^{+0.083}_{-0.69}$	$1.96 \rightarrow 2.41$
$\theta_{13}/^\circ$	$8.60^{+0.13}_{-0.13}$	$8.22 \rightarrow 8.98$	$8.41^{+0.18}_{-0.14}$	$7.9 \rightarrow 8.9$	$8.45^{+0.16}_{-0.14}$	$8.0 \rightarrow 8.9$
$\delta_{\text{CP}}/^\circ$	221^{+39}_{-28}	$144 \rightarrow 357$	238^{+41}_{-33}	$149 \rightarrow 358$	218^{+38}_{-27}	$157 \rightarrow 349$
$\frac{\Delta m_{21}^2}{10^{-5}\text{eV}^2}$	$7.39^{+0.21}_{-0.20}$	$6.79 \rightarrow 8.01$	$7.34^{+0.17}_{-0.14}$	$6.92 \rightarrow 7.91$	$7.55^{+0.20}_{-0.16}$	$7.05 \rightarrow 8.24$
$\frac{\Delta m_{32}^2}{10^{-3}\text{eV}^2}$	$2.454^{+0.029}_{-0.031}$	$2.362 \rightarrow 2.544$	$2.419^{+0.035}_{-0.032}$	$2.319 \rightarrow 2.521$	$2.424^{+0.03}_{-0.03}$	$2.334 \rightarrow 2.524$
IO	$\Delta\chi^2 = 10.4$		$\Delta\chi^2 = 9.5$		$\Delta\chi^2 = 11.7$	
$\frac{\sin^2\theta_{12}}{10^{-1}}$	$3.10^{+0.13}_{-0.12}$	$2.75 \rightarrow 3.50$	$3.03^{+0.14}_{-0.13}$	$2.65 \rightarrow 3.45$	$3.20^{+0.20}_{-0.16}$	$2.73 \rightarrow 3.79$
$\theta_{12}/^\circ$	$33.82^{+0.78}_{-0.75}$	$31.62 \rightarrow 36.27$	$33.40^{+0.87}_{-0.81}$	$30.92 \rightarrow 35.97$	$34.5^{+1.2}_{-1.0}$	$31.5 \rightarrow 38.0$
$\frac{\sin^2\theta_{23}}{10^{-1}}$	$5.65^{+0.17}_{-0.22}$	$4.36 \rightarrow 6.10$	$5.57^{+0.17}_{-0.24}$	$4.44 \rightarrow 6.03$	$5.51^{+0.18}_{-0.30}$	$4.53 \rightarrow 5.98$
$\theta_{23}/^\circ$	$48.8^{+1.0}_{-1.2}$	$41.4 \rightarrow 51.3$	$48.2^{+1.0}_{-1.4}$	$41.8 \rightarrow 50.9$	$47.9^{+1.0}_{-1.7}$	$42.3 \rightarrow 50.7$
$\frac{\sin^2\theta_{13}}{10^{-2}}$	$2.259^{+0.065}_{-0.065}$	$2.064 \rightarrow 2.457$	$2.18^{+0.08}_{-0.07}$	$1.95 \rightarrow 2.43$	$2.220^{+0.074}_{-0.076}$	$1.99 \rightarrow 2.44$
$\theta_{13}/^\circ$	$8.64^{+0.12}_{-0.13}$	$8.26 \rightarrow 9.02$	$8.49^{+0.15}_{-0.14}$	$8.0 \rightarrow 9.0$	$8.53^{+0.14}_{-0.15}$	$8.1 \rightarrow 8.9$
$\delta_{\text{CP}}/^\circ$	282^{+23}_{-25}	$205 \rightarrow 348$	247^{+26}_{-27}	$193 \rightarrow 346$	281^{+23}_{-27}	$202 \rightarrow 349$
$\frac{\Delta m_{21}^2}{10^{-5}\text{eV}^2}$	$7.39^{+0.21}_{-0.20}$	$6.79 \rightarrow 8.01$	$7.34^{+0.17}_{-0.14}$	$6.92 \rightarrow 7.91$	$7.55^{+0.20}_{-0.16}$	$7.05 \rightarrow 8.24$
$\frac{\Delta m_{32}^2}{10^{-3}\text{eV}^2}$	$-2.510^{+0.030}_{-0.031}$	$-2.601 \rightarrow -2.419$	$-2.478^{+0.035}_{-0.033}$	$-2.577 \rightarrow -2.375$	$-2.50^{+0.04}_{-0.03}$	$-2.59 \rightarrow -2.39$

concerns its absolute value only. Nothing has been discovered yet about the sign of Δm_{32}^2 . This leads to two mass schemes, named the normal ordering (NO):

$$m_1 < m_2 < m_3 \quad (1.32)$$

and inverted ordering (IO):

$$m_3 < m_1 < m_2 \quad (1.33)$$

Observations signal less agreement with experimental data of the inverted mass ordering compared to the normal ordering. This is measured quantitatively with an excess in the χ^2 test for the IO best fit: $\Delta\chi^2 = \chi_{\text{IO}}^2 - \chi_{\text{NO}}^2 > 0$. We collect the best-known measurements of the oscillation parameters in the 3 neutrino scheme in table 1.3.

1.2.3 Neutrino masses

In this paragraph, we present the main techniques exploited to extend the SM and give mass to neutrinos. The crucial point is to introduce new particles that behave like the neutrinos but are singlets of the SM interactions, these are called sterile neutrinos ν_{si} for $i = 1, \dots, m$. These new particles do not

break the fundamental properties of the SM, namely, gauge symmetry and renormalizability. It is possible, then, to extend the SM building two kinds of mass terms:

$$-\mathcal{L}_{M_\nu} = (M_D)_{ij} \bar{\nu}_{si} \nu_{Lj} + \frac{1}{2} (M_N)_{ij} \bar{\nu}_{si} \nu_{sj}^c + \text{h.c.} \quad (1.34)$$

where the ν_{sj}^c field is the charge conjugate field for the j -th sterile neutrino and ν_{Lj} is the i -th SM left-handed neutrino. We designed two complex mass matrices: M_D of dimension $m \times 3$ and M_N of dimension $m \times m$. The gauge symmetry of the SM is indeed respected, since the sterile neutrino couples only with the active neutrinos and do not contribute to any interaction with the SM gauge bosons.

The two lagrangian contributions just written are a Dirac-like term that can arise from an SSB of a Yukawa interaction with the Higgs boson, such as $Y_{ij}^\nu \bar{\nu}_{si} \phi^\dagger L_{Lj}$, and a Majorana term that violates the total lepton number conservation but is allowed since the ν_{Si} do not carry any additional conserved charge.

The equation 1.34 can be formatted in a compact shape introducing a vector of $3 + m$ neutrinos $\boldsymbol{\nu} = (\boldsymbol{\nu}_L, \boldsymbol{\nu}_s^c)$:

$$-\mathcal{L}_{M_\nu} = \frac{1}{2} \begin{pmatrix} \bar{\boldsymbol{\nu}}_L^c & \bar{\boldsymbol{\nu}}_s \end{pmatrix} \begin{pmatrix} 0 & M_D^T \\ M_D & M_N \end{pmatrix} \begin{pmatrix} \boldsymbol{\nu}_L \\ \boldsymbol{\nu}_s^c \end{pmatrix} + \text{h.c.} = \bar{\boldsymbol{\nu}}^c M_\nu \boldsymbol{\nu} + \text{h.c.} \quad (1.35)$$

The resulting matrix M_ν is symmetric and can be diagonalized to retrieve the mass eigenvalues $(m_1, m_2, m_3, \dots, m_{3+m})$ with the transformation induced by a unitary mixing matrix V^ν :

$$\boldsymbol{\nu} \rightarrow \boldsymbol{\nu}_{\text{mass}} = (V^\nu)^\dagger \boldsymbol{\nu}, \quad M_\nu \rightarrow \text{diag}(m_k) = (V^\nu)^T M_\nu V^\nu \quad \text{for } k = 1, \dots, 3+m \quad (1.36)$$

The neat effect on equation 1.35 is:

$$\begin{aligned} -\mathcal{L}_{M_\nu} &= \frac{1}{2} \sum_{k=1}^{3+m} m_k [(\bar{\boldsymbol{\nu}}_{\text{mass}}^c)_k (\boldsymbol{\nu}_{\text{mass}})_k + (\bar{\boldsymbol{\nu}}_{\text{mass}})_k (\boldsymbol{\nu}_{\text{mass}}^c)_k] \\ &= \frac{1}{2} \sum_{k=1}^{3+m} m_k (\bar{\boldsymbol{\nu}}_M)_k (\boldsymbol{\nu}_M)_k \end{aligned} \quad (1.37)$$

where we have defined²:

$$\boldsymbol{\nu}_M = \boldsymbol{\nu}_{\text{mass}} + \boldsymbol{\nu}_{\text{mass}}^c = V^{\nu\dagger} \boldsymbol{\nu} + (V^{\nu\dagger} \boldsymbol{\nu})^c \quad (1.38)$$

It is easy to check that the fields in $\boldsymbol{\nu}_M$ are Majorana neutrinos since they satisfy the condition $\boldsymbol{\nu}_M = \boldsymbol{\nu}_M^c$. The Majorana condition imposes a further constraint on the spinor representation of the fields and acts halving the number of independent complex components of the spinor from four (Dirac

²The charge conjugation matrix acts on spinors like:

$$\Psi^c := C^{-1} \Psi C = C \bar{\Psi}^T$$

$$\bar{\Psi}^c := C^{-1} \bar{\Psi} C = \Psi^T C$$

Hence the bilinears $(\bar{\boldsymbol{\nu}}_{\text{mass}})_k (\boldsymbol{\nu}_{\text{mass}})_k + (\bar{\boldsymbol{\nu}}_{\text{mass}}^c)_k (\boldsymbol{\nu}_{\text{mass}}^c)_k$ cancel in equation 1.37.

spinors) to two (Majorana spinors). The situation is analogous to the scalar case, where a two real-component complex field ϕ reduces to a single real scalar field imposing the reality condition $\phi = \phi^*$.

Equation 1.38 can be inverted to obtain the 3 left-handed active neutrinos of the SM:

$$\nu_{Li} = P_L \sum_{j=1}^{3+m} V_{ij}^\nu (\nu_M)_j \quad \text{for } i = 1, 2, 3 \quad (1.39)$$

where P_L is the left chiral projector as usual.

We presented the generic workflow that allows extending the SM to include neutrino masses. We see that the neutrino mass terms arise from the inclusion of a number m of sterile neutrinos. In this context, the SM left-handed neutrinos are retrieved with a superposition of $3+m$ Majorana neutrino fields by a mixing matrix V^ν of rank $3+m$. In the following paragraphs, we will present some examples of practical realizations of this general framework.

Dirac neutrinos Setting $M_N = 0$ in equation 1.35 equals to exclude Majorana mass terms from the model lagrangian 1.34, namely to impose lepton number conservation. In the particular case of $m = 3$, we have a sterile partner for each neutrino in the SM that can be seen as the missing right-handed component of a four-spinor Dirac field for the neutrino.

The mass matrix M_ν can be diagonalized with the following transformations:

$$\nu_{Li} \rightarrow (V_L^\nu)_{ij} \nu_{Lj}, \quad \nu_{si} \rightarrow (V_R^\nu)_{ij} \nu_{sj}, \quad M_D \rightarrow \text{diag}(m_1, m_2, m_3) = V_R^{\nu\dagger} M_D V_L^\nu \quad (1.40)$$

where V_L^ν and V_R^ν are two 3×3 unitary matrices.

Then, the lagrangian mass term becomes:

$$-\mathcal{L}_{M_\nu} = \sum_{k=1}^3 m_k (\bar{\nu}_D)_k (\nu_D)_k \quad (1.41)$$

which is obtained by defining:

$$\nu_D = V_L^\nu \nu_L + V_R^{\nu*} \nu_s^c \quad (1.42)$$

Hence, the weak doublet of the SM neutrino fields is retrieved inverting the previous formula acting with the left-handed chiral projector P_L :

$$\nu_L = P_L V_L^\nu \nu_D \quad (1.43)$$

This extension of the SM introduces 3 sterile neutrinos that provide the missing right-handed degrees of freedom to SM neutrinos. The theory presents a low-energy matter content different from the original SM, which cannot be seen as a low-energy effective field theory of the model. Moreover, the model does not explain why the neutrinos are much lighter than the charged leptons. This sounds strange since both leptons and quarks acquire masses with the same Yukawa mechanism: up and down-type quarks in the same doublet have comparable masses, while this would not be true for the leptons and the neutrinos.

The see-saw mechanism The presence of a non-zero Majorana mass matrix M_N in equation 1.35 opens the possibility to explain the appearance of just 3 active light neutrinos observed so far, with the introduction of the see-saw mechanism. This model predicts that the 3 active light neutrinos are accompanied by m heavy neutrinos with mass much higher than the scale of the electroweak symmetry breaking v .

The mechanism can be understood by inspecting a 2×2 matrix:

$$A = \begin{pmatrix} 0 & M \\ M & N \end{pmatrix} \quad (1.44)$$

with $M \ll N$. The eigenvalues of the matrix are given by:

$$\lambda_{(+)} = \frac{N + \sqrt{N^2 + 4M^2}}{2} \rightarrow N \lambda_{(-)} = \frac{N - \sqrt{N^2 + 4M^2}}{2} \rightarrow -\frac{M^2}{N} \quad (1.45)$$

One of the two eigenvalues is suppressed by the magnitude of N , while the other is amplified by it, hence the name see-saw.

In the general case, the matrix M_D from equation 1.35 can be diagonalized through the adjoint action of a unitary matrix V^ν , obtaining the following neutrino mass lagrangian terms:

$$-\mathcal{L}_{M_\nu} = \frac{1}{2} \bar{\nu}_l M^l \nu_l + \frac{1}{2} \bar{N} M^h N \quad (1.46)$$

where the two mass matrices M^l and M^h are given by:

$$M^l \simeq -V_l^T M_D^T M_L^{-1} M_D V_l, \quad M^h \simeq V_h^T M_N V_h \quad (1.47)$$

and

$$V^\nu \simeq \begin{bmatrix} \left(1 - \frac{1}{2} M_D^\dagger M_N^{*-1} M_N^{-1} M_D\right) V_l & M_D^\dagger M_N^{*-1} V_h \\ -M_N^{-1} M_D V_l & \left(1 - \frac{1}{2} M_N^{-1} M_D M_D^\dagger M_N^{*-1}\right) V_h \end{bmatrix} \quad (1.48)$$

where V_l and V_h are 3×3 and $m \times m$ unitary matrices, respectively. Such as in the 2-dimensional toy case, the M^l is proportional to the inverse matrix M_N^{-1} , while the heavier mass matrix contains M_N . In this case, the SM is a good low-energy effective field theory and, further, both the light and heavy neutrinos are Majorana particles.

Neutrino masses from generic new physics In the previous examples, we extended the standard model introducing new lagrangian terms that respected the fundamental properties of the SM, namely gauge invariance and renormalizability. In general, new physics (NP) beyond the standard model might arise at energy scales Λ_{NP} much higher than those currently probed by the current experiments. Then, like in the first Fermi's theory of weak interactions, it should be possible to include non-renormalizable terms in the lagrangian that are suppressed by powers of the characteristic scales of the new theory Λ_{NP} : the theory in this case manifests as non-renormalizable interactions at scales lower than Λ_{NP} , but is, in fact, renormalizable at higher energies.

The least suppressed NP effects come from dimension 5 operators. Considering the SM model fields and imposing the gauge symmetry, we can build the following term:

$$\mathcal{O}_5 = \frac{Z_{ij}^\nu}{\Lambda_{\text{NP}}} (\bar{L}_{Li} \phi) (\phi^T \bar{L}_{Li}^C) + \text{h.c.} \quad (1.49)$$

where the Z^ν is a $n \times n$ matrix of coefficients, which leads after SSB to the Majorana mass term for the left-handed neutrinos:

$$-\mathcal{L}_{M_\nu} = \frac{Z_{ij}^\nu}{2} \frac{v^2}{\Lambda_{\text{NP}}} \bar{\nu}_{Li} \nu_{Lj}^c + \text{h.c.} \quad (1.50)$$

Then, in this case the mass matrix of the neutrino fields is given by:

$$(M_\nu)_{ij} = Z_{ij}^\nu \frac{v^2}{\Lambda_{\text{NP}}} \quad (1.51)$$

which contains the suppressed factor v^2/Λ_{NP} , that would explain why the neutrinos have such low masses compared to the other particles in the theory (i.e. charged leptons).

The lagrangian term breaks both the total lepton number and the flavor symmetry $U(1)_e \times U(1)_\mu \times U(1)_\tau$ and, in absence of further symmetries at the level of the Z_{ij}^ν coefficients, we expect lepton flavor mixing and CP violation, as discussed in the previous section on neutrino oscillation 1.2.2. Moreover, we stress that the see-saw mechanism might be seen as a particular model of NP theory: if we consider Z^ν to be a $(3+m) \times (3+m)$ matrix and $M_N = \Lambda_{\text{NP}}$, the mass coefficients can be arranged to contain 3 active light neutrinos with mass suppressed by the NP theory scale plus m heavy sterile neutrinos.

1.3 Monte Carlo techniques

1.3.1 Numerical Integration

Both theoretical and experimental particle physics need to evaluate complex high-dimensional integrals whose analytical solution is not always known. It is of paramount importance to be able to compute them numerically and several methods are known for centuries. These algorithms in general require to sample points in the integration domain and evaluate the integrand function in them. The simplest classical formulae have been developed for 1-dimensional integration and are usually split between Newton-Cotes type and Gaussian quadrature rules. The former evaluates the integrand at equally spaced abscissas points, as opposed to the latter. In this discussion, we focus on the Newton-Cotes type rules only, leaving the reader to specialized articles for further details [29].

Newton-Cotes type formulae

The Newton-Cotes type rules compute an integral over a finite interval, weighting the integrand function evaluated at equally spaced abscissas with suitable coefficients. The following equation shows the simplest rule, namely

the trapezoidal rule:

$$\int_{x_0}^{x_0+\Delta x} dx f(x) = \frac{\Delta x}{2} [f(x_0) + f(x_0 + \Delta x)] - \frac{(\Delta x)^3}{12} f''(\xi) \quad (1.52)$$

where $\xi \in [x_0, x_0 + \Delta x] \subset \mathbb{R}$. This procedure can be repeated to cover macroscopic intervals $[x_0, x_n]$, containing a set of $n + 1$ abscissas $\{x_i | x_i = x_0 + i \cdot \Delta x\}_{i=0}^n$:

$$I = \int_{x_0}^{x_n} dx f(x) = \frac{x_n - x_0}{n} \sum_{i=0}^n w_i f(x_i) - \frac{1}{12} \frac{(x_n - x_0)^3}{n^2} \tilde{f}'' \quad (1.53)$$

with $w_0 = w_n = 1/2$ and $w_i = 1$ for $1 \leq i \leq n - 1$. Also \tilde{f}'' is the average of all the $f''(\xi_i)$ values in the sub-intervals:

$$\tilde{f}'' = \frac{1}{n} \sum_{i=0}^n f''(\xi_i) \quad (1.54)$$

for some $\xi_i \in [x_i, x_{i+1}]$. Equation 1.53 is an exact formula for the integral I. However, the term with the second derivative of the integrand function should be evaluated in a point dependent on I itself and, being unknown a priori, it is usually dropped. This approximation results in an error of order $\mathcal{O}(n^{-2})$ at the price of $\mathcal{O}(n)$ function evaluations.

Another formula that leads to a better approximation is Simpson's rule evaluating the integrand function in three points:

$$\int_{x_0}^{x_2} dx f(x) = \frac{\Delta x}{3} [f(x_0) + 4f(x_1) + f(x_2)] - \frac{(\Delta x)^5}{90} f^{(4)}(\xi) \quad (1.55)$$

which gives:

$$I = \int_{x_0}^{x_n} dx f(x) = \frac{x_n - x_0}{n} \sum_{i=0}^n w_i f(x_i) - \frac{1}{180} \frac{(x_n - x_0)^5}{n^4} \tilde{f}^{(4)} \quad (1.56)$$

where this time n should be an even number, $w_0 = w_n = 1/3$ and for $1 \leq i < n$, $w_i = 4/3$ if i is odd, $w_i = 2/3$ if i is even. Again, the second term is usually dropped, but this time it goes to zero way faster than the trapezoidal rule one, namely as $\mathcal{O}(n^{-4})$.

For the sake of completeness, we give here the prescriptions more refined approximations rules. The Newton's 3/8 rule, which employs 4 integrand evaluations for each sub-interval, but does not improve the final approximation error:

$$\int_{x_0}^{x_3} dx f(x) = \frac{3\Delta x}{8} [f(x_0) + 3f(x_1) + 3f(x_2) + f(x_3)] - \frac{3(\Delta x)^5}{80} f^{(4)}(\xi) \quad (1.57)$$

and the five-points Boole's rule:

$$\int_{x_0}^{x_4} dx f(x) = \frac{2\Delta x}{45} [7f(x_0) + 32f(x_1) + 12f(x_2) + 32f(x_3) + 7f(x_4)] - \frac{8(\Delta x)^7}{945} f^{(6)}(\xi) \quad (1.58)$$

which has an error that scales as $\mathcal{O}(n^{-6})$.

In general, if the number of derivatives for the error term is $k + 1$, the rule is said to be of degree k and the approximation error behaves like $\mathcal{O}(n^{-k})$. It can be shown that an even $2k$ -starting point rule does not improve the degree of the odd $(2k - 1)$ -rule: one has to resort to the $(2k + 1)$ -point formula to gain better precision. Although higher degree formulae provide errors that decay faster, it can be verified that the w_i coefficients start growing large in magnitude and with opposite signs, leading to numerical cancellations that do not improve consistently the approximations. Moreover, k -degree Newton-Cotes rules assume that the integrand function is differentiable at least k times, with continuous derivative: applications of the rule to functions not satisfying this requirement provide a wrong error estimate. Therefore, higher-order rules are not used in practice.

Multi-dimensional integration

The results presented in the previous paragraph refer to 1-dimensional integration only. Here, we focus on extending the discussion to multi-dimensional integrals. Let f be a function defined over a d -dimensional volume $\mathcal{M} \subseteq \mathbb{R}^d$ and consider the integral:

$$I = \int_{\mathcal{M}} d\mu(x) f(x_1, \dots, x_d) \quad (1.59)$$

where $\mu(x)$ is some measure function on the integration domain, such that $\mu(\mathcal{M})$ is the volume of \mathcal{M} itself. The trapezoidal formula 1.53 can be extended to the multi-dimensional case sampling n points along each of the d the 1-dimensional axes projections of the function f . That is, building a d -dimensional histogram covering the integration volume:

$$I = \frac{\mu(\mathcal{M})}{n^d} \sum_{i_1=0}^n \cdots \sum_{i_d=0}^n w_{i_1} \dots w_{i_d} f(x_{i_1}, \dots, x_{i_d}) + \mathcal{O}(n^{-2}) \quad (1.60)$$

where the integrand function is evaluated in the nd sampled points x_{i_k} for $i = 0, \dots, n$ and $k = 1, \dots, d$. The total number of points used to cover the d -dimensional set is $N = (n + 1)^d \approx n^d$, which leads to an approximation error of order $\mathcal{O}(N^{-2/d})$. The same argument holds for the other Newton-Cotes type formulae, showing how their scaling behavior is optimum in the 1-dimensional case, but rather poor when the dimensionality increases. This problem can be regarded as the *curse of dimensionality*, namely the issue afflicting integration and histogram methods for which the number of points required to cover a multi-dimensional space grows exponentially with the number of dimensions. The next paragraph introduces a technique suited for integration in a high number of dimensions: Monte Carlo integration.

1.3.2 Monte Carlo Integration

Monte Carlo integration relies on a probabilistic approach to the measure of sets: inside an event space Ω , it could be possible to measure the volume of a subset $\mathcal{M} \subseteq \Omega$, drawing a sequence of random events $\{\omega_i\}_{i=0}^N$ and keeping track of the number of events that fall inside the subset \mathcal{M} , N_{in} . The measure μ of the subset \mathcal{M} , in the limit of large N , is approximated by the ratio:

$$\mu(\mathcal{M}) = \lim_{N \rightarrow \infty} \mu(\Omega) \frac{N_{in}}{N} \quad (1.61)$$

This idea can be transposed to find the value I of the integral of a multi-dimensional function f , defined as in equation 1.59. Further, we assume that f is square integrable. In the following, we normalize to unity the volume of the integration domain; the general case can be retrieved using dimensional analysis, multiplying quantities appearing in equations by a suitable power of $\mu(\mathcal{M})$. The Monte Carlo estimate E_N of the integral I is given by the following formula:

$$E_N = \frac{1}{N} \sum_{n=1}^N f(x_n) \xrightarrow{N \rightarrow \infty} I \quad (1.62)$$

where $\{x_n\}_{n=1}^N$ represent random points where the function f should be evaluated. In the large N limit, the MC estimate equals the integral.

An estimation of the error for approximating the integral I with a finite N computation of the MC estimate E_N should be discussed defining the variance $\sigma^2[f]$ of the function f :

$$\sigma^2[f] := \int_{\mathcal{M}} d\mu(x) (f(x) - I)^2 \quad (1.63)$$

The variance for the MC estimate can be found by integrating over each of the randomly drawn points:

$$\sigma^2[E_N] = \int_{\mathcal{M}} d\mu(x_1) \dots d\mu(x_N) (E_N - I)^2 = \frac{\sigma^2[f]}{N} \quad (1.64)$$

which can be derived first proving that $\int d\mu(x)(f(x) - I) = 0$ and then working out the square in equation 1.64, followed by the integration on the drawn points $\{x_n \in \mathcal{M}\}_{n=1}^N$. As opposed to the exact remainders associated with the Newton-Cotes type formulae (see paragraph 1.3.1) this error has a probabilistic interpretation: evaluating the integrand function on a finite sample of N points, the average error that one commits approximating $I \approx E_N$ is $\frac{\sigma[f]}{\sqrt{N}}$. Equivalently, due to Central Limit Theorem, equation 1.64 implies that the sequence of random variables $\{(E_n - I)\}_{n=1}^N$ converges in probability to a centered gaussian with standard deviation of $\sigma[f]/\sqrt{N}$, where $\sigma[f]$ is the integrand function standard deviation. In practice, the exact value for the variance of the MC estimation $\sigma^2[E_N]$ is unknown and an approximated formula is employed:

$$S_N^2 = \frac{1}{N-1} \sum_{n=1}^N (f(x_n) - E_N)^2 = \frac{1}{N} \sum_{n=1}^N (f(x_n))^2 - E_N^2 \quad (1.65)$$

An immediate consequence of equations 1.64 and 1.65 is that the approximation error of the MC estimation scales as $\mathcal{O}(N^{-1/2})$ with the number of function evaluations, which unfortunately is rather poor compared to the 1-dimensional trapezoidal or Simpson's rules. However, by construction, the error does not depend on the dimensionality d of the integration domain \mathcal{M} . Hence, the MC integration is particularly suited to evaluate high dimensional integrals. We report here the master formula for MC integration:

$$I \approx E_N \pm S_N = \frac{1}{N} \sum_{n=1}^N f(x_n) \pm \left[\frac{1}{N-1} \sum_{n=1}^N (f(x_n) - E_N)^2 \right]^{1/2} \quad (1.66)$$

Variance Reducing Techniques

The approximated formula of the variance of the MC integral, equation 1.65, is the ratio of the variance of the integrand function $\sigma^2[f]$ and the number of function evaluations N . It follows that if it is possible to somehow reduce the numerator, the poor $\mathcal{O}(N^{-1/2})$ behavior can be improved dramatically. Several variance-reducing techniques have been designed for this purpose: we present the ideas behind the main strategies in this paragraph.

Stratified sampling Stratified sampling consists in dividing the integration domain into smaller sub-domains, perform an MC integration in each of them separately and, finally, gather all the contributions to provide the final MC estimate of the integral. This technique is supported by the following property of the Riemann integral: let $\{\mathcal{M}_i\}_{i=0}^k$ a numerable family of disjoint subsets of the integration domain \mathcal{M} , such that $\cup_{i=0}^k \mathcal{M}_i = \mathcal{M}$, then the following equation holds:

$$I = \int_{\mathcal{M}} d\mu(x) f(x) = \sum_{i=0}^k \int_{\mathcal{M}_i} d\mu(x) f(x) \quad (1.67)$$

Therefore, the MC estimate of the integral I becomes:

$$E_N = \sum_{i=1}^k \frac{\mu(\mathcal{M}_i)}{N_i} \sum_{n=1}^{N_i} f(x_{in}) \quad (1.68)$$

where we have drawn N_i random points for each subset \mathcal{M}_i .

The variances of the function in each subset add up together to retrieve the variance of the MC estimate. Note that the $\mu(\mathcal{M}_i)$ is not unity anymore and must be included explicitly in the formula (dimensional analysis helps infer the correct power of the integration volume in each equation):

$$\sigma^2[E_N] = \sum_{i=0}^k \frac{\mu^2(\mathcal{M}_i)}{N_i} \sigma^2[f]_{\mathcal{M}_i} \quad (1.69)$$

with:

$$\begin{aligned} \sigma^2[f]_{\mathcal{M}_i} &= \frac{1}{\mu(\mathcal{M}_i)} \int_{\mathcal{M}_i} d\mu(x) \left(f(x) - \frac{I}{\mu(\mathcal{M}_i)} \right)^2 \\ &= \frac{1}{\mu(\mathcal{M}_i)} \int_{\mathcal{M}_i} d\mu(x) f(x)^2 - \left(\frac{1}{\mu(\mathcal{M}_i)} \int_{\mathcal{M}_i} d\mu(x) f(x) \right)^2 \end{aligned} \quad (1.70)$$

It can be shown that the value of the MC variance in equation 1.69 can be minimized by an appropriate choice of the points sampled for each subset N_i . Here, we consider the case with $K = 2$ and infer the general rule. If there are only two subsets a and b , we parametrize the number of points where to evaluate the integrand function in the two subsets with N_a and $N_b = N - N_a$ respectively, where N stands for the total number of sampled points $\{x_{in}\}$. Taking the derivative with respect to N_a , the formula for $\sigma^2[E_N]$ can be minimized:

$$\frac{\partial \sigma^2[E_N]}{\partial N_a} = - \left(\frac{\mu(\mathcal{M}_a)}{N_a} \sigma_a \right)^2 + \left(\frac{\mu(\mathcal{M}_b)}{N - N_a} \sigma_b \right)^2 \stackrel{!}{=} 0 \quad (1.71)$$

where σ_i is a short-hand for $\sigma[f] \big|_{\mathcal{M}_i}$. So, solving for N_a :

$$\frac{N_a}{N} = \frac{\mu(\mathcal{M}_a) \sigma_a}{\mu(\mathcal{M}_a) \sigma_a + \mu(\mathcal{M}_b) \sigma_b} \quad (1.72)$$

This result shows how to minimize the variance of the MC integration splitting the integration domain into 2 parts. We can generalize it by claiming that the least possible variance for an MC integration can be obtained drawing in each subset \mathcal{M}_i a fraction of points equal to the relative product of the volume of the subset $\mu(\mathcal{M}_i)$ times the variance of the integrand function evaluated in it. This means that evaluations of $f(x)$ must be concentrated in subsets where the potential error given by high variance of the integrand function is the highest, namely where the function is both large or rapidly changing.

Importance sampling The importance sampling technique refers to a change of variables in the integration, resulting in a new integrand function. We show in this paragraph that carefully tweaking this transformation leads to more efficient computation. Formally, we have:

$$I = \int_{\mathcal{M}_i} d\mu(x) f(x) = \int_{\mathcal{M}} d\mu(x) p(x) \frac{f(x)}{p(x)} \quad (1.73)$$

where the function $p(x)$ can be chosen to be positive and normalized to unity, namely a probability density function (pdf). Assuming that we can sample random points following the pdf distribution $x_n \sim p(x)$, then the MC integration becomes:

$$E_N = \frac{1}{N} \sum_{n=1}^N \frac{f(x_n)}{p(x_n)} \quad (1.74)$$

After this transformation, the new variance for the MC integral is given by $\sigma[f/p]/\sqrt{N}$, which is estimated by:

$$S_N^2 = \frac{1}{N} \sum_{n=1}^N \left(\frac{f(x_n)}{p(x_n)} \right)^2 - E_N^2 \quad (1.75)$$

Zero variance can be achieved by choosing $p(x) = f(x)/I$, but, of course, this cannot be done since we do not know the exact value of the integral. However, the variance can be reduced by choosing $p(x)$ as close as possible to $f(x)$

or, equivalently, requiring that the new integrand function $f(x)/p(x)$ is as flat as possible. It should be noted, though, that choosing a $p(x)$ that is zero or approximately zero in a region with non-zero $f(x)$ results in a divergence in equation 1.75 and a consequent erroneous estimation of the MC integral variance. Note that this behavior is not detected by the MC integration algorithm if this region of divergence is small and the randomly sampled points fall outside it. This argument signal that some attention should be paid when choosing the function $p(x)$.

Multi-channel Monte Carlo Importance sampling introduces a transformation that acts on the whole integration domain flattening the integrand function and ensuring that random sampling produces an efficient computation of the integral. However, when the integrand function exhibits multiple sharp peaks in localized different regions it is very unlikely to find a suitable change of variables that accommodates them all. The key idea behind a multi-channel MC is that when the single peak structures of $f(x)$ are known, it is possible to transform each contribution with an independent transformation. Each transformation is called a channel and defines a dedicated probability density function. An MC integration on a single channel contributes to the final result only for the corresponding peak, since the sampling is inevitably more focused around that region of the integration domain and probably under-populating the others.

Multi-channel MC requires listing all the probability density functions $p_i(x)$ associated with each change of variables and to select each channel with a probability α_i for $i = 1, \dots, m$, such that the α s sum up to unity. The desired integral is computed by substituting $p(x) = \sum_{i=1}^m \alpha_i p_i(x)$ in equation 1.73:

$$I = \sum_{i=1}^M \alpha_i \int_{\mathcal{M}} dP_i(x) \frac{f(x)}{p(x)} \quad (1.76)$$

where $dP_i(x) = d\mu(x)p_i(x)$. The algorithms are usually implemented by fixing the number of function evaluations N and selecting each channel with probability α_i : approximately yielding $N_i \approx \alpha_i N$ function evaluations for each channel. The MC estimation of the integral I is, then:

$$E_N = \frac{1}{N} \sum_{i=1}^m \sum_{n_i=1}^{N_i} \frac{f(x_{n_i})}{p(x_{n_i})} \quad (1.77)$$

and a corresponding variance, analogously to equation 1.75:

$$\sigma^2[E_N] = \frac{1}{N} \sum_{i=1}^m \alpha_i \int_{\mathcal{M}} dP_i(x) \left(\frac{f(x)}{p(x)} \right)^2 - I^2 \quad (1.78)$$

Since the values of α_i do not affect the MC estimate of the integral, but only the estimated variance of the integral, a careful choice of the α_i coefficients may lead to better results. An iterative method to adjust the α_i in order to minimize $\sigma^2[E_N]$ is presented in [30].

Control variates An alternative technique related to importance sampling is known as the method of control variates: in this application, a function $g(x)$ is subtracted to the original integrand $f(x)$, introducing a new integrand function $(f(x) - g(x))$ and leaving as the remainder term a possibly known integral of $g(x)$:

$$I = \int_{\mathcal{M}} d\mu(x) f(x) = \int_{\mathcal{M}} d\mu(x) (f(x) - g(x)) + \int_{\mathcal{M}} d\mu(x) g(x) \quad (1.79)$$

In principle, the $(f(x) - g(x))$ integration should be associated with a smaller variance to benefit from the transformation. It is known that this method is stabler than the importance sampling method, since the $g(x)$ function does not introduce singularities in the integration function.

1.3.3 Adaptive Monte Carlo: VEGAS algorithm

The variance-reducing techniques presented just above require some knowledge of the integrand function to be exploited. It would be desirable, instead, to design methods that act in an automated way: given a function on the integration domain, they choose the best strategy to enhance algorithm efficiency. This is exactly the purpose of adaptive techniques, namely those algorithms in which the integrand function properties are learned at runtime. In particular, VEGAS [31, 32] is a tool that employs importance sampling in high dimensions to iteratively shape an estimate of the optimal pdf:

$$p_{\text{best}}(x) = \frac{|f(x)|}{\int_{\mathcal{M}} d\mu(x) |f(x)|} \quad (1.80)$$

A multi-dimensional histogram of the absolute value of the integrand function is computed at each iteration. The number of bins along each dimension is kept constant during the process, while gradually adjusting their width. The objective is to produce a finer grid in regions providing large contributions to the integral and a coarser grain in the integration domain portions with "low-activity". As a consequence of the *curse of dimensionality*, a d -dimensional histograms require an exponential number of bins with respect to the number of dimensions d to cover the integration domain. Therefore, scalability in the VEGAS algorithm is ensured considering only separable functions for $p(x)$:

$$p(x) = p_1(x_1) \cdot p_2(x_2) \cdot \dots \cdot p_d(x_d) \quad (1.81)$$

This way, it is possible to work independently along each dimension with the marginals probability functions $p_i(x_i)$.

The algorithm acts in two phases: exploration and evaluation. VEGAS first explores the integration domain to adapt the grid to the integrand function shape, starting from a naive uniform distribution for $p(x)$ and adapting the widths of the bins following the criteria described above: after some repetitions a stable grid configuration is reached. At this point, the grids are frozen and the evaluation phase starts: several MC integrations are performed and their results are aggregated into a final output. Given M integral

evaluations, the intermediate estimations for the integral E_i and its variances S_i^2 are averaged into the final quantities \bar{E} and $S_{\bar{E}}^2$ with the following rules:

$$\bar{E} = S_{\bar{E}}^2 \sum_{i=1}^M \frac{E_i}{S_i^2}, \quad \frac{1}{S_{\bar{E}}^2} = \sum_{i=1}^M \frac{1}{S_i^2}, \quad (1.82)$$

The intermediate E_i and S_i^2 are computed with the usual formulae for importance sampling, equations 1.74 and 1.75 respectively. The algorithm also performs checks on the intermediate evaluations to ensure that the S_i^2 are reliable estimates of the MC error. For this purpose, internally, a χ^2 per degree of freedom is computed with the following equation:

$$\chi^2/\text{dof} = \frac{1}{M-1} \sum_{i=1}^M \frac{(E_i - \bar{E})^2}{S_i^2} \quad (1.83)$$

Consistent estimates give χ/dof values approximately equal to 1.

1.3.4 Sample generation

MC integrators assume the ability to randomly sample points in the integration domain and evaluate the corresponding integrand function values: a naive approach draws points uniformly on the integration domain to update the estimates for the integral and its variance (see equation 1.66). Modern scientific libraries already have implemented algorithms to sample from uniform as well as many other notable probability distributions [33, 34]. Unfortunately, this is not sufficient, since a basic Monte Carlo integration is known to perform poorly when complex integrands are involved. The importance sampling technique, then, provides a method to gain efficiency requiring that sample points are drawn from a chosen probability density function that is close as possible to the integrand. In the next paragraphs, we introduce the most widely used methods to produce samples following a given pdf.

In the following, the cumulative distribution function for a 1-dimensional random variable X following a probability distribution function $p(x)$ is:

$$P(x) = \text{Prob}(X \leq x) = \int_{-\infty}^x dt p(t) \quad (1.84)$$

The definition can be extended naturally to higher dimensional random variables.

Inverse transform method

The inverse transform method gives a recipe to draw random numbers following an arbitrary $p(x)$. For each random variable X following the pdf $p(x)$ it can be defined a new random variable $U = P(X)$ that follows the uniform probability in the unit interval. It is possible, then, to invert the formula finding the inverse function of the cumulative distribution, which always exists since F is monotonically increasing by construction. Provided that the P^{-1} can be written analytically, then, sampling a uniform random number in the unit interval u and computing:

$$x = P^{-1}(u) \quad (1.85)$$

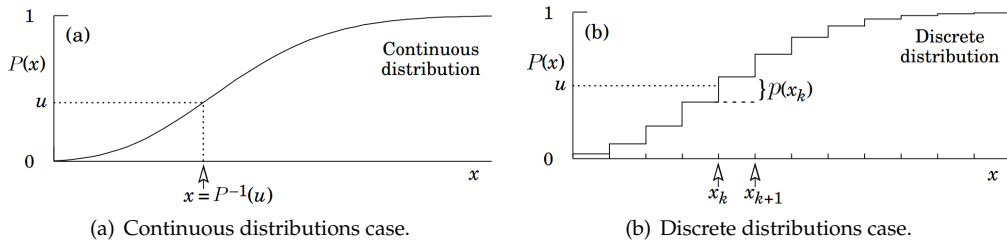


Figure 1.2: The inverse transform method for sampling random numbers according to some probability distribution function $p(x)$.

yields a number distributed according to the desired pdf function $p(x)$. Figure 1.2 depicts the idea behind the inverse transform method for both continuous and discrete random variables. In the latter case, the cumulative function is step-like and the desired output x_k is the one that satisfies:

$$P(x_k) \leq u < P(x_{k+1}) \quad (1.86)$$

Acceptance-rejection method

The inverse transform method is strongly limited by the fact that the inverse function must be known exactly. Therefore, Von Neumann developed an algorithm [35] to sample random numbers according to a pdf $p(x)$ when the inverse transform method hypothesis cannot be fulfilled. The idea relies on the assumption that $p(x)$ is bounded from above by C times a pdf $h(x)$: $p(x) \leq Ch(x)$. Both $p(x)$ and $h(x)$ are normalized, hence $C \geq 1$ follows. The choice of $h(x)$ should be done to be able to generate random samples from it easily: often this is set to the uniform distribution.

The method requires knowledge of the pdf $p(x)$ only and works as follows. First, generate a single $x \sim h(x)$. Second, uniformly draw a random number u in the unit interval. Then, check the following inequality:

$$uCh(x) \leq p(x) \quad (1.87)$$

If the equation is satisfied accept x , reject it otherwise. Repeating the procedure many times produces a large set of random numbers following the $p(x)$ distribution. The efficiency of this method is constrained by the probability at which the acceptance happens: if a point x is generated in a region where $p(x) \ll Ch(x)$, it is very likely that the point will be rejected. That's why figure 1.3(b) suggests a trick to improve the naive acceptance-rejection method: the quantity C can be chosen piecewise constant, in order to keep the ratio of $p(x)$ and $Ch(x)$ as close as possible to unity.

The Metropolis algorithm

The approaches presented in the last two paragraphs are rather simple and they are not employed for realistic applications and complex use cases. Quite often it is required to generate numbers following multi-dimensional probability distributions. When the number of dimensions d grows large, a Markov

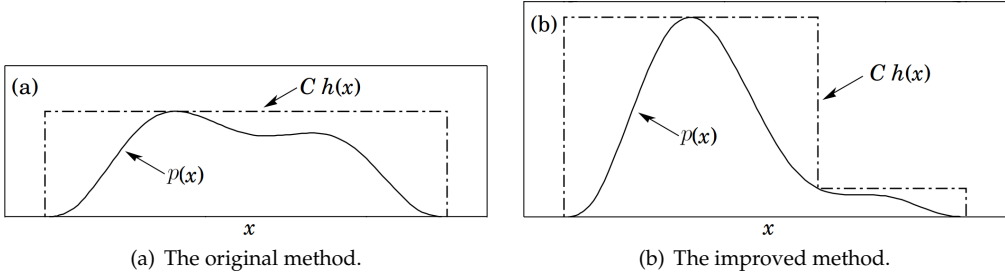


Figure 1.3: The acceptance-rejection method for sampling random numbers according to some probability distribution function $p(x)$.

Chain Monte Carlo (MCMC) technique, like the Metropolis algorithm [36], performs way better than the naive acceptance-rejection method.

The Metropolis algorithm is essentially a random walk in the space where the multi-variate pdf $p(x)$ is defined: it produces a chain of states x_1, \dots, x_n , that eventually follows the $p(x)$ function. This happens if two assumptions of ergodicity and detailed balance are verified. Ergodicity means that every possible state of the system can be reached within a finite number of steps: this allows to pick a random initial state being sure that the equilibrium state will be reached at some point. Detailed balance is a statement of reversibility of the system: it claims that the probability flow outgoing from state x_{n-1} to the next state in the chain x_n equals the ingoing probability flow from x_n to x_{n-1} . Formally, it is defined by the following equation:

$$p(x_{n-1})\pi(x_{n-1}, x_n) = p(x_n)\pi(x_n, x_{n-1}) \quad (1.88)$$

where $\pi(x_{n-1}, x_n)$ is the transition probability to step from state x_{n-1} to state x_n and, of course, $p(x_n)$ is the probability of being in state x_n .

Each iteration of the Metropolis algorithm consists of the following list of actions.

1. At step n , randomly generate a new candidate state x_{n+1} .
2. Compute the discriminative quantity $\Delta S = -\log \frac{p(x_{n+1})}{p(x_n)}$.
3. If $\Delta S < 0$, accept the candidate state as the new state.
4. Else, accept the candidate state with probability $p(x_{n+1})/p(x_n)$.
5. Repeat from the first point.

Point 3 and 4 can be absorbed into the definition of a single transition probability

$\pi(x_n, x_{n+1}) = \min(1, e^{-\Delta S})$, that satisfies the detailed balance condition. The intuitive explanation of the algorithm is that the system spends more time in a higher probability state, rather than in points associated with low probability regions. In particular, if the new state has a higher probability than the old one, it gets certainly accepted, conversely less probable states are accepted only with probability $p(x_{n+1})/p(x_n)$.

In practice, this algorithm initially starts in a random state and evolves naturally after some iterations towards an equilibrium state where the detailed balance condition holds. The ergodicity property ensures that convergence to the equilibrium is reached independently of the starting point. However, this process might take some time and, for particularly complex use cases, the system might be trapped in metastable states for an unknown number of steps. Moreover, successive states are not independent at equilibrium since the system exhibits a typical correlation length ξ . Therefore, it is really difficult to obtain an unbiased sample of points. A solution might be to save only those states in the chain with a time distance proportional to ξ^2 , which is known as the decorrelation time in random walk theory. The main problem with this technique is the fact that systems can acquire very large correlation lengths, especially while experiencing phase transitions.

1.3.5 Phase space generation from particle collisions

The methods described above find many applications in particle physics. Both in fixed order calculations and event generators the problem arises to generate phase space points, namely the 4-momenta of n particles with masses m_1, \dots, m_n . The goal is to generate sets of particles 4-momenta p_1, \dots, p_n for collision events following physical distributions.

The n -particle phase space is given by the following quantity:

$$d\Phi_n(P; p_1, \dots, p_n) = (2\pi)^4 \delta^{(4)}(P - \sum_i p_i) \prod_{i=1}^n \frac{d^4 p_i}{(2\pi)^4} (2\pi) \delta(p_i^2 - m_i^2) \Theta(p_i^0) \quad (1.89)$$

$$= (2\pi)^4 \delta^{(4)}(P - \sum_i p_i) \prod_{i=1}^n \frac{d^3 \mathbf{p}_i}{(2\pi)^3 2p_i^0} \quad (1.90)$$

where the 4-dimensional Dirac delta expresses momentum conservation law. In general, there are two basic approaches to the problem. The first [37] is based on a recursive relationship producing a sequential or hierarchical approach to phase space sampling. The second is a democratic one dubbed RANdom Momenta Booster (RAMBO) [38], where massless particles are produced in a flat phase space and subsequent boosting transformations enforce the physical constraints to output the final distribution.

Hierarchical approach A simple recursion rule can be derived from the n -body phase space equation. The objective is to create an algorithm that allows the generation of events containing n final state particles with given masses $\{m_1, \dots, m_n\}$. The output event will be obtained by a sequence of $1 \rightarrow 2$ particle branchings.

From the p_1, \dots, p_n output momenta, consider the auxiliary momenta q_i defined as the sum of all the output momenta with an index less or equal to i : $q_i = \sum_{j=1}^i p_j$. Also, set the resonant mass parameters to $M_i^2 = q_i^2$. Then, it

is possible to insert the following two identities in 1.89:

$$1 = \int d^4 q_{n-1} \delta^{(4)}(q_{n-1} - \sum_{i=1}^{n-1} p_i) \quad (1.91)$$

$$1 = \int dM_{n-1}^2 \delta(q_{n-1}^2 - M_{n-1}^2) \quad (1.92)$$

which to obtain:

$$\begin{aligned} d\Phi_n(P; p_1, \dots, p_n) &= dM_{n-1}^2 \delta(q_{n-1}^2 - M_{n-1}^2) d^4 q_{n-1} \delta^{(4)}(q_{n-1} - \sum_{i=1}^{n-1} p_i) \\ &\quad (2\pi)^4 \delta^{(4)}(P - \sum_i p_i) \frac{d^3 \mathbf{p}_n}{(2\pi)^3 2E_n} \prod_{i=1}^{n-1} \frac{d^4 p_i}{(2\pi)^4} (2\pi) \delta(p_i^2 - m_i^2) \\ &= dM_{n-1}^2 \frac{d^3 \mathbf{q}_{n-1}}{2M_{n-1}} \frac{d^3 \mathbf{p}_n}{(2\pi)^3 2E_{p_n}} \delta^{(4)}(P - p_n - q_{n-1}) \\ &\quad d\Phi_n(q_{n-1}; p_1, \dots, p_{n-1}) \\ &= dM_{n-1}^2 \frac{1}{2\pi} d\Phi_2(P; p_n, 1_{n-1}) d\Phi_n(q_{n-1}; p_1, \dots, p_{n-1}) \end{aligned} \quad (1.93)$$

This equation underlines that the n -particle phase space can be reduced to an $(n-1)$ -particle phase space through the radiation of a particle with momentum p_n by an intermediate state with mass M_{n-1} .

The recursive relation can be repeated introducing multiple sequential branchings in the process to take care of all the external particles, resulting in:

$$d\Phi_n = \frac{1}{(2\pi)^{n-2}} dM_{n-1}^2 \dots dM_2^2 d\Phi_2(n) \dots d\Phi_2(2) \quad (1.94)$$

where $d\Phi_2(i) = d\Phi_2(q_i; p_i, q_{i-1})$ is a shorthand for the contribution given by the decay $q_i \rightarrow p_i q_{i-1}$.

It is possible to work out the integration of the Dirac delta in the two body phase space for a particle of momentum q_i that decays in two others with momenta p_i and q_{i-1} respectively, the result is:

$$\begin{aligned} d\Phi_2(i) &= \frac{d^3 \mathbf{p}_i}{(2\pi)^3 2E_i} \frac{d^3 \mathbf{q}_{i-1}}{(2\pi)^3 2M_{i-1}} (2\pi)^4 \delta^{(4)}(q_i - p_i - q_{i-1}) \\ &= \frac{\lambda^{1/2}(q_i^2, q_{i-1}^2, p_i^2)}{(2\pi)^2 8M_i^2} d\Omega_i \end{aligned} \quad (1.95)$$

recalling that $q_i^2 = M_i^2$ and where $d\Omega = d\cos\theta_i d\phi_i$ is the solid angle differential element of the two outgoing particles i and $i-1$ and the characteristic λ function is defined by:

$$\lambda(x, y, z) = x^2 + y^2 + z^2 - 2xy - 2xz - 2yz \quad (1.96)$$

which is symmetric under the $x \longleftrightarrow y$ exchange.

Inputs: Incoming momentum P , output masses m_1, \dots, m_n .
Outputs: Final state particle 4-momenta $\{p_1^\mu, \dots, p_n^\mu\}$ weighted by w .

Set $i \leftarrow n$, $q_i \leftarrow P$, $M_i \leftarrow \sqrt{q_i^2}$

While $i > 1$:

Lorentz transform to rest frame of q_i with Λ_ν^μ

Sample uniformly $u_{i1}, u_{i2} \in [0, 1]$

$\phi_i \leftarrow 2\pi u_{i1}$ and $\cos \theta_i \leftarrow 2u_{i2} - 1$

If $i \geq 3$:

Sample uniformly $u_{i3} \in [0, 1]$

Set $M_{i-1} \leftarrow \sum_{j=1}^{i-1} \mu_{i-1} + u_{i3} (M_i - \mu_i)$

Else:

Set $M_{i-1} \leftarrow m_1$

Set $|\mathbf{p}'_i| \leftarrow \frac{\lambda^{1/2}(M_i^2, M_{i-1}^2, m_i^2)}{2M_i}$ and $\mathbf{p}'_i \leftarrow |\mathbf{p}'_i| (\sin \theta_i \cos \phi_i, \sin \theta_i \sin \phi_i, \cos \theta_i)$

Define 4-momenta $p'^\mu_i \leftarrow (\sqrt{|\mathbf{p}'_i|^2 + m_i^2}, \mathbf{p}'_i)$, $q'^\mu_i \leftarrow (\sqrt{|\mathbf{p}'_i|^2 + M_{i-1}^2}, -\mathbf{p}'_i)$

Lorentz transform back to the lab frame with Λ_ν^μ

If $i = 2$:

$p_1 \leftarrow q_1$

$i \leftarrow i - 1$

Set the weight w of the generated event to equation 1.99

Table 1.4: The hierarchical approach to sample weighted n -body phase space configurations.

Inserting equation 1.95 into the recursive relation 1.94 we obtain the result for the n -body phase space with $n - 1$ sequential splittings:

$$d\Phi_n(P; p_1, \dots, p_n) = (2\pi)^{4-3n} 2^{3-2n} dM_{n-1}^2 \dots dM_2^2 \prod_{i=2}^n \frac{\lambda^{1/2}(M_i^2, M_{i-1}^2, p_i^2)}{2M_i} d\Omega_i \quad (1.97)$$

where the masses M_i in subsequent decays are constrained by the kinematics to respect the inequalities:

$$\mu_i \leq M_i \leq M_{i+1} - m_{i+1} \quad (1.98)$$

where $\mu_i = \sum_{j=1}^i m_j$.

The ratio in the product of equation 1.97 turns out to be equal to the absolute value of the 3-momentum $|\mathbf{p}_i|$ in the rest frame of the decaying intermediate particle M_i . Therefore, it is possible to design the following algorithm to hierarchically generate phase space events containing n final state particles with $\{m_1, \dots, m_n\}$ masses. The pseudocode describing the algorithm is contained in table 1.4 and produces n particles momenta configurations that should be weighted with the following quantity, which takes into account the jacobians of the transformations induced by the uniform random sampling:

$$w = \frac{(2\pi)^{3-2n} 2^{1-n}}{M_n (M_2 - \mu_2)} \prod_{i=2}^n (M_i - \mu_i) \sqrt{\lambda(M_i^2, M_{i-1}^2, m_i^2)} \quad (1.99)$$

RAMBO

In contrast to the hierarchical approach which generates weighted events, the RAndom Momenta BOoster (RAMBO) [38] produces a set of n physical

4-momenta with total momentum P , drawing uniformly numbers from the unit hyper-cube in \mathbb{R}^{4n} . The algorithm treats differently the production of massless and massive particles.

We first discuss the massless case. The n -massless particle phase space element is given by:

$$d\Phi_n = (2\pi)^4 \delta^{(4)}\left(P - \sum_i p_i\right) \prod_{i=1}^n \frac{d^4 p_i}{(2\pi)^3} \delta(p_i^2) \Theta(p_i^0) \quad (1.100)$$

To derive the RAMBO algorithm, instead, we consider the alternative form:

$$dR_n = \prod_{i=1}^n \frac{d^4 p_i}{(2\pi)^3} \delta(q_i^2) \Theta(q_i^0) (2\pi)^4 f(q_i^0) \quad (1.101)$$

where we have replaced the 4-dimensional Dirac delta expressing the momentum conservation with a generic function depending on the temporal component of the q_i momenta, $f(q_i^0)$. This function is needed to keep the total phase space volume finite. Integrating over the Dirac delta to implement the on-shell condition of the particles, we obtain:

$$dR_n = (2\pi)^{4-2n} \mathbf{x} f(\mathbf{x}) \Theta(\mathbf{x}) d^n \mathbf{x} \quad (1.102)$$

which shows how the integrals over the different particle momenta decouple in this case.

We define a Lorentz plus a scaling transformation connecting the RAMBO 4-momenta and the physical p_i ones. The transformation is characterized by the vector \mathbf{b} and the scaling factor x , as follows:

$$\begin{aligned} \gamma &= \frac{Q^0}{M} = \sqrt{1 + \mathbf{b}^2}, \quad a = \frac{1}{1 + \gamma}, \quad x = \frac{\sqrt{P^2}}{M} \\ Q^\mu &= \sum_{i=1}^n q_i^\mu, \quad M = \sqrt{Q^2}, \quad \mathbf{b} = -\frac{1}{M} \mathbf{Q} \end{aligned} \quad (1.103)$$

Therefore, the transformations linking the two sets are $x H_{\mathbf{b}^\mu(q_i)}$ and its inverse

$\frac{1}{x} H_{-\mathbf{b}^\mu(p_i)}$, such that:

$$p_i^0 = x(\gamma q_i^0 + \mathbf{b} \cdot \mathbf{q}_i), \quad \mathbf{p}_i = x[\mathbf{q}_i + \mathbf{b} q_i^0 + a(\mathbf{b} \cdot \mathbf{q}_i) \mathbf{b}] \quad (1.104)$$

It is possible to show that expressing the RAMBO phase space element in terms of the momenta p_i , the following equation holds:

$$\begin{aligned} dR_n &= \frac{d^4 p_i}{(2\pi)^3} \delta(p_i^2) \Theta(p_i^0) (2\pi)^4 \delta^{(4)}\left(P - \sum_{i=1}^n p_i\right) \\ &\cdot \left(\prod_{i=1}^n f\left(\frac{1}{x} H_{-\mathbf{b}^\mu(p_i)}\right) \right) \frac{(P^2)^2}{x^{2n+1} \gamma} d^3 \mathbf{b} dx \end{aligned} \quad (1.105)$$

This equation factorizes the RAMBO phase space in the usual physical n -body phase space for massless particles plus a contribution S_n given by the second

line of equation 1.105, which depends on the choice of the auxiliary function $f(x)$. Fixing $f(x) = e^{-x}$ and performing the integrals over the \mathbf{b} and x parameters the S_n equals to:

$$S_n = 2\pi(P^2)^{2-n} \frac{\Gamma(\frac{3}{2}) \Gamma(n-1) \Gamma(2n)}{\Gamma(n + \frac{1}{2})} \quad (1.106)$$

which depends on the total invariant mass P^2 only.

Therefore, it can be possible to generate the n massless particles with the following receipt:

1. Generate n 4-momenta q_i^μ with isotropic angular distribution and energy sampled from the $q_i^0 e^{-q_i} dq_i^0$ probability density function. This can be done by sampling uniformly $4n$ random numbers in the unit interval and combining them with:

$$\begin{aligned} c_i &= 2u_{i1} - 1, & \phi_i &= 2\pi u_{i2}, & q_i^0 &= -\log(u_{i3}u_{i4}) \\ q_i^1 &= q_i^0 \sqrt{1 - c_i^2} \cos \phi_i, & q_i^2 &= q_i^0 \sqrt{1 - c_i^2} \sin \phi_i, & q_i^3 &= q_i^0 c_i \end{aligned} \quad (1.107)$$

2. Transform the set of RAMBO momenta q_i into the physical ones p_i with the help of the transformation appearing in equation 1.104.
3. Attach to the produced configuration the flat weight:

$$w_0 = (2\pi)^{4-3n} \left(\frac{\pi}{2}\right)^{n-1} \frac{(P^2)^{n-2}}{\Gamma(n)\Gamma(n-1)} \quad (1.108)$$

In the massive case, there exists a similar approach that exploits the massless case generation with a further transformation that allows providing 4-vectors associated with massive particles. As a result, the event weight is no longer constant over the phase space, but depends on the generated momenta. The algorithm is modified in the following way.

1. Generate a set of momenta for the massless particles p_i .
2. Compute the massive particle momenta k_i from the rescaled massless momenta ξp_i^μ :

$$k_i^\mu = \left(\sqrt{m_i^2 + (p_i^0)^2}, \xi \mathbf{p}_i \right) \quad (1.109)$$

where the parameter ξ is a constant quantity, constrained by the equation $\sqrt{P^2} = \sum_{i=1}^n \sqrt{m_i^2 + (\xi p_i^0)^2}$, which should be usually solved numerically.

3. Attach the momentum configuration dependent weight $w = w_0 w_m$ to the event, where w_0 is given by equation 1.108 and:

$$w_m = (P^2)^{2-n} \left(\sum_{i=1}^k |\mathbf{k}_i| \right)^{2n-3} \left(\prod_{i=1}^n \frac{|\mathbf{k}_i|}{k_i^0} \right) \left(\sum_{i=1}^n \frac{|\mathbf{k}_i|^2}{k_i^0} \right)^{-1} \quad (1.110)$$

Introduction to deep learning and its physics applications

Contents

2.1 Fundamental definitions and techniques of machine learning	33
2.1.1 Learning algorithms	34
2.1.2 Neural networks	37
2.1.3 Optimization methods	44
2.2 Review of AI applications in particle physics	47
2.2.1 Motivation	48
2.2.2 Jet physics	49
2.2.3 Non-collider physics (neutrino)	55
2.2.4 Tracking	59

In this chapter we review the basic concepts of machine learning (ML), introducing learning algorithm and neural networks from the basics to the definitions of the state-of-the-art techniques in this field of research. We include also an overview of the most widely used optimization methods, exploited to fit these algorithms on the input data.

We then collect the main artificial intelligence (AI) results in particle physics by classifying the plethora of different models with respect to the particular physics problem they aim to solve.

2.1 Fundamental definitions and techniques of machine learning

In this section, we present the principles of machine learning. We first define what a learning algorithm is and which kind of tasks ML tries to solve. We inspire by the exhaustive exposure of [39, ch. 5]. Then, we introduce the fundamental building blocks of neural networks (NN), namely artificial neurons, and how they are organized in feed-forward (FF) layers to form a first simple NN example. We review the most widely used kinds of layers in the literature, focusing, in particular, on the convolutional and attention layers, which are the hot topics in the computer vision field. In the last part of the section, we describe the main algorithms used to optimize neural networks.

2.1.1 Learning algorithms

An ML algorithm is a model that can learn from data. A definition of what such a learning algorithm dates back to 1997 [40]:

Definition. *A computer program is said to learn from experience E with respect to some class of tasks T and performance measure P , if its performance at tasks in T , as measured by P , improves with experience E .*

In the following paragraphs, we briefly give intuitive descriptions and examples of the abstract entities introduced in the quote: the task, the performance measure and the experience.

The task The task refers to the goal of the learning process. It is important to underline that learning is not identified with the task, but it is the way of achieving the ability to perform the task. Tasks in ML are usually described by how the model processes examples. An example is a collection of n quantitative features, measured from some object, that we want the model to inspect. This way we can encode an example as a vector $\mathbf{x} \in \mathbb{R}^n$. For instance, we treat a squared grayscale image as a vector in $\mathbb{R}^{n \times n}$, where each component is a 8 bit integer, taking values in the $[0, 255]$ range, representing the corresponding pixel's intensity.

The following list reports a summary of the most common machine learning tasks.

- **Classification:** in this type of task, the program is asked to specify which of m categories some input belongs to. Hence, the model will attempt to learn a function $f : \mathbb{R}^n \rightarrow \{1 \dots m\}$, which maps an example \mathbf{x} to its category $y = f(\mathbf{x})$.
- **Machine Translation:** in this type of task, the network takes as input a sequence of symbols in some language and aims to convert them from that native language to another. ML algorithms are employed also in natural language translations, like English-Italian translations.
- **Density estimation:** in this type of estimation problem, the model is trained to output a function $p_{model} : \mathbb{R}^n \rightarrow \mathbb{R}$, where $p_{model}(\mathbf{x})$ can be interpreted as a probability density function on the space where the examples were drawn from.

The performance metric To assess the ability of the algorithm to accomplish some task, we have to define a measure that quantifies the performance. The performance metric happens to be designed specifically for each task the model should be optimized for. For classification and transcription, the accuracy $acc.$ is often a good choice, namely the ratio between the number of examples where the model makes a correct prediction over the total. Alternatively, we can measure the error rate, also called $0 - 1$ loss, which is equal to $1 - acc.$. Of course, the metrics are task-specific and sometimes it is desirable to design a custom loss function that reflects which features we would

like the model to learn, rather than which system's behaviors we want to penalize.

A central concept in ML is generalization: we do not want the algorithm to fit the distribution of the input data, we would like it to learn features underlying data, instead. This is necessary to achieve good performance of examples that are completely new to the model, that is when performing inference on new data. It is common, then, to have two distinct collections of examples (datasets): the training dataset and the test one. The former is exploited by the model to tweak its parameters, while the latter is used to assess its performance.

The experience ML algorithms, depending on what kind of experience they are allowed to receive during the learning process, can be grouped into three main categories: supervised, unsupervised and reinforcement learning models.

- Unsupervised learning algorithms experience a dataset containing many features. The model has to capture this information, learning the true probability distribution function $p(\mathbf{x})$ underlying the examples. The key idea is that the optimization of the cost function and the data themselves are enough to accomplish the given task.
- Supervised learning algorithms are trained on examples with known target labels. That is, each point in the dataset comes with information about the truth: the model is adapted through a trial and error process to output the desired value. For instance, the MNIST [41] database is a collection of 60,000 grayscale 28×28 pixels images of handwritten digits, plus a vector of labels that identifies the correct category of each image. In this training mode, a model tries to predict the correct label y from an example \mathbf{x} , or, in other words, it tries to reproduce the conditional probability density function $p(y|\mathbf{x})$.
- In reinforcement learning algorithms, an agent has to learn how to interact with an environment to maximize a reward function. Models of this kind have to learn to take decisions to be successful. Therefore, robotics represents a natural field of application of these techniques.

The term supervised arises from the fact that the model is taught by the labels what to do, while in unsupervised learning the database completely lacks this information. It is worth noting that these categories are not formally defined and always well separated as there are models that can be used to accomplish different tasks. We would also like to mention that other variants of the learning paradigm exist, such as semi-supervised learning, meta-learning and multi-instance learning to name a few.

Generalization As we stated above, the central challenge in ML is to build models which perform well on new unseen data. This idea remarks the difference between an optimization problem and an ML algorithm: the former is a process in which we seek the model's best configuration in parameter space to reduce the training error, while in the latter we want the generalization error (also called test error) to be small. The generalization error is

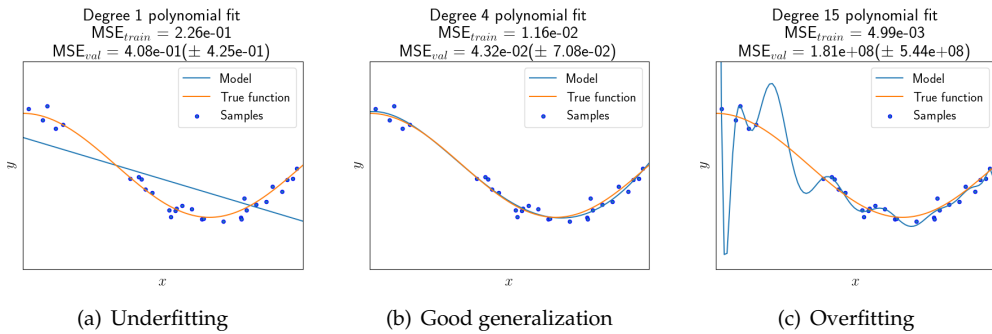


Figure 2.1: Three limit cases. *Left panel*, the linear output model has not captured the curvature present in the data. Training errors are high: underfitting. *Central panel*, the model fits well all the data: good generalization. *Right panel*, the model interpolates the samples with a complicated function with low training error, but high validation error: overfitting. The figure source code is inspired from the Scikit-learn [42] package documentation.

the expected value of the error on a new unseen input. Practically, it can be evaluated by averaging over the performance achieved on the collection of examples called test dataset.

In general, it is not possible to gain insights on the test error knowing just the training error, since train and test datasets represent two distinct collections. To be able to affect the generalization error with training, we make two claims on how the datasets are collected. First, the datasets should contain independent examples. Second, these examples should be sampled from the same probability distribution p_{data} , dubbed data generating distribution. The two hypotheses of independent and identically distributed examples ensure that the training error sets an upper limit for the generalization error. It is possible, then, to influence the final performance of an ML algorithm by monitoring and reducing two fundamental quantities: the training error itself and its gap from the test error.

When we do not manage to reduce one of such measures, we face two classical undesired behaviors of an ML algorithm, called respectively underfitting and overfitting. The former means that the model's parameters are not optimized enough to perform the task and more training steps are required to lower the fundamental quantities. The latter, instead, means that the algorithm is not learning the true data-generating distribution, but it is fitting the training points with a complex function. Borderline cases are displayed in figure 2.1.

To better explain the concept, we can intuitively think about a student. Underfitting corresponds, of course, to the situation in which the student learned the topic just superficially. The student, when is able to generalize, has mastered the subject and can ingeniously apply what he has learned, is the best; whereas when he just parrots back the lesson, he is simply overfitting the issue.

Within the ML field, we protect ourselves from these two bad behaviors, by stopping the optimization algorithm at the right time. The question is, of course, to understand which is the right time. A common technique used to

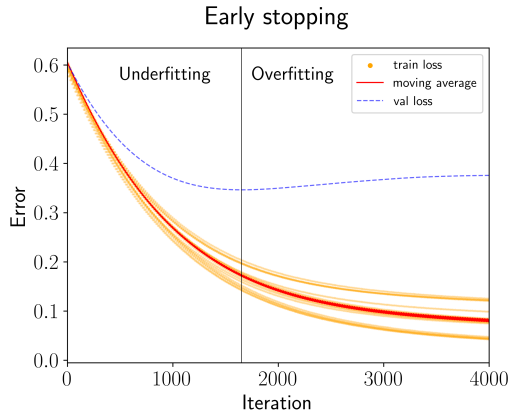


Figure 2.2: Typical trends of training and generalization (over the validation set) errors during training. Eventually, the training curve flattens (orange points and red curve), while the validation loss starts increasing. This behavior signals overfitting and the black line marks the best moment to stop the optimization algorithm, namely, as soon as the generalization gap starts increasing.

address this problem is early stopping. At each optimization iteration, both the training error and the generalization error are evaluated. The training error is given by the loss function value, while an estimate for the generalization error is computed on a separate set of examples, usually called the validation dataset. The validation dataset is a collection of examples that are not used for optimization but are generally employed to tweak some untrainable parameters of the model. Figure 2.2 shows the typical trend of the error functions during training: according to the early stopping prescription, the training should be stopped when the gap between training and validation error starts increasing. This roughly provides a trade-off between underfitting and overfitting regimes.

We have described what an ML algorithm is following Mitchell’s definition [40]. We linked it to a statistical modeling procedure, where the algorithm optimizes its output by processing vectorial examples and tries to grasp the true underlying data generating distribution p_{data} . Since this distribution is usually quite complicated, we have to be sure that our model will be capable of correctly reproducing it. This motivations, supported by the universal approximation theorem [43, 44] lead us to introduce neural networks (NNs) as function approximants that can achieve the goals of an ML algorithm.

2.1.2 Neural networks

We introduce the concept of the NN explaining the characteristics of artificial neurons, named like this because their behavior resembles that of a biological neuron. Furthermore, neurons can be arranged together to form layers, which are the building blocks of neural networks, that in turn can accomplish an incredible variety of tasks, if properly designed and tuned. We overview the different types of layers widely employed in the literature and explain how it is possible to fix a very large number of parameters to allow the pro-

Name	Support	Equation
Linear	\mathbb{R}	$\varphi(x) = x$
Rectified Linear Unit (ReLU)	\mathbb{R}^+	$\varphi(x) = \max(0, x)$
LeakyReLU	\mathbb{R}	$\varphi_\alpha(x) = \begin{cases} \alpha x & \text{is } x < 0 \\ x & \text{if } x \geq 0 \end{cases}$
Exponential Linear Unit (ELU)	$(-\alpha, \infty)$	$\varphi_\alpha(x) = \begin{cases} \alpha(e^x - 1) & \text{is } x \leq 0 \\ x & \text{if } x \geq 0 \end{cases}$
Hyperbolic tangent	$(-1, 1)$	$\varphi(x) = \tanh(x)$
Logistic (a.k.a. sigmoid)	$(0, 1)$	$\varphi(x) = \sigma(x) = 1 / (1 + e^{-x})$
Softmax	$(0, 1)$	$\varphi_m(x_k) = e^{x_k} / (\sum_{i=1}^m e^{x_i})$

Table 2.1: List of the most common activation functions. The parameter α in ReLU and ELU is an input positive constant. The SoftMax activation is typical of multi-class problems: $\varphi_m(x_k)$ is the probability to obtain the k -th category out of a total of m classes.

cess of learning. With this in mind, we hint at the main ideas behind the most common optimization algorithms.

An artificial neuron is defined as a function $f_{\mathbf{w},b} : \mathbb{R}^n \rightarrow \mathbb{R}$ that maps a collection of k input signals $\mathbf{x} = \{x_0, \dots, x_{k-1}\}$ to an output:

$$y = f_{\mathbf{w},b}(\mathbf{x}) = \varphi_{\mathbf{w},b}(w_j x_j + b) \quad (2.1)$$

where \mathbf{w} is a vector of k weights and b is a real coefficient called bias; in general, we refer to these quantities as the model's parameters θ . It is interesting to note the role of the so called activation function φ , because it introduces the opportunity to have non-linearities in an otherwise affine transformation. Table 2.1 lists the most common activations used by ML models.

It is possible to group a set of n neurons to form a dense layer. Hence, the vector of w_j weights and the bias b become an $n \times k$ matrix w_{ij} and an n -dimensional vector b_i , respectively. The layer has now n outputs:

$$y_i = f(o_i) = \varphi(w_{ij} x_j + b_i) \quad \text{for } i = 0, \dots, n-1 \quad (2.2)$$

where we employed Einstein's convention of implicitly summing over repeated indices. Figure ?? pictorially displays the i -th neuron inside a layer and figure 2.4 plots a collection of neurons to form a feed forward or dense layer.

We now look to several classes of layers that employ alternative operations to process inputs. Such layers are more specialized than the general feed-forward one: each of them has a peculiar structure and therefore is best suited to solve particular tasks.

Convolutional layers Convolution is a mathematical operation on two functions of a real argument. Let, then, $f, g : \mathbb{R} \rightarrow \mathbb{R}$ be two real valued functions. Their convolution is the function $(f * g) : \mathbb{R} \rightarrow \mathbb{R}$, defined by the following mapping:

$$t \mapsto (f * g)(t) = \int_{-\infty}^{+\infty} f(\tau)g(t - \tau)d\tau \quad (2.3)$$

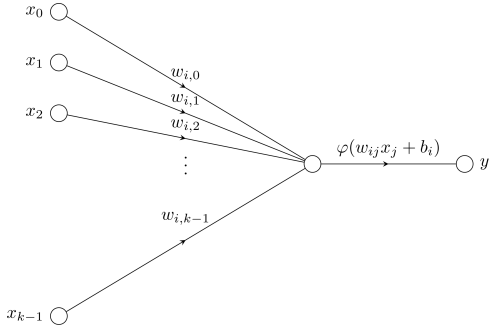


Figure 2.3: An artificial neuron.

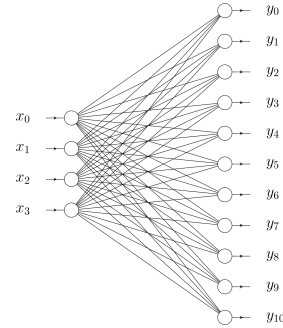
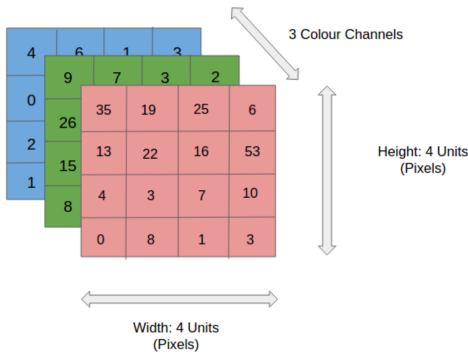
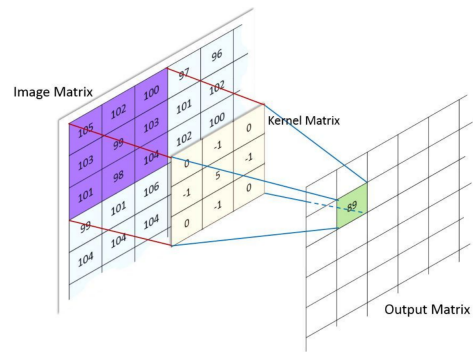


Figure 2.4: A Feed-Forward or dense layer.



(a) An RGB image represented as a grid.



(b) Convolution on a pixel.

Figure 2.5: Images, both grayscale and RGB, are represented by rank 3 tensors. Convolution is the state-of-the-art operation in ML for image processing.

In general, we can look at convolution, as an operator that applies a filtering function g on an input function f : g is called kernel in ML applications and the output is sometimes named the feature map. Furthermore, if g is also a probability density function (pdf), the output $f * g$ is an average of f weighted with the pdf g , or, equivalently, the expected value of f by means of g .

To apply convolution within an ML framework, we introduce a discretized form of this operation: the arguments of real functions become integer indices. Convolutional layers are usually employed, with great success, to process images, which can be seen as grids of pixels described by rank 3 tensors, as in figure 2.5(a): the first two indices identify the row and the column in the grids, while the third one refers to the pixel's channels, which mixes primary colors. One-channeled images are grayscale, otherwise descriptions with three (RGB for red, green, and blue) or four channels (RGBA for red, green, blue and alpha, which measures transparency) are suited for colored ones.

The convolutional kernel K contains all the layer's information and it is represented by a tensor with the following index structure: the first two labels refer to the size of the filtering window (row and columns), the third one runs from 1 to the number of channels in the input image c_{in} , while the

last corresponds to the number of channels in the output image c_{out} . Convolution is the operation in which we apply these multi-dimensional filters to different subsets, with shapes equal to the filtering window, of consecutive pixels in the input image. Mathematically we write:

$$O_{i,j,k} = \sum_{l=0}^{n_r-1} \sum_{m=0}^{n_c-1} \sum_{n=1}^{c_{in}} I_{i \times r + l, j \times s + m, n} K_{l,m,n,k} \quad (2.4)$$

where we introduced the possibility to have strides r and s . Figure 2.5(b) visually shows the convolution operation with single-channeled input, kernel and outputs.

The stride parameters tell the model not to inspect each consecutive subset of pixels: the convolution in this case skips respectively r and s image's cells in each direction before taking again the convolution operation. The stride option affects the information overlap between near pixels in the output image: having minimum strides in each direction, namely equal to one, ensures that the maximum amount of information is retained within the output image. Nonetheless, this is computationally expensive and sometimes, in fact, does not improve the performance of the model. The choice of these parameters is in any case dataset-specific.

Looking at equation 2.4, it is clear that there is an issue when the kernel deals with cells next to the boundaries: there, the sum's indices would go out of range for the input image. A solution consists in carrying on the convolution operation only until the kernel lies entirely inside the image. This option is called `valid` convolution by ML libraries. Of course, the output image will be shrunk in comparison to the input one. The opposite behavior is the `same` convolution, in which the layer implicitly zero-pads the image to have input and output images of the same shape. The `same` option has the drawback that pixels near the borders of the input image influence a smaller amount of cells in the output than the ones in the middle. Optimality between these alternatives, of course, is not an absolute fact, but strongly depends on the input data: the best choice lies, in general, somewhere between the `valid` and the `same` modes.

Three key ideas support the introduction of convolutional layers in neural networks: sparse interactions, parameter sharing and equivariant representations. In the following, we give a brief introduction to these concepts, to motivate the intense usage of convolutional layers in the literature.

Figure 2.4 showed the connections established by a dense layer with the input; in particular, we highlight that each neuron inside the layer is linked with each component of the input vector. Due to this aspect, dense layers are also called fully connected. The number of weights used by a single layer scales linearly with the dimensionality of the inputs. Moreover, images span a two-dimensional space and their number of pixels grows quadratically with the size of the image edge, even containing millions of pixels in the case of high-resolution pictures. It is clear, then, that inspecting images with fully connected layers can be very computationally expensive, both in terms of storing the whole amount of weights and working out the matrix multiplication operations.

The introduction of convolutional layers allows having a smaller number of weights, depending only on the size of the kernel K , which is often

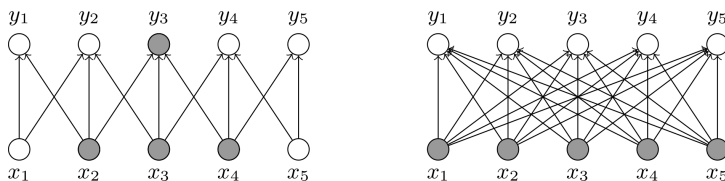


Figure 2.6: Sparse interactions vs full connectivity. Grey shaded circles the central node receptive field. *Left:* convolutional layer with kernel size equal to three, stride one and same padding. *Right:* fully connected layer. Each neuron in the output is linked to every neuron in the input. Even with this simple model, we have a large number of edges in the graph.

way smaller than the input image. We refer to this property of a convolutional layer saying that it presents sparse interactions or sparse connectivity. The dense layer indeed can be seen as a fully connected graph with nodes corresponding to the input and output vector components. The graph associated with the convolutional layer, instead, can be obtained by the previous one retaining only the edges that connect pixels closer than the kernel size. This is optimal for image analysis since in this field we are often interested in looking for patterns arising within a small portion of the image: linking together very distant pixels might be just an overshooting. Sparse connectivity is the natural way to address these issues. Figure 2.6 graphically reviews the concept.

We previously mentioned that storing the enormous number of weights of dense layers may become expensive in terms of memory usage. Convolutional layers provide a simple answer to this problem, called parameter sharing. When training a fully connected layer, the model has to learn the correct weight for each link in the graph. In convolutional layers, instead, the model has to learn a small set of kernel weights and then re-apply them (this consists in sharing parameters) to inspect each portion of the image, resulting in a dramatic reduction of the total amount of memory needed to store the model.

Due to this form of parameter sharing, the model inherits the well-desired property called translation equivariance. In particular, we say that a function f is equivariant to a function g if $f(g(x)) = g(f(x))$. In the present case, convolution is equivariant to translations means that the application order of the two processes on the input image does not matter: if we slightly move the input image and then compute the convolution, the result will be the same as if we made the convolution and then shifted the output. We can also say that a convolutional layer looks for certain features in the input, no matter where they are.

Convolutional layers represent very useful and efficient tools to analyze images, but they usually come with another operation that modifies further their output values. This operation is called pooling. Different types of pooling layers exist, but they all exploit the same idea: they replace the value of each output unit of a convolutional layer with a statistical metric that aggregates information from the nearby pixels. Of course, different metrics are possible: the most used are max pooling [45], average pooling, weighted average pooling and L^2 norm pooling. Pooling is useful because it makes the output invariant under small translations of the input. Indeed, if we apply

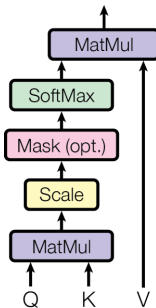


Figure 2.7: The attention mechanism.

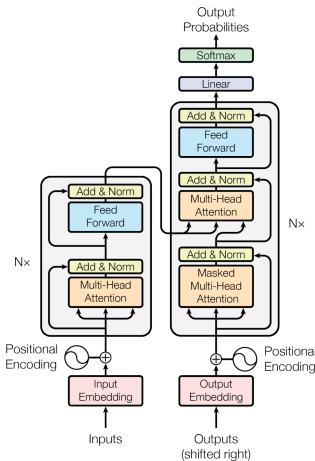


Figure 2.8: The Transformer model.

max pooling over a small area, results would be the same if we shifted by a small amount the input image before because the maximum would be obtained inside the same small area.

Attention mechanism The introduction of the attention mechanism [46] marked a milestone in the field of deep learning, especially among the Natural Language Processing (NLP) models. This particular kind of layer was, indeed, firstly designed and exploited in Transformers architectures to handle sequences of data representing sentences of words. However, given its great success, a plethora of variants have been proposed to either provide improvements on the standard technique or adapt the model to other input structures, such as images. In particular, the Hugging Face¹ community published a large collection of such models [47], which includes the majority of the most widely used architectures. In this paragraph we give an overview of the original work on attention, leaving its alternatives to the interested reader.

The attention mechanism works as in figure 2.7: it accepts three inputs named key $\mathbf{k} \in \mathbb{R}^{L \times d_k}$, query $\mathbf{q} \in \mathbb{R}^{L \times d_q}$ and value $\mathbf{v} \in \mathbb{R}^{L \times d_v}$, respectively. The inputs are encoded in matrices, representing sequences of length L where each element is a vector with an input-dependent dimension $d_k/q/v$. The input vectors are initially transformed into a projection space by three independent matrices of trainable parameters: $W_k \in \mathbb{R}^{d_h \times d_k}$, $W_q \in \mathbb{R}^{d_h \times d_k}$ and $W_v \in \mathbb{R}^{d_o \times d_v}$. Notice that both queries and keys are projected into a space with the same dimensionality.

After this first transformation, the query $Q = W_q \mathbf{q} \in \mathbb{R}^{L \times d_h}$ and key $K = W_k \mathbf{k} \in \mathbb{R}^{L \times d_h}$ quantities are multiplied together to form a matrix of

¹<https://huggingface.co/docs/transformers/index>
<https://github.com/huggingface/transformers>

attention weights according to the following equation:

$$A_{ik} = \text{SoftMax} \left(\frac{QK^T}{\sqrt{d_h}} \right)_{ik} = \frac{\exp(Q_{ij}K_{kj}/\sqrt{d_h})}{\sum_{m=1}^L \exp(Q_{ij}K_{mj}/\sqrt{d_h})} \in \mathbb{R}^{L \times L} \quad (2.5)$$

where the quantity $\sqrt{d_h}$ acts as a normalization factor in the QK^T matrix product.

The SoftMax operation is included to ensure that each row vector of the attention matrix is correctly normalized and represents a probability density function on the sequence space \mathbb{R}^L . The final output of the attention layer is given by the matrix multiplication of the attention matrix and the projected value vector:

$$\text{Attention}(Q, K, V)_{ij} = A_{ik}V_{kj} \in \mathbb{R}^{L \times d_o} \quad (2.6)$$

As a consequence, each row in the attention matrix is a vector of weights that mixes the elements of the value input. In other terms, the element A_{ik} can be interpreted as the amount of attention that the model pays to the k -th word of the value sentence to produce the i -th token of the output. The most widely used form of attention is, in fact, the self-attention, which is obtained from equation 2.6 setting the inputs as $\mathbf{q} = \mathbf{k} = \mathbf{v}$.

The attention operation showed incredible flexibility and tremendously improved the performance of language models, allowing them to scale towards larger and larger architectures containing billions of parameters. The success of the attention operation lies in the fact that it is the learning process itself that gives importance to some features of the inputs rather than others. Moreover, the entire input sequence is allowed to influence the output, providing improved model capacity and expressiveness. The attention operation can be easily parallelized since it is mainly comprised of matrix multiplications: therefore, a multi-head attention version has been defined by the original authors, where multiple attention layers work in parallel to obtain output sequences which are concatenated and eventually passed through a last matrix of weights for further mixing.

Besides the main advantages of introducing the attention mechanism, which also include the ability to handle inputs of varying sizes, the construction operation of the weight matrix does not scale well with the length of the input sequence. Indeed, the complexity grows as $\mathcal{O}(L^2)$ and large amount of memory is needed to hold the computation if the length of the sequence reaches hundreds or thousands of elements. Efforts to achieve a more efficient attention computation have been made in the literature: among them, we note the Performer [48], where the authors try to approximate the softmax function with kernel methods to achieve linear complexity of the overall attention transformation.

The attention mechanism has been also exploited in the treatment of kind of data different than 1-dimensional sequences of words: the Visual Transformer (ViT) [49] and its variants successfully applied these models to computer vision tasks. The main difficulty for attention-based models in processing images is the fact that, as opposed to CNNs, they completely lack geometrical inductive biases. This implies that training is more difficult and unstable, especially in the early stages of optimization.

2.1.3 Optimization methods

In the previous sections we discussed several kinds of network layers, which are the building blocks of neural network architectures. Layers can be stacked one on top of the other to design a custom pipeline that computes the desired outputs. Neural networks are comprised of input and output layers, plus a certain number of hidden layers that sequentially connect the first two. In general, we can represent a neural network by a directed graph whose nodes are the different layers and the edges encode the data processing flow.

Feed-Forward neural networks (FFNN) form, in particular, directed acyclic graphs comprised of fully connected layers. For this simple form of network, it is possible to define the width of each hidden layer as its number of neurons as well as the depth of the network, being the number of hidden layers. The width and the depth influence the number of trainable parameters θ in the model and, hence, its complexity. A NN can be viewed as a family of functions $\{f(\mathbf{x})\}_\theta$ as θ varies in a high-dimensional parameter space. Theoretically, as stated by the universal approximation theorem [43, 44], a NN can approximate any continuous function on a compact subset of \mathbb{R}^n with a particular choice of θ . Flexibility, then, makes NNs fundamental tools in ML algorithms, where we try to guess the data-generating distribution. The challenge consists, of course, in finding the best parameter configuration with an efficient training algorithm. Such a process is called optimization.

In this section, we explain the main ideas behind optimization algorithms found in ML literature: we take a look at gradient descent, momentum-driven and adaptive optimizers. As stated above, the improvements of a model during training are assessed by computing the value of a performance function associated with it, often called cost or loss function \mathcal{L} . As a general prescription, the problem of learning is cast in the form of an optimization problem: the goal is to find the point in the multi-dimensional parameter space that corresponds to the minimum of the cost function.

The optimization is usually accomplished in three different steps.

1. Feed the model with a batch of examples from the dataset and obtain the corresponding outputs (feed-forwarding).
2. Find the gradient of the loss function with respect to the model's parameters (back-propagation [50]). This is done with an automatic differentiation algorithm, always implemented by ML libraries.
3. Update the model's weights according to a particular updating rule (depends on the optimization algorithm chosen).

An epoch of training is the time taken to pass all the training dataset data into this algorithm. The whole training consists of multiple epochs, generally until the loss function converges around a minimum value. We refer to this process as gradient descent.

An important quantity that influences the training is called batch size. The first step of the algorithm does not say how many samples should be contained in a batch for the forward pass. The usual approach consists in dividing the dataset into mini-batches of fixed size and shuffling randomly the training points at the end of each epoch. This introduces random fluctuations in the optimization process helping the algorithm to explore better the

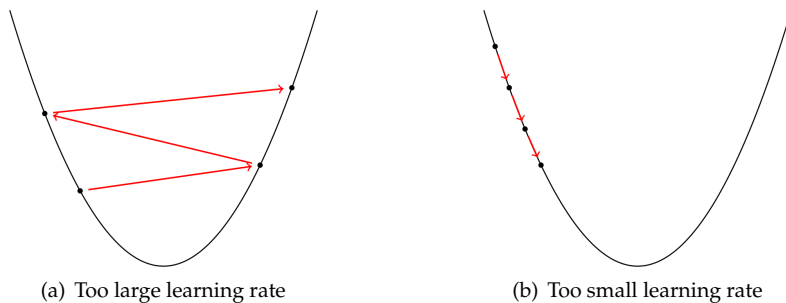


Figure 2.9: Different learning rate behaviors: one-dimensional problem with a quadratic loss function. This example is meaningful since every function can be approximated by a quadratic polynomial if we sit sufficiently close to a minimum.

weights space. The number of examples in each mini-batch, namely the batch size, can drift the process towards two alternative behaviors. If the batch size is too low, subsequent gradient updates will tend to fluctuate and provide opposite contributions, yielding algebraic cancellations that stop the overall optimization. On the other hand, a batch size that is too high will average out the information carried by each example, leading to sub-optimal results.

Step 2 and 3 are driven by back-propagation, which is at the core of the learning process: derivatives of the loss function with respect to the model's trainable parameters are computed by applying the chain rule from the output backward to the inputs of the model. The overall gradient is a vector in the space of the weights and it is exploited to jump from one configuration of the model to another that provides the highest possible negative change in the loss function. The following equation describes the update rule for the Stochastic Gradient Descent (SGD) algorithm, which gives the simplest recipe to implement the optimization process:

$$\theta \leftarrow \theta - \eta \nabla_{\theta} \mathcal{L} \quad (2.7)$$

Of course, the gradient computed during a batch update is only an estimate of the loss function associated with the task: the better the data, the better the approximation of the true gradient and the easier the optimization.

The parameter η in equation 2.7 is called learning rate and it is arguably the most important non-trainable parameter of a neural network. The learning rate controls the process of descending the gradient and must be fine-tuned for every architecture, dataset and task. Two undesired behaviors can arise when the learning rate is not properly set. Figure 2.9 sketches what happens in a simple one-dimensional case with a quadratic loss function, if the learning rate is too large or too low. In the former case, the training progresses too slowly and hardly converges to the minimum. In the latter, the network parameters receive big increments and the loss function oscillates around the minimum value, actually never reaching it. These effects get incredibly enhanced in the optimization of non-convex multi-dimensional problems, causing training failures. Other issues, such as instability of the optimization, vanishing and exploding gradients motivate the research of more effective algorithms.

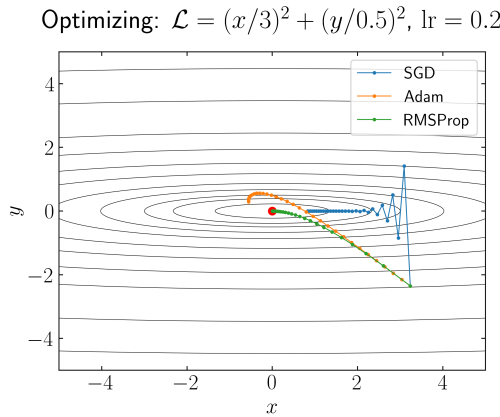


Figure 2.10: Optimization of an elliptical loss function with different optimization algorithms. The red point is the loss function global minimum. Gradients give great contributions in the vertical direction, presenting in an oscillating pattern and leading to slow convergence of SGD. RMSProp and Adam algorithms solve this issue through momentum.

We introduce two of the most widely used optimization algorithms: RMSProp and Adam. SGD performs badly when it has to come across a path in the loss function landscape where gradients in one direction are greater than gradients in all other directions (like ravines). In figure 2.10 we draw this situation in a two-dimensional problem. Ravines often occur around local minima and cause the algorithm to oscillate in the direction of the steepest change, making only very little progress along the rift. A technique called momentum was invented to reduce oscillations and provide a stabler convergence to the minimum. As a result, the stability of this method allows setting learning rates to larger values, speeding up the algorithm. The idea behind momentum is driven by classical point dynamics: if a ball is thrown down a hill, it accelerates increasing its momentum and going downhill faster and faster. When momentum is high, it is more difficult for the ball to make sharp turns in the wrong direction.

RMSProp optimizer, first introduced by Geoffrey Hinton in the lectures of his Coursera class², implements these ideas. During the t -th step, it adds a fraction γ of the update vector relative to the last step $\mathbf{v}(t-1)$ to the current gradient update vector:

$$\mathbf{v}(t) = \gamma \mathbf{v}(t-1) + \eta \nabla_{\theta} \mathcal{L} \quad (2.8a)$$

$$\theta \leftarrow \theta - \mathbf{v}(t) \quad (2.8b)$$

where η is the learning rate as usual and γ is called momentum. The momentum term is usually set to a 0.9 or a similar value. This way the update vector \mathbf{v} account for the sum of all the past collected gradients weighted with the exponential dumping parameter γ :

$$\mathbf{v}(t) = \gamma^t \mathbf{v}(0) + \eta \sum_{k=0}^t \gamma^{t-k} \mathbf{g}_k \quad (2.9)$$

²http://www.cs.toronto.edu/~tijmen/csc321/slides/lecture_slides_lec6.pdf

where g_t is a shorthand for the gradient with respect to the network's weights at step t , $\nabla_{\theta_t} \mathcal{L}$. The problem with this method is that as more steps are taken in the same direction, \mathbf{v} keeps increasing and when the minimum is reached its value is too high for the ball to be slowed down at the optimum point.

Nesterov accelerated gradient (NAG) method tries to face this problem, by computing gradients of the loss function not in the current position θ , but approximately in the position where the ball will be after the update:

$$\mathbf{v}(t) = \gamma \mathbf{v}(t-1) + \eta \nabla_{\theta - \gamma \mathbf{v}(t-1)} \mathcal{L} \quad (2.10a)$$

$$\theta \leftarrow \theta - \mathbf{v}(t) \quad (2.10b)$$

Different algorithms were proposed in ML literature after the introduction of RMSProp. The development of optimization methods is an active research field, because new proposals always appear trying to gather all the benefits from previous methods while introducing new advancements. The adaptive moment (Adam) [51] estimation optimizer is one of the most used algorithms in the ML literature. It is a method that computes adaptive learning rates for each parameter, storing an exponentially decaying average of past squared gradients v_t along with a moving average of past gradients m_t (similar to momentum). The algorithm is based on the following equations:

$$g_t \leftarrow \nabla_{\theta} \mathcal{L} \quad (2.11a)$$

$$m_t \leftarrow \beta_1 m_{t-1} + (1 - \beta_1) \cdot g_t \quad (2.11b)$$

$$v_t \leftarrow \beta_2 v_{t-1} + (1 - \beta_2) \cdot g_t^2 \quad (2.11c)$$

$$\hat{m}_t \leftarrow m_t / (1 - \beta_1^t) \quad (2.11d)$$

$$\hat{v}_t \leftarrow v_t / (1 - \beta_2^t) \quad (2.11e)$$

$$\theta_t \leftarrow \theta_{t-1} - \eta \cdot \hat{m}_t / (\sqrt{\hat{v}_t} + \epsilon) \quad (2.11f)$$

where parameters β_1 and β_2 control the exponential decay rate of gradients and are usually set to 0.9 and 0.999, respectively. ϵ is a small regularizing factor to prevent division by zero, default implementation suggest to set it to 10^{-8} . η is the learning rate.

m_t and v_t are estimates of the first and the second raw moments, their unbiased forms \hat{m}_t and \hat{v}_t are used to update network's parameters. Initial values for m_0 and v_0 parameters are fixed to 0. In the ball example going downhill, Adam method can be compared to a heavy ball moving with friction that prefers flat minima in the error surface. Since this is an adaptive method, learning rate schedules are not needed, because the magnitude of the updates is automatically adjusted according to the form of the loss function.

2.2 Review of AI applications in particle physics

This section summarizes the main applications of deep learning in particle physics. The presented literature is inspired by general and specialized reviews collected in [52], in particular [53, 54].

2.2.1 Motivation

Particle physics produces huge datasets. For example, LHC collects data from protons, organized in bunches colliding at ~ 40 MHz frequency, with $\mathcal{O}(10^8)$ sensors. Each collision produces a large number of particles, whose properties must be measured and stored. Gathering this enormous amount of data might give physicists enough statistics to study interesting rare events. These facts highlight that not only the quantity of collected data is immense, but also its dimensionality. Therefore, machine learning is a set of techniques of paramount importance in this scenario, providing automation in data processing and dimensionality reduction of such information.

For years, physicists in the High Energy Physics (HEP) domain investigated machine learning techniques like neural networks, support vector machines, genetic algorithms and predominantly boosted decision trees (BDTs) implemented in the TMVA framework [55]. This approach was based on the idea of engineering high-level low-dimensional quantities from raw detector data to be fed as multiple inputs to multivariate analysis (MVA) and provided important boosts in many data analysis tasks. However, it was clear that reducing the input dimensionality consisted in discarding a large part of potentially interesting information, leading to inherently limited algorithms. As a consequence, these tools often struggled to provide competitive performance in applications where the dimensionality gap between raw data and extracted features grew large.

Starting in 2012, the computer science community achieved important results in training big neural networks [56–58], converging to models able to provide outperforming solutions against traditional approaches. These publications set the stage for further investigation of deep learning techniques in many other research fields, including particle physics. Moreover, this explosion of research activity was helped by the recent technical improvements in hardware accelerators and their spread as consumer-grade products, granting high-quality computational power at affordable prices. In HEP, this wave mostly translated into the idea that engineered features, designed at cost of time and great intellectual effort, could have been replaced by high-dimensional low-level raw information if processed by deep enough models.

Besides producing large datasets, the particle physics field is especially suited for the proliferation of deep learning applications thanks to the availability of labeled datasets from Monte Carlo event generators. These programs aim to simulate the physics world employing probabilistic laws, accurately describing particle interactions hierarchically from the sub-atomic scales, all the way up to include the macroscopic long-range effects of physics theories. [59–63] represent modern examples of Monte Carlo event generators. The role of the artificial intelligence tools in this picture is often to grasp the probability laws of nature from sets of observations (like particle momenta and charge) and estimate the corresponding Monte Carlo truths (such as the type of a particle or even an interaction between particles in the event).

The rest of the section is dedicated to an overview of the main results in particle physics obtained with deep learning models. We split the plethora of models proposed in the literature by their sector of application. Among physics at colliders, we identify four main areas: jet physics, tracking, fast

simulation and anomaly detection. In this work, we focus on AI applications to jet physics and tracking being entangled with the reconstruction process at colliders. We remark that fast simulation is mainly achieved with the implementation of Generative Adversarial Networks (GAN) [64]: the model generates the specific detector response with a fast inference pass of the GAN generator, producing physical distributions from synthetic random numbers. The anomaly detection applications, instead, are mainly devoted to beyond Standard Model (BSM) searches through the identification of exotic signatures of events or tensions between data and theory that signal the presence of some new physics mechanism. In this area, model-dependent searches aim to identify new kinds of particles or interactions through classification, such as in [65–68], while model independent approaches [69, 70] design ad-hoc strategies to look for new physics with a model agnostic approach. Conversely, in dealing with non-collider physics, we restrict our attention to the advancements in deep learning tools for neutrino physics only, given its prominent role in the present thesis work.

2.2.2 Jet physics

Events at HEP colliders are interpreted in the Quantum Chromo Dynamics (QCD)

framework, namely building a hierarchical picture, which approximates the underlying physics into several non-interacting regimes that happen at different time scales. Due to the Heisenberg uncertainty principle, also different characteristic energy ranges are associated with these subprocesses.

Hence, each event is first associated with a hard scattering subprocess involving partons found inside the protons and interacting at high energy. Then, all the initial and final state particles are subject to a process called parton showering, which takes place at lower energy and is computed within the Monte Carlo software. The showering algorithm consists in recursive branchings, where each initial or final state particle undergoes multiple subsequent splittings in a $1 \rightarrow 2$ fashion, resulting in a tree structure. At this stage, a large number of particles is created and eventually, their momenta directions are mostly focused in a collimated region around the particle initiating the shower, called a jet. Finally, the output of such process can be fed as input to a hadronization model, which takes into account infra-red (or long-range) effects of non-perturbative QCD and builds a final realistic picture of the event. The described algorithms are key ingredients for the Monte Carlo event generators, which manage to link the predictions of physics theories with the outcomes of the measuring experiments at colliders.

Machine learning applications to jet physics mainly involve classification algorithms and include flavor tagging, jet substructure tagging, quark-gluon tagging and pileup removal. All the tagging tasks are related to the identification of the shower initiating particle from the knowledge of the properties of either the final particles representing the tree leaves of the jet or the whole tree nodes itself. Flavor tagging classifies the jet among heavy (c , b , t) or light (u , d , s) quarks, gluons or $W/Z/H$ bosons. Jet substructure tagging, instead, discriminates between $W/Z/H$ and t jets. Finally, quark-gluon tagging is the ability to distinguish between the two kinds of particles contributing to the main source of background in HEP events, sometimes named QCD

background.

Pileup is a concept that roots in the design of accelerators machines: in order to increase the probability to produce interactions, at colliders, bunches of protons tightly packed together are smashed against each other, rather than individually. The luminosity \mathcal{L} is a measure of such compactness: the higher the luminosity, the more the protons are squeezed together and increase the number of collisions. As a consequence, it is likely that for each beam crossing, more than one couple of protons scatters, emitting soft radiation at wide angles named pileup (PU), as opposed to the interesting hard interaction often referred as leading vertex (LV). Pileup is extensively studied at colliders and depends on the machine operative setup. For example, at LHC, each PU vertex roughly contributes for 0.6 GeV/rad^2 of the detector deposited energy [71–73]. Hence, considering an average number of pileup collisions per beam crossing of $n_{\text{PU}} \sim 100$ and characteristic jet radius of $R = 1.0$, each jet might suffer for about 200 GeV of pileup contamination.

The data collected by Atlas and CMS experiments up to run II estimated an average $n_{\text{PU}} \sim 20$, while for run III and HL-LHC, this quantity is expected to increase to $n_{\text{PU}} \sim 80$ and $n_{\text{PU}} \sim 200$, respectively. Pileup interactions modify the shape of the observables reconstructed in the events, affecting jet properties like its overall momentum and mass, rather than jet multiplicity in the event. Being able to design automatic tools to mitigate those effects is expected to be one of the biggest data analysis challenges during the forthcoming LHC phases. These considerations justify the importance given to pileup mitigation strategies at colliders.

The next paragraphs will review the proposed techniques in the literature concerning the described two areas of jet tagging and pileup removal. Both of them try to present the advancements in the research activity as it evolved during the last decades. from the point of view of the different data representations of jet objects used as inputs of the several neural network architectures proposed.

Jet Physics - tagging

Jet tagging mainly concerns classification algorithms. Since the early '90s, shallow artificial neural networks have been used to detect the type of jet-initiating particles. In these initial years, the predominant approach was to feed neural networks, comprised of just a few layers, with event features tailor-made for the specific task or, sometimes, by packing jet information into small vectors of fixed size, containing the most representative characteristics of the object.

Following this idea, [74] exploited a neural network with 3 fully connected hidden layers with 6 neurons each, to process the 4-momenta of the four leading particles within a jet, to discriminate between quarks and gluons. [75], instead, implemented a neural network to distinguish between b and c jets at LEP, with the help of the Fortran77 JETNET 3.0 library [76], which represented the de facto standard for machine learning in HEP physics during those early years.

The advent of deep learning and the improvements in hardware accelerator technologies paved the way for new strategies to solve the jet tagging problem. [77] processed for the first time entire events through neural

networks: their insight was to encode calorimeter information, namely the particle deposited energy (or equivalently its transverse momentum p_T) as a regular grid in the pseudorapidity η and azimuthal angle ϕ plane, forming an image. The pixels of the image contained raw event information that can be used to compute discriminative quantities. The authors implemented a recipe to compute the Fisher linear discriminant [78] after some physics-inspired preprocessing of the images. The algorithm was tested for W boson tagging against QCD background, providing performance improvements against the traditional discrimination method based on N-subjettiness (τ_2/τ_1) [79, 80].

Raw inputs-based neural network tools started being investigated extensively from that point onwards. Examples can be found in top quark tagging tasks [81] and jet substructure classification (namely, understanding if the considered jet is due to a showering of a low-mass single particle or a massive particle decaying into multiple fast-moving lighter objects producing overlapping jets in the calorimeter, like for the $W \rightarrow qq$ process) [82]. Another application of this framework has been presented by [83], who studied the dependency of trained models on the Monte Carlo truths labels in the training datasets. The key observation pointed out that the supervised learning algorithm might bias the model predictions following the QCD approximations employed by the specific generator used to collect the dataset, rather than focusing on learning the underlying true laws of nature. The work raised the problem of the interpretability of neural networks in the jet physics research field for the first time, finding large discrepancies when testing the models on datasets produced by different generators. The authors' final assertion underlined the need to deeply understand how the input information is exploited to extract the output and what assumptions a trained architecture relies on.

The calorimeter tower representation of [77] has then proven to be a powerful representation of jets events, mainly thanks to the success of Convolutional Neural Networks (CNNs) [57]. Indeed, [84] exploited CNNs to inspect the (η, ϕ) plane deposited energy encoding of jet events. They proposed a network to identify highly boosted W bosons against the quark-gluon QCD background. The inputs were initially cast to grayscale images (one channel only), however further developments considered also multi-channel input images. In particular, [85] proposed to build a three-channel RGB image tensor stacking information from charged and neutral particles' transverse momenta, plus the number of charged particles measured within each pixel area.

The standard calorimeter tower images were not the only image-like encoding that has been studied in the literature: an alternative strategy has been given by the Lund Jet Plane [86]. It considers kinematic variables arising while rewinding backward the Cambridge Aachen clustering algorithm [87, 88], attempting to reconstruct a de-clustering history of a jet. The output of this procedure is an ordered set of variables that characterizes a jet object and can be seen as an image tensor. According to the authors, this description should provide greater output interpretability as well as discrimination power when employed in classification tasks.

Although the image based successfully tackled the jet classification problem multiple times, CNNs rely on the assumption that pixels form a perfect

grid, while it is known that actual detectors' geometry is not perfectly regular. Moreover, jet images often contain sparse features which lead to inefficient processing by convolutional kernels. Hence, different data representation strategies have been investigated. A jet object is the result of a clustering algorithm³, which generates a list of jet constituent particles. As a consequence, it can be represented as a sequence of tracks and vertices, forming an acyclic-directed graph or, equivalently, a tree. The complication arising from adopting this encoding scheme is mostly given by the variable length size of the sequences, which cannot be handled by standard Feed Forward Neural Networks.

[90] overcame this difficulty by proposing a Recursive Neural Network architecture comprised of Long Short Term Memory (LSTMs) [91] cells, able to deal with variable-size inputs. The work takes into account other solutions involving Feed Forward Neural Networks supported by input truncation and zero padding. The authors presented a comparison of the different strategies applying them to the problem of light (u, d, s, c) versus heavy quark (b) jet flavor classification, achieving similar performance for the different models. Since then, several algorithms based on RNNs have been proposed to become part of the Atlas [92, 93] and CMS [94, 95] software stack and many more have been published to exploit variable size inputs [96, 97].

The introduction of RNNs allowed for the treatment of the jet as lists and trees of particles. However, even if some natural ordering is obtained by clustering like in the k_t -algorithm, this is just an approximation. Imposing an ordering often means establishing a spatio-temporal relationship between particles to be identified as a history producing a specific final state. However, quantum mechanics principles break down the causality concepts of space and time relying on probabilistic laws. Therefore, the most natural way to represent a jet object would be to decouple from this artificial ordering and process it like an unordered set of particles described by their 4-momenta and quantum numbers. Designing an architecture with the ability to deal with unordered sets of particles would then be desirable. Graph neural networks, deep sets and point clouds networks achieve this objective.

[98] implemented a RelNet [99] to accomplish W jet tagging against QCD background: particles are regarded as graph nodes and the adjacency matrix is learned to aggregate information between nodes through a message-passing operation. [100] constrained a network architecture acting on deep sets, to build infra-red and collinear (IRC) safe observables: the information in each particle observable is then aggregated with a global permutation-invariant operation. The authors implement two different networks called EnergyFlow and ParticleFlow, which consider IRC-safe and non-IRC-safe quantities, respectively. [101] proposed to use the EdgeConv operation [102] on the k -nearest neighbors points of each particle in a point cloud. The point cloud jet representation encodes an event as a matrix where each row represents a vector of properties associated with each particle.

Figure 2.11 shows how the neural network input representations for jet physics evolved through time. Table 2.2, instead, summarizes all the relevant applications of machine learning and deep learning to jet physics.

³A modern C++ implementation of jet definitions and clustering algorithms is given by the FASTJET 3.0 [89] library.

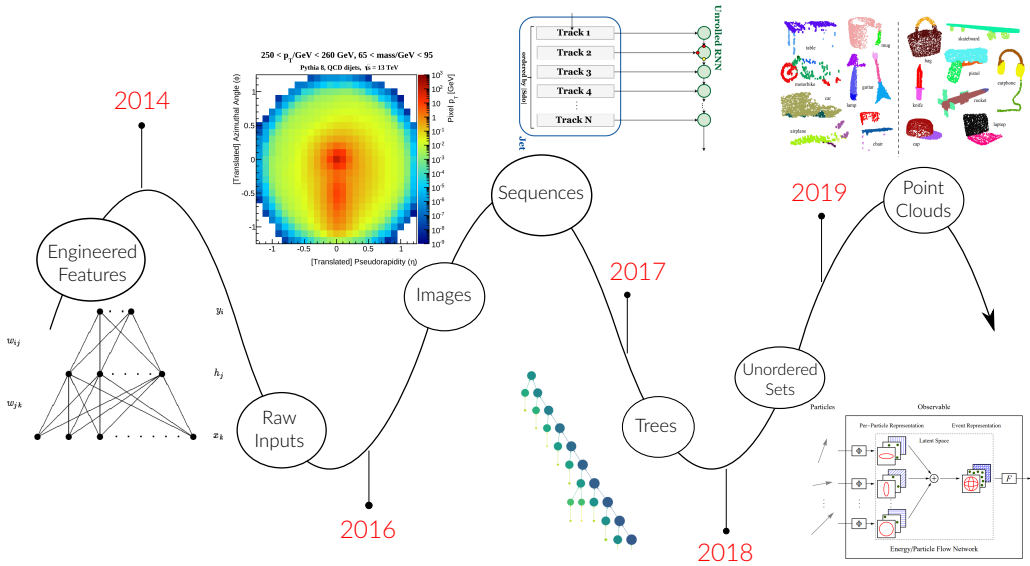


Figure 2.11: The data structure timeline of physics jets: only engineered features were used as input to neural networks before 2014; after [77], several encoding structures have been investigated to efficiently represent jets. The descriptive pictures in the chart are taken, in order of appearance, from: [76, 84, 92, 97, 100, 103].

Table 2.2: Summary of the proposed architectures for jet classification. The table is inspired from [104].

	quark/gluon	W/Z	H	b/c	t
Image	[85, 105, 106]	[82, 84]	[107]		[108, 109]
Sequences	[106]			[92]	
Tree	[97]	[110, 111]			[109]
Graph			[98]		
Unordered set	[100]				
Point Cloud	[101]				[101, 109]

Jet Physics - pileup mitigation

Pileup contribution from charged particles can be removed almost completely thanks to the excellent vertex resolution at the ATLAS and CMS detectors [112–114]. These particles are identified and removed from the event with the charged-hadron subtraction (CHS) procedure [115]. The challenge comes from pileup radiation due to neutral particles, which must be taken into account with specialized algorithms. The rich literature on traditional methods can be categorized on the level of detail these tools act on. A first technique, known as jet areas subtraction [116], relied on calibrating jet level information, scaling its 4-momentum by a relevant factor. However, this procedure did not manage to mitigate the pileup contribution effectively for the computation of several subjet observables.

Therefore, other algorithms have been proposed to act on the internal jet structure, namely at the subjet level. Examples of such tools are usually classified as jet constituents pre-processing, jet or event grooming, subjet corrections and constituent corrections. Grooming, in particular, progressively removes jet constituents contaminated by pileup, cutting the tree description of a jet arising from clustering algorithms through filtering [117], pruning [118, 119] and trimming [120]. SoftKiller [121], instead, is a popular event-level grooming algorithm that equally divides the (η, ϕ) plane in patches of a certain area and imposes a cut-off p_T^{cut} on the transverse momentum cumulated on the patches, such that half of the patches are radiation free. This tool has been used by several works as a benchmark to test the goodness of the proposed models.

Finally, the most advanced pileup mitigating algorithms act at the deepest level, working on a particle-by-particle basis [122–124]. Among those, an excellent example is PUPPI, which evaluates a scaling factor for each particle 4-momentum in the event, by computing a local shape variable α , which collects information about each particle neighborhood. The α distribution for charged particles, for which pileup information is known thanks to the CHS method, can be exploited to extract the scaling weight for each neutral particle. The net effect is to correct jet and subjet observables of interest for physics analysis as if the pileup effects have been switched off.

Machine learning applications for pileup removal mainly act at the particle level, since, as already discussed in this chapter, they can extract useful information from the low-level description of events. The first application of this framework was PUMML [125], a Convolutional Neural Network to inspect RGB images in the (η, ϕ) plane. The three RGB channels convey information about the transverse momenta of all neutral particles, all charged pileup particles and all charged leading vertex particles, respectively. The architecture is trained in a supervised way to output the missing p_T of the neutral leading vertex particles. Performance comparisons were presented against SoftKiller and PUPPI algorithms for the reconstruction of mass and transverse momentum distributions of the LV jets.

Other models have been proposed in subsequent years, trying to take advantage of the different technologies developed in the computer vision research field: [126] introduced PUPPIML, a network working on a graph representation of the event. After subtracting the charged pileup particles, the

remaining ones are arranged in a graph where all pairs of particles closer than a fixed radius R_1 in the (η, ϕ) plane (default value is $R_1 = 0.3$) are connected by an edge. This graph is processed by several Gated Recurrent Units (GRU) [127] and outputs a binary score for each particle to discriminate between leading vertex and pileup. The authors claimed performance improvements up to $\sim 30\%$ of PUPPIML against PUPPI on the resolution of jet-related quantities and even higher ones with respect to SoftKiller.

PUMA [128] exploits the attention mechanism [46] to tackle the pileup mitigation task in realistic detector scenarios, corresponding to extreme setups with $n_{PU} \sim 200$. The performance was tested against classical benchmarks, like CHS and PUPPI, showing large improvements in the key reconstructed jet variable distributions. The authors judged this work as an important achievement in showing the usefulness of statistically-learned algorithms during the HL-LHC phase.

Beyond the supervised algorithms presented in the paragraphs above, some alternative approaches have been proposed. [129] implemented a grooming procedure within a reinforcement learning (RL) framework: a jet is represented as a binary tree graph where each node i is described by a Lund plane derived variable $\mathcal{T}^{(i)}$, containing the state vector observed by the RL agent as well as a pointer to the parent node and the two child ones. The algorithm concerns applying recursively a policy function π_g to all the nodes in the graph. The policy function outputs the probability to groom or not a node in the tree, which determines the action of the RL agent on the environment. The agent is trained through a smooth reward function carefully designed to optimize the resolution of kinematic variables both at the graph and node level, such as the mass of the resulting jet or the fact that a node contributes to the wide-angle soft radiation (PU) rather than to the hard-collinear emission (LV), respectively.

A semi-supervised learning approach for Graph Neural Networks, named Graph SSL, has been investigated by [130]. The main advantage introduced by this technique is the possibility to train directly on real detector data, without the need of Monte Carlo truth labels. The algorithm is based on supervised training to learn charged particles' properties, while inference is done on neutral particles, which represents the main challenge in the identification of pileup. A careful masking procedure is required to train effectively on charged particles as if they were neutral ones. This method allows for avoiding the complex issues regarding the dependence of the models on Monte Carlo datasets and the high costs in terms of simulation time to reproduce physics processes with Monte Carlo generators. The authors benchmarked Graph SSL against PUPPI and observed performance improvements both for the accuracy in the LV-PU identification at the particle level and regarding the resolution of the reconstructed jet quantities.

2.2.3 Non-collider physics (neutrino)

This section presents the applications of deep learning in neutrino physics. For sake of brevity, we restrict our attention to experiments focusing on neutrino oscillations only. Nevertheless, a large number of experiments are concentrating their efforts in this field, as explained in section 1.2. In the field of neutrino physics, deep learning is mainly investigated as a tool for event clas-

sification and automated reconstruction algorithms. The former task is well established in the physics community since the end of the 20th century as a robust strategy to select signal and reject background events, while the latter is still an open issue and many techniques are currently being inspected.

The first neural network application to neutrino event classification is given by [131] in the context of the SNO experiment. The network contains a modest $\mathcal{O}(700)$ number of trainable parameters employing a shallow feed-forward neural network with $\mathcal{O}(30)$ inputs engineered on detector hit patterns and count a single hidden layer with 20 neurons, to distinguish between four classes of neutrino interactions:

- Charge current (CC): $\nu_e + {}^2\text{H} \rightarrow p + p + e^-$;
- Electron scattering (ES): $\nu_x + e^- \rightarrow \nu_x + e^-$;
- Chlorine neutral current (NC): $n + {}^{35}\text{Cl} \rightarrow {}^{36}\text{Cl} + \gamma$;
- Deuteron neutral current (ND): $n + {}^2\text{H} \rightarrow {}^3\text{H} + \gamma$.

The investigation of artificial neural networks eventually spread among neutrino physicists. The main cause of this success can be found in the detector data format: most of the detectors built for detecting neutrinos produce image-like data, which can be processed with the help of modern computer vision and convolutional neural network techniques. As a consequence, two decades after the SNO paper, the NO ν A collaboration [132] proposed to build a CNN to identify neutrino background interactions [133]. The network, named Convolutional Visual Network (CVN), is comprised of two GoogLeNet [134] separate branches inspecting (x, y) and (y, z) hit projections, respectively. The two resulting output tensors are concatenated and fed into a classifier to extract the desired multi-class score. It is interesting to notice that the two views are not concatenated along the channel axis like in RGB images: the authors recognize that each coordinate pixel in 2D projection would overlap unrelated features, as they do not refer to the same (x, y, z) spatial 3D point. The network is trained to compute the ν_e appearance and ν_μ disappearance rates. This work marked a milestone in the field since it became the first neural network-based analysis whose results were included in a physics publication [135].

The GoogLeNet architecture has also been exploited by [136] to search for neutrino-less double beta decay $0\nu\beta\beta$ [137] process at the NEXT experiment. In this application, as opposed to the NO ν A one, three 2D projections of event images are concatenated like RGB images. The authors highlight an improvement against the traditional "blob" discrimination method, see fig. 2.12. The techniques just reviewed try to process images with CNNs, achieving better performance than baseline methods. In recent years, several other articles and many experimental collaborations showed interest in developing CNN-based classifiers, showing the performance superiority of this approach compared to the traditional methods of event classification [133, 138–142].

CNNs have also proved useful in several tasks of reconstruction. First, they have been used to tackle regression problems, namely to predict the interacting neutrino energy value [143] or its direction in the frame of reference of the detector [140, 144]. Then, they helped in identifying non-empty

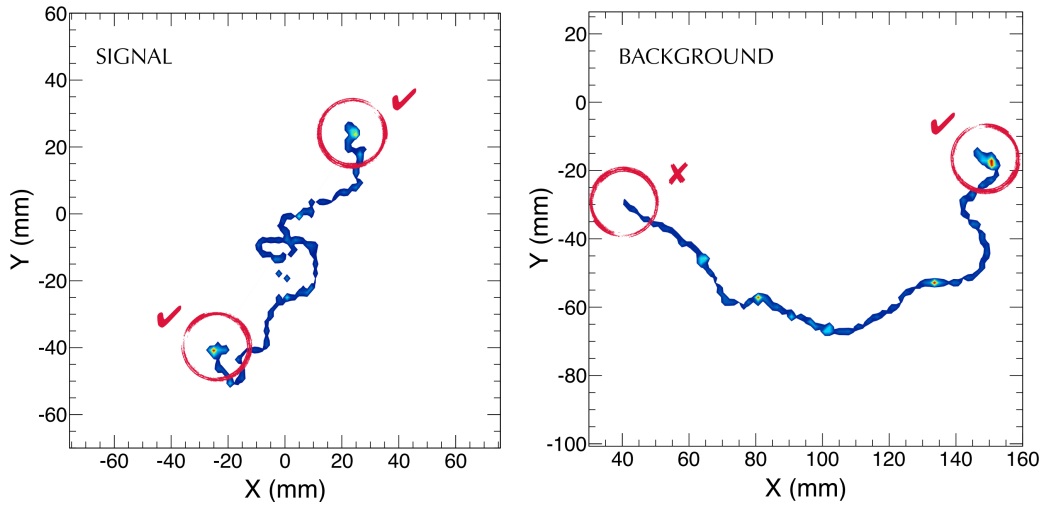
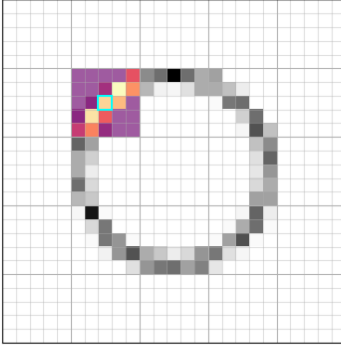


Figure 2.12: Monte Carlo simulation of signal ($0\nu\beta\beta$ decay of ^{136}Xe) and background (single electron of energy equal to the Q value of ^{136}Xe) events in gaseous xenon at 15 bar. The picture shows the energy deposition heatmap colored from blue (low deposition) to red (large deposition). The signal consists of two electrons emitted from a common vertex, resulting in a region (blob) of intense deposition at both track ends. Conversely, the background shows one blob only, leading to cut-off-based discrimination, if the two blobs are properly reconstructed.

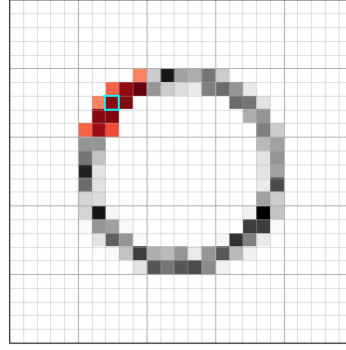
activity regions, drawing bounding boxes around interactions to discard uninteresting parts of the input images: this technique is called Faster-Region Convolutional Neural Network (Faster-CNN). Alternatively, [145] exploit a model inspired by the U-Net architecture [146] to precisely locate track endpoints and shower vertices. Finally, [147–149] implemented CNNs aiming at segmenting the input images to assign each pixel to a type of particle drifting in the detector, detecting Region Of Interest (ROI) coordinates in raw data in 2-dimensional planes and 1-dimensional channels, respectively.

Although Convolutional Neural Network models are the de-facto standard in image processing, neutrino detectors often collect data with special features that cause these techniques to be inefficient. The majority of the events recorded by these experiments contain sparse long 1-dimensional tracks with locally dense features. The result is that large portions of such images are empty, leading to a waste of computational resources when inspected with convolutional filters: those filters, indeed, transform equally both the empty spaces and signal regions. Additionally, the huge quantity of sensors in these detectors gathers information into high-resolution images with $\mathcal{O}(10^6)$ of pixels, that barely fit the memory constraints of modern hardware accelerating devices.

During the last few years, then, the neutrino community has dedicated a great effort to design better encodings and experiment novel techniques to analyze such data. In this picture, Sparse Convolutional Neural Networks (Sparse CNNs) [150] and Graph Neural Networks (GNNs) [151] have been investigated. Two architectures based on Sparse CNNs, acting with convolutional filters on non-zero pixels only, have been implemented by [152, 153].



(a) Normal 2-dimensional convolution: single kernel transformation.



(b) Sparse 2-dimensional convolution: single kernel transformation.

Figure 2.13: The cyan pixel highlights the current convolution pixel. The normal convolution kernel operates on all pixels within the kernel window, while the sparse one acts on non-zero neighboring pixels only.

The operation, depicted by figure 2.13(b), allows to store the event data in an efficient sparse format and dramatically decrease the number of operations required by each convolutional layer forward pass.

On the other hand, GNNs provided performance improvements in processing data from detectors with irregular geometry like IceCube [154] and JUNO [155]. Besides this success, even if the data graph encoding is not always a natural choice when dealing with either image or point cloud data, several works [156–158] showed good results implementing these architectures for event classification and other reconstruction tasks.

The use of GNNs is subject to two major issues. First, there is no standard choice of encoding neutrino data into a graph. Luckily, the sparsity of neutrino images allows identifying detector hits as graph nodes, resulting in graphs of manageable sizes (usually up to a few thousand nodes). Node connectivity, instead, is use-case dependent. The majority of the authors reviewed in this paragraph use similar approaches with small modifications: they rely on some distance metric, computed between each pair of nodes i and j in the graph, and a pre-defined cut-off value d_{cut} above which no edge between the corresponding nodes is drawn. Alternatively, they propose to weight each edge with a normalized version of the distance metric value itself, such that distant nodes have a suppressed information flow in the network. The second problem related to this approach is the additional overhead represented by the graph construction operation: this is often done through dedicated algorithms, like in [155, 156], and must be repeated for all events inevitably increasing the pre-processing wall-time.

In table 2.3 we collect the main deep learning applications to neutrino oscillation experiments found in the literature. The table groups the works published by several collaborations into five task categories:

- event classification, which encompasses event topology, interaction classification and background rejection;

Table 2.3: Review of the deep learning for neutrino physics publications. The first column identifies which detector the publication focuses on. PilarNet [159] is a general-purpose open dataset for LArTPCs data. Note: [152] was published before the PilarNet [159] dataset but deals with similar data and objectives. The citations are color-coded based on the neural network type implemented in the relative work: FFNNs, CNNs, GNNs, Hexagonal CNNs, Sparse CNNs, Quantum CNNs .

	Event classification	Regression	Object detection	Graph	Segmentation
SNO	[131]	-	-	-	-
NEXT	[160]	-	-	-	-
Daya Bay	[138]	-	-	-	-
NO ν A	[133]	[143]	-	-	-
MicroBooNE	[139, 142]	-	[139]	-	[147] [161]
KM3NeT/ORCA	[140]	[140]	-	-	-
DUNE / pDUNE	[141] [162]	[144]	-	[158]	[148]
JUNO	[163]	[155]	[155]	[155]	-
SuperFGD (T2K)	-	-	-	[157]	-
IceCube	[154]	[164]	-	[154]	-
ArgoNeuT	-	-	-	-	[149]
PilarNet	-	-	[145]	[156]	[152, 153]

- regression, grouping neutrino energy reconstruction and neutrino direction reconstruction;
- object detection, that collects interaction localization (vertex reconstruction, bounding box drawing around pixel activity), track end-point localization and shower starting-point localization;
- graph operations, that include background rejection (graph classification), clustering (node classification), 3D reconstruction (graph cleaning through node classification) and primary particle classification (edge classification);
- segmentation, receiving contribution from pixel-level particle identification, instance segmentation and region of interest (ROI) finding.

2.2.4 Tracking

Tracking is a central process of reconstruction at colliders, it consists in grouping detector hits within an event produced by a charged particle interacting in the inner detector region and moving inside a static magnetic field. The traditional approach is based on four different phases: hit clustering, track seed finding, track building and track fitting. The present discussion gives a brief overview of the traditional method employed to solve the tracking problem and it is inspired by specialized reviews on tracking strategies at LHC, [165–167].

The tracking process consists in sequentially reducing with clustering algorithms the number of data from $\mathcal{O}(10^8)$ detector readout channels, to $\mathcal{O}(10^4)$ hits containing energy depositions and finally to $\mathcal{O}(10^3)$ tracks per event. The hierarchical approach starts with hit clustering, which consists in finding the 3–dimensional locations of hits and the corresponding deposited energies from the pixel-level raw data readouts.

After this first stage, the two most computationally expensive steps take place. First, the hits in the inner detector are processed to identify triplets, which consist of the minimum number of points to estimate two important track parameters, namely the curvature and the perigee with respect to the center of the interaction region. The three hits in each triplet form a seed for the final track. Therefore, this step fixes the final track multiplicity.

Second, once the seeds are selected, the proper track construction process starts: the trajectory is sequentially extrapolated from the triplet from the inner to the outer layers of the detector. Many pattern recognition techniques have been designed to tackle this problem, ranging from global methods, such as conformal mapping and Hough transform [168], to local ones, like the track road methods. However, the most efficient algorithm in use is the Kalman filter [169–171]. A more refined version of the original algorithm, the Combinatorial Kalman Filter [172], is leveraged to build tracks from seeds, including the possibility to keep track of branching when multiple candidate points are identified within the same layer and eventually, discard the fake tracks with high efficiency.

The final stage of the tracking problem, namely track fitting, requires estimating the track parameters for each reconstructed trajectory. These include the location of the interaction vertex, the direction of the track along with its curvature and the momentum associated with the interacting particle. Moreover, tests to remove outliers that do not belong to the track are performed in this final phase to further refine the output. This technique achieves almost perfect performance, meaning that the investigation of new methods is devoted to optimizing the existing software implementation and trying to reduce CPU usage time.

However, the next generation High Luminosity LHC (HL-LHC) phase [173], starting from 2026, will see an increase in the current luminosity setup of the Large Hadron Collider by a factor of 10, putting these low-level reconstruction tools under enormous stress. It is expected, in this collider configuration, a great improvement in the hit detector occupancy and the particle tracking software should be able to manage charged particles at a rate of $\mathcal{O}(50 \text{ MHz})$. The traditional approach does not scale at such regimes. A naive solution would be to limit the reconstruction to detector regions around specific calorimetry depositions compatible with rare signatures like leptons or jets with high p_T . However, this approach will completely neglect other phenomena that might hide in discarded regions, like low p_T ones. Hence, alternative methods are currently under investigation.

In this context, the HEP.TrkX project [174] aims to study deep learning solutions to the particle tracking issue. The main outcome has been a model [175] combining CNNs and Recurrent Neural Networks (RNNs), mainly employing Long Short Term Memories (LSTMs) cells, to reconstruct tracks within a simplified detector simulation. The generated data involve straight-line tracks and neglect all other kinds of physical complexities, such as track curvature, material effects and detection inefficiencies. The model is trained to solve two tasks in particular: a 2-dimensional single-track reconstruction starting from seeded hits and an end-to-end estimation of the track parameters without any seeding.

Detector data are projected onto two axes representing the detector layer and the channel within each specific layer. The tool opens for the possibility

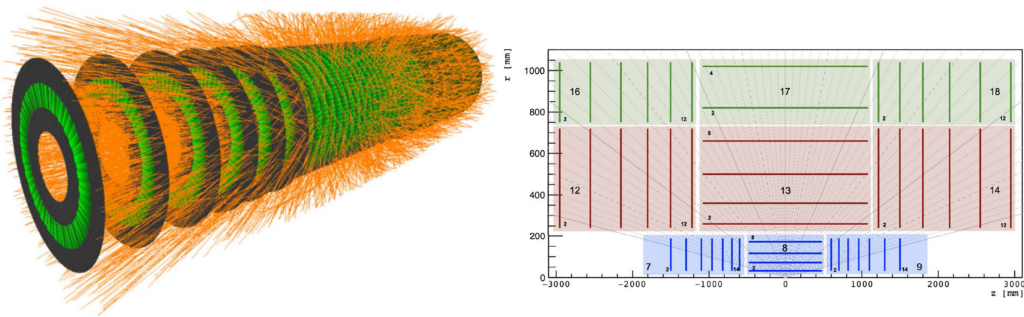


Figure 2.14: A sample event from the simulated TrackML dataset. The left panel shows a collision event with the TrackML detector picture and the right image is a schematic representation of the upper half of the detector projected on the r - z plane. The figure is taken from [178].

of encoding irregular layer geometries of varying size with two strategies: either zero padding the input to retrieve a regular rectangular grid, or through an autoencoder-like architecture that embeds each layer input into a fixed-size vector representation with the help of a dense network, followed at the end of the pipeline by another fully connected layer that projects back the output into the original layer dimensionality. The data encoding based on bi-dimensional images has also been exploited by [176], the key idea is again to model the recursive track-following approach of the Kalman filter through an LSTM, showing promising results in a semi-realistic detector simulation.

Other approaches based on Graph Neural Networks (GNNs) have been introduced by [177] driven by the observation that the image-like representation of the data would not be able to manage realistic use cases matching the HL-LHC conditions. Indeed, the collider and detector updates will provide high-dimensional and sparse data due to the increased number of detector layers built with irregular geometries, which would probably cause inefficiencies in the standard approaches with CNNs. The authors advocate the investigation of methods acting on the space-point representation of data, instead, involving variable amounts of hits per event and exploiting the full detector resolution.

In 2018, the TrackML competition [179] took off within the HEP community with the intent of finding the best candidate for the future particle tracking algorithm. The desired feature of such a tool would be to achieve the best performance score across several metrics reflecting the need to target high reconstruction efficiencies with the fastest algorithm in terms of inference time. Figure 2.14 shows an event example from the TrackML dataset, highlighting a large number of tracks to be reconstructed and the complex detector design.

Following this competition, HEP.TrkX evolved into the Exa.TrkX project [180] which investigated a wide variety of models to solve the task, mainly through GNNs [181, 182]. The project finally published an article [178] summarizing the GNN pipeline on the TrackML dataset, towards a first validation on ATLAS and CMS real detector data. The potential of GNNs has also been exploited on implementations for specific hardware acceleration, mainly provided by Field Programmable Gate Arrays (FPGAs) [183].

Part II

Monte Carlo event generators on hardware accelerators

Interpolating parton distribution functions

Contents

3.1	Parton Distribution Functions	65
3.2	LHAPDF: the Les Houches Accord PDF	66
3.3	PDFFlow: interpolating PDFs on GPUs	68
3.3.1	Methodology	68
3.3.2	Software design and benchmarks	70
3.3.3	Physics examples	74

In this chapter, we discuss the implementation of PDFFlow [184, 185], a Parton Distribution Function (PDFs) access tool. We first briefly introduce PDFs in HEP and LHAPDF, the state-of-the-art framework for PDF values interpolation, LHAPDF. The last section of the present chapter contains a detailed description of our novel implementation of such kind of technology. We show that PDFFlow software can leverage hardware acceleration to speed up the computation while obtaining the same outputs of the previous solutions.

3.1 Parton Distribution Functions

Parton Distribution Functions are of paramount importance in HEP since they universally describe the inner content of hadrons and their partonic structure. At leading order in perturbation theory, PDFs $f_i(x; Q^2)$ represent the probability to extract a parton of flavor i with a given momentum fraction x from a hadron, when probed at an energy scale Q^2 . At higher orders, this naive probability interpretation is not true anymore, since PDF positivity cannot be ensured. Nevertheless, these functions respect at all orders particular relationships, known as sum rules, which constrain their normalization, since integrating over the momentum fraction of the parton and summing all the possible parton flavors yield the momentum of the parent hadron:

$$\sum_i \int_0^1 dx f_i(x; Q^2) = 1 \quad (3.1)$$

Further, the baryon number conservation leads to the following equation:

$$\int_0^1 (f_i(x, Q^2) - \bar{f}_i(x, Q^2)) = n_i \quad (3.2)$$

where i takes values on the parton flavors and counts the valence partons of the specific baryon involved in the formula: for example, for the proton the non-zero n_i s are $n_u = 2$ and $n_d = 1$. For completeness, \bar{f}_i denotes the antiquark PDFs for flavor i . Equations 3.1 and 3.2 are intended to be satisfied at all orders for every fixed factorization scale Q^2 . For fixed x the evolution of the PDFs with respect to the factorization scale Q^2 is given by a set of partial differential equations known as the DGLAP equations.

PDFs are a crucial object for both theoretical and experimental aspects of collider physics: they must be convoluted with the partonic cross section $\hat{\sigma}_{i,j}$ to compute the total event cross-section:

$$\sigma(Q^2) = \sum_{i,j} \int_0^1 dx_1 dx_2 f_i(x_1, Q^2) f_j(x_2, Q^2) \sigma_{i,j}(x_1, x_2, Q^2) \quad (3.3)$$

where the sum runs on all the partonic flavors of the two partons i and j picked from the two colliding hadrons, respectively. The PDFs cannot be derived from first principles only, since they encode the long-distance effects of non-perturbative QCD. Therefore, they are fitted on experimental data by PDF fitting collaboration following different assumptions and methodologies [186–188]. The measurement of PDFs is influenced by several parameters like renormalization and factorization scales as well as the running of the QCD strong coupling α_s : hence, PDFs are grouped into sets containing replicas, taking into account the variations of these quantities.

3.2 LHAPDF: the Les Houches Accord PDF

During the 90s, PDFLIB [189] has been the main software dedicated to accessing PDF values. Written in the Fortran language, it originally gathered about 100 different PDF sets. However, the consistent production of measurements by PDF fitting collaborations like CTEQ and MRST highlighted that storing the PDF values within the library itself was not an option due to the unbearable memory requirements. Therefore, the first versions of the LHAPDF software [190, 191] tackled the issue proposing to store only PDF starting values at low Q^2 scale and evolving them through the DGLAP equation to reach high energies.

Again, this solution was eventually surpassed around the mid–2000s mainly due to the large amount of custom code required by each different PDF parametrization to be included in the framework and the need to modernize the algorithms for the Q^2 –evolution. As a consequence, the PDF collaborations decided to provide external files collecting entire PDF grid values of fitted points in the (x, Q^2) plane together with routines to access them and interpolate values between grid knots. This choice decoupled the PDF values to the LHAPDF library, but at the same time filled it with a plethora of methods to read the multitude of available formats. Given the Fortran static memory allocation, this resulted in large memory portions of code never accessed by the user focusing on some specific methods only.

A decade later, LHAPDF 6 [192] finally ported the software to C++ language, also providing a Python interface. The program is built around the object-oriented programming philosophy, in a way that allows the user to

easily extend the library to incorporate custom code. The PDF function values are accessed through a powerful cascading metadata system following a universally agreed format, allowing the PDF fitting collaboration to provide new measurements independently from the LHAPDF software release development. PDF grid values can be accessed by instantiating a `PDF` class object representing parton density functions for several parton flavors and calling its `PDF::xfxQ(...)` and `PDF::xfxQ2(...)` methods: the only difference being in the energy scale argument, which should be squared in the latter case. Note that the output value is always in the $xf(x, Q^2)$ format, which is the standard in PDF sets.

The agreed format for presenting the PDF grids contains values at discrete knots in the (x, Q^2) plane. Points position in the grid is PDF set dependent and usually ranges from very small momentum fractions x of the order of $\mathcal{O}(10^{-9})$ to 1 and from few GeV to $\mathcal{O}(100 \text{ TeV})$ in the Q energy scale. For example, the `NNPDF31_nlo_as_0118` PDF set shows $x \in [10^{-9}, 1]$ and $Q \in [1.65, 10^5] \text{ GeV}$. The knots are not sampled uniformly, to allow PDF discontinuities across quark mass thresholds, like in the case of the b quark whose mass $m_b = 4.92 \text{ GeV}$. The grid limits are accessed via the `PDF::xMin()`, `PDF::xMax()` and `PDF::QMin()`, `PDF::QMax()` methods. Sometimes a PDF grid is organized into multiple sub-grids.

A value $xf(x, Q^2)$ within the grid boundaries can be retrieved by interpolating neighbor node values with a specific method. The default behavior implemented by LHAPDF is to interpolate plane values through cubic Hermite splines in the $(\log x, \log Q)$ space. This algorithm requires sampling 4 neighbor knot values as in figure 3.1(a) and performing a log-bicubic interpolation. In regions close to the grid boundaries, where the number of neighbor points is not enough to perform such interpolation, the software automatically switches to bilinear interpolation, which requires 2 neighbor knots only.

Outside the grid boundaries, some extrapolation method is required. Multiple choices are available within the LHAPDF 6 library, the simplest one being to raise an error if a point outside the grid range is queried. Another option is to freeze the grid edges, returning the PDF value at the closest grid knot. However, the default extrapolation method is the legacy extrapolation system from LHAPDF 5, proposed by the MSTW collaboration: figure 3.1(b) shows the regions where the three behaviors for the low- x , low- Q and high- Q extrapolation take place.

When a low- x value is queried for a specific energy scale Q , a continuation to x is guaranteed by linear extrapolation from the two lowest x_0 and x_1 knots in the PDF grid. If the PDF values are sufficiently positive, namely they both exceed a threshold set to 10^{-3} , their logarithm is used in the extrapolation, otherwise, xf is exploited. The same method is implemented for the high- Q region extrapolation.

For the low- Q value extrapolation a different method is employed. The LHAPDF framework interpolates the anomalous dimension $\gamma(Q^2)$, namely $\gamma(Q^2) = \partial \log xf(x, Q^2) / \partial \log Q^2$, between the value at Q_{min} and 1 for $Q \ll Q_{min}$ with the following rule:

$$xf(x, Q^2) = xf(x, Q_{min}^2) \left(Q^2 / Q_{min}^2 \right)^{\frac{\gamma(Q_{min}^2) - 1}{Q_{min}^2} Q^2 + 1} \quad (3.4)$$

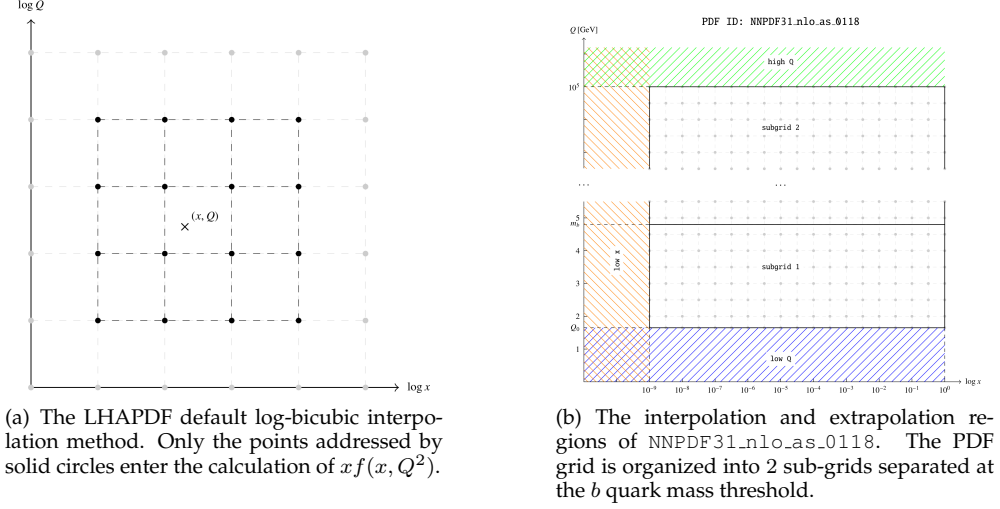


Figure 3.1: Scheme of the LHAPDF algorithm for PDF values access. The grid knots spacing is uniform for convenience only, real PDF grids are not uniform in the $(\log x, \log Q)$ plane.

This ensures that the following limiting behaviors are verified:

$$xf(x, Q^2) \rightarrow \begin{cases} xf(x, Q_{min}^2) \left(\frac{Q^2}{Q_{min}^2} \right)^{\gamma(Q_{min}^2)} & \text{for } Q^2 \rightarrow Q_{min}^2 \\ xf(x, Q_{min}^2) \frac{Q^2}{Q_{min}^2} & \text{for } Q^2 \rightarrow 0 \end{cases} \quad (3.5)$$

In regions where both the x and Q values need extrapolations, first the corresponding x -algorithm is performed, then the results are passed through the continuation function for Q -values.

Integral to the parton distribution function description is the correct evolution of the strong running coupling $\alpha_s(Q)$, which depends on the energy scale Q at which it is evaluated. Therefore, the PDF sets are accompanied by a sample of measurements of α_s at different energies and LHAPDF implements interpolating and extrapolating methods similar to the PDF ones. The provided grid exhibits knots on the $\log Q$ line. The interpolation algorithm is again a cubic Hermite spline, while for $Q > Q_{max}$ a constant value $\alpha_s(Q_{max})$ is returned and for $Q > Q_{min}$ a logarithmic gradient continuation similar to the low- x behavior of the PDF is implemented.

3.3 PDFFlow : interpolating PDFs on GPUs

3.3.1 Methodology

The PDFFlow package [184, 185] follows the VegasFlow [193, 194] concept to vectorize operations on the program inputs. The neat result is that transformations that should have been done sequentially on independent points are now done altogether on the whole sample. As a consequence, scalar input arguments of the functions become vectors with the size of the number of

Table 3.1: Description of the system used for the matrix multiplication benchmark: hardware and software information.

Software	Version	Hardware specific	Value
Python	v3.10	CPU model	Intel Xeon Gold 6130
NumPy	v1.23	CPU cores	64 @ 2.10 GHz
TensorFlow	v2.10	CPU RAM	192 GB
		GPU model	Nvidia Tesla V100
		GPU memory	32 GB

desired events to be computed. Hardware accelerators, like GPUs, provide massive speed-up factors in highly parallel environments like the present one. However, the programming skills required to port the code and optimize it into a suitable format for such devices represent a strong limit for the current applications.

We present a prescription to port the code into a format compatible with hardware accelerators leveraging the Python language and Google’s Machine Learning TensorFlow library [195]. Indeed, the `PDFFlow` package is implemented by exploiting TensorFlow primitives, which are natively designed to be GPU-friendly. Therefore, the tool automatically inherits the TensorFlow portability on hardware accelerators. We wrap each custom function code with the `tf.function` decorator triggering the computation of a `tf.Graph`: this induces a transformation on Python static data types and operations into `tf.Tensor` and `tf.Operation` primitives, respectively. The process automatically builds an implicit operational graph, which optimizes the code and runs seamlessly on multiple devices like multi-thread CPUs, GPUs and, if the operations are supported by the TensorFlow library version, even on TPUs. A little overhead in the running time is introduced by this function conversion to load the corresponding `tf.Graph` in memory. Luckily this step is done only once, namely when the piece of code wrapped by `tf.function` is executed for the first time.

To show the capabilities of this method, we design a toy example to assess the speed of the matrix multiplication operation for different implementations. We multiply a matrix of size $100 \times n$ times a vector of length n of random numbers sampled from the normal distribution. We let the size n span a wide range of values from 10^2 to a maximum of 10^6 . Table 3.1 collects the hardware and software specifics employed in this study. Note that this represents the latest stable version of the software available on the Python Package Index (PyPI) [196] at the time of the `PDFFlow` article [184] publication (July 2021). However, the present discussion is valid for all the `v2.x` TensorFlow versions. We test for different implementations of the matrix multiplication function in Python explicitly defined in figure 3.2:

- a matrix multiplication implemented in pure Python code with list comprehensions;
- a NumPy [197] implementation exploiting the `np.matmul` function;
- a TensorFlow implementation wrapping the code with the `@tf.function` decorator.

Figure 3.3 shows the behavior of the different implementations of the matrix multiplication as a function of the matrix column size n . The TensorFlow implementation runs either on CPU or GPU, while the others are CPU only. We note that the maximum size for the parameter n is strictly dependent on the device memory hosting the computation: the GPU will raise an Out Of Memory (OOM) error if the size of the tensors exceeds the available memory, thus interrupting the job. On the other hand, the CPU is more flexible and tries, nevertheless, to handle the computation at the price of a great slowdown: this is due to the CPU exhausting the RAM memory and trying to exploit the hard disk memory instead. The buses connecting the RAM and the CPU ensure way faster communications than the ones between the CPU and the hard disk: this motivates the performance breakdown.

As a rule of thumb, the expected memory used by an algorithm can roughly be estimated by summing the memory allocated for each tensor created in the routine. However, TensorFlow always reserves some small amount of memory (about $\mathcal{O}(100 \text{ MB})$) for internal operations depending on the algorithm itself. Even neglecting this little memory overhead, an a priori estimation of the memory used by a script might be difficult to compute, especially for complex operations. Therefore, the user should be approximately aware of the amount of memory he needs and possibly run memory tests before deploying his tool.

The plot in figure 3.3 displays that the first calls to the `tf.function` decorated code present an overhead time due to the `tf.Graph` construction; the subsequent function executions, instead, manifest the improvements of these operations against the more common Python and NumPy versions. Another feature that is evident in the graph is the almost constant performance of the TensorFlow program running on the GPU device: indeed, this behavior is expected until the whole GPU memory gets exhausted.

As a final remark, the TensorFlow CPU curve has the best performance for low sizes of the input matrix, even exceeding the GPU one in this region. This effect is probably caused by the fact that the CPU has to place the tensors on the GPU before launching the computation and the elapsed time can be comparable to the effective computing time for small-size operations.

In the rest of this chapter, we discuss the performance improvements brought by the introduction of this prescription into state-of-the-art software for parton distribution function value access.

3.3.2 Software design and benchmarks

Figure 3.4 depicts the PDFFlow design, which follows the LAHPDF6 concept. The `mkPDF()` function instantiates the desired PDF representation, given by the `PDF` class. A `PDF` object stores all the quantities and algorithms needed for the interpolation of both the PDF itself and the strong running coupling α_s . Notable member methods in the class are the trace methods (`trace` and `alphas.trace`) and interpolating methods (two for the PDF and two for α_s), contained in the green dashed boxes in the figure. The tracing methods trigger the building of the `tf.Graph` relative to the PDFFlow operations. Calling these methods before querying interpolation points allows ahead-of-time compilation of all the functions declared within the tool.

The interpolating methods include a call to a `Subgrid` class object. `Subgrid`


```
import numpy as np
import tensorflow as tf

def py_function(x, y):
    """The Python function with list comprehension."""
    return [
        sum(xx * yy[0] for xx, yy in zip(x_row, y))
        for x_row in x
    ]

def np_function(x, y):
    """The NumPy function."""
    return np.matmul(x, y)

input_signature=[
    tf.TensorSpec(shape=[10, None], dtype=tf.float32),
    tf.TensorSpec(shape=[None, 1], dtype=tf.float32),
]

@tf.function(input_signature=input_signature)
def tf_function(x, y):
    """The TensorFlow function."""
    return tf.matmul(x, y)
```

Figure 3.2: Matrix multiplication functions code snippet. The `@tf.function` decorator requires to define the shape of the input tensors, where `None` signal a variable length dimension.

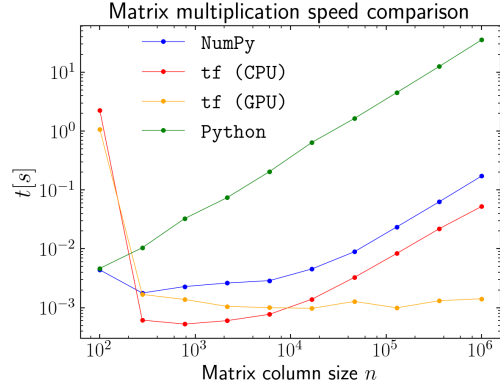


Figure 3.3: Time comparison of different matrix multiplication implementations.

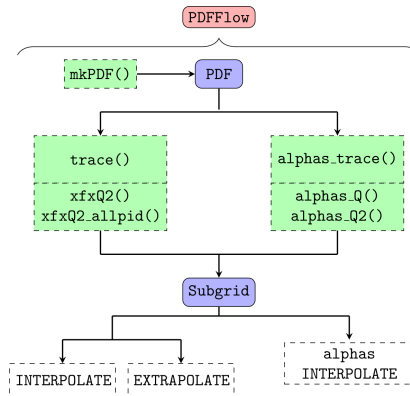


Figure 3.4: PDFFlow flowchart. Blocks are color-coded as follows: red for the tool, violet for classes, green for functions and class methods, and white for interpolation algorithms.

Device	CPU model	CPU cores	CPU RAM	GPU(s) model	GPU memory
C	Intel i7-6700K	4 @ 4.2GHz	16GB @ 3000MHz	Nvidia RTX2080	8GB
P0	AMD 2990WX	32 @ 3-4.2GHz	128GB @ 3000MHz	-	-
P1	Intel i9-9980XE	18 @ 3-4.4GHz	128GB @ 2666MHz	Nvidia TITAN V Nvidia RTX2080TI	12GB 12GB
P2	Intel Xeon Gold 6126	6 @ 2.6-3.7GHz	20GB @ 2133MHz	Nvidia V100 (2x)	32GB

Table 3.2: Description of the systems in which the different codes have been run.

stores PDF grid data and includes a switch to enable interpolation on α_s grid knots. This class gives access to algorithms that implement the actual computation of PDFFlow outputs, represented by white boxes in the flowchart and briefly described below.

The interpolation procedure implemented in PDFFlow follows the prescription originally implemented in LHAPDF6, namely the log-bicubic interpolation in terms of x and Q^2 and the extrapolation methods presented in section 3.2. The PDF data files stored in the LHAPDF directories are directly loaded into `tf.Tensor` objects so it is not necessary to install new sets or formats. The interpolation algorithms compute independently query points belonging to different sub-grids of the PDF set. Special care is taken about regions in the (x, Q^2) plane close to quark mass thresholds and grids x edges, where the minimum number of knots required for bicubic interpolation is not available.

Similar to the PDF interpolation procedure, the evaluation of the running of the strong coupling, $\alpha_s(Q)$ is performed using a log-cubic interpolation with constant extrapolation from the $(\alpha_s(Q), Q)$ nodes stored in the PDF metadata file. The implementation includes the improved treatment of the sub-grids mechanism and takes into account the impact of flavor thresholds on $\alpha_s(Q)$ evolution.

We introduce now the interpolation accuracy and performance benchmarks results between PDFFlow v1.0 and LHAPDF v6.3.0 libraries. All the studies presented here and in the next section, where we discuss actual physics examples, are done exploiting the hardware pointed out in table 3.2. The consumer-grade hardware (C) consists of a standard desktop computer with gaming level specifics. Different research groups have access to professional grade hardware which is better suited for the kind of computation described in this part of the thesis. In particular, this corresponds to many-threaded CPUs and GPUs with enough memory to hold the necessary kernels for very complicated computations. For the CPU-based calculation, we use the P0 system with a medium-level processor in terms of clock speed, while for the GPU-based calculations we use two different machines: P1 with a very powerful processor, which greatly reduces the latency of the calculation for CPU-based operation such as the accumulation of the final results, and P2, a less powerful CPU and a more limited RAM size which can add an important overhead to the communications between the CPU and the GPU. In exchange, the V100 GPUs have greater memory size which reduces the frequency of communications between the main memory and the device.

To measure and compare the PDF interpolation accuracy between PDFFlow and LHAPDF, we define a relative difference:

$$r_i(x, Q) = \frac{|x f_i^{\text{PDFFlow}}(x, Q) - x f_i^{\text{LHAPDF}}(x, Q)|}{|x f_i^{\text{LHAPDF}}(x, Q)| + \epsilon}, \quad (3.6)$$

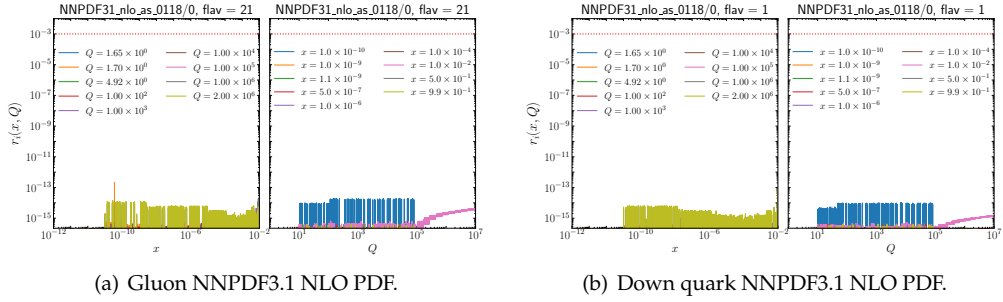


Figure 3.5: PDFFlow vs LHAPDF relative difference for the NNPDF3.1 NLO central PDF. In both the sub-figures, the first column refers to differences in a grid of x points for fixed Q values, while the second column shows differences in a grid of Q values for fixed x .

where $xf_i(x, Q)$ is the numeric value of a PDF flavour i evaluated at a given momentum fraction x and energy Q , and $\epsilon = 10^{-16}$ is a ratio stabilizer. In figure 3.5 we plot this relative difference for the NNPDF3.1 central PDF at Next-to-Leading Order (NLO) for the gluon and down quark flavor values. In both cases, we plot first the error as a function of x for fixed values of the energy scale Q and the opposite for the second image. We prove that PDFFlow interpolated values are compatible with LHAPDF ones, since the error is several orders of magnitude lower than the fixed threshold of 10^{-3} , which was set by LHAPDF itself during the upgrade from version v5 to v6. Similar results can be achieved by comparing different PDF sets, we present a complete set of numerical comparisons for the MMHT2014 NLO PDF [186] in figure 3.11 at the end of the present chapter.

We remark that the pattern of the errors showed in all the presented accuracy plots is determined by the rounding errors due to the representation of numbers with finite precision in the machine. Another source of discrepancy might be given by the different implementations of the low-level primitives between the specific libraries exploited by the PDFFlow and LHAPDF tools. These small fluctuations can be neglected as long as they prove to be much lower than the 10^{-3} threshold set above.

A similar benchmark is made on the interpolation of the strong running coupling $\alpha_s(Q)$. We compute the same relative error $r_{\alpha_s}(Q)$ with the help of equation 3.6, after replacing the $xf_i(x, Q^2)$ PDF value with $\alpha_s(Q)$. Figure 3.6 demonstrate that, again, the values interpolated by PDFFlow are equal up to rounding errors to the LHAPDF ones. In terms of performance speed, we conduct a benchmark analog to the one presented in section 3.3.1: we measure the elapsed time to interpolate sets of (x, Q^2) points by PDFFlow and LHAPDF. The query points are distributed within the PDF grid boundaries, whereas each set has a logarithmically increasing size across different evaluations. The resulting data are collected in figure 3.7. We observe a great performance improvement when running PDFFlow default configuration on CPU, thanks to the built-in multi-threading CPU support. Concerning GPU results, the performance improvement is huge and opens the possibility to construct new models and applications with parallel evaluations. Note that, as opposed to figure 3.3, the time excess in the first call of the PDFFlow inter-

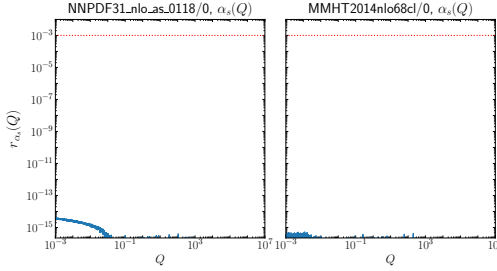


Figure 3.6: PDFFlow vs LHAPDF relative difference for $\alpha_s(Q)$ interpolation. The left and right panels refer to NNPDF3.1 NLO and MMHT14 NLO sets, respectively.

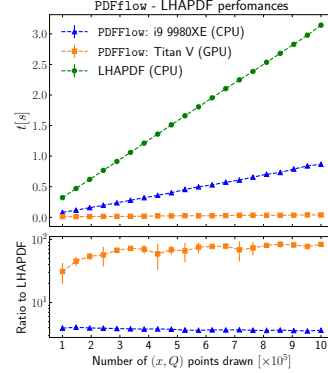


Figure 3.7: PDFFlow vs LHAPDF running time comparison. Top and bottom rows plot respectively the absolute and relative execution time as functions of the input size.

polation function is not visible in this plot, since the `tf.Graph` is built ahead of time invoking the `PDF.trace()` method.

3.3.3 Physics examples

This paragraph introduces several physics examples, developed in the HEP context, that exploit the PDFFlow software operating in synergy with VegasFlow to evaluate interesting quantities at different orders of perturbation theory.

Single t -quark production at LO

We present a calculation of the cross-section for single top quark t production process at Leading Order (LO) at LHC, namely $pp \rightarrow t + 1\text{-jet}$. The only contributing diagram is the $q\bar{q} \rightarrow t\bar{b}$ one depicted in figure 3.8. The cross-section is returned by an integrator algorithm, computing the integral over the phase space of the matrix element squared times the luminosity factor, which contains the PDF evaluation. We assess the performance of two alternative setups involving on one hand VegasFlow and PDFFlow and on the other MG5_AMC@NLO [63] v3.0.2 plus LHAPDF. The two tools share the same physical parameters configuration, such as the top quark mass $m_t = 173.2 \text{ GeV}$ and the center of mass energy fixed at $\sqrt{s} = 8 \text{ GeV}$, matching the LHC end of Run 1 conditions. In both cases, the central member of the NNPDF3.1 NLO set PDF is used. Figure 3.8 collects the integration time needed to reach an absolute precision of at least $2 \cdot 10^{-3} \text{ pb}$ and a relative error of $4 \cdot 10^{-5}$ on the target cross section value. We observe a great speed-up of the VegasFlow and PDFFlow runs on all the different devices, especially for GPUs.

Higgs production on VBF at NLO

In the second example, we consider the Vector Boson Fusion (VBF) Higgs production process at NLO. This higher-order computation provides an in-

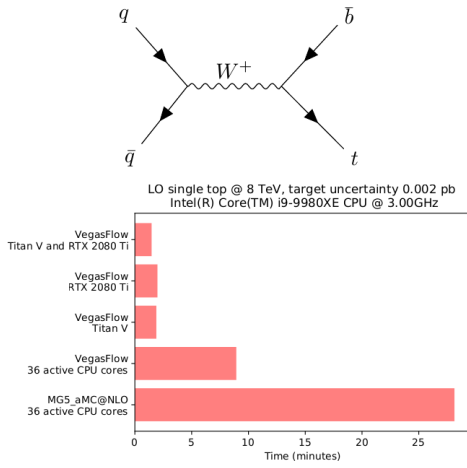


Figure 3.8: Single top quark production. Top row: Feynman diagram. Bottom row: comparison of the execution time between PDFFlow and VegasFlow code against MG5_AMC@NLO.

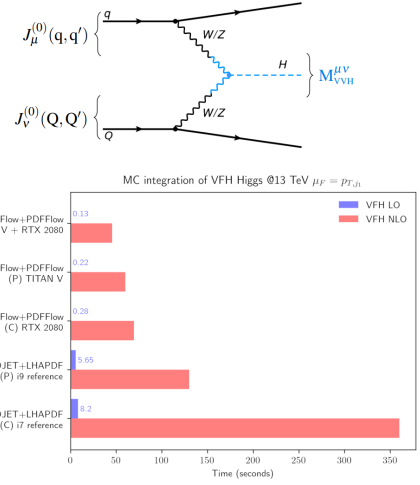


Figure 3.9: Quark initiated VBF Higgs production. Top row: Born Feynman diagram. Bottom row: comparison of the execution time between PDFFlow and VegasFlow code against NNLOJET plus LHAPDF.

Figure 3.10: The examples figures

interesting benchmark of our software, given the added complexity of the phase space integration. Full implementation of a parton-level Monte Carlo simulator such as NNLOJET [198] or MCFM [199] is beyond the scope of this work, which is to provide a proof of concept for an NLO computation. We exploit, instead, a simplified version [200] of the NNLOJET process implemented in Fortran 95 programming language which uses LHAPDF as the PDF access tool.

We limit ourselves to the quark-initiated W-boson-mediated process: the Born Feynman diagram is visible in the top panel of figure 3.9. At NLO, instead, a gluon is radiated from any of the quark lines. This process is characterized by a non-trivial phase space, containing divergences appearing when the intermediate quark propagator goes on the mass shell. The singularities must cancel with the poles in the corresponding virtual diagrams to have a finite result for the fixed-order computation. Phase space cuts as well as a suitable subtraction scheme have to be implemented to regularize the divergent behavior of the real radiation integrand. To be comparable with the original Fortran implementation in [200] we also choose the antenna subtraction method at NLO as described in [201, 202].

The NNLOJET code is heavily optimized for CPU and CPU-cluster usage so it provides a good benchmarking ground for our python-TensorFlow implementation which is to be run on a GPU. Although our strategies for phase space point sampling and subtraction methods are not specifically dedicated to GPU computing and could represent suboptimal choices, we achieve competitive performance against NNLOJET, leading us to believe that a fully op-

N_{rep}	LHAPDF CPU	PDFFlow GPU	PDFFlow CPU
10	0.08s	0.07s	0.05s
50	0.41s	0.35s	0.28s
100	0.83s	0.69s	0.56s
200	1.87s	1.46s	1.12s
300	2.85s	1.29s	1.79s
400	3.63s	1.69s	2.12s

Table 3.3: Time required to evaluate all 11 flavours from N_{rep} members of NNPDF3.1 NLO in a grid of 2415 points in x , using the P1 system.

timized implementation of NLO (and NNLO) computations on GPUs can lead to drastic performance gains. The results are presented in the bottom plot of figure 3.9 for both consumer and professional-grade hardware. It is interesting to discover that our implementation reaches a competitive time performance even on cheaper devices, opening a notable discussion regarding economic and environmental (i.e. power usage and carbon footprint) perspectives on the usage of our tool.

As a final remark, we note that our software stack is currently able to store and run in parallel an MC integration involving an order of a million events. We believe that this result can be further optimized for GPU computing, paving the way for more complex integrands and virtual diagram structures at higher orders (NNLO) in perturbation theory.

Multi-PDF members evaluation

The PDFFlow package includes the possibility to load multiple members of a PDF set at once. This capability allows to access values in the (x, Q^2) plane for all the specified PDFs. This functionality targets the field of PDF determination: theoretical predictions for experimental data points are computed through the convolution of FastKernel tensors [203] with PDFs evaluated in a grid of x points. As discussed in [204], we expect performance improvements of FastKernel-like operations when running parallel multi-PDF member evaluation on GPU. Such a result is particularly relevant for fitting methodologies based on the NNPDF methodology, where PDF replicas could be obtained simultaneously in a single GPU card.

We test the multi-PDF option of PDFFlow against the usual LHAPDF implementation which sequentially loops on single points. In table 3.3 we show the total evaluation time required to compute the 11 flavors of NNPDF3.1 NLO, namely the flavors for d, u, s, c, b quarks plus their anti-particles and the gluon, for a different number of members N_{rep} . In this benchmark, we exploit the P1 system to compute FastKernel tensors composed of a total of 2415 points in x . We highlight that PDFFlow on CPU and GPU times are always smaller when compared to LHAPDF thanks to the parallel graph evaluation. On the other hand, GPU results are better in the large N_{rep} regime. We conclude that the multi-PDF member evaluation implemented in PDFFlow may accelerate computations where a large number of PDF members and x points are required, thus opening the possibility to perform a full PDF fit in a single GPU device.

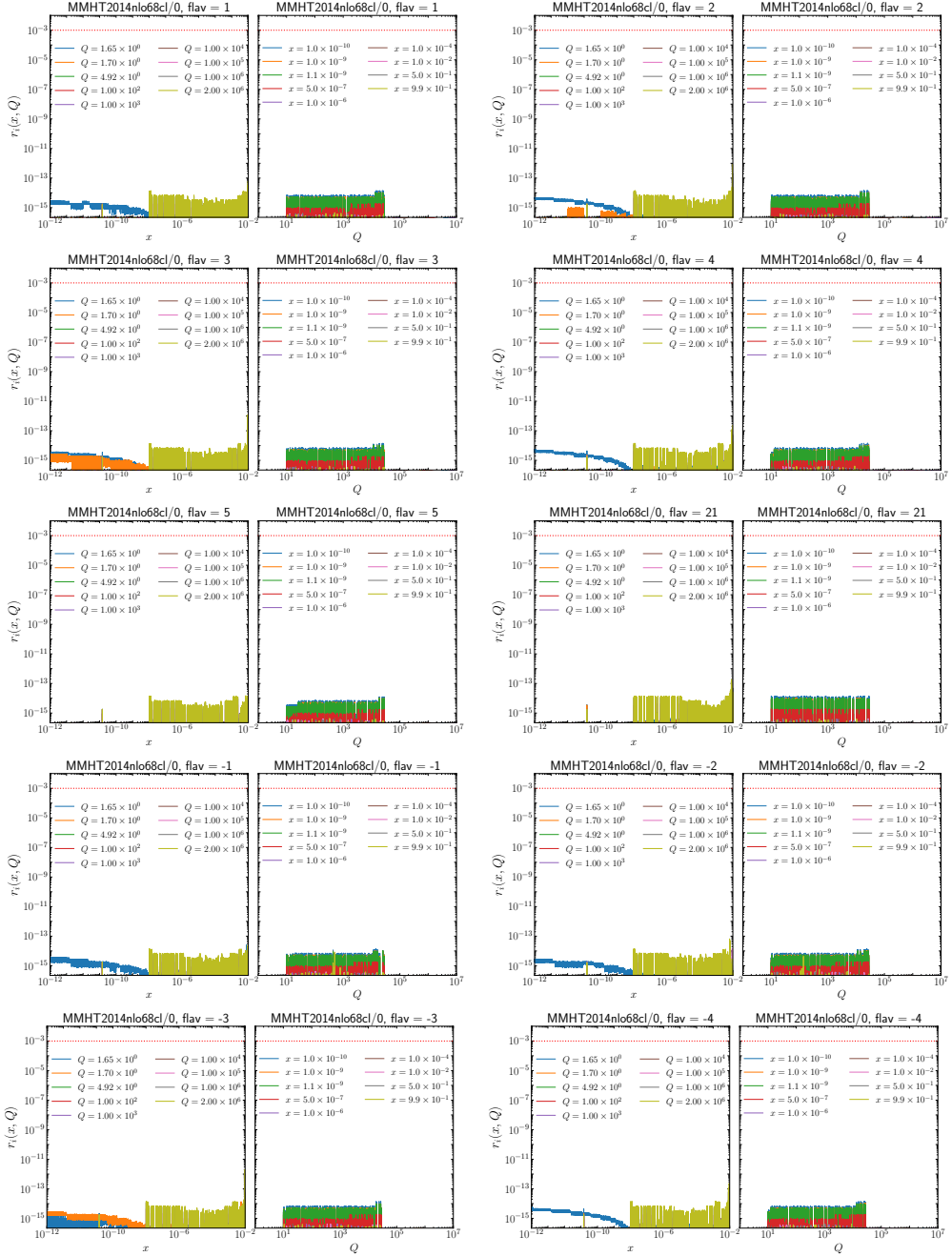


Figure 3.11: Relative difference between PDF_{low} and LHAPDF (same as 3.5) for the MMHT2014 NLO set for all flavors.

MadFlow : a Monte Carlo event generator on GPUs

Contents

4.1 The MadFlow design	80
4.1.1 Evaluation of matrix elements routines	82
4.1.2 Phase space generation	84
4.1.3 Unweighted event exporter	84
4.2 Physics examples	85
4.2.1 MadFlow accuracy	85
4.2.2 MadFlow performance	87
4.3 Conclusion and outlook	89

The VegasFlow and PDFFlow packages represent a first step towards a complete general-purpose Monte Carlo framework for event simulation of particle physics processes running across multiple devices and architectures, in particular, hardware accelerators. In this section, we extend the ideas presented in chapter 3 to complete a full suite of tools able to automate the computation of leading order cross sections and the generation of the associated unweighted events. We show how to build a library with all the ingredients needed to implement a full Monte Carlo simulation in a modern, extensible and maintainable way.

The most important result introduced in this chapter is a feasibility study testing the ability of our software to successfully handle a high number of Feynman diagrams, usually derived from processes with final state high jet multiplicities, employing a full computation on GPU devices. We note that an independent effort is currently being dedicated to port the MG5_AMC@NLO [63] software on GPU, namely a project dubbed “Madgraph 4 GPU” [205, 206]. The idea is to implement a library coded in CUDA programming language [207] to allow MG5_AMC@NLO to run on Graphics cards. The MadFlow [208, 209] concept tackles the issue from a different perspective, though: it aims to provide an MC simulator based on modern software able to run automatically on different hardware setups without requiring any specific architecture knowledge for either the developer and the user. Furthermore, we note that CUDA-based libraries are compatible with the TensorFlow framework: this, in principle, allows “Madgraph 4 GPU” matrix element calls to be integrated into MadFlow to gain the best performance out of the two worlds. To date, up to the authors’ knowledge, MadFlow is the first attempt to implement a full parton-level automated platform-agnostic MC event generator.

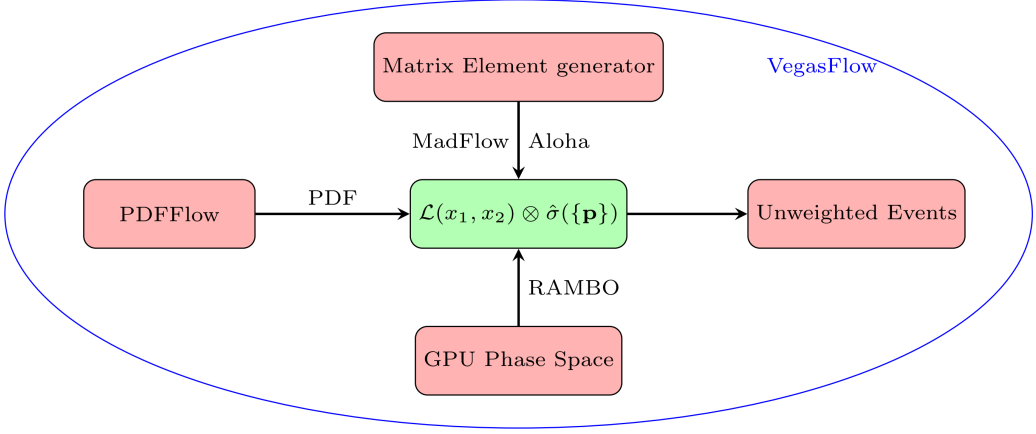


Figure 4.1: The MadFlow tool-suite includes all the needed ingredients for MC event generation on hardware accelerators: on top of the VegasFlow MC integrator, the GPU phase space generator constructs physical points to be fed in the computation of the luminosity factor done with PDFFlow and the evaluation of the partonic cross section $\hat{\sigma}$ through the ME computation. The final results are presented as unweighted events.

The chapter is organized as follows. In section 4.1 we initially describe the high-level design of the MadFlow package [210] and provide more details about its specific modules in the subsequent paragraphs. Section 4.2 presents all the physics examples implemented to test the capabilities of the new software. We show radical improvements in all the benchmarks with respect to the MG5_AMC@NLO state-of-the-art approach relying on CPU-only computations.

4.1 The MadFlow design

The generation of simulated events at hadron colliders, such as LHC, is driven by the following master formula expressing the calculation of the cross-section σ for a given process $pp \rightarrow X_n$ with n partons in the final state:

$$\sigma(pp \rightarrow X_n) = \sum_{a,b} \int d\Phi_n(x_1, x_2, \mathbf{p}) \mathcal{L}(x_1, x_2) |\mathcal{M}(a, b \rightarrow X)|^2 \quad (4.1)$$

where the sum runs over all the initial parton flavors and the differential phase space depends on the initial parton momenta fractions x_1, x_2 plus the final state n partonic 4-momenta $\mathbf{p} = p_1, \dots, p_n$. In this discussion we neglect the parton shower and all the other complexities (such as hadronization models, underlying event treatment etc.) related to a complete description of a physical final state measurable experimentally. Equation 4.1 instructs about the ingredients needed to implement a full parton-level MC event generator:

1. a phase space generator able to apply any fiducial cut and output the relevant $d\Phi_n$ contribution;

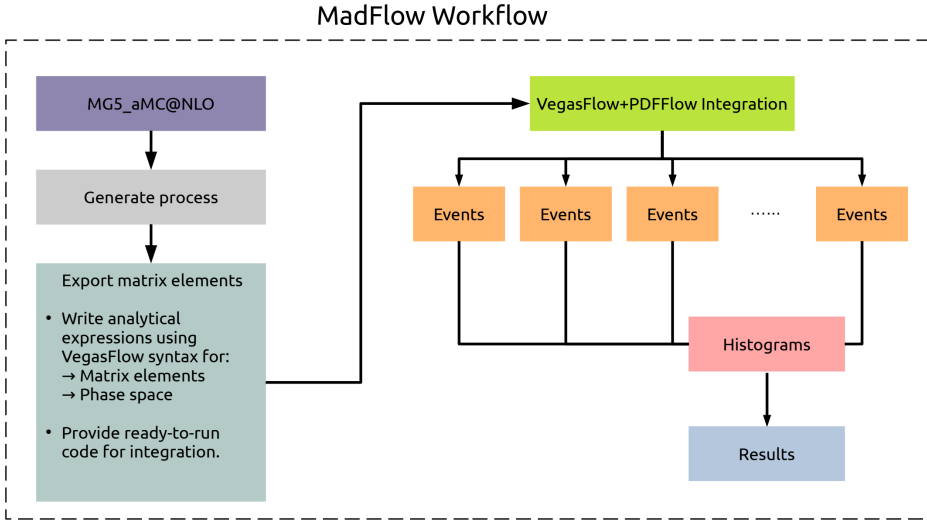


Figure 4.2: The MadFlow design. The MG5_AMC@NLO plugin exports the code for the ME evaluation and connects the various MadFlow components to perform the parallel MC integration. Eventually, unweighted events are produced along with the MC estimation for the cross-section.

2. a PDF and strong running coupling value access tool to compute the luminosity function \mathcal{L} ;
3. a general method to evaluate the Matrix Element (ME) modulus squared $|\mathcal{M}|^2$;
4. an MC integrator, defining a strategy to compute the final cross-section value;
5. an algorithm to store the generated events in a suitable format for computing observables and histogramming differential distributions.

To design a general-purpose MC generator that can exploit hardware accelerators, all the items listed above must be carefully implemented to take advantage of the parallel nature of the problem respecting the independence of the transformations that each sampled point undergoes. In particular, PDFFlow and VegasFlow already represent valid solutions to issues number 2 and 4, respectively. The missing ingredients in the list require the implementation of an efficient phase space generator able to load random points on GPU devices, a vectorized implementation of the ME computation and, finally, a prescription to save asynchronously such phase space points following physical distributions. The fact that the storage procedure acts asynchronously is crucial to avoid spoiling the performance improvements gained from the parallel GPU computation through expensive I/O operations. Figure 4.1 explicitly depicts all the modules that encompass the MadFlow framework.

Figure 4.2 represents schematically how the MadFlow package works, which essentially involves two main steps: the process generation and the actual MC integration. As an entry point, we rely on the MG5_AMC@NLO package with its ability to write process-specific code for the generation of MC

events: the functions for the ME evaluation, see paragraph 4.1.1, and the integration routines are generated at runtime. Since the produced code must be interfaced with MadFlow, we implement an MG5_AMC@NLO plugin which ensures that the syntax and the prescriptions exploited in the various tools connected to our framework are respected. The plugin creates a script that runs the parallel MC integration at LO within MadFlow and outputs the unweighted events needed for further analysis.

The goal of MadFlow is to provide the foundation for future high-precision MC simulations so they can efficiently take advantage of hardware development. In its current version, MadFlow provides the necessary tools for the automated computation of LO calculations for any number of particles. Higher-order computations can be implemented by building upon the provided LO template. Parameters and model definitions are provided by MG5_AMC-compatible parameter and run cards to allow a comfortable transition between the two frameworks for both the user and the developer point of view.

4.1.1 Evaluation of matrix elements routines

The MG5_AMC@NLO package is a Python meta-code, namely a code that produces other code. The output script can be phrased into three different languages to easily accommodate user needs: Python, C++ and Fortran. The idea is that the user first specifies the model lagrangian and inputs the process of interest, which leads to an algorithm to compute the corresponding amplitude. Within the MG5_AMC@NLO interface, the `import model`, `generate` and `output` commands produce the desired code to evaluate a query process.

As an example, the $pp \rightarrow t\bar{t}$ scattering is computed within the Standard Model and written to the `my_directory` folder with the following instructions:

```
import model sm
generate p p > t t~
output my_directory
```

The `import` statement loads the relevant FEYNRULES [211] package complying with the Universal FEYNRULES Output (UFO) format [212] describing the query theory: a Python module listing the particles, the parameters and a set of interactions fully specifying the underlying physics. The FEYNRULES were originally thought as a package for MATHEMATICA calculations, however the introduction of the UFO format allowed the user to incorporate them into MADGRAPH5 to easily test new theories producing events and comparing the results against experimental data in a quick and modular way.

The `generate` syntax triggers the search for the Feynman diagrams that contribute to the query process. The program first lists all the possible topologies compatible with the requested interaction. The invalid graphs should then be groomed: an efficient recursive method to determine whether a graph is relevant or should be discarded has been included in the framework since the release of the MADGRAPH5 version [213].

After all the diagrams are generated, the algorithm to compute the S-matrix element is built with dedicated optimization techniques to enhance the performance of ME evaluation. These methods rely on the computation

of helicity amplitudes and color decomposition to ensure that the complexity of the algorithm grows linearly with the number of Feynman diagrams identified before, which, in turn, depend factorially on the number of external particles in the process.

The techniques usually used for analytical ME results are based on Lorentz indices contraction and Dirac matrices trace technology. However, this approach is quadratically dependent on the number of Feynman diagrams since all the cross-diagram interference terms must be calculated individually. The overall number of such operations forbids computing with this method the matrix elements involving high parton multiplicities, typically beyond $2 \rightarrow 4$ processes. As a consequence, different algorithms are considered: the Helicity Amplitude Subroutines (HELAS) [214] tool sums amplitudes contributions for given helicities of the external particles, while the QCD color-flow decomposition [215] gather different terms into gauge invariant groups named dual amplitudes. The ALOHA application [216] automates this approach and is indeed incorporated into MG5_AMC@NLO.

The `output` request, finally, provides the user with the scripts produced by ALOHA combining three different kinds of functions: external particles, off-shell (connecting inner particle propagators with external legs through vertices) and on-shell (joining together various pieces of the diagrams) routines.

To produce a ME evaluation program compatible with a vectorized MC event generator, we design an MG5_AMC@NLO plugin, consisting of an exporter module that outputs the components just described in a format fulfilling the requirements imposed by Tensorflow primitives. Once the plugin is integrated into MG5_AMC@NLO, it is accessed with the following commands:

```
import model sm
generate p p > t t~
output pyout my_directory
```

which produces the desired MadFlow code, instead of the usual MG5_AMC@NLO one, inside the `my_directory` folder.

Concerning the plugin implementation side, particular attention has been dedicated to casting the ALOHA routines into a device-agnostic TensorFlow code. The major complexity in the realization of the algorithm regards replacing the wavefunctions routines abiding by the TensorFlow ControlFlow rules. The difficulty comes from the fact that it is not easy to include conditional statements in vectorized code. Moreover, GPU devices suffer in general from branching, since the hardware is kept busy until both sides of a conditional are completed. In the worst-case scenario, the majority of the GPU threads remain idle waiting for the completion of an expensive operation acting on just a few points. The ALOHA vertices rules, instead, being mostly comprised of algebraic operations are straightforward to implement in this framework.

We give here an example considering the $pp \rightarrow t\bar{t}$ process. There are two sub-processes contributing to the final amplitude: $u\bar{u} \rightarrow t\bar{t}$ and $gg \rightarrow t\bar{t}$. In turn, the amplitude with the gluon has both the s and t channels open. Figure 4.3 shows the three leading order possible diagrams. The MadFlow plugin exporter, therefore, generates two Python files according to the two avail-

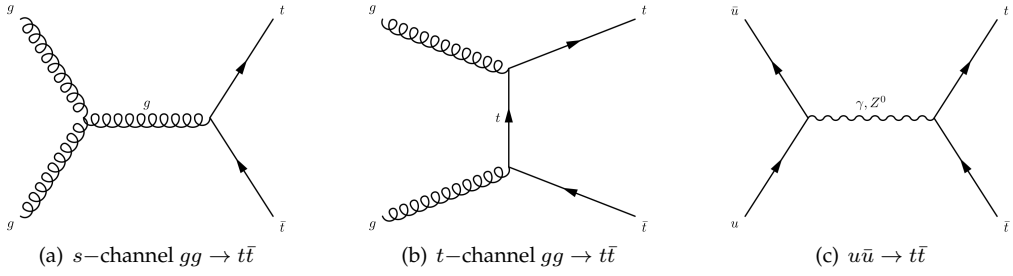


Figure 4.3: The diagrams contributing to the $pp \rightarrow t\bar{t}$ process.

able sub-processes: `matrix_1_uux_ttx.py` and `matrix_1_gg_ttx.py`. Further, each matrix element file is accompanied by the relative `aloha_<***>.py`, a script containing the ALOHA wavefunctions and vertices routines written with TensorFlow primitives. Each matrix element file contains a `Matrix` class implementing a `smatrix` method linking together the Feynman rules to evaluate the corresponding ME with the techniques described above: namely, looping over helicity amplitudes and aggregating them into gauge invariant groups according to color decomposition. Finally, the exporter creates a `leading_order.py` file which collects the instructions to launch the MadFlow computation, joining all the pieces present in figure 4.1. This includes calls to `VegasFlow`, `PDFFlow` and the GPU phase space sampler that we describe in the following paragraph.

4.1.2 Phase space generation

The MadFlow phase space generator implements a vectorized version of the RAMBO algorithm (see section 1.3.5 for a description of this technique). This method can produce a vector of physical 4-momenta to be exploited as input of the `smatrix` method of the ME. The approach produces a flat phase space, democratically giving the same importance to all regions. As a result, the ME topology is not taken into account, avoiding introducing excessive complexity in the implementations at the expense of the MC integration efficiency. Future releases of the MadFlow package will focus on improving the sampling technique to enhance the behavior of the MC generator especially when a large number of final-state particles is requested.

4.1.3 Unweighted event exporter

The MadFlow software focuses on producing samples of unweighted events following physical distributions. This is, by definition, a key ingredient for an MC generator. The standard output format for such events in HEP is the Les Houches Event (LHE) 3.0 one [217]. Such a format is based on XML markup language to represent generated events as a list of `<event>` tags containing the produced particles along with their PDG code, 4-momenta, mass and color flow information. The workflow first generates weighted events, which means that each one contributes to the overall physical distributions differently according to its weight. An unweighting procedure allows the production of a sample where each event has the same importance. This implies

that histogramming physical distributions can be done without assigning a weight to each entry, hence the name unweighted events.

The collection of weighted events is done asynchronously to the matrix element computation in MadFlow. The reason is that communication between the hardware accelerating device and the CPU host may slow down the hard computation. Therefore, we implement a custom Python context manager named `LheWriter`, whose `lhe_parser` method constantly takes care of gathering the phase space points sampled during the VegasFlow integration in a separate CPU thread to eventually dump the corresponding LHE tags to file. We ensure that this operation is done independently of the GPU calculations wrapping the call to the `LheWriter.lhe_parser()` method thanks to the TensorFlow `tf.py_function()` primitive.

The unweighting prescription is taken from MG5_AMC@NLO and works as an acceptance-rejection algorithm (see paragraph 1.3.4): after looking for the highest weight w_{\max} in the list, the algorithm produces a random number in the unit interval with uniform probability, then a query event is accepted if its weight w_{event} is higher than the product of the random number times the maximum weight in the sample. This ensures that each event is accepted with a probability proportional to the ratio of the weights $w_{\text{event}}/w_{\max}$.

A consequence of this method is that if there are many events with low weight compared to the maximum one, the algorithm acceptance efficiency $\epsilon = N_{\text{accepted}}/N_{\text{tot}}$ will be low. This highlights a sub-optimal phase space sampling behavior, yielding many ME evaluations at points that give low contributions to the integral. We observe that the naive RAMBO approach implemented in MadFlow has, in fact, a rather poor efficiency $\epsilon \sim 5\%$, meaning that future package releases will aim to improve this quantity by introducing dedicated sampling techniques. Examples of improved sampling methods include weight optimization of multi-channel Monte Carlo, previously described in section 1.3.2, and single-diagram enhancement method already implemented by MADEVENT [218].

4.2 Physics examples

In this section we present some usage examples of the MadFlow package, demonstrating the precision of the software in terms of the accuracy of the final observable distributions. The MG5_AMC@NLO software represents the reference benchmark software in all the experiments.

We consider the simulation of events at LO for hadronic processes at colliders with center of mass energy of $\sqrt{s} = 13$ TeV. This configuration matches the Run II LHC setup, which was running from 2015 to 2018. In the following different processes are considered. All results presented in this study are obtained with the software stack described in table 4.1.

4.2.1 MadFlow accuracy

We consider observable distributions for the $gg \rightarrow t\bar{t}$ process obtained with both the original MG5_AMC@NLO implementation and the novel MadFlow approach. Figure 4.4 represents the differential distributions concerning the final state top transverse momentum $p_{T,\text{top}}$ and pseudorapidity η_{top} . The

Software	Version
MadFlow	0.1
VegasFlow	1.2.1
PDFFlow	1.2.1
MG5_AMC@NLO	3.1.0
TensorFlow	2.5.0
Nvidia CUDA drivers	11.3
ROCm drivers	4.2.0
TensorFlow-rocm	2.4.1

Table 4.1: Description of the software used for the different MadFlow experiments. The last two lines regard the software compiled for Radeon/AMD architectures.

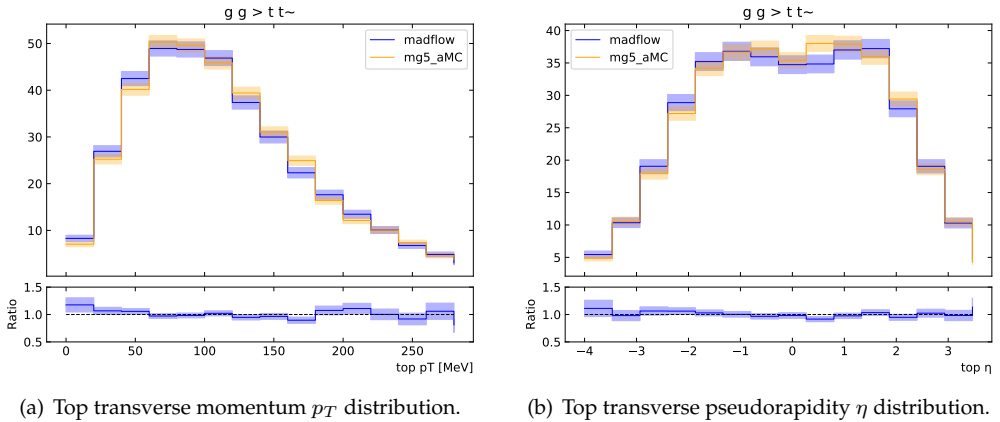


Figure 4.4: Leading order differential cross sections for $gg \rightarrow t\bar{t}$ process at $\sqrt{s} = 13$ TeV. In both panels, the top row shows the histogram distributions output by MadFlow and MG5_AMC@NLO, while the bottom one represents the ratio of the two to highlight the statistical agreement.

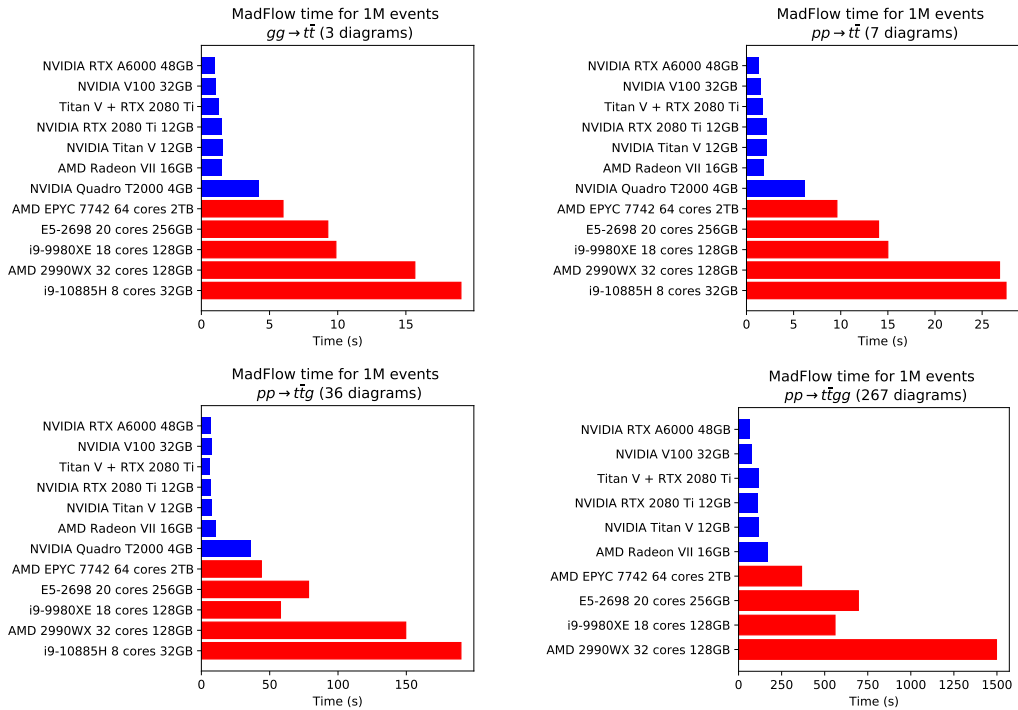


Figure 4.5: MadFlow integration timings for different processes: $gg \rightarrow t\bar{t}$ (top left), $pp \rightarrow t\bar{t}$ (top right), $pp \rightarrow t\bar{t}g$ (bottom left), $pp \rightarrow t\bar{t}gg$ (bottom right). Comparison of the results for consumer and professional-grade CPUs (red bars) and GPUs (blue bars) hardware. The plots report the available memory alongside each related device name. We note a systematic performance improvements for GPU cards.

unity of measure of the top row plots is set to fb/GeV and fb, respectively. The bottom row panels, instead, show the ratio between the MadFlow and MG5_AMC@NLO results. The pictures confirm a sufficient level of agreement between the two implementations for the same level of target accuracy between 2 – 5% for each bin.

4.2.2 MadFlow performance

We are interested in testing the speed of MadFlow on different platforms. Therefore we measure the total amount of time required to integrate 10^6 events for different processes with an increasing number of involved partons and, consequently, factorially increasing the number of diagrams: we consider $gg \rightarrow t\bar{t}$ (3 diagrams), $pp \rightarrow t\bar{t}$ (7 diagrams), $pp \rightarrow t\bar{t}g$ (36 diagrams), $pp \rightarrow t\bar{t}gg$ (267 diagrams). In all the experiments we apply a cut on the transverse momentum of the final state particles: $p_T > 30$ GeV.

In figure 4.5 we summarize the results of the performed benchmarks on various Intel and AMD CPU platforms (red bars) optionally hosting Nvidia or AMD GPUs (blue bars) spanning from consumer to professional-grade hardware. The blue bars underline the superiority of MadFlow running on GPU cards. The Nvidia Ampere architecture-equipped devices, such as the

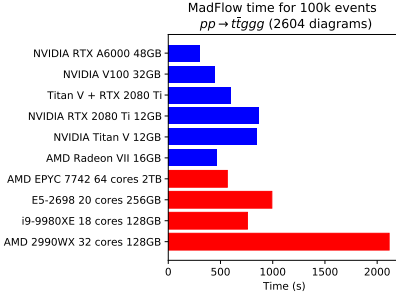


Figure 4.6: $pp \rightarrow t\bar{t}ggg$ process MadFlow timings.

RTX A6000, represent the latest generation of GPU technology and outperform the previous versions based on the Tesla setup. The AMD brand with its AMD Radeon VII model, instead, is a good alternative to the Nvidia solutions providing performance competitive with respect to the most professional-grade GPUs at more affordable prices.

The red bars show the MadFlow performance when running on CPU devices configured to exploit all the available cores. Although we highlight the supremacy of GPU hardware, we see that some top-level chips, such as the AMD Epyc 7742, can achieve performance similar to consumer-level GPUs, like the Quadro T2000. Nonetheless, we note that the code contains by no means any specific GPU optimization, which would be a desirable feature when developing the software toward production mode. As a final remark, we claim that the GPU speed-up highly depends on the number of events requested per device, meaning that the maximum performance is achieved when the computation exactly fills the entire available memory.

According to section 4.1, the goal of the MadFlow software is to provide hardware acceleration for future higher-order computations. Of course, when including NLO or even NNLO contributions, the number of Feynman diagrams substantially increases. It is then naturally interesting to test if the program can successfully handle complex computations. To this extent, we evaluate the performance of our code to simulate 10^5 events for the $pp \rightarrow t\bar{t}ggg$ process, which counts 2604 Feynman diagrams. The results shown in figure 4.6 confirm that GPU performance are competitive even accounting for such a huge number of contributions, remarking the strong potential of hardware accelerators for higher-order HEP simulations.

The final test presented in this section designs a comparison between the MadFlow

and the MG5_AMC@NLO frameworks' performance. In table 4.2, we report the total amount of time per event for the processes listed above for an Intel i9-9980XE CPU system with 18 cores and 128 GB of RAM hosting an Nvidia Titan V 12 GB. The results follow the trend of the other benchmarks, presenting a dramatic increase in the number of evaluated events per second by the GPU device as opposed to the CPU. At the same time, going towards more complex processes and increasing the number of diagrams requires also a larger amount of memory to hold the computation, decreasing the perfor-

Process	MadFlow	MadFlow	MG5_AMC (μ s)
	CPU (μ s)	GPU (μ s)	
$gg \rightarrow t\bar{t}$	9.86	1.56	20.21
$pp \rightarrow t\bar{t}$	14.99	2.20	45.74
$pp \rightarrow t\bar{t}g$	57.84	7.54	93.23
$pp \rightarrow t\bar{t}gg$	559.67	121.05	793.92

Table 4.2: Comparison of event computation time for MadFlow and MG5_AMC@NLO on Intel i9-9980XE system with 18 cores and 128 GB of RAM for CPU simulation and Nvidia Titan V 12 GB for GPU simulation.

mance gains granted by the GPU.

4.3 Conclusion and outlook

We have presented and tested a new approach for the generalization of Monte Carlo event generation on hardware accelerators. The MadFlow package encompasses a series of tools implemented with fast and maintainable code that can express complex analytical expressions into hardware-specific languages without the need to introduce complicated operations. We tested the software's effectiveness to simulate multiple scenarios on hardware accelerators. We plan to develop further the MadFlow algorithm, including specific optimization methods for vectorized phase space sampling to enhance event generation efficiency and eventually make a first step towards the automation of the Next-to-Leading Order computations taking advantage of hardware accelerators.

Part III

Deep learning models for neutrino physics

Denoising ProtoDUNE-SP Raw Data with deep learning

Contents

5.1 The ProtoDUNE Single Phase design	93
5.1.1 Field response	96
5.1.2 Electronics response and digitization	99
5.2 Signal processing and deconvolution method in LArTPCs	100
5.3 Deep learning strategies for ProtoDUNE raw data denoising	102
5.3.1 Proposed models	103
5.3.2 Experimental results	107

This chapter deals with the implementation of deep learning solutions for the raw data denoising algorithm at ProtoDUNE Single Phase (SP) detector, the first step of the event reconstruction pipeline at Liquid Argon Time Projecting Chamber (LArTPC) detectors. We first give an overview of the ProtoDUNE-SP detector design and its geometry and including a characterization of signal processing in LArTPCs, namely, how signals first get formed and then are revealed inside such kind of experimental apparatus.

After that, we discuss the current implementation of the deconvolution method, the state-of-the-art technique implemented by several neutrino experimental collaborations. Finally, the last section of this chapter describes our novel solutions for denoising ProtoDUNE-SP simulation data with deep neural networks [219] and, in particular, with graph neural networks.

5.1 The ProtoDUNE Single Phase design

The Deep Underground Neutrino Experiment (DUNE) [220] is a major experiment in the neutrino oscillation research field. It will be based between Fermilab (Illinois) and the Sanford Underground Research Facility (SURF) in South Dakota, the latter hosting the DUNE Far Detector (FD) [221–223]. The FD, with its four modules containing a fiducial mass of 10 kt of liquid argon will be the largest Liquid Argon Time Projecting Chamber ever built. The CERN Neutrino Platform, instead, currently hosts the ProtoDUNE-SP detector [224], a prototype of the DUNE FD that faithfully reproduces most of the FD components, but extrapolating the total LAr mass in scale 1:20.

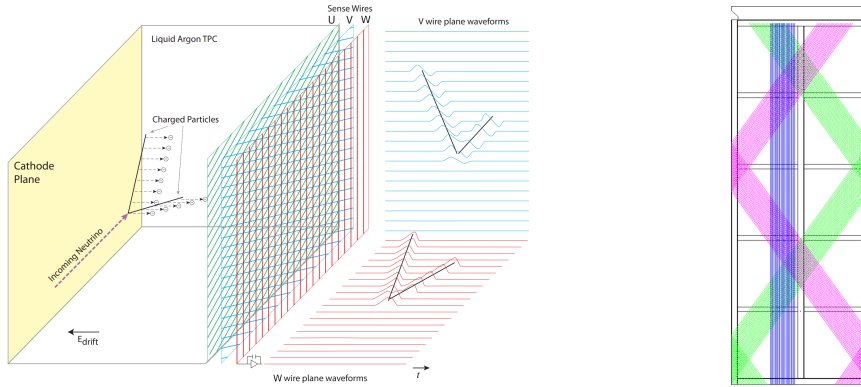


Figure 5.1: Sketch of the ProtoDUNE-SP detector. Only one drift chamber is depicted, the other extends to the left of the CPA.

Figure 5.2: Wires wrapping around a ProtoDUNE-SP APA plane: U, V and W planes in green, magenta and blue, respectively.

The realization of the ProtoDUNE detector is an essential part of the DUNE FD development program and has four main objectives. First, to refine the production and installation procedures of the FD detector modules. Second, to test the basic detector performance to validate its design, which is a crucial point in the roadmap of the DUNE FD realization. Third, to calibrate the detector efficiency in revealing particles of a different kind. This has to be done thanks to the collection of large samples of test beam data, that in turn will allow implementing dedicated software solutions for the Monte Carlo simulation. Fourth, to prove the long-term operational stability of the detector and prevent risks of continued operations on the DUNE FD modules.

The ProtoDUNE-SP design is sketched in figure 5.1: the active TPC is a 6 m high, 7 m wide and 7.2 m deep box. A field cage surrounding the volume supports and isolates the detector. The space is divided by a central cathode plane, named Cathode Plane Assembly (CPA), that separates the two drift volumes. The sides of the detector, instead, are paved by three adjacent 6 m high and 2.3 m wide Anode Plane Assemblies (APAs). Each APA consists of a support where three parallel planes of sense wires are wrapped around along different orientations to provide three independent views of the events, allowing 3-dimensional reconstruction. Figure 5.2 shows the orientation of the three U, V and W wire planes. The first two wire planes, U and V, are oriented forming angles of 35.7° and -35.7° with respect to the vertical, while the last plane W is directed along the vertical. A total of 2560 readout channels are attached to the APA wires, resulting in 15360 channels included in the whole structure.

The CPA is kept at a tension of -180 kV, while the APA wire layers are held at -370 V (U plane), 0 V (V plane) and 820 V (W plane) to establish a quasi uniform electric field of intensity 500 V/cm. A report of the installation and the test beam runs taken before the LHC Long Shutdown 2 at the end of 2018 is available in [225].

We present a qualitative overview of how an interaction within the detector fiducial volume is revealed by the experimental apparatus leading to

the formation of the raw signal inside LArTPCs. At the moment a particle enters the detector fiducial volume, it may interact with Argon nuclei producing ionization electrons and Argon ions pairs. The intense electric field provided by the CPA accelerates the charged particles in opposite directions: the positive ions are attracted towards the center of the cage against the CPA, while the electrons drift in the opposite direction and get collected by the APA wires. We stress that the ionization electrons induce current on the sense wires in the two first APA wire planes U and V, but are indeed collected only by the last plane W. Therefore, the U and V wire bundles are often called induction planes, while we refer to the W one as the collection plane.

The motion of charges inside the detector volume generates a detector response, given by the combined effects of different contributions. The overall simulation within a LArTPC environment can be simplified into five different pieces that should be convoluted together to provide the final detector measurement M :

$$M = (Depo \otimes Drift \otimes Duct + Noise) \otimes Digit \quad (5.1)$$

The definition of the ingredients included in the equation above follows.

- *Depo*: the initial distribution of ionization electrons created by energy depositions. It is modeled by point-like depositions q_i at positions \mathbf{r}_i and times t_i :
 $Depo_i(q_i, t_i, \mathbf{r}_i)$
- *Drift*: describes the drift of the initial ionization charge towards the APAs, due to the uniform electric field \mathbf{E} . The output is the number of electrons and their space-time distribution arriving at a distance of $x_{rp} = 10$ cm from the APAs. The imaginary plane parallel to the APA at x_{rp} distance is called response plane. The propagation of the initial charge until the response plane is characterized by diffusion along longitudinal and transverse directions producing a final charge distribution with longitudinal and transverse standard deviations:

$$\sigma_{L,T} \simeq \sqrt{2D_{L,T}t_{drift}} \quad (5.2)$$

where $D_{L,T}$ are diffusion coefficients in argon [226] and t_{drift} is the time the electron takes to reach the response plane. The final space charge distribution is given by:

$$Depo_i \otimes Drift \rightarrow Depo_i \left(q_i, t_i + t_{drift}, \mathbf{r}_i \Big|_{x=x_{rp}}, \sigma_L, \sigma_T \right) \quad (5.3)$$

- *Duct*: includes the field and electronics responses discussed in sections 5.1.1 and 5.1.2, respectively.
- *Noise*: the inherent electronics noise that must be added to the electronics readouts to produce a realistic measurement. It can be simulated as a random walk in the frequency domain to produce a time-dependent noise contribution for each readout channel.

- *Digit*: the digitized version of the electronics signal recorded by the detector.

In the following, we present a qualitative introduction to the *Duct* components, namely field response and electronics response, and the digitization procedure done by LArTPCs. The discussion follows [227] which is tailored on the MicroBooNE detector [228], but can be applied in general to all LArTPCs including ProtoDUNE-SP.

5.1.1 Field response

The induced current i on a wire by a charge q moving in its proximity is governed by the Ramo theorem [229] and its generalized forms [230, 231]:

$$i = -q \mathbf{E}_w \cdot \mathbf{v}_q \quad (5.4)$$

where \mathbf{v}_q is the drifting velocity of the charge and \mathbf{E}_w is a weighting field, that is a function of the geometry of the electrodes. The operative measure of the weighting field is done while keeping the target wire at unit potential, setting all the others to ground, removing the drifting charge and measuring the electric field in the space surrounding the electrode. The generalized versions take into account non-linear effects and configurations in which electrodes are placed within multiple dielectric mediums. The instantaneous drift velocity of the charge in the case of the LArTPC depends mainly on the geometry of the APAs and liquid argon temperature.

The qualitative behavior of the field response function is better understood considering Green's reciprocity theorem: the moving charge q_m induces current on a sense wire I, which, in turn, corresponds to a movement of charges Q_I on the wire itself. The two quantities are related by the formula:

$$q_m \cdot V_m = Q_I \cdot V_I \quad (5.5)$$

where V_m is the potential induced at the position of the charge by the sense wire kept at potential V_I .

The induced current, or field response, can be obtained by taking the time derivative of the charges moving on the electrode I:

$$i = \frac{dQ_I}{dt} = q_m \cdot \nabla V_w \cdot \frac{d\mathbf{r}}{dt} \quad (5.6)$$

where we have introduced the dimensionless weighting voltage $V_w = V_m/V_I$, which assumes values in the unit range. The last equation, in particular, is equivalent to equation 5.4 putting $-\mathbf{E}_w = \nabla V_w$. The integral through time of the current induced on the electrode is given by the work done to bring the charge q_m within the weighting potential from a starting position A to an end position B :

$$\int i dt = q_m (V_w^B - V_w^A) \quad (5.7)$$

In [227], the field response is computed for a single ionization electron through a simulation with the Garfield software [232]. The simulation assumes a 2-dimensional wire geometry and nominal wire potential compatible with the MicroBooNE detector setup, however, the results presented

here can be easily generalized to ProtoDUNE and other LArTPC detectors. The authors, simulate an electron starting at a position 10 cm away from the first wire layer, namely U plane and approaching the APA. Different electron paths are displayed in figure 5.3(a) depending on the starting position, which is discretized along the direction transverse to the drifting direction by a 0.3 mm shift. The picture shows that, due to the uniform electric field, the electron approaches the APA passing next to the U and V planes (the first and second encountered layers) and gets collected by the W collection plane.

Figures 5.3(b), 5.3(c), 5.3(c) plot the simulated weighting potential of a wire in the three different APA planes U, V and W respectively. The weighting potential is maximum in the coincidence of the considered wire and decreases for increasing distance. The plots highlight that each APA plane acts shielding the weighting potential of the wires of the other APA layers. Indeed, figure 5.3(c) has a V_w that extends towards the inner region of the detector, but only small $\sim 5\%$ fractions of the weighting field pass beyond the second line of wires. The weight potential of the wire on the V plane is concentrated in the inter-electrode space being shielded both by the first and the last APA layer. The collection wires are shielded both by the two former layers, instead.

A consequence of equation 5.7 is that each wire is sensible to the induced current by an ionization electron only if it moves inside a region where the weighting potential has a spatial increment or a decrement appreciably different from zero. As an ionization electron approaches the first induction plane, it moves towards higher regions of the associated weighting potential and the induced current is positive. As soon as the particle moves away from the wire and continues towards the far side of the detector, the induced current switches to negative values and forms the typical bipolar sign for the induction waveforms recorded by the LArTPC electronics, see figure 5.4.

Once the electron passes the first induction wire, it starts inducing current also on the collection wire. Since the paths of q_m eventually end onto a collection wire, the induced current on the V plane electrodes is always positive, resulting in unipolar peaks in the waveforms in figure 5.4.

As a consequence, the integrated current on an induction plane wire for an ionization electron originating on the cathode plane is zero because the drift trajectory starts from a position where the weighting field is zero and ends on a collection plane wire, where again $V_w = 0$. On the other hand, the integrated current on a collection plane wire in the same situation equals to a single electron charge, since the starting weighting potential is again zero, but the final potential is equal to unity, referring to the collection wire. In general, this is not true for ionization electrons originating in the inner detector, since the starting weighting potential is not zero there. However, the weighting potentials fall to zero rather quickly, reaching $\mathcal{O}(10^{-2})$ values at distances of ~ 10 cm away from the APAs.

When an ionization electron is created inside the LArTPC, also the corresponding argon ion is generated. The ion drifts in the electron's opposite direction and, in principle, influences the field response function. The contribution, however, is negligible, since the drift velocity of the ions is far slower than the ionization electrons due to their mass:

$$v_{e^-} \sim 1 \text{ mm}/\mu\text{s}, \quad v_{Ar^+} \sim 5 \text{ mm/s} \quad (5.8)$$

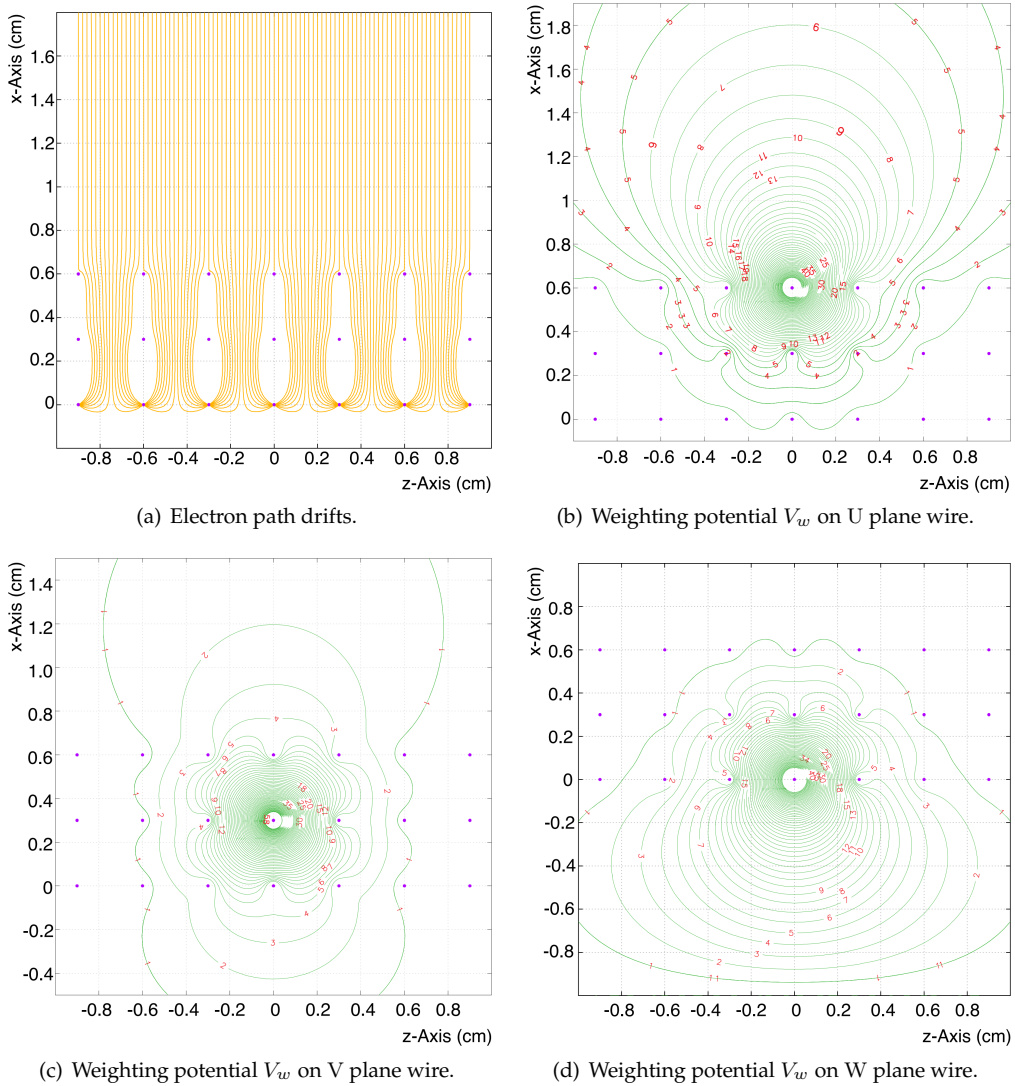


Figure 5.3: The electron path drift and weighting potential in the Garfield simulation from [227]. The equipotential lines are labeled by numbers from 1 to 60 indicating the percentage with respect to V_w^{\max} , namely the electric potential on the considered wire.

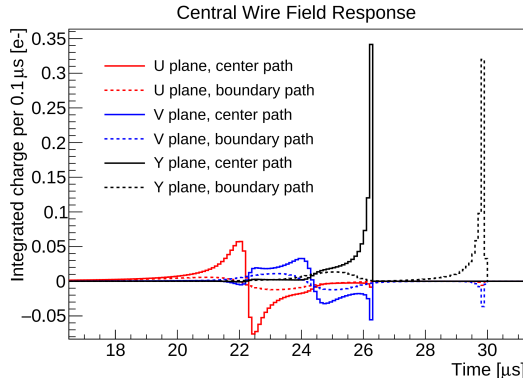


Figure 5.4: The waveforms due to single electron drift in the Garfield simulation by [227]. The solid waveforms refer to an electron starting position directly in front of the considered wires (center path). The dashed waveforms consider the shifted electron path starting from the boundary of the simulation volume. This shows that drifting particles influence the measured current also on distant wires.

5.1.2 Electronics response and digitization

Once the induced current on a sense wire is received, a pre-amplifier amplifies and shapes the signal. The pre-amplifier settings include the gain and the peak time. These two parameters control the height, width and time position of the peak measured from a unit input impulse at time $t = 0$. In particular, the gain is defined as the output waveform amplitude and, for LArTPCs experiments such as MicroBooNE and ProtoDUNE-SP, there are four different configurations of this quantity: 4.7 mV/fC, 7.8 mV/fC, 14 mV/fC, 25 mV/fC. The peaking time is defined as the time difference between 5% of the peak at the rising edge and the peak. Four peaking times can be configured in the cold electronics setup in MicroBooNE and ProtoDUNE-SP: 0.5 μ s, 1.0 μ s, 2.0 μ s and 3.0 μ s. Figure 5.5(a) shows the different pre-amplifier responses for a fixed gain value of 4.7 mV/fC. Notice that the signal amplitude is always the same for different peaking times since it is dependent on the gain setting only. The four peaking time setups are important to satisfy the Nyquist theorem [233] for different sampling rates: an analogic periodical signal can be correctly reconstructed only if the sampling frequency, used to digitize the signal, is greater than double the highest frequency in the signal spectrum.

The output of the pre-amplifier is further analyzed by two independent RC filters to remove the baseline. The RC response function for a single impulse located in the origin, $\delta(t)$, is displayed in figure 5.5(b). Both the single RC behavior and the double independent RC \otimes RC RC circuits responses are shown in the plot. The effect of the introduction of such electronics is visible in the long or large waveforms, especially for collection plane wire.

The output waveforms are digitized at a sampling rate of 2 MHz for both MicroBooNE and ProtoDUNE-SP and stored in a 12 bit analog-to-digital converter (ADC) values. This sampling rate corresponds to discretized readout steps, usually called TDC ticks, of 0.5 μ s each. In particular, the ProtoDUNE-SP event readout time window lasts 3 ms, yielding in each event an overall sequence of 6000 ADC values per readout channel. Each measured event

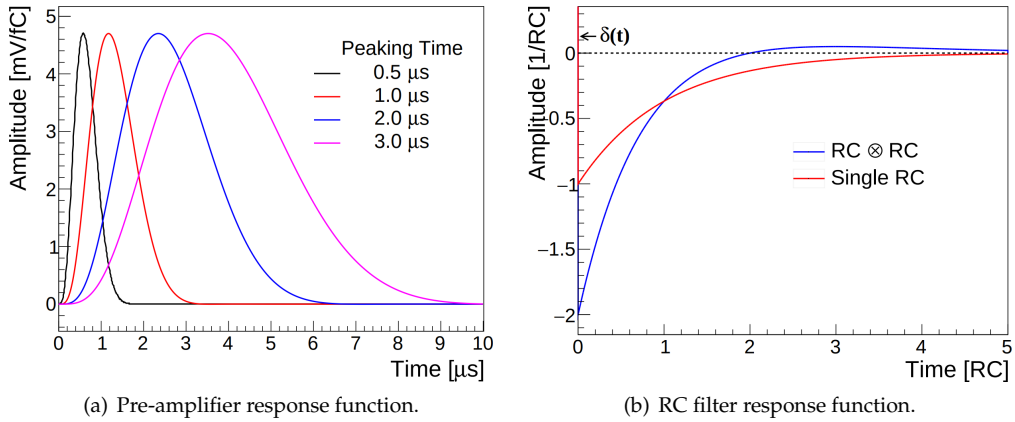


Figure 5.5: The MicroBooNE electronics response to an impulse signal located at $t = 0$: left panel plots the pre-amplifier response function for 4.7 mV/fC. Both diagrams are taken from the study in [227].

by ProtoDUNE-SP can then be cast into an image-like matrix of resolution 15360×6000 , where the axes refer to the readout channel and the TDC tick, respectively. In the LArTPC jargon, we often refer to each pixel ADC value as a raw digit. The image representation of the ProtoDUNE-SP data will be exploited in section 5.3 to introduce our novel deep learning approach to raw data denoising.

5.2 Signal processing and deconvolution method in LArTPCs

Noise has a great impact on the reconstruction efficiency in LArTPCs. The standard noise removal strategy is deconvolution, a technique that we will explain in the following. Sometimes, in real detector scenarios, excess noise may require a dedicated noise filter design, like in the case of MicroBooNE [234]. Time or 1-dimensional deconvolution has been introduced by [235] in the context of the ArgoNeuT experiment. The 2-dimensional version of the algorithm, which takes into account noise spatial dependencies between neighboring wires, has proven more effective and has been exploited by [227, 236].

A 2-dimensional algorithm is needed because the weighting potential of a wire in a LArTPC is appreciably non-zero in regions surrounding nearby electrodes. As a consequence the charge moving in the volume influences with a sizeable contribution not only the closest readout channels but also the neighboring ones. For simplicity, we present the deconvolution method first in 1-dimension and then provide the 2-dimensional extension.

Deconvolution is a mathematical technique used to reconstruct an original signal $S(t)$, given a measured signal $M(t')$, which is the result of a convolution operation between the original signal and a detector response function $R(t, t')$:

$$M(t') = \int_{-\infty}^{+\infty} dt R(t, t') S(t) \quad (5.9)$$

The detector response function equals the measured signal for an original impulse signal $S(t) = \delta(t - t_0)$. The response function can be taken as a time-invariant function depending on the time difference between reception and measurement of signal: $R(t, t') = R(t - t')$. The convolution is turned into a function multiplication in the frequency domain through the Fourier transform: $M(\omega) = R(\omega) \cdot S(\omega)$. Therefore, in principle, it could be possible to retrieve the original signal in the frequency domain by computing the ratio:

$$S(\omega) = \frac{M(\omega)}{R(\omega)} \quad (5.10)$$

Taking the inverse Fourier transform allows to work out the original signal waveform in the time domain $S(t)$. However, this is not always possible since the measured signal includes the contribution of inherent electronic noise that is unknown a priori and, further, in real detectors, the response function $R(\omega)$ is rapidly decreasing for large frequencies ω . As a consequence of equation 5.10, the second effect yields a vanishing denominator at high frequencies, resulting in a dominant noise contribution in the reconstructed signal. The solution to these problems is to include a filtering function $F(\omega)$ that mitigates the discussed effects:

$$S_f(\omega) = \frac{M(\omega)}{R(\omega)} \cdot F(\omega) \quad (5.11)$$

The reconstructed signal $S(t)$ retrieved with this equation is called deconvolved signal.

Usually, a Wiener filter [237] is designed exploiting the expected quadratic signal $\overline{S^2(\omega)}$ and noise $\overline{N^2(\omega)}$ functions in the frequency domain:

$$F(\omega) = \frac{\overline{R^2(\omega)S^2(\omega)}}{\overline{R^2(\omega)S^2(\omega)} + \overline{N^2(\omega)}} \quad (5.12)$$

Unfortunately, there are different problems in the implementation of this ideal approach, mainly due to the impossibility of shaping exactly the expected signal and noise frequency spectrum. First, because the field response depends on the event topology, namely different ionizing tracks inside the LArTPC produce different signals due to 3-dimensional effects. Second, by definition, the filter spectrum at zero frequency is a quantity lower than unity. The Fourier transform of a function equals the integral of the original function in the time domain, then the quantity $S(\omega = 0)$ is the integrated charge on a sense wire during a readout time window. The introduction of the Wiener filter in equation 5.12 leads to a non-conservation of the number of ionization electrons on the wire:

$$S(\omega = 0) = \int d\omega S(t) \equiv Q^{\text{tot}} \rightarrow S_f(\omega = 0) = S(\omega) \cdot F(\omega) \Big|_{\omega=0} \equiv Q_f^{\text{tot}} < Q^{\text{tot}} \quad (5.13)$$

These issues drove the neutrino experimental collaboration to implement Wiener-inspired filters, rather than actual Wiener filters. Nonetheless, this naive description allows to understand the core of the algorithms behind the the main noise mitigation techniques at LArTPCs.

The 2-dimensional extension of this approach takes into account the detector response functions of wires nearby a central one. We consider the measured signal $M_i(t_0)$ on the i -th wire at a time t_0 :

$$M_i(t_0) = \int_{-\infty}^{+\infty} dt (\dots + R_1(t_0 - t) \cdot S_{i-1}(t) + R_0(t_0 - t) \cdot S_i(t) + R_1(t_0 - t) \cdot S_{i+1}(t) + \dots) \quad (5.14)$$

where S_i represents the real signal waveform on the wire i . R_0 is the average detector response function associated with the reference wire, while R_1 is the average detector response linked to a wire one step next to the reference wire. The average is taken on all the possible electron drift paths that end on the considered wire. In principle, it is possible to include in the sum the contributions provided by n wires.

The Fourier transform of equation 5.14 results in replacing the convolutions with normal multiplications, allowing a description of the algorithm through a matrix multiplication notation:

$$\begin{pmatrix} M_0(\omega) \\ M_1(\omega) \\ \vdots \\ M_{n-2}(\omega) \\ M_{n-1}(\omega) \end{pmatrix} = \begin{pmatrix} R_0(\omega) & R_1(\omega) & \dots & R_{n-2}(\omega) & R_{n-1}(\omega) \\ R_1(\omega) & R_0(\omega) & \dots & R_{n-3}(\omega) & R_{n-2}(\omega) \\ \vdots & \vdots & \ddots & \vdots & \vdots \\ R_{n-2}(\omega) & R_{n-3}(\omega) & \dots & R_0(\omega) & R_1(\omega) \\ R_{n-1}(\omega) & R_{n-2}(\omega) & \dots & R_1(\omega) & R_0(\omega) \end{pmatrix} \cdot \begin{pmatrix} S_0(\omega) \\ S_1(\omega) \\ \vdots \\ S_{n-2}(\omega) \\ S_{n-1}(\omega) \end{pmatrix} \quad (5.15)$$

The problem of finding the real wire signals $S_i(t)$ can be solved through inversion of the response function matrix and inverse Fourier transform. Additionally, a filtering matrix can be applied to suppress high frequency noises as in the 1-dimensional case.

In practice, in the real software for LArTPC signal processing the 2-dimensional deconvolution is followed by a region of interest (ROI) finding and gaussian peak fitting in those regions. Further, low-frequency filter cuts linear baseline subtraction are applied to induction plane waveforms to compute the gaussian peak widths and the final deconvolved charge over each electrode. Figure 5.6 depicts the signal processing workflow implemented by Micro-BooNE. The DUNE software employs an analogous setup.

5.3 Deep learning strategies for ProtoDUNE raw data denoising

In this section, we introduce the novel deep learning approach to raw digit denoising at ProtoDUNE-SP. We employ an approach based on the image representation of ProtoDUNE-SP data. We first give an overview of the deep learning models proposed to tackle the task, specifically with Graph Neural Networks. Then, we proceed to describe the experiments we conduct on simulated data at ProtoDUNE-SP, including a discussion on the training methods of our Neural Networks. Finally, we present a comparison of the denoised outputs both from our deep learning models and the baseline approach focused on deconvolution, currently implemented within the DUNE software framework. This section is based on the work we published in [219].

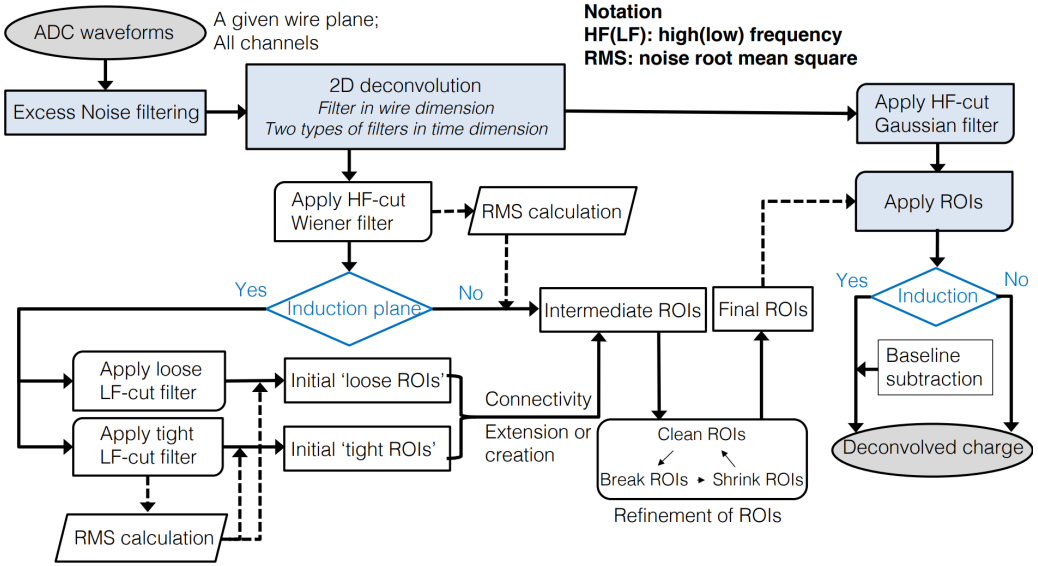


Figure 5.6: The signal processing flowchart is currently implemented by neutrino experiments such as MicroBooNE and DUNE. The figure is taken from [227].

5.3.1 Proposed models

Convolutional Neural Networks (CNNs), as described in section 2.1.2, are the state-of-the-art technique in image processing. They are based on a sequence of filtering kernels, whose parameters are trained with gradient descent optimization to perform some tasks. The convolution operation outputs a feature vector for each pixel of the input image. This vector is, indeed, a function of the pixel values in a small neighborhood around the pixel, also named the receptive field. The receptive field is constrained by the size of the kernel window. Stacking more convolutional layers one on top of the other, namely increasing the depth of the CNN, is a method to enlarge this quantity to make the output sensible to more information. The expected result is an enhancement of the overall network performance. We present an alternative approach to the problem: we enrich the model with different operations hoping to increase the expressiveness of the internal representation. The key idea is to exploit graph-like architectures to include non-local correlations between pixel values in the transformation.

Graph Convolutional Neural Network

We implement a Graph Convolutional Neural Network (GCNN) adapted from [238, 239], which propose to introduce a new operation in a denoising neural network called Edge Conditioned Convolution (ECC), defined for the first time in [240]. We exploit a simplified version of the ECC layer: the output representation is obtained pixel-wise averaging a common convolution with a 3×3 filtering window and a Non-Local Aggregation (NLA) operation. The insight is that the ordinary convolution inspects the values of

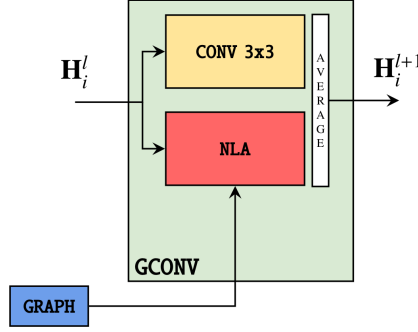


Figure 5.7: The GCONV layer. The input vector \mathbf{H}_i^l is updated to \mathbf{H}_i^{l+1} by means of NLA and 2D convolution operations. NLA relies on a previously computed KNN graph.

the neighboring pixels, while NLA exploits long-distance information. Figure 5.7 shows the described transformations wrapped by a new kind of layer, dubbed in the following Graph Convolution (GCONV).

The NLA builds a k -NN query graph connecting each pixel to its k closest one in feature space considering the Euclidean distance. Once the k closest pixels are identified, their feature vector is combined by a feed-forward layer to output the updated representation. If at layer l , the i -th of an n -pixel input image is described by the feature vector $\mathbf{H}_i^l \in \mathbb{R}^{d_l}$, the result of an NLA operation is:

$$\mathbf{H}_i^{l+1} = \sigma \left(\frac{1}{|\mathcal{N}_i^l|} \sum_{j \in \mathcal{N}_i^l} \Theta^l (\mathbf{H}_i^l - \mathbf{H}_j^l) + \mathbf{W}^l \mathbf{H}_i^l + \mathbf{b}^l \right) \in \mathbb{R}^{d_{l+1}} \quad (5.16)$$

where \mathcal{N}_i^l is the k -neighborhood of pixel i in the space of all the pixels feature vectors at layer l . $\{\Theta^l, \mathbf{W}^l\} \in \mathbb{R}^{d_{l+1} \times d_l}$ and $\mathbf{b}^l \in \mathbb{R}^{d_{l+1}}$ are trainable weights and biases shared throughout pixels. σ is the element-wise sigmoid function.

We observe that the operation above finds the k -nearest neighbors for each pixel in the input graph, namely builds a k -NN graph. This requires an amount of memory proportional to the area squared of the input image. The reason is that the complexity of a k -NN query algorithm is quadratic in the number of points since all the possible $N - 1$ distances pairs must be checked and sorted for each of the N points in the graph, leading to an $\mathcal{O}(N^2)$ scaling behavior. Our approach is to compute at once the $N \times N$ matrix of pixels pair distances and store it in memory, after that only the top k contributions for each pixel are considered, resulting in a final $N \times k$ tensor. An alternative strategy would be to compute the matrix looping on all the points saving in memory only the $N \times k$ matrix (with $k \ll N$). Although the latter method optimizes the algorithm memory footprint avoiding storing the intermediate large result, it sacrifices GPU execution time performance.

With this choice, we still have to take care of memory constraints. As an example, considering a batch of 32 input images of 128×128 pixels and employing single precision 32-bit floating point numbers, the graph construction operation burden is of order $\mathcal{O}(30 \text{ MB})$. If the architecture involves

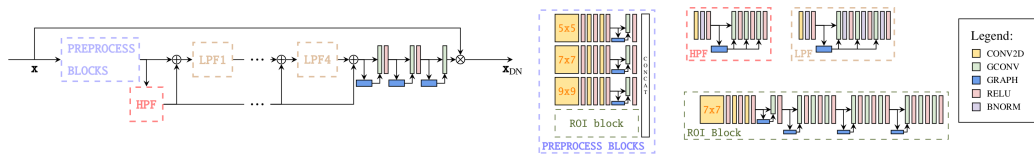


Figure 5.8: The GCNN neural network architecture. Input and output are batches of noisy \mathbf{x} and denoised \mathbf{x}_{DN} images, respectively. The network is organized as low-pass (LPF) and high-pass (HPF) filters as in [239]. As explained in section 5.3.2 we concatenate an ROI block, pre-trained on background vs signal binary segmentation, with multi-scale preprocessing layers.

multiple graph building operations and we allow higher batch sizes to stabilize the training process, a consumer-grade GPU with $\mathcal{O}(16 \text{ GB})$ memory gets easily saturated. Given that the actual raw data from ProtoDUNE-SP are way bigger than the 128×128 image in the example, we have to limit the model input image size to just small crops of the original data, as explained in the training paragraph of section 5.3.2.

Figure 5.8 depicts the GCNN network. Note the final residual connection in the top branch: the usual sum has been replaced by an element-wise multiplication. The choice is motivated by the nature of the input images, which are mainly comprised of long tracks separated by empty space. In regions without any signal, it could be easier to learn how to clean the noise multiplicatively rather than additively. The network, in principle, does not have to learn to perfectly profile the noise and subtract it, instead, we can teach the model to predict a mask on the input image to cut down the uninteresting regions by multiplying the pixels values with small numbers.

U-shaped Self-Constructing Graph Network

As reported in the previous section, the main limitation of the GCNN network is the memory burden due to the k -NN graph operation, allowing to feed only pieces of the original image. The cropping method, unfortunately, prevents establishing very long correlations between pixels and leads to poor time performance during inference on large datasets, because the tiles must be sequentially fed into the GPU and prevent full parallelism.

As an alternative approach to the GCNN, we build upon the work presented in [241]. The authors introduced the Self Constructing Graph-Network (SCG-Net) model for image segmentation of satellite pictures. They first extract a low-dimensional representation of a high-resolution input image with the help of a CNN. Then, two fully connected layers are trained to build a graph on the pixels, returning the adjacency matrix as well as the vectors of features associated with the nodes. At this stage, the graph is further transformed by a couple of graph layers chosen between the spectral-based Graph Convolutional Network [242] and the spatial-based Graph Isomorphism Network [243]. Finally, the original size image is retrieved through bilinear interpolation.

Upsampling through the interpolation method seems a natural approach when the images contain dense features since there is a more gradual change in the pixel values of a small neighborhood. In that context, a certain de-

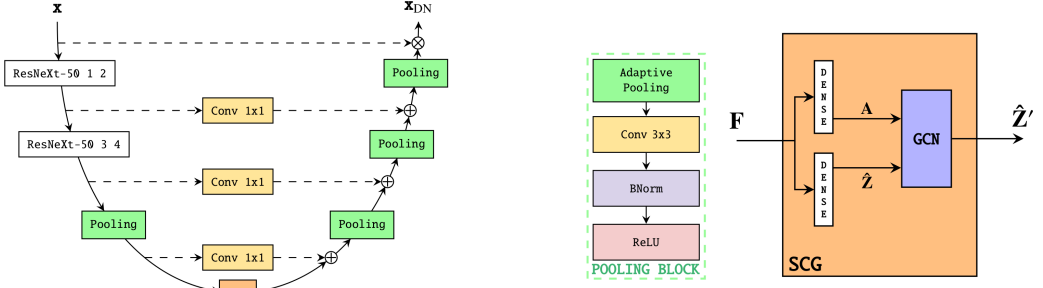


Figure 5.9: The USCg-Net architecture. The adaptive pooling layer has a two-fold utility: in the left branch it downscales the input, while in the right one, it provides upsampling. We employ the first 4 blocks of a pre-trained ResNeXt-50 in the shallowest layers of the network. The blocks respectively contain 9, 12, 18 and 9 convolutional layers. The horizontal dashed lines represent residual connections with a 1×1 convolution for enhanced expressivity and are employed to match the number of image channels between the left and right branches. The SCG layer builds the adjacency matrix \mathbf{A} and the vectors of node features $\hat{\mathbf{Z}}$ to be passed into a GCN layer to output the final representation of the nodes $\hat{\mathbf{Z}}'$.

gree of blurred edges can be considered acceptable and tolerated. Our use case, however, is rather peculiar in this sense: we believe that acting on images containing sparse and localized features potentially with a single up-sampling operation washes out the fine-grained information contained in the input. Therefore, we design an architecture that gradually rebuilds the original image size in multiple steps.

We introduce the U-shaped Self Constructing Graph Network (USCg-Net), where a U-Net-like [146] network structure with residual connections carries the information all the way through the data pipeline. Figure 5.9 shows the USCg-Net architecture. The pooling blocks contain the Adaptive pooling layer, which is responsible for resizing its inputs. A pre-trained ResNeXt-50 [244] with a 32×4 template is employed to construct an initial feature map serving as input of the SCG layer. The early-layer representation of the pre-trained network should be generic enough to catch the spatial features of the inputs and drift the training process during the initial phases of the optimization. We remark the residual skip connections between the downsampling and upsampling branches of the network. The usual sum has been replaced by a convolution with a 1×1 kernel to increase the complexity of the network. Finally, the residual link displays the same multiplication trick employed for the GCNN network.

The SCG layer is at the core of the network: it turns the image into a graph allowing distant connections between pixels. The input is an image $\mathbf{F} \in \mathbb{R}^{h \times w \times d}$ and maps it into the adjacency matrix $\mathbf{A} \in \mathbb{R}^{n \times n}$ and node feature vectors $\hat{\mathbf{Z}} \in \mathbb{R}^{n \times c}$ through two encoding dense layers. In the previous formulae, d and c are respectively the input and output channel dimensions and $n = h \times w$ is the number of extracted nodes. In our experiment we further transform the graph encoding through the GCN layer, leaving the investigation of other options to future works. $\hat{\mathbf{Z}}'$ can be finally projected

dunetpc	n events	p energy (GeV)
v08_24_00	10	2
v09_10_00	70	0.3, 0.5, 1, 2, 3, 6, 7

Table 5.1: Datasets for training and testing. The two samples differ in producer package version, size and event beam energies. The second dataset contains 10 events for each p energy specified.

back into the full-size image $\in \mathbb{R}^{h \times w \times c'}$ by the pooling blocks in the right branch of the USCG-Net.

5.3.2 Experimental results

In this section, we describe the experiments conducted to validate our models. We proceed to introduce the datasets generate to carry on the study, the training methodology and the actual results.

Datasets

We describe here the datasets employed to train and test the proposed models. We remark that the present results have been tested on simulated events only: the inclusion of detector data is beyond the scope of this first stage of the investigation. We, therefore, simulate interactions within the ProtoDUNE-SP detector through the LArSoft [245] framework, in particular with the `dunetpc` package. We consider events containing the interactions induced by a proton beam of various energies and cosmic rays with the Argon targets. Our supervised training approach is based on simulated raw digits. The simulation software includes the possibility to switch off the electronics noise affecting the charge depositions: we employ this information as target outputs for the denoising models.

Table 5.1 lists the composition of the generated datasets. In figure 5.10 and 5.11 we show visual examples from v08_24_00 and v09_10_00 datasets. The plots contain simulated raw digits, and 1-dimensional waveforms extracted from the channel marked with the orange dashed line. We refer to waveforms with and without noise contributions as noisy and clear waveforms, respectively. We consider the v08_24_00 dataset a simplified version since it is smaller and contains easier features to denoise and segment than the v09_10_00 one. v09_10_00, indeed, is generated according to a detector data-driven approach. In the latter sample, clear waveforms are non-zero even in regions without signal, this reflects the impossibility to measure peaks with infinite resolution. Moreover, low-frequency negative tails recorded just after big spikes are visible in figure 5.13.

We split our datasets in 80/10/10% slices for training, validation and testing. The validation set is used to choose the best model, while the test set is employed to present the final results given in this section. We aggregate the performance results for each metric in a single measurement: that is the mean \bar{x} and the standard error of the mean σ of the sampling distribution, representing the metric expected value and its uncertainty. This criterion influences also the selection of the best model during training, namely, the network checkpoint at the epoch end that achieves the lowest upper bound

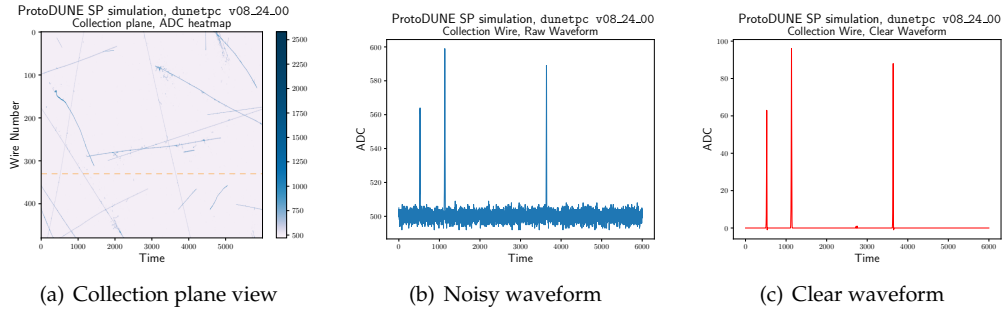


Figure 5.10: Example taken from `dunetpc v08.24.00` dataset. The horizontal orange dashed line in the first panel marks the channel to extract the waveforms from.

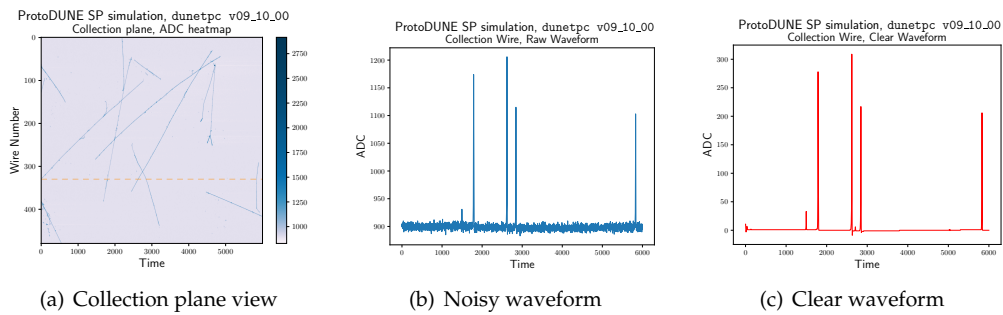


Figure 5.11: Example taken from `dunetpc v09.10.00` dataset. The horizontal orange dashed line in the first panel marks the channel to extract the waveforms from.

$\bar{x} + \sigma$ of the loss function interval. With this choice, we aim to minimize both the bias and the variance of the model.

We remark that a single event at ProtoDUNE-SP is comprised of multiple views of the activity in the detector. Therefore, one event does not count only as one training point for our neural network. The GCNN network processes tiles of the original images. Considering crops of size 32×32 , each event in the dataset contains $9 \cdot 10^4$ of those. The USCG-Net, instead, processes entire views. The two datasets account for 18 and 126 of such views used to assess the model performance and the associated uncertainty. Note that the dimensionality of the output image is of the order of millions of pixels, each one contributing to the evaluation of the final performance metric.

Network training

We employ the same pre-processing procedure for all our models, namely, we subtract the median value from each ProtoDUNE-SP view independently. According to the approach currently adopted by DUNE and based on the discussion in section 5.2, the median value gives a good estimate of the noise pedestal quantity. The median subtraction step is fundamental to have waveform values centered around zero and it is expected to provide accuracy enhancements and training stability. The inputs are further normalized in the unit interval to prevent gradient divergence as it is a technique commonly exploited in machine learning applications.

The GCNN data processing is constrained by the memory issues described above. As already anticipated, we employ a data parallel approach, cropping the inputs into 32×32 pixels images and processing every tile independently. This solution requires some subtleties in the training process due to the nature of the inputs.

Given the sparsity of the input images, it is likely that the majority of the crops contain little to no signal. It is meaningless to feed the network with multiple empty crops. To speed up the training, we decide to train on just a subset of the available crops. This choice, in turn, triggers a second issue: sampling randomly the subset of crops provides an extremely unbalanced dataset, where we are very likely to miss crops containing interesting charge depositions. Hence, we fix the percentage of crops containing signal to balance the signal-to-background pixel ratio: in our experiments, we keep this quantity at 99%. The cropping procedure works as follows. We mark as signal all the pixels in clear waveforms that have non-zero ADC value count in a plane view. Then, we sample randomly the desired number of crop centers, complying with the exact ratio of signal to background percentage. Finally, within the plane views we specify a bounding box around the drawn centers.

We pre-train the Region Of Interest (ROI) block of the GCNN network for image segmentation, which is a classification task at the pixel level with labels usually belonging to a finite set of exhaustive and mutually exclusive classes. The ROI block, indeed, is trained to distinguish between pixels that contain or not electron-induced current signals. The Roi Block is then attached as in 5.8 to the GCNN network, which is trained for image denoising, which is a regression aiming at subtracting the noise contributions from each pixel intensity.

The two parts of the network are optimized following an ad-hoc strat-

egy. First, we pre-train the ROI block alone on image segmentation for 100 epochs, storing the best weight configuration: at this stage, the block learns to distinguish between signal and background, i.e. empty pixels. We employ the standard binary classification loss function, namely binary cross-entropy. The optimizer follows the AMSGrad variant [246] of the Adam algorithm [51] with a starting learning rate of 10^{-3} . After pre-training completion, we train the full GCNN network on image denoising for 50 epochs and save the best-performing model on the validation dataset.

We choose again AMSGrad as the optimization algorithm for the full denoising network, however, this time, we set the initial learning rate to a slightly higher value $9 \cdot 10^{-3}$. We also build a custom loss function made of two contributions: the mean squared error (MSE) \mathcal{L}_{MSE} between labels and outputs and a loss function \mathcal{L}_{ssim} derived from the statistical structural similarity index measure (stat-SSIM) [247]. stat-SSIM for two images \mathbf{x} and \mathbf{y} , is obtained through the following equation:

$$\text{stat-SSIM}(\mathbf{x}, \mathbf{y}) = \frac{1}{n_p n_c} \sum_{pc} \left(\frac{2\mu_x \mu_y + \epsilon_\mu}{\mu_x^2 + \mu_y^2 + \epsilon_\mu} \times \frac{2E[(\mathbf{x} - \mu_x)(\mathbf{y} - \mu_y)] + \epsilon_\sigma}{E[(\mathbf{x} - \mu_x)^2] + E[(\mathbf{y} - \mu_y)^2] + \epsilon_\sigma} \right)_{pc} \quad (5.17)$$

where μ_i is a shorthand for the image \mathbf{i} expected value $E[\mathbf{i}]$, which is computed through convolution with an 11×11 Gaussian kernel of standard deviation $\sigma = 3$. All the other expectation values in the equation are calculated by convoluting the quantity appearing in the argument with the same Gaussian filter. ϵ_μ and ϵ_σ are two regulators that limit the maximum resolution at which the fractions in the equations are computed, imposing a cut-off on the mean and variance expected values, respectively.

When both the numerator and the denominator of the fraction reach much smaller values than the corresponding ϵ , the output gets close to one. In the experiments, ϵ_μ and ϵ_σ are fixed to 0.5^2 . This choice implies that, for the stat-SSIM computation, we estimate the means and standard deviations of the distributions at scales larger than half of one ADC value, namely the granularity of the recorded detector hits. The result is finally averaged over the entire image containing n_p pixels and n_c channel dimensions. The quantity in equation 5.17 takes values in the range $[-1, 1]$ and approaches 1 only if $\mathbf{x} = \mathbf{y}$.

The associated loss function is then given by $\mathcal{L}_{ssim} = 1 - \text{stat-SSIM}$: it is a perceptual loss, in the sense that tries to assess the fidelity of the image by focusing on structural information. It relies on the idea that pixels may have strong correlations, especially when they are spatially close. In contrast, MSE evaluates absolute differences of pixels, without taking into account any dependence amongst them. More details on the interpretation of these quantities can be found in [248]. The two contributions in the loss function are weighted as follows: $\mathcal{L} = \alpha \cdot \mathcal{L}_{MSE} + (1 - \alpha) \cdot w \cdot \mathcal{L}_{ssim}$. We fine-tune the multiplicative parameter $w = 10^{-3}$, to balance the gradients with respect to the model's trainable parameters provided by the two terms in the sum. The parameter α is fixed to 0.84 as in [249].

In the rest of this section, we will refer, with a slight abuse of notation, to a CNN as a GCNN network with Graph Convolutional layers replaced by plain Convolutional ones.

The training of the USCG-Net is straightforward: cropping is not used,

so no sampling method is needed. Although the entire model fits in a single GPU with 16 GB of memory, we prefer to employ a sliding window mechanism as in the original SCG-Net paper [241]. We split the raw digits matrix along the time dimension with a 2000 pixel wide window and stride of 1000 pixels. After the forward pass, the results are combined by averaging predictions on overlapping regions. The USCG-Net is trained to minimize the MSE function between model outputs and clear raw digits, with AMSGrad optimizer and a learning rate of 10^{-3} . We dropped the stat-SSIM contribution from the loss function after we experienced training convergence problems including that term in the experiment.

Experimental results

The metrics used to assess the goodness of our models and benchmark them against the state-of-the-art approach are four: structural similarity index measure (stat-SSIM), mean squared error (MSE) and peak signal-to-noise ratio (pSNR) are the standard for image denoising tasks; the last is a custom one, dubbed integrated mean absolute error (iMAE) and will be defined below.

The pSNR is a function of the MSE between a noise-free image \mathbf{x} and a denoised one \mathbf{y} :

$$\text{pSNR}(\mathbf{x}, \mathbf{y}) = 10 \cdot \log_{10} \frac{\max^2(\mathbf{x})}{\text{MSE}(\mathbf{x}, \mathbf{y})} \quad (5.18)$$

Note that the pSNR and stat-SSIM increase for better reconstruction of the signal in the data, while the opposite happens for the MSE. We observe that these three quantities struggle to grasp the goodness of the baseline model. Indeed, it aims at fitting gaussian peaks in masked regions, rather than reconstructing the precise shape of the spike contained in the raw digits. Hence, the baseline tool performs inevitably poorly on the considered metrics and specifically, up to our knowledge, there is no default metric in the literature to assess its performance. Nonetheless, we define a custom quantity that tries to compare the different approaches: we highlight that the deconvolution process does not preserve waveform amplitudes, but their integrals, namely the charge on the ProtoDUNE-SP wires. For such reason, we decide to evaluate the integrated Mean Absolute Error (iMAE) on the wires integrated charge:

$$\text{iMAE}(\mathbf{x}, \mathbf{y}) = \frac{1}{n_w} \sum_{w=1}^{n_w} \left| \sum_t (\mathbf{x} - \mathbf{y})_{wt} \right| \quad (5.19)$$

where the sum inside the absolute value runs over time for the whole readout window, while the outer sum aggregates the result over the wire dimension.

The deconvolution approach does not preserve amplitudes because of the filtering function applied in Fourier space. If such a filter is normalized, then the transformation preserves the integral. Furthermore, the deconvolution outputs are known up to an overall normalization constant, which we fit on the datasets to minimize the iMAE quantity. We show that, although we perform this operation on the outputs of the baseline tool for a fair comparison against our models, they nonetheless achieve a worse iMAE score. Table 5.2 collects the metrics values evaluated on the `v08_24_00` dataset. We gather

Model	stat-SSIM	PSNR	MSE	iMAE
Baseline	-	-	-	5391 \pm 1622
CNN $\nu 08$	0.471 \pm 0.008	67.3 \pm 1.2	0.57 \pm 0.03	287 \pm 12
GCNN $\nu 08$	0.512 \pm 0.011	70.12 \pm 1.4	0.30 \pm 0.01	191.4 \pm 2.6
USCG $\nu 08$	0.988 \pm 0.005	72.66 \pm 1.54	0.17 \pm 0.02	95.5 \pm 8.5
USCG $\nu 09$	0.926 \pm 0.007	72.3 \pm 1.5	0.18 \pm 0.02	76.3 \pm 8.2

Table 5.2: Test metrics for denoising on $\nu 08_24_00$ dataset. Results for collection plane and 2 GeV beam energy only. $\nu 08$ or $\nu 09$ in the first column refer to which dataset the corresponding model was trained on.

Model	stat-SSIM	PSNR	MSE	iMAE [$\times 10^3$]
Baseline	-	-	-	5.86 \pm 0.52
CNN $\nu 08$	0.37 \pm 0.02	57.3 \pm 1.4	5.79 \pm 0.88	4.16 \pm 0.36
GCNN $\nu 08$	0.40 \pm 0.02	57.7 \pm 1.5	5.27 \pm 0.69	4.51 \pm 0.39
USCG $\nu 08$	0.65 \pm 0.05	61.1 \pm 1.6	2.3 \pm 0.2	2.18 \pm 0.29
USCG $\nu 09$	0.81 \pm 0.07	61.8 \pm 1.7	1.99 \pm 0.19	2.25 \pm 0.23

Table 5.3: Test metrics for denoising on $\nu 09_10_00$ dataset. Results for collection plane and 2 GeV beam energy only. $\nu 08$ or $\nu 09$ in the first column refer to which dataset the corresponding model was trained on.

$\nu 09_10_00$ dataset results in table 5.3. We present the scores only for the events with 2 GeV beam energy, since we find a flat distribution of the considered metrics in the energy parameter. Figures 5.12 and 5.13 show samples of labels and denoised waveforms.

USCG-Net-like networks exceed GCNN-like ones in all the collected metrics. In order to have a first assessment of the quality of the neural network generalization power, we train two versions of the USCG-Net: one on the $\nu 08_24_00$ dataset and the other on the $\nu 09_10_00$ dataset. We decide not to train the GCNN-like networks on the $\nu 09_10_00$ dataset after we observed difficulties in training convergence as well as long training times on such a big dataset. We evaluate these networks on both datasets.

Following expectations, the networks trained and applied on the same dataset lead to better performance. The only exceptions are given by the iMAE columns, where the USCG-Net trained on the dataset opposite to the testing one, achieves the best iMAE score. The stat-SSIM index score drops significantly for GCNN-like networks. All the networks, nonetheless, show hints of overall good generalization power when they are applied to datasets not used for training. This fact is well supported by the PSNR columns, which show that even the worst model achieves competitive results. We underline that the USCG-Net is not trained according to the stat-SSIM quantity: adding an extra term in the loss function containing such a term could be considered a point of further development of the present research.

As a final remark, we observe that the USCG-Net performs better than the other architectures. Although a thorough investigation of the motivations behind this performance gap has not been carried out yet, we advance two possible hypotheses to try to explain this behavior. The first idea lies in the ability of the USCG-Net to process entire planes at once, managing to connect pixels very far apart. This might enhance the performance due to the particular nature of the inputs: muons inside ProtoDUNE-SP are revealed by the

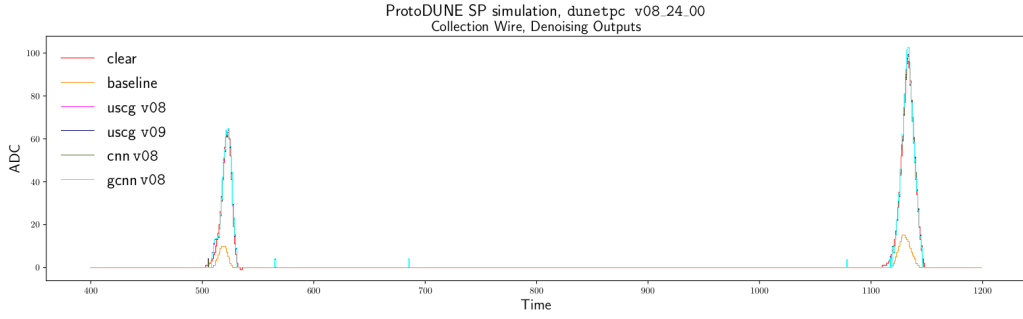


Figure 5.12: Detail of a raw waveform from `dunetpc v08_24_00` dataset: label, traditional algorithm and neural network outputs. The version, `v08` or `v09`, next to the model name in the legend refers to which dataset the corresponding model was trained on.

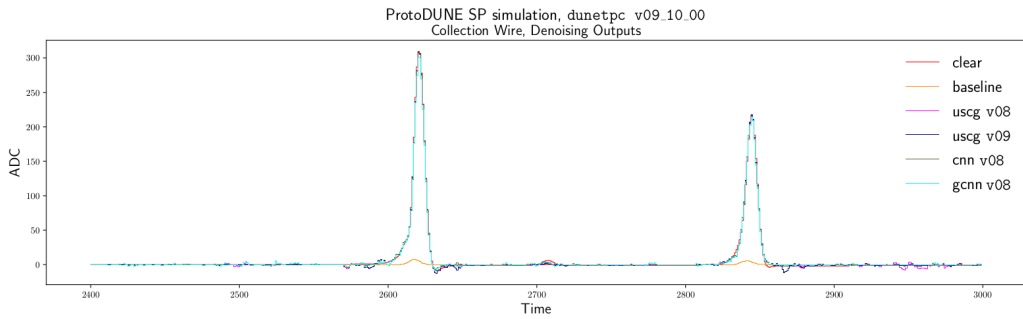


Figure 5.13: Detail of a raw waveform from `dunetpc v09_10_00` dataset: label, traditional algorithm and neural network outputs. The version, `v08` or `v09`, next to the model name in the legend refers to which dataset the corresponding model was trained on.

detector as tracks that extend for hundreds of centimeters, i.e. they span big portions of the raw digit images as in figure 5.10 and figure 5.11. Therefore, the USCG-Net network is allowed to reconstruct entire track objects. This is not possible with the cropping approach used for the GCNN network, which inspects portions of inputs independently, inevitably splitting the signal.

The second insight is linked to the fact that we exploited a pre-trained `ResNeXt-50` network in the early layers of the USCG-Net architecture. Instead, the GCNN network is trained from scratch with randomly initialized weights. It is a common technique in deep learning to exploit some layers of a network pre-trained on a different task to help the training convergence. This procedure is known as transfer learning. The key point is that the pre-trained layers should already contain some basic domain knowledge that will not have to be learned anymore. In our particular image-processing use case, it could be like we were allowing the network to start the training with some general knowledge of the geometrical objects that it might find within an input image. This helped the whole training to converge to a more performant minimum of the loss function search space.

Clustering at ProtoDUNE-SP with supervised learning

Contents

6.1 The Pandora framework	115
6.2 The Cluster Merging Network	121

In this chapter, we present the implementation of a neural network trained to solve the slicing problem. Slicing is an essential step in the reconstruction workflow for neutrino detectors and, in particular, this work applies to ProtoDUNE-SP detector. We set the stage by introducing the Pandora framework, a dedicated software for event reconstruction in physics experiments. Pandora is widely employed by many neutrino collaborations. In the second section of this chapter, we detail a novel deep learning approach to the problem, namely the Cluster Merging Network [250].

6.1 The Pandora framework

Event reconstruction at physics experiments is the process of extracting high-level features from a collection of detector electronics signals to determine the event particle content along with their properties. The output of such workflow is a list of particle objects associated with their corresponding detector signals. The Pandora framework [251] is a multi-pattern recognition software dedicated to reconstruction, firstly built for linear collider experiments, such as the International Linear Collider (ILC) [252] and the Compact Linear Collider (CLIC) [253], and then extended to LArTPC detectors. In particular, it has been tested in the context of the MicroBooNE experiment [254]. In the following we will focus on applications to LArTPC detectors only, giving an overview of the Pandora reconstruction framework.

The Pandora software development kit (SDK) is a tool implemented in C++ programming language and defines the data structures needed to run several reconstruction algorithms. It is specifically designed to be interfaced with external Event Data Models (EDMs), such as the one provided by LArSoft [245] which implements the simulation software for LArTPCs. The Pandora application can run in standalone mode providing an algorithm to export the LArSoft simulated events into the Pandora format and vice-versa. In this scenario, Pandora defines two kinds of structures: Input and Algorithm

objects. Products of the first kind are created by the Pandora application before running the reconstruction algorithms and cannot be changed by them. On the other hand, the Algorithm objects are created and modified by reconstruction algorithms.

The Pandora SDK implements three kinds of Input Objects. *CaloHit*: represents a space point deposition in the detector and is the fundamental building block of the Pandora event representation. Each CaloHit is associated with the x , y , z detector coordinates and the relative deposited energy E . Within a LArTPC a CaloHit is built from processed raw signals of the form discussed in chapter 5: a single peak in an ROI region is fitted with N multiple Gaussians to allow the possibility to have several single depositions within a single peak. Each fitted gaussian in the peak is turned as a separate CaloHit. LArTPC raw data are described by a drift coordinate (x coordinate) and a readout channel number identifier, indeed, Pandora CaloHits are initially given a null y component and a z component referring to the position of the wire where the signal was first detected in the wire pitch direction. The transformation from the wire plane representation to the canonical detector 3-dimensional cartesian coordinate system involves a rotation-like operation that requires at least two wire plane coordinates to be known for each CaloHit. An additional flag for each CaloHit signals which of the 3 different wire planes (U, V or W) recorded the corresponding signal.

Track: represents a collection of CaloHits objects arranged in a continuous pattern. Beyond the CaloHits and their attributes belonging to the Track object, this holds other global information like associated particle momentum and trajectory direction. The Track object can also have methods to retrieve the parent, daughter and sibling relationships with other Tracks with the intent to build a particle tree to describe the interaction hierarchy contained in the event.

MCParticle: is an object collecting true information from simulation (of course, detector data do not hold this kind of details) about an event particle. This kind of data structure is carried within Pandora mostly for development reasons, as it allows to cheat parts or even entire algorithms in the reconstruction workflow. It can also be used to measure performance metrics for the tools' implementations. The key idea is that the best method should reproduce as much as possible the true information contained in the MCParticle objects and the related MCParticleLists.

The Pandora framework implements also Algorithm objects: auxiliary products that represent outputs at various steps of the reconstruction process. Below we introduce the most important ones.

Cluster: represents a collection of CaloHits carrying space and energy information. It also usually contains estimations of Cluster global properties, such as results of energy or geometrical fits. Being an Algorithm object, Pandora implements also operations that allow the algorithms to create, read, split and merge different Cluster objects.

Vertex: this object might not correspond to a true CaloHit deposition, but it is rather the output of a fitting procedure on the available event CaloHits. It identifies the exact space point where an interaction took place during the readout window. It naturally holds also information about the particle involved in the interaction, highlighting the parent-daughter structure of the physical scattering.

ParticleFlowObject (PFO): this can be seen as the final reconstruction output. It is a class containing all the information gathered through several algorithms about an event particle. A PFO instance is linked with all the information that a physics analysis might desire to investigate: as such, it is associated with Clusters, Tracks and Vertices objects belonging to the particle and it is conveniently put in the decay tree hierarchy representing the event history wrap-up.

Pandora implements reconstruction in a modular way: the framework encompasses $\mathcal{O}(100)$ algorithms and is easily extended via sub-classing thanks to the Object Oriented paradigm, it is built around. The modularity of Pandora prefers to split the reconstruction process into several small steps with dedicated algorithms, rather than a single end-to-end procedure: this ensures more fine-grain control on the workflow and the ability to switch between multiple implementations of the same method. The instructions and the list of algorithms that should be run by the Pandora application are contained in XML settings files.

The modularity of Pandora abstracts also the detector geometry to handle different setups: specific geometry settings collect all the parameters needed to design the detector where to run the reconstruction in. The main parameters included in a geometry file for a LArTPC detector are the number of drift chambers with their spatial extent in the cartesian frame of reference. The orientation of the wires in each wire plane with respect to the vertical, which fixes the wire pitch direction. The detector gaps simulate unresponsive channels or regions populated with a low number of wires if any. The current Pandora framework supports different geometries for LArTPC detectors, such as ICARUS [255], MicroBooNE, ProtoDUNE-SP, ProtoDUNE Dual Phase (DP) [256] and the DUNE Far Detector. In the following, we will focus on ProtoDUNE-SP only, but the discussion can be easily generalized to all the different LArTPC realizations.

Figure 6.1 represents the flowchart of a Pandora run for a ProtoDUNE-SP reconstruction event. The inputs are the 2-dimensional CaloHits from either simulation or real detector data. The diagram, then, splits the process into three main pipelines, namely *PandoraCosmic*, *slicing* and *PandoraTestBeam*. The first step aims at reconstructing the CaloHits belonging to cosmic rays (CRs): many LArTPC detectors are built underground (such as the DUNE FD) and are shielded by hundreds of meters of rock, however, others are surface detectors (like MicroBooNE and ProtoDUNE) and they record events contaminated by CR muons interacting at high angles in the fiducial volume producing long ionization tracks. This effect is even more emphasized by the long readout windows of a few milli-seconds required to observe LArTPCs signals due to the rather small electron drift speed, which includes many CR tracks in each event. For example, we expect an $\mathcal{O}(50)$ of CR interactions for each event at ProtoDUNE-SP (readout window of 3 ms). The *PandoraCosmic* outputs a list of *Muon3DParticles* that unambiguously identifies the CR muons CaloHits that will not be available for the next steps.

The *slicing* algorithm runs just after the first main pipeline and its goal is to group the CaloHits related to the same main interacting particle and its subsequent decays. The output of such a procedure is comprised of multiple sets of CaloHits named slices.

The *PandoraTestBeam* pipeline further analyzes the CaloHit remnants

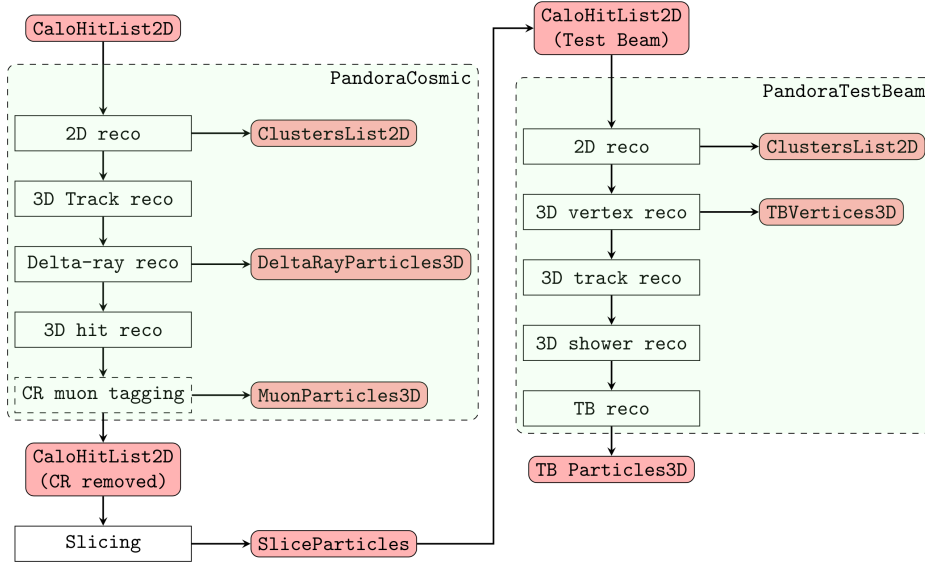


Figure 6.1: Scheme of the Pandora reconstruction workflow for a ProtoDUNE-SP event. The red blobs refer to data structures that serve as inputs for the Pandora algorithms or their products. White boxes identify high-level reconstruction step and are gathered into two main pipelines: *PandoraCosmic* and *PandoraTestBeam*. In the middle, the slicing algorithm aims at isolating the Test Beam related CaloHits. The CR muon tagging algorithm, labeled by a dashed box, is taken from the LArSoft implementation.

from the previous steps and aims at reconstructing the data structures related to the test beam (TB) depositions. In other detectors involving neutrino beams from accelerator sources, such as MicroBooNE, this pipeline is replaced by the analogous *PandoraNu*, described in detail by [254]. The final output of such groups of algorithms is a list of test beam or neutrino 3-dimensional particles that are inserted in the event interaction tree.

PandoraCosmic pipeline The *PandoraCosmic* pipeline is track-oriented, given that CRs generate long ionization tracks in the detector rather than particle showers. The inputs of this pipeline are all the 2-dimensional CaloHits extracted from an event generated by LArSoft. At ProtoDUNE-SP, we identify three main CaloHitLists associated with the three wire planes U, V and W. Each CaloHitList undergoes a 2-dimensional clustering procedure that groups together the hits employing topological algorithms. The objective of this first stage is to create high-purity small clusters to be merged afterward, rather than complete ones. Purity is the fraction of hits in a cluster that indeed belong to the true MCParticle associated with the cluster. On the other hand, completeness is the percentage of the true MCParticle CaloHits that are included in the Cluster2D.

After the first clusters are created, the Pandora framework tries to associate and extend the clusters to increase completeness without affecting the purity. This is done by extracting geometrical information about cluster pairs considering geometrical information such as cluster proximity and orienta-

tion. A further cluster refinement is done with the output of this merging step looking for clusters that should be split, instead. Indeed, clusters that present discontinuities or intersections in the overall track envelope are split into two clusters to preserve the purity metric.

Once the three separate `ClustersList2D` are generated, the 3-dimensional reconstruction algorithms aim to match the different 2-dimensional plane views into a single detector view. The key idea is to link together the different `Cluster2D` objects from the three views if they refer to the same `Track3D`. Several algorithms run in this step to identify and resolve ambiguities among the different plane views. Two main algorithms known as `ThreeDTransverseTracks` and `ThreeDLongitudinalTracks` achieve these goals for ionization tracks with a long or small extension in the x drift coordinate, respectively.

The CR ray muons often generate small secondary particle interactions out of their main ionization tracks. These are secondary electrons that trigger small curly depositions known as delta rays. At this stage of the reconstruction the `CaloHits` related to these particles are already grouped into clusters, but they still un-assigned to any 3-dimensional object. The `DeltaRayMatching` algorithm aims at identifying these delta rays and linking them to their parent muon track based on their proximity.

The input 2-dimensional `CaloHits` are grouped into clusters and tracks and, at this stage, Pandora populates the list of 3-dimensional `CaloHits` reconstructed from the input ones. The CR reconstruction terminates with identifying the track's end-points (the starting point is always at the highest y value since CRs come from above), creating a `Muon3DParticle` along with `Vertices` objects at each delta ray emission. Before exiting the pipeline, the `CaloHits` associated with the reconstructed CR objects are removed from the input lists.

Slicing After cosmic rays removal by the previous pipeline, the `CaloHits` should contain only the TB or the neutrino-associated hits, depending on the specific LArTPC application. However, since failures in CR identification might occur, whatever downstream pipeline, namely `PandoraTestBeam` or `PandoraNu`, should be able to handle CR remnants properly. Therefore, Pandora runs at this intermediate stage the slicing algorithm: its primary objective is to separate the CR remnants `CaloHits` from the TB or neutrino ones. As a plus, it proceeds to assign the available `CaloHits` to separate clusters based on the main interacting parent particle. This way, not only the TB or ν particles are kept divided from the rest of the `CaloHits`, but also it should be easier to run once more the reconstruction on the CR remnants.

The Pandora implementation of the slicing algorithm is based on topological considerations and completely ignores the energy information contained by the `CaloHits`. The core methods connected with this algorithm are the `ThreeDSlidingFit` and the `ThreeDSlidingConeFit`, which respectively consist in fitting a track and shower envelope around the available clusters in the 3-dimensional space after a first fit has been done on the 2-dimensional objects projections. The resulting tracks and shower clusters are allowed to seed a new slice if they group more than 50 `CaloHits`. Once a new slice is created all the clusters associated with the seeding one are gathered inside the same slice. The association of each candidate cluster is done through pointing (mainly orientation and parent-daughter relationship) and

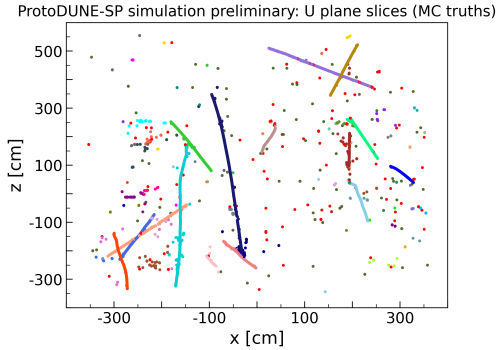


Figure 6.2: Cosmics rays and test beam event: U plane view. Hits with the same color belong to the same main Monte Carlo simulated particle.

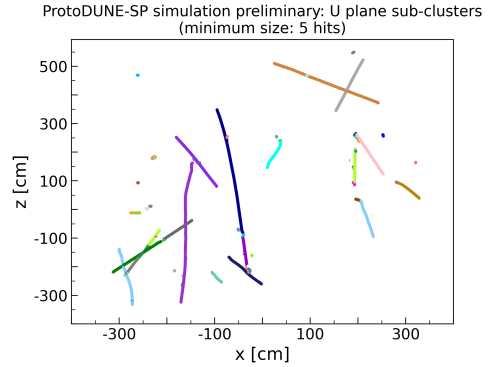


Figure 6.3: U plane view: 2D initial clusters with more than 5 hits computed by Pandora.

proximity (minimum inter-cluster distance) conditions with the main seeding cluster for track-like products and percentage overlapping with the main shower cone envelope for the shower-like ones.

The algorithm ensures that all the clusters get tested to be included into a slice traversing all the possible clusters with a Breadth First Search approach. This way, the CaloHits associated with each seeding cluster are collected inside their relevant slice. However, it can be the case that small isolated clusters do not get linked with any slice because they do not pass the conditional statements listed above. The software, therefore, takes care of these remaining clusters building a 3-dimensional k-d tree graph for fast cluster querying: the k-d tree nodes are fixed to the positions of the CaloHits already in the slices and the centroid point of each remnant cluster is checked to be included in the slice of the closest k-d tree node.

Figure 6.2 provides an example of the slicing tool output for an event with cosmic rays plus a test beam. At ProtoDUNE-SP TB is a mixture of charged particles with given energy (mainly p , e^+ and π^+). The hits in the image are color-coded, depending on which final slice they belong to.

PandoraTestBeam The `PandoraTestBeam` pipeline is associated with the reconstruction of the CaloHits due to the test beam interactions with the liquid Argon. The test beam at ProtoDUNE is mainly comprised of hadrons, while neutrinos are the main constituents of the beam flux to which MicroBooNE is exposed. Even if the composition of the beams is different, Pandora treats the two problems almost in the same way. We stress that the input CaloHits of this step should not contain CR muon tracks anymore, even if remnants can still be addressed at this level.

The TB pipeline differs from the CR one mainly by two aspects: the vertex selection and the reconstruction of primary electromagnetic showers. In particular, the vertex reconstruction starts considering all the possible vertex candidates in the 3-dimensional space as a result of the `CandidateVertexCreation` algorithm. Pandora proceeds, then, to evaluate a score metric for each

vertex candidate to identify the fittest, which turns out to be the one with the maximum score. The metric is built around three different contributions that can be weighted to tunable parameters to tweak the relative importance of each factor.

The first contribution is dubbed as *energy kink* and depends on the sum of each cluster total reconstructed energy projected on each 2-dimensional view, plus an impact parameter measuring the displacement of each cluster from the vertex. The idea is that secondary interactions downstream of the interaction vertex should be less energetic than primary particles, such as TB ones or CR.

The second contribution describes the *asymmetry* of the vertex splitting: it has been introduced to suppress vertex candidates that arise in the middle of long tracks, splitting the depositions into approximately the same number of downstream and upstream CaloHits. Pandora favors configurations with large values of such asymmetry parameters, underlining that the vertex occurs near the track end-points.

The last factor influencing the vertex metric is the *beam deweighting score*, which measures the z coordinate placement of the vertex. The vertex position is better placed at low values of the z coordinate, which means near the TB source. This quantity strongly depends on the normalized z position of the candidate vertex.

Once the TBVertices3D vector is computed, Pandora starts the track and shower reconstruction. The former aims at finding the CR remnants, along with TB particles (such as protons, pions and muons) that produce track-like depositions; the latter identifies two kinds of objects: shower spines and shower branches. The shower-like clusters are divided into two categories by the length of the associated 2-dimensional clusters: long clusters are spines and are typically oriented towards the interaction vertex, while the shorter ones represent branches and might also be displaced from the main spine. The algorithm dedicated to recursively building up the 2-dimensional showers is named ShowerGrowing. After this stage, the shower projections are matched into the 3-dimensional objects by resolving all the possible ambiguities that may arise.

Further algorithms refine and complete the high-level objects created during the PandoraTestBeam pipeline so far. Therefore, a second 3-dimensional reconstruction is run with less stringent thresholds to ensure that all the CaloHits are conveniently placed in their corresponding object. The Pandora software is finally ready to build the particle hierarchy wrap-up, recursively looking from the primary particles to their daughters while tagging all the primary and secondary interaction vertices in the event.

6.2 The Cluster Merging Network

Network design We introduce the novel slicing method based on the Cluster Merging Network (CM-Net) [250]: an agglomerative clustering algorithm, in which we train a neural network to decide if sub-clusters from a 2D initial cluster pair should be merged or not. A successful link of two 2D clusters should happen if they are formed by hits generated by the same interaction. This information is available in the simulation and it is used as the ground

ProtoDUNE-SP simulation preliminary: Pandora 2D initial clusters purity
Purities mean value: 0.98180 +/- 0.08011

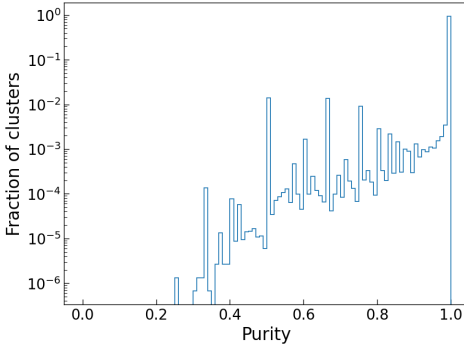


Figure 6.4: 2D initial clusters purity. The histogram is peaked towards high purity values.

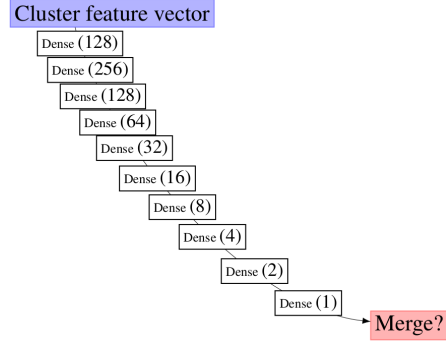


Figure 6.5: The CM-Net network architecture: given a feature vector of the cluster pair, outputs the probability that the cluster pair should be merged.

truth in the CM-Net supervised training. The objective is to build an undirected graph, where the nodes are the 2D initial clusters in an event plane view and the resulting different disconnected parts of the graph are interpreted as slices. Eventually, two specific 2D hits in a plane view will belong to the same slice if there exists a path in the graph connecting their corresponding 2D initial clusters.

We underline that this method is not able to split an initial 2D cluster into two parts. Thus, amending reconstruction errors arising from a previous step of the Pandora reconstruction is not possible. This approach is supported by the fact that the Pandora reconstructed objects show high purity, that is the percentage of hits in a 2D initial cluster falling in the same Monte Carlo true slice, even before the slicing takes place. Figure 6.4 captures this behavior: since a cluster merging procedure can only lower the purity of the resulting set with respect to the initial cluster purities, this benchmark sets an upper bound of the purity of the CM-Net approach. The mean of the purity histogram exceeds 90%.

Figure 6.5 depicts our CM-Net, which is realized as a stack of fully connected layers, with sigmoid final activation. The CM-Net takes as input a vector of fixed size for each pair of sub-clusters in the plane view. The array contains a set of 29 intra-cluster features computed independently for each sub-cluster. We add the same quantities extracted from the sample of hits that would be obtained by merging the two candidate sub-clusters. Finally, we concatenate two more inter-cluster scalar measures. The total length of the network input vector is therefore of 89 elements.

Table 6.1 collects the inter-cluster and intra-clusters engineered features. We group the quantities into different categories. Five standard values mainly come from the Pandora reconstruction and measure the importance of the cluster in the event, in terms of the percentage of hits over the total in the plane view, the average position in the plane and the expected direction of the cluster. The latter is a quantity available within the Pandora framework and gives information about the expected direction of the track envelope in the plane.

Intra-cluster features		
Standard stats (5)	Hits percentage	$ h_C /h_{\text{tot}}$
	Hits mean position	$\bar{\mathbf{h}} = (\bar{h}_x, \bar{h}_y)$
	Cluster expected direction	$\mathbf{v} = (v_x, v_y)$
Covariance matrix (10)	Elements	$Cov[h_x, h_y]_{ij}$
	Eigenvalues	λ_1, λ_2
	Eigenvalues importance	$\lambda_1/(\lambda_1 + \lambda_2)$
	Eigenvectors	$\mathbf{v}_{\lambda_1}, \mathbf{v}_{\lambda_2}$
Post-PCA (9)	Cluster end-points	$\mathbf{h}^t, \mathbf{h}^l, \mathbf{h}^r, \mathbf{h}^b$
	Max end-points distance	$\max_{i,j} \ \mathbf{h}^i - \mathbf{h}^j\ $
Calorimetry (2)	Hit mean energy	\bar{E}
	Hit energy std	σ_E
TPC view (3)	One-hot vector for U,V,W	
Inter-cluster features		
Geometric stats (2)	Minimum inter-cluster distance	$\min_{C_1, C_2} \ \mathbf{h}_{C_1} - \mathbf{h}_{C_2}\ $
	Expected angular separation	$ \hat{\mathbf{v}}_1 \cdot \hat{\mathbf{v}}_2 $

Table 6.1: List of the extracted intra and inter-cluster features. The first column groups the features into categories: the number in parentheses highlights how many components of the final feature vector the specific category gathers.

The covariance matrix informs mainly about the shape of the point cloud formed by the sub-cluster, namely how the hits are distributed in the plane. Hence, we collect the elements of the covariance matrix as well as its eigenvalues $\lambda_{1,2}$ and eigenvectors $\mathbf{v}_{\lambda_{1,2}}$. We further compute the importance of the first eigenvalue normalizing it to the sum of the two: $\lambda_1/(\lambda_1 + \lambda_2)$.

The Principal Component Analysis (PCA) allows us to rotate and rescale the position of each sub-cluster hit, identifying the directions of maximal variance. Once the point cloud is transformed with the PCA algorithm, it is easy to identify the hits at the boundaries of the point cloud $\mathbf{h}^{t,l,r,b}$ (top, left, right, bottom) in the new (x', z') plane, since they are now the furthest ones away from the origin. Also, we consider the maximum euclidean pair distance among the set of such end-point hits.

As opposed to the Pandora geometric approach, in this work, we include the

calorimetry information, adding to the feature vector the mean and standard deviation of the hit deposited energies.

Finally, we complete the list of the intra-cluster features with a one-hot vector referring to which plane view the sub-cluster belongs to. This is a 3–element array corresponding to the different U, V and W planes.

The inter-cluster features read two scalar entries: the minimum inter-cluster distance between hits and the expected angular separation, namely the cosine of the angle between the two sub-cluster expected directions. In principle, the former value should be inversely correlated to the probability that two sub-clusters belong, in fact, to the same track. The latter quantity is conveniently computed through the modulus of the inner product of the unit

vectors $\hat{\mathbf{v}}_{1,2}$ pointing towards the sub-cluster's expected directions.

Dataset The dataset used to train and test our model collects only simulated data, testing on detector data is out of the scope of the present work and can be addressed in the future. We simulate 600 events for training and 300 for testing purposes with the help of the LArSoft [245] framework. Each event represents a test beam of charged particles with certain energy plus cosmic rays interactions within ProtoDUNE-SP. We produce the same amount of events for each of the available test beam energies: 0.3, 0.5, 1, 2, 6, 7 GeV. We remind the reader that each event is composed of three different plane views and, in turn, it contains $\mathcal{O}(10\text{ k})$ hits and $\mathcal{O}(500)$ clusters of various size. We expect that each event contains $\mathcal{O}(50)$ main interactions to be grouped into slices.

Training We train the CM-Net with the following setup. After collecting all the possible 2D input cluster pairs from the events in the training dataset, we filter out the negative examples (those that should not be merged) to reach a 50% balance on the two classes. We reserve an array with 10% of the examples as a validation dataset. Validation is employed to choose the best model during training, namely, the checkpoint on the epoch end that achieves the best validation accuracy. The CM-Net is optimized using the Stochastic Gradient Descent (SGD) [257] algorithm with a learning rate $\eta = 5 \cdot 10^{-3}$ and the binary cross-entropy as the loss function.

After training, we exploit the CM-Net to build the clusters graph: an edge between a cluster pair is drawn if the output of the network exceeds a certain threshold. In our experiment, we fix this threshold to 0.9. We choose such a high value to lower as much as possible the false positive rate: a single positive mispredicted edge can cause a macroscopic effect at the graph level. It is possible, indeed, that false positive edges establish a bridge between two large disconnected parts of the graph, linking them together when, in fact, they should remain separate. The final CM-Net graph prediction is turned into a set of slices containing 2D detector hits, that can be compared against the state-of-the-art Pandora slicing method output.

Results We build a benchmark to compare the goodness of the CM-Net slicing reconstruction against the current Pandora implementation. Since ProtoDUNE-SP is a surface detector, it is crucial to correctly identify and keep separate slices associated with test beam (TB) hits and cosmic rays (CR) hits. We remind the reader that in our experiments, we simulate a TB made of charged particles with a given energy. The goal is to define metrics that allow us to tag the status of the reconstruction on a plane view basis. Such figures of merit are the purity and the completeness of a reconstructed TB slice: purity is the fraction of hits in a reconstructed TB slice that is shared with the TB slice; completeness is the fraction of hits from the true TB slice that is shared with the reconstructed TB slice.

Based on these definitions, we mark each plane in the test set with a flag within the following set: `correct`, `split` or `lost`. Figure 6.6 illustrates the tagging procedure. The first branching depends on the multiplicity of the reconstructed slices containing true TB hits. If all true TB hits fall into

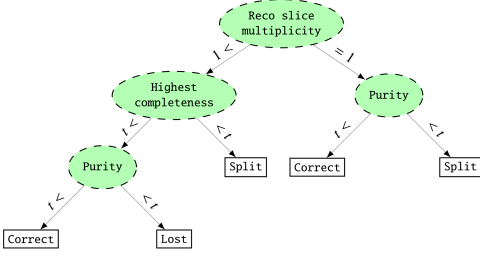


Figure 6.6: Test beam benchmark flowchart: marks each plane view as `correct`, `split` or `lost`. The threshold is $t = 90\%$.

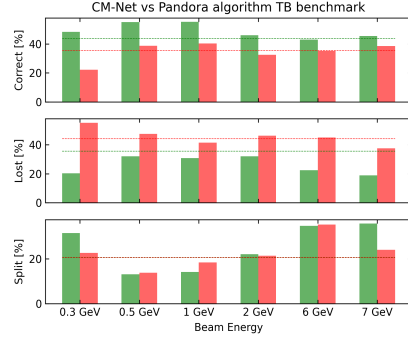


Figure 6.7: Reconstructing MC TB slices: green bars for CM-Net, red bars for Pandora. Dashed lines represent the overall TB energy score. Rows from top to bottom represent correct, lost and bottom percentages.

the same reconstructed slice, the only discriminant on the reconstruction status is its purity: above 90% purity threshold, the plane view is said to be `correct`, otherwise is `lost`. The optimal output should not involve multiple TB slices. Nonetheless, we allow a small margin of error in our tagging procedure, when the highest reconstructed TB slice has both completeness and purity above 90%. Conversely, if completeness is below the threshold, the plane is naturally marked as `split` or if the output, instead, falls short in purity, it provides the evidence that the TB slice has inevitably been merged (`lost`) into a CR larger slice.

Figure 6.7 collects the results of the TB reconstruction benchmark. The top row shows that CM-Net achieves better accuracy than the current Pandora baseline for all the available beam energies. The improvement of our algorithm has to be identified in the less number of clusters marked as `lost`. The CM-Net algorithm presents similar performance for all available TB energies for both the `correct` and `lost` kind of predictions, while it achieves worse score for the `split` category for at the lowest (0.3 GeV) and highest (7 GeV) ends of the TB energy range.

We showed that the proposed model outperforms the state-of-the-art implementation within the Pandora framework. This approach is compatible with the Pandora interface and can be appointed for integration into the software in the future. Further work directions include the assessment of the relative importance of each input feature in the CM-Net final prediction, as well as the optimization of the network architecture itself, inspecting new and more flexible solutions, such as the attention mechanism [46] and its variants. Those networks might exploit the data structure more naturally, avoiding manually selecting and extracting feature arrays of fixed size from the clusters.

Future directions

In this section, we introduce the main ideas to further developments of the research presented in this thesis work. We point out the main objectives for each of the four main results delivered by this study.

PDFFlow The development of the `PDFFlow` software is considered complete. The challenge is to provide code maintenance through time, understanding and matching the needs of the users of the package both from the point of view of theoretical and experimental physicists. The implementation is sufficiently modular that should allow to easily include new algorithms to extend the capabilities of the tool.

MadFlow The fundamental end-point for the successful spread of the `MadFlow` framework among the HEP community is the need to promote the software to include next-to-leading order calculations in an automated way, exploiting the full potential of hardware accelerators. The present work marked an important milestone showing the possibility to hold the computation of a high number of events even for complicated processes with multiple final state partons. This sheds light on the feasibility to go to higher order in perturbation theory. However, such computations involve complex subtraction techniques to take care of QCD infrared singularities that might reveal difficult to implement within the TensorFlow library.

Other chances to improve the `MadFlow` software within reach are the development of a more efficient and GPU-compatible phase space sampler. The current implementation of RAMBO for GPU employs a flat phase space that represents a potential shortcoming in the whole pipeline: complex query processes might introduce instabilities in the `VegasFlow` cross-section integration and reduce the overall event generation efficiency, requiring sampling more events than the GPU might hold, inevitably slowing down the entire run. Possible solutions can be investigated from studying adaptive sampling methods also implemented by the `MG5_AMC@NLO` package.

Continuous integration and continuous development can be interesting approaches for the maintenance of the `MadFlow` package in the future: the idea is to design a fully automated test suite to check corner cases and identify potential bugs in the `MadFlow` implementation to deploy the code in production mode.

Denoising ProtoDUNE-SP raw data Interpretability is one of the main issues related to deep learning, which represents a big question mark on the behavior of these algorithms in new environments. The main future research goal for both denoising and slicing deep learning applications should be to test the networks with larger datasets and eventually on real data. This investigation might require the implementation of automated solutions for the management of the deep learning resources: efficient data storing and retrieval from collected databases, continuous training techniques to inspect new models and automatically triggered hyperparameter search strategies. The deployment of these methods requires advanced software engineering knowledge and experience.

Specific objectives for further developments of the networks implemented in the context of ProtoDUNE-SP raw data denoising are the integration within the LArSoft framework to allow easier comparison with the methods currently used by the DUNE collaboration. This means scanning the suitable solutions to interface the Python code, in which the Graph Neural Networks are implemented, with the LarSoft C++ program.

Other interesting opportunities for further investigation of deep learning methods in this study are model optimization and parameter pruning techniques to provide faster inference with the presented neural networks architectures.

Slicing algorithm at ProtoDUNE-SP A full test comparison with the Pandora implementation of the model shall be the first phase of the future development of this research. The subsequent step would be to integrate our solution within the Pandora framework and test it on real detector data.

Further optimization of the current approach we introduced would be desirable to provide faster inference performance. The starting point would be to replace the sequential processing of the pairs of 2-dimensional sub-clusters in each plane view with more efficient operations. The bottleneck might be represented by the fact that the number of sub-cluster pairs to be inspected grows quadratically with the number of sub-clusters. An interesting approach is given by the application of the attention mechanism to the entire array of detector hits in each plane view. This would allow to process entire plane views at the hit level with a single network forward pass, rather than considering just sub-clusters pairs only. The increased complexity of the algorithm would then require careful training process management, although it might result in improved output performance.

Bibliography

- [1] J. Albrecht, et al., *Comput. Softw. Big Sci.* **3**(1), 7 (2019). DOI 10.1007/s41781-018-0018-8. URL <https://doi.org/10.1007/s41781-018-0018-8>
- [2] S. Amoroso, et al., *Comput. Softw. Big Sci.* **5**(1), 12 (2021). DOI 10.1007/s41781-021-00055-1. URL <https://doi.org/10.1007/s41781-021-00055-1>
- [3] S.F. Novaes, in *10th Jorge Andre Swieca Summer School: Particle and Fields* (1999), pp. 5–102. URL <https://arxiv.org/abs/hep-ph/0001283>
- [4] J.M. Butterworth, *Philosophical Transactions of the Royal Society A: Mathematical, Physical and Engineering Sciences* **374**(2075), 20150260 (2016). DOI 10.1098/rsta.2015.0260. URL <https://royalsocietypublishing.org/doi/abs/10.1098/rsta.2015.0260>
- [5] E.R. Paudel, *BMC Journal of Scientific Research* **4**(1), 65 (2021). DOI 10.3126/bmcjsr.v4i1.42253. URL <https://doi.org/10.3126/bmcjsr.v4i1.42253>
- [6] M.E. Peskin, D.V. Schroeder, *An Introduction to quantum field theory* (Addison-Wesley, Reading, USA, 1995)
- [7] P.W. Higgs, *Phys. Rev. Lett.* **13**, 508 (1964). DOI 10.1103/PhysRevLett.13.508. URL <https://link.aps.org/doi/10.1103/PhysRevLett.13.508>
- [8] Standard Model. URL <https://www.physik.uzh.ch/groups/serra/StandardModel.html>
- [9] F.J. Gilman, K. Kleinknecht, B. Renk, *Eur. Phys. J. C* **15**, 110 (2000). DOI 10.1007/BF02683407. URL <https://doi.org/10.1007/BF02683407>
- [10] L.L. Chau, W.Y. Keung, *Phys. Rev. Lett.* **53**, 1802 (1984). DOI 10.1103/PhysRevLett.53.1802. URL <https://link.aps.org/doi/10.1103/PhysRevLett.53.1802>
- [11] M. Kobayashi, T. Maskawa, *Progress of Theoretical Physics* **49**(2), 652 (1973). DOI 10.1143/PTP.49.652. URL <https://doi.org/10.1143/PTP.49.652>
- [12] R.L. Workman, Others, *PTEP* **2022**, 083C01 (2022). DOI 10.1093/

- ptep/ptac097. URL <https://pdg.lbl.gov/2022/reviews/rpp2022-rev-ckm-matrix.pdf>
- [13] S. Schael, et al., Phys. Rept. **427**, 257 (2006). DOI 10.1016/j.physrep.2005.12.006. URL <https://arxiv.org/abs/hep-ex/0509008>
 - [14] B. Pontecorvo, Sov. Phys. JETP **6**, 429 (1957)
 - [15] B. Pontecorvo, Zh. Eksp. Teor. Fiz. **34**, 247 (1957)
 - [16] Z. Maki, M. Nakagawa, S. Sakata, Prog. Theor. Phys. **28**, 870 (1962). DOI 10.1143/PTP.28.870. URL <https://doi.org/10.1143/PTP.28.870>
 - [17] B. Pontecorvo, Zh. Eksp. Teor. Fiz. **53**, 1717 (1967)
 - [18] V.N. Gribov, B. Pontecorvo, Phys. Lett. B **28**, 493 (1969). DOI 10.1016/0370-2693(69)90525-5
 - [19] J.D. Vergados, H. Ejiri, F. Simkovic, Rept. Prog. Phys. **75**, 106301 (2012). DOI 10.1088/0034-4885/75/10/106301. URL <https://arxiv.org/abs/1205.0649>
 - [20] S. Dell’Oro, S. Marcocci, M. Viel, F. Vissani, Adv. High Energy Phys. **2016**, 2162659 (2016). DOI 10.1155/2016/2162659. URL <https://doi.org/10.1155/2016/2162659>
 - [21] S.M. Bilenky, J. Hosek, S.T. Petcov, Phys. Lett. B **94**, 495 (1980). DOI 10.1016/0370-2693(80)90927-2
 - [22] V. Barger, K. Whisnant, R.J.N. Phillips, Phys. Rev. Lett. **45**, 2084 (1980). DOI 10.1103/PhysRevLett.45.2084. URL <https://link.aps.org/doi/10.1103/PhysRevLett.45.2084>
 - [23] C. Giganti, S. Lavignac, M. Zito, Prog. Part. Nucl. Phys. **98**, 1 (2018). DOI 10.1016/j.ppnp.2017.10.001. URL <https://arxiv.org/abs/1710.00715>
 - [24] R.L. Workman, Others, PTEP **2022**, 083C01 (2022). DOI 10.1093/ptep/ptac097. URL <https://pdg.lbl.gov/2022/reviews/rpp2022-rev-neutrino-mixing.pdf>
 - [25] K. Abe, et al., Phys. Rev. D **97**(7), 072001 (2018). DOI 10.1103/PhysRevD.97.072001. URL <https://doi.org/10.1103/PhysRevD.97.072001>
 - [26] Esteban, I. and others. Nufit4.1 at nufit webpage (2021). URL <http://www.nu-fit.org>
 - [27] F. Capozzi, E. Lisi, A. Marrone, A. Palazzo, Prog. Part. Nucl. Phys. **102**, 48 (2018). DOI 10.1016/j.ppnp.2018.05.005. URL <https://arxiv.org/abs/1804.09678>
 - [28] P.F. de Salas, D.V. Forero, C.A. Ternes, M. Tortola, J.W.F. Valle, Phys. Lett. B **782**, 633 (2018). DOI 10.1016/j.physletb.2018.06.019. URL <https://arxiv.org/abs/1708.01186>
 - [29] K.E. Atkinson, *An Introduction to Numerical Analysis*, 2nd edn. (John Wiley & Sons, New York, 1989). URL http://www.math.science.cmu.ac.th/docs/qNA2556/ref_na/Katkinson.pdf
 - [30] R. Kleiss, R. Pittau, Comput. Phys. Commun. **83**, 141 (1994). DOI 10.1016/0010-4655(94)90043-4. URL <https://arxiv.org/abs/hep-ph/9405257>
 - [31] G.P. Lepage, J. Comput. Phys. **27**, 192 (1978). DOI 10.1016/0021-9991(78)90004-9. URL <https://inspirehep.org>

- [net/literature/119196](https://inspirehep.net/literature/119196)
- [32] G.P. Lepage. VEGAS: AN ADAPTIVE MULTIDIMENSIONAL INTEGRATION PROGRAM (1980). URL <https://inspirehep.net/literature/153221>
- [33] L. Lönnblad, Computer Physics Communications **84**(1), 307 (1994). DOI [https://doi.org/10.1016/0010-4655\(94\)90217-8](https://doi.org/10.1016/0010-4655(94)90217-8). URL <https://www.sciencedirect.com/science/article/pii/S0010465594902178>
- [34] R. Brun, F. Rademakers, Nucl. Instrum. Meth. A **389**, 81 (1997). DOI [10.1016/S0168-9002\(97\)00048-X](https://doi.org/10.1016/S0168-9002(97)00048-X). URL <http://cds.cern.ch/record/491486?ln=en>
- [35] G.E. Forsythe, Mathematics of Computation **26**(120), 817 (1972). URL <http://i.stanford.edu/pub/cstr/reports/cs/tr/72/254/CS-TR-72-254.pdf>
- [36] W.K. Hastings, Biometrika **57**, 97 (1970). DOI [10.1093/biomet/57.1.97](https://doi.org/10.1093/biomet/57.1.97). URL <https://doi.org/10.1093/biomet/57.1.97>
- [37] E. Byckling, K. Kajantie, *Particle Kinematics: (Chapters I-VI, X)* (University of Jyväskylä, Jyväskylä, Finland, 1971). URL <https://inspirehep.net/literature/1251349>
- [38] R. Kleiss, W.J. Stirling, S.D. Ellis, Comput. Phys. Commun. **40**, 359 (1986). DOI [10.1016/0010-4655\(86\)90119-0](https://doi.org/10.1016/0010-4655(86)90119-0). URL <https://cds.cern.ch/record/164736/files/198601282.pdf>
- [39] I.J. Goodfellow, Y. Bengio, A. Courville, *Deep Learning* (MIT Press, 2016). URL <http://www.deeplearningbook.org>
- [40] T.M. Mitchell, *Machine learning* (McGraw-hill New York, 1997). URL <http://www.cs.cmu.edu/~tom/mlbook.html>
- [41] D. Li, IEEE Signal Processing Magazine **29**(6), 141 (2012). DOI [10.1109/MSP.2012.2211477](https://doi.org/10.1109/MSP.2012.2211477). URL <https://ieeexplore.ieee.org/document/6296535/authors#authors>
- [42] F. Pedregosa, et al., Journal of Machine Learning Research **12**, 2825 (2011). URL <https://arxiv.org/abs/1201.0490>
- [43] K. Hornik, M. Stinchcombe, H. White, Neural Netw. **2**(5), 359 (1989). URL <https://dl.acm.org/doi/10.5555/70405.70408>
- [44] D.X. Zhou, Applied and Computational Harmonic Analysis **48**(2), 787 (2020). DOI <https://doi.org/10.1016/j.acha.2019.06.004>. URL <https://www.sciencedirect.com/science/article/pii/S1063520318302045>
- [45] Y.T. Zhou, R. Chellappa, in *IEEE 1988 International Conference on Neural Networks* (1988), pp. 71–78 vol.2. DOI [10.1109/ICNN.1988.23914](https://doi.org/10.1109/ICNN.1988.23914). URL <https://doi.org/10.1109/ICNN.1988.23914>
- [46] A. Vaswani, N. Shazeer, N. Parmar, J. Uszkoreit, L. Jones, A.N. Gomez, L. Kaiser, I. Polosukhin, in *Advances in Neural Information Processing Systems*, vol. 30, ed. by I. Guyon, U.V. Luxburg, S. Bengio, H. Wallach, R. Fergus, S. Vishwanathan, R. Garnett (Curran Associates, Inc., 2017), vol. 30. URL <https://proceedings.neurips.cc/paper/2017/file/3f5ee243547dee91fbd053c1c4a845aa-Paper.pdf>
- [47] T. Wolf, L. Debut, V. Sanh, J. Chaumond, C. Delangue, A. Moi, P. Cistac, T. Rault, R. Louf, M. Funtowicz, J. Davison, S. Shleifer, P. von

- Platen, C. Ma, Y. Jernite, J. Plu, C. Xu, T.L. Scao, S. Gugger, M. Drame, Q. Lhoest, A.M. Rush, in *Proceedings of the 2020 Conference on Empirical Methods in Natural Language Processing: System Demonstrations* (Association for Computational Linguistics, Online, 2020), pp. 38–45. URL <https://www.aclweb.org/anthology/2020.emnlp-demos.6>
- [48] K. Choromanski, et al., CoRR **abs/2009.14794** (2020). URL <https://arxiv.org/abs/2009.14794>
- [49] A. Dosovitskiy, L. Beyer, A. Kolesnikov, D. Weissenborn, X. Zhai, T. Unterthiner, M. Dehghani, M. Minderer, G. Heigold, S. Gelly, J. Uszkoreit, N. Houlsby, CoRR **abs/2010.11929** (2020). URL <https://arxiv.org/abs/2010.11929>
- [50] G. Rumelhart, D. E. adnd Hinton, R.J. Williams, *Nature* **323**, 533 (1986). DOI 10.1038/323533a0. URL <https://doi.org/10.1038/323533a0>
- [51] D.P. Kingma, J. Ba. Adam: A method for stochastic optimization (2017). URL <https://arxiv.org/abs/1412.6980>
- [52] HEP ML Community. A Living Review of Machine Learning for Particle Physics (2022). URL <https://iml-wg.github.io/HEPML-LivingReview/>
- [53] D. Guest, K. Cranmer, D. Whiteson, *Annual Review of Nuclear and Particle Science* **68**(1), 161 (2018). DOI 10.1146/annurev-nucl-101917-021019. URL <https://doi.org/10.1146%2Fannurev-nucl-101917-021019>
- [54] P. F., M. Groh, C. Tunnell, K. Warburton, *International Journal of Modern Physics A* **35**(33), 2043005 (2020). DOI 10.1142/s0217751x20430058. URL <https://arxiv.org/abs/2008.01242>
- [55] H. Voss, A. Höcker, J. Stelzer, F. Tegenfeldt, in *Proceedings of XI International Workshop on Advanced Computing and Analysis Techniques in Physics Research — PoS(ACAT)*, vol. 050 (2009), vol. 050, p. 040. DOI 10.22323/1.050.0040. URL <https://pos.sissa.it/050/040>
- [56] A. Krizhevsky, I. Sutskever, G. Hinton, in *Proceedings of the 25th International Conference on Neural Information Processing Systems - Volume 1* (Curran Associates Inc., Red Hook, NY, USA, 2012), NIPS’12, pp. 1097–1105. URL <https://dl.acm.org/doi/10.5555/2999134.2999257>
- [57] Y. LeCun, Y. Bengio, G. Hinton, *Nature* **521**, 436 (2015). DOI 10.1038/nature14539. URL <https://doi.org/10.1038/nature14539>
- [58] J. Schmidhuber, *Neural Networks* **61**, 85 (2015). DOI 10.1016/j.neunet.2014.09.003. URL <https://www.sciencedirect.com/science/article/pii/S0893608014002135>
- [59] S. Agostinelli, J. Allison, K. Amako, J. Apostolakis, et al., *Nuclear Instruments and Methods in Physics Research Section A: Accelerators, Spectrometers, Detectors and Associated Equipment* **506**(3), 250 (2003). DOI [https://doi.org/10.1016/S0168-9002\(03\)01368-8](https://doi.org/10.1016/S0168-9002(03)01368-8). URL <https://www.sciencedirect.com/science/article/pii/S0168900203013688>
- [60] T. Sjöstrand, S. Mrenna, P. Skands, *Journal of High Energy Physics* **2006**(05), 026 (2006). DOI 10.1088/1126-6708/2006/05/026. URL <https://doi.org/10.1088%2F1126-6708%2F2006%2F05/026>

- 2F05%2F026
- [61] M. Bähr, S. Gieseke, M. Gigg, D. Grellscheid, K. Hamilton, Latunde-Da., S. Plätzer, P. Richardson, M. Seymour, A. Sherstnev, B. Weber, *The European Physical Journal C* **58**, 639 (2008). DOI 10.1140/epjc/s10052-008-0798-9. URL <https://doi.org/10.1140/epjc/s10052-008-0798-9>
 - [62] T. Gleisberg, S. Höche, F. Krauss, M. Schönherr, S. Schumann, F. Siegert, J. Winter, *Journal of High Energy Physics* **2009**(02), 007 (2009). DOI 10.1088/1126-6708/2009/02/007. URL <https://doi.org/10.1088/1126-6708/2009/02/007>
 - [63] J. Alwall, R. Frederix, S. Frixione, V. Hirschi, F. Maltoni, O. Matteleaer, H.S. Shao, T. Stelzer, P. Torrielli, M. Zaro, *Journal of High Energy Physics* **2014** (2014). DOI 10.1007/JHEP07(2014)079. URL [https://doi.org/10.1007/JHEP07\(2014\)079](https://doi.org/10.1007/JHEP07(2014)079)
 - [64] I. Goodfellow, J. Pouget-Abadie, M. Mirza, B. Xu, D. Warde-Farley, S. Ozair, A. Courville, Y. Bengio, in *Advances in Neural Information Processing Systems*, vol. 27, ed. by Z. Ghahramani, M. Welling, C. Cortes, N. Lawrence, K. Weinberger (Curran Associates, Inc., 2014), vol. 27. URL <https://proceedings.neurips.cc/paper/2014/file/5ca3e9b122f61f8f06494c97b1afccf3-Paper.pdf>
 - [65] P. Baldi, P. Sadowski, D. Whiteson, *Nature Commun.* **5**, 4308 (2014). DOI 10.1038/ncomms5308. URL <https://doi.org/10.1038/ncomms5308>
 - [66] O. Cerri, T.Q. Nguyen, M. Pierini, M. Spiropulu, J.R. Vlimant, *JHEP* **05**, 036 (2019). DOI 10.1007/JHEP05(2019)036. URL <https://arxiv.org/abs/1811.10276>
 - [67] E. Bernreuther, T. Finke, F. Kahlhoefer, M. Krämer, A. Mück, *SciPost Phys.* **10**(2), 046 (2021). DOI 10.21468/SciPostPhys.10.2.046. URL <https://doi.org/10.21468/SciPostPhys.10.2.046>
 - [68] D. Cogollo, F.F. Freitas, C.A. de S. Pires, Y.M. Oviedo-Torres, P. Vasconcelos, *Phys. Lett. B* **811**, 135931 (2020). DOI 10.1016/j.physletb.2020.135931. URL <https://doi.org/10.1016/j.physletb.2020.135931>
 - [69] R.T. D’Agnolo, A. Wulzer, *Phys. Rev. D* **99**(1), 015014 (2019). DOI 10.1103/PhysRevD.99.015014. URL <https://doi.org/10.1103/PhysRevD.99.015014>
 - [70] R.T. d’Agnolo, G. Grosso, M. Pierini, A. Wulzer, M. Zanetti, *Eur. Phys. J. C* **82**(3), 275 (2022). DOI 10.1140/epjc/s10052-022-10226-y. URL <https://doi.org/10.1140/epjc/s10052-022-10226-y>
 - [71] M. Cacciari, G.P. Salam, G. Soyez, *JHEP* **04**, 005 (2008). DOI 10.1088/1126-6708/2008/04/005. URL <https://doi.org/10.1088/1126-6708/2008/04/005>
 - [72] M. Cacciari, G.P. Salam, S. Sapeta, *JHEP* **2010** (2010). DOI 10.1007/JHEP04(2010)065. URL [https://doi.org/10.1007/JHEP04\(2010\)065](https://doi.org/10.1007/JHEP04(2010)065)
 - [73] M. Rubin, *JHEP* **05**, 005 (2010). DOI 10.1007/JHEP05(2010)005. URL [https://doi.org/10.1007/JHEP05\(2010\)005](https://doi.org/10.1007/JHEP05(2010)005)
 - [74] L. Lönnblad, C. Peterson, T. Rönkvallsson, *Phys. Rev. Lett.* **65**, 1321 (1990). DOI 10.1103/PhysRevLett.65.1321. URL <https://link.>

- [aps.org/doi/10.1103/PhysRevLett.65.1321](https://doi.org/10.1103/PhysRevLett.65.1321)
- [75] T. Behnke, D. Charlton, *Physica Scripta* **52**(2), 133 (1995). DOI 10.1088/0031-8949/52/2/002. URL <https://iopscience.iop.org/article/10.1088/0031-8949/52/2/002>
- [76] C. Peterson, T. Rönkvallsson, L. Lönnblad, *Computer Physics Communications* **81**(1), 185 (1994). DOI [https://doi.org/10.1016/0010-4655\(94\)90120-1](https://doi.org/10.1016/0010-4655(94)90120-1). URL <https://www.sciencedirect.com/science/article/pii/0010465594901201>
- [77] J. Cogan, M. Kagan, E. Strauss, A. Schwartzman, *JHEP* **02**, 118 (2015). DOI 10.1007/JHEP02(2015)118. URL [https://doi.org/10.1007/JHEP02\(2015\)118](https://doi.org/10.1007/JHEP02(2015)118)
- [78] R.A. Fisher, *Annals of Eugenics* **7**(2), 179 (1936). DOI <https://doi.org/10.1111/j.1469-1809.1936.tb02137.x>. URL <https://onlinelibrary.wiley.com/doi/abs/10.1111/j.1469-1809.1936.tb02137.x>
- [79] J. Thaler, K. Van Tilburg, *JHEP* **03**, 015 (2011). DOI 10.1007/JHEP03(2011)015. URL [https://doi.org/10.1007/JHEP03\(2011\)015](https://doi.org/10.1007/JHEP03(2011)015)
- [80] J. Thaler, K. Van Tilburg, *JHEP* **02**, 093 (2012). DOI 10.1007/JHEP02(2012)093. URL [https://doi.org/10.1007/JHEP02\(2012\)093](https://doi.org/10.1007/JHEP02(2012)093)
- [81] L.G. Almeida, M. Backović, M. Cliche, S.J. Lee, M. Perelstein, *JHEP* **07**, 086 (2015). DOI 10.1007/JHEP07(2015)086. URL [https://doi.org/10.1007/JHEP07\(2015\)086](https://doi.org/10.1007/JHEP07(2015)086)
- [82] P. Baldi, K. Bauer, C. Eng, P. Sadowski, D. Whiteson, *Phys. Rev. D* **93**(9), 094034 (2016). DOI 10.1103/PhysRevD.93.094034. URL <https://arxiv.org/abs/1603.09349>
- [83] J. Barnard, E.N. Dawe, M.J. Dolan, N. Rajcic, *Phys. Rev. D* **95**(1), 014018 (2017). DOI 10.1103/PhysRevD.95.014018. URL <https://arxiv.org/abs/1609.00607>
- [84] L. de Oliveira, M. Kagan, L. Mackey, B. Nachman, A. Schwartzman, *JHEP* **07**, 069 (2016). DOI 10.1007/JHEP07(2016)069. URL [https://doi.org/10.1007/JHEP07\(2016\)069](https://doi.org/10.1007/JHEP07(2016)069)
- [85] P.T. Komiske, E.M. Metodiev, M.D. Schwartz, *JHEP* **01**, 110 (2017). DOI 10.1007/JHEP01(2017)110. URL <https://arxiv.org/abs/1612.01551>
- [86] F.A. Dreyer, G.P. Salam, G. Soyez, *JHEP* **12**, 064 (2018). DOI 10.1007/JHEP12(2018)064. URL [https://doi.org/10.1007/JHEP12\(2018\)064](https://doi.org/10.1007/JHEP12(2018)064)
- [87] Y.L. Dokshitzer, G.D. Leder, S. Moretti, B.R. Webber, *JHEP* **08**, 001 (1997). DOI 10.1088/1126-6708/1997/08/001. URL <https://doi.org/10.1088/1126-6708/1997/08/001>
- [88] M. Wobisch, T. Wengler, in *Workshop on Monte Carlo Generators for HERA Physics (Plenary Starting Meeting)* (1998), pp. 270–279. URL <https://arxiv.org/abs/hep-ph/9907280>
- [89] M. Cacciari, G.P. Salam, G. Soyez, *Eur. Phys. J. C* **72**, 1896 (2012). DOI 10.1140/epjc/s10052-012-1896-2. URL <https://doi.org/10.1140/epjc/s10052-012-1896-2>

- [90] D. Guest, J. Collado, P. Baldi, S.C. Hsu, G. Urban, D. Whiteson, *Phys. Rev. D* **94**, 112002 (2016). DOI 10.1103/PhysRevD.94.112002. URL <https://link.aps.org/doi/10.1103/PhysRevD.94.112002>
- [91] S. Hochreiter, J. Schmidhuber, *Neural Computation* **9**(8), 1735 (1997). DOI 10.1162/neco.1997.9.8.1735. URL <https://doi.org/10.1162/neco.1997.9.8.1735>
- [92] ATLAS Collaboration. Identification of Jets Containing b -Hadrons with Recurrent Neural Networks at the ATLAS Experiment (2017). URL <https://inspirehep.net/literature/1795312>
- [93] ATLAS Collaboration. Optimisation and performance studies of the ATLAS b -tagging algorithms for the 2017-18 LHC run (2017). URL <https://inspirehep.net/literature/1795306>
- [94] CMS Collaboration. Heavy flavor identification at CMS with deep neural networks (2017). URL <https://cds.cern.ch/record/2255736>
- [95] CMS Collaboration. Performance of heavy flavour identification algorithms in proton-proton collisions at 13 TeV at the CMS experiment (2017). URL <https://cds.cern.ch/record/2263801>
- [96] S. Egan, W. Fedorko, A. Lister, J. Pearkes, C. Gay. Long short-term memory (Lstm) networks with jet constituents for boosted top tagging at the LHC (2017). DOI 10.48550/ARXIV.1711.09059. URL <https://arxiv.org/abs/1711.09059>
- [97] T. Cheng, *Comput. Softw. Big Sci.* **2**(1), 3 (2018). DOI 10.1007/s41781-018-0007-y. URL <https://doi.org/10.1007/s41781-018-0007-y>
- [98] I. Henrion, J. Brehmer, J. Bruna, K. Cho, K. Cranmer, G. Louppe, G. Rochette, in *Workshop on Deep Learning for Physical Sciences of the 31st Annual Conference on Neural Information Processing Systems (NIPS17)* (2017). URL https://ml4physicalsciences.github.io/2017/files/nips_dlps_2017_29.pdf
- [99] A. Santoro, D. Raposo, D.G.T. Barrett, M. Malinowski, R. Pascanu, P. Battaglia, T. Lillicrap. A simple neural network module for relational reasoning (2017). DOI 10.48550/ARXIV.1706.01427. URL <https://arxiv.org/abs/1706.01427>
- [100] P.T. Komiske, E.M. Metodiev, J. Thaler, *JHEP* **01**, 121 (2019). DOI 10.1007/JHEP01(2019)121. URL [https://doi.org/10.1007/JHEP01\(2019\)121](https://doi.org/10.1007/JHEP01(2019)121)
- [101] H. Qu, L. Gouskos, *Phys. Rev. D* **101**(5), 056019 (2020). DOI 10.1103/PhysRevD.101.056019. URL <https://doi.org/10.1103/PhysRevD.101.056019>
- [102] Y. Wang, Y. Sun, Z. Liu, S.E. Sarma, M.M. Bronstein, J.M. Solomon, *ACM Trans. Graph.* **38**(5) (2019). DOI 10.1145/3326362. URL <https://doi.org/10.1145/3326362>
- [103] C.R. Qi, H. Su, K. Mo, L.J. Guibas. Pointnet: Deep learning on point sets for 3d classification and segmentation (2016). DOI 10.48550/ARXIV.1612.00593. URL <https://arxiv.org/abs/1612.00593>
- [104] A.J. Larkoski, I. Moutl, B. Nachman, *Phys. Rept.* **841**, 1 (2020). DOI 10.1016/j.physrep.2019.11.001. URL <https://doi.org/10.1016/j.physrep.2019.11.001>

- [105] ATLAS Collaboration. Quark versus Gluon Jet Tagging Using Jet Images with the ATLAS Detector (2017). URL <https://inspirehep.net/literature/1795319>
- [106] CMS Collaboration. New Developments for Jet Substructure Reconstruction in CMS (2017). URL <https://cds.cern.ch/record/2275226>
- [107] J. Lin, M. Freytsis, I. Moutl, B. Nachman, JHEP **10**, 101 (2018). DOI 10.1007/JHEP10(2018)101. URL [https://doi.org/10.1007/JHEP10\(2018\)101](https://doi.org/10.1007/JHEP10(2018)101)
- [108] G. Kasieczka, T. Plehn, M. Russell, T. Schell, JHEP **05**, 006 (2017). DOI 10.1007/JHEP05(2017)006. URL [https://doi.org/10.1007/JHEP05\(2017\)006](https://doi.org/10.1007/JHEP05(2017)006)
- [109] A. Butter, et al., SciPost Phys. **7**, 014 (2019). DOI 10.21468/SciPostPhys.7.1.014. URL <https://doi.org/10.21468/SciPostPhys.7.1.014>
- [110] G. Louppe, K. Cho, C. Becot, K. Cranmer, JHEP **01**, 057 (2019). DOI 10.1007/JHEP01(2019)057. URL [https://doi.org/10.1007/JHEP01\(2019\)057](https://doi.org/10.1007/JHEP01(2019)057)
- [111] A. Andreassen, I. Feige, C. Frye, M.D. Schwartz, Eur. Phys. J. C **79**(2), 102 (2019). DOI 10.1140/epjc/s10052-019-6607-9. URL <https://doi.org/10.1140/epjc/s10052-019-6607-9>
- [112] S. Chatrchyan, et al., JINST **9**(10), P10009 (2014). DOI 10.1088/1748-0221/9/10/P10009. URL <https://doi.org/10.1088/1748-0221/9/10/P10009>
- [113] ATLAS Collaboration. Characterization of interaction-point beam parameters using the pp event-vertex distribution reconstructed in the atlas detector at the lh (2010). URL <https://inspirehep.net/literature/1203962>
- [114] ATLAS Collaboration. Performance of primary vertex reconstruction in proton-proton collisions at $\sqrt{s}=7$ tev in the atlas experiment (2010). URL <https://inspirehep.net/literature/1204019>
- [115] CMS Collaboration. Pileup Removal Algorithms (2014). URL <https://inspirehep.net/literature/1311934>
- [116] M. Cacciari, G.P. Salam, Phys. Lett. B **659**, 119 (2008). DOI 10.1016/j.physletb.2007.09.077. URL <https://arxiv.org/abs/0707.1378>
- [117] J.M. Butterworth, A.R. Davison, M. Rubin, G.P. Salam, Phys. Rev. Lett. **100**, 242001 (2008). DOI 10.1103/PhysRevLett.100.242001. URL <https://arxiv.org/abs/0802.2470>
- [118] S.D. Ellis, C.K. Vermilion, J.R. Walsh, Phys. Rev. D **80**, 051501 (2009). DOI 10.1103/PhysRevD.80.051501. URL <https://arxiv.org/abs/0903.5081>
- [119] S.D. Ellis, C.K. Vermilion, J.R. Walsh, Phys. Rev. D **81**, 094023 (2010). DOI 10.1103/PhysRevD.81.094023. URL <https://arxiv.org/abs/0912.0033>
- [120] D. Krohn, J. Thaler, L.T. Wang, JHEP **02**, 084 (2010). DOI 10.1007/JHEP02(2010)084. URL <https://arxiv.org/abs/0912.1342>
- [121] M. Cacciari, G.P. Salam, G. Soyez, Eur. Phys. J. C **75**(2), 59 (2015). DOI 10.1140/epjc/s10052-015-3267-2. URL <https://arxiv.org/abs/>

- 1407.0408
- [122] D. Bertolini, P. Harris, M. Low, N. Tran, JHEP **10**, 059 (2014). DOI 10.1007/JHEP10(2014)059. URL <https://arxiv.org/abs/1407.6013>
 - [123] P. Berta, M. Spousta, D.W. Miller, R. Leitner, JHEP **06**, 092 (2014). DOI 10.1007/JHEP06(2014)092. URL <https://arxiv.org/abs/1403.3108>
 - [124] ATLAS Collaboration. Constituent-level pile-up mitigation techniques in ATLAS (2017). URL <https://inspirehep.net/literature/1620091>
 - [125] P.T. Komiske, E.M. Metodiev, B. Nachman, M.D. Schwartz, JHEP **12**, 051 (2017). DOI 10.1007/JHEP12(2017)051. URL <https://arxiv.org/abs/1707.08600>
 - [126] J. Arjona Martínez, O. Cerri, M. Pierini, M. Spiropulu, J.R. Vlimant, Eur. Phys. J. Plus **134**(7), 333 (2019). DOI 10.1140/epjp/i2019-12710-3. URL <https://arxiv.org/abs/1810.07988>
 - [127] K. Cho, B. van Merriënboer, D. Bahdanau, Y. Bengio. On the properties of neural machine translation: Encoder-decoder approaches (2014). DOI 10.48550/ARXIV.1409.1259. URL <https://arxiv.org/abs/1409.1259>
 - [128] B. Maier, S.M. Narayanan, G. de Castro, M. Goncharov, C. Paus, M. Schott, Mach. Learn. Sci. Tech. **3**(2), 025012 (2022). DOI 10.1088/2632-2153/ac7198. URL <https://doi.org/10.1088/2632-2153/ac7198>
 - [129] S. Carrazza, F.A. Dreyer, J. Phys. Conf. Ser. **1525**, 012111 (2020). DOI 10.1088/1742-6596/1525/1/012111. URL <https://doi.org/10.1088/1742-6596/1525/1/012111>
 - [130] T. Li, S. Liu, Y. Feng, G. Paspalaki, N. Tran, M. Liu, P. Li. Semi-supervised Graph Neural Networks for Pileup Noise Removal (2022). URL <https://arxiv.org/abs/2203.15823>
 - [131] S.J. Brice. The results of a neural network statistical event class analysis (1996). URL <https://sno.phy.queensu.ca/str/SNO-STR-96-001.pdf>
 - [132] D.S. Ayres, et al. The NOvA Technical Design Report (2007). DOI 10.2172/935497. URL <https://inspirehep.net/files/1e897a237c85bae0087a7f644e9ad832>
 - [133] A. Aurisano, A. Radovic, D. Rocco, A. Himmel, M.D. Messier, E. Niner, G. Pawloski, F. Psihas, A. Sousa, P. Vahle, JINST **11**(09), P09001 (2016). DOI 10.1088/1748-0221/11/09/P09001. URL <https://arxiv.org/abs/1604.01444>
 - [134] C. Szegedy, L. Wei, J. Yangqing, et al., in *2015 IEEE Conference on Computer Vision and Pattern Recognition (CVPR)* (2015). DOI 10.1109/CVPR.2015.7298594. URL <https://arxiv.org/abs/1409.4842>
 - [135] P. Adamson, L. Aliaga, D. Ambrose, et al., Phys. Rev. Lett. **118**, 231801 (2017). DOI 10.1103/PhysRevLett.118.231801. URL <https://link.aps.org/doi/10.1103/PhysRevLett.118.231801>
 - [136] J. Renner, et al., JINST **12**(01), T01004 (2017). DOI 10.1088/1748-0221/12/01/T01004. URL <https://iopscience.iop.org/article/>

- 10.1088/1748-0221/12/01/T01004
- [137] J. Schechter, J.W.F. Valle, Phys. Rev. D **25**, 2951 (1982). DOI 10.1103/PhysRevD.25.2951. URL <https://lib-extopc.kek.jp/preprints/PDF/1982/8206/8206284.pdf>
 - [138] E. Racah, S. Ko, P. Sadowski, W. Bhimji, C. Tull, S. Oh, P. Baldi, Prabhat. Revealing Fundamental Physics from the Daya Bay Neutrino Experiment using Deep Neural Networks (2016). URL <https://arxiv.org/abs/1601.07621>
 - [139] R. Acciarri, et al., JINST **12**(03), P03011 (2017). DOI 10.1088/1748-0221/12/03/P03011. URL <https://arxiv.org/abs/1611.05531>
 - [140] S. Aiello, et al., JINST **15**(10), P10005 (2020). DOI 10.1088/1748-0221/15/10/P10005. URL <https://arxiv.org/abs/2004.08254>
 - [141] B. Abi, et al., Phys. Rev. D **102**(9), 092003 (2020). DOI 10.1103/PhysRevD.102.092003. URL <https://arxiv.org/abs/2006.15052>
 - [142] P. Abratenko, et al., Phys. Rev. D **103**(9), 092003 (2021). DOI 10.1103/PhysRevD.103.092003. URL <https://doi.org/10.1103/PhysRevD.103.092003>
 - [143] L. Hertel, L. Li, P. Baldi, J. Bian, in *Workshop on Deep Learning for Physical Sciences of the 31st Annual Conference on Neural Information Processing Systems (NIPS17)* (2017). URL https://ml4physicalsciences.github.io/2017/files/nips_dlps_2017_7.pdf
 - [144] J. Liu, J. Ott, J. Collado, B. Jargowsky, W. Wu, J. Bian, P. Baldi. Deep-Learning-Based Kinematic Reconstruction for DUNE (2020). URL <https://arxiv.org/abs/2012.06181>
 - [145] L. Dominé, P.C. de Soux, F. Drielsma, D.H. Koh, R. Itay, Q. Lin, K. Terao, K.V. Tsang, T.L. Usher, Phys. Rev. D **104**(3), 032004 (2021). DOI 10.1103/PhysRevD.104.032004. URL <https://arxiv.org/abs/2006.14745>
 - [146] O. Ronneberger, P. Fischer, T. Brox, in *Medical Image Computing and Computer-Assisted Intervention – MICCAI 2015* (Springer International Publishing, Cham, 2015), pp. 234–241. DOI 10.1007/978-3-319-24574-4_28. URL https://doi.org/10.1007/978-3-319-24574-4_28
 - [147] C. Adams, et al., Phys. Rev. D **99**(9), 092001 (2019). DOI 10.1103/PhysRevD.99.092001. URL <https://arxiv.org/pdf/1808.07269.pdf>
 - [148] H. Yu, et al., JINST **16**(01), P01036 (2021). DOI 10.1088/1748-0221/16/01/P01036. URL <https://arxiv.org/abs/2007.12743>
 - [149] R. Acciarri, et al., JINST **17**(01), P01018 (2022). DOI 10.1088/1748-0221/17/01/P01018. URL <https://arxiv.org/abs/2103.06391>
 - [150] B. Graham, M. Engelcke, L. van der Maaten, in *2018 IEEE/CVF Conference on Computer Vision and Pattern Recognition* (2018), pp. 9224–9232. DOI 10.1109/CVPR.2018.00961. URL <https://arxiv.org/abs/1711.10275>
 - [151] F. Scarselli, M. Gori, et al., IEEE Transactions on Neural Networks **20**(1), 61 (2009). DOI 10.1109/TNN.2008.2005605. URL <https://doi.org/10.1109/TNN.2008.2005605>

- [152] L. Dominé, K. Terao, Phys. Rev. D **102**(1), 012005 (2020). DOI 10.1103/PhysRevD.102.012005. URL <https://arxiv.org/abs/2004.08254>
- [153] D.H. Koh, P. Côte De Soux, L. Dominé, F. Drielsma, R. Itay, Q. Lin, K. Terao, K.V. Tsang, T.L. Usher. Scalable, Proposal-free Instance Segmentation Network for 3D Pixel Clustering and Particle Trajectory Reconstruction in Liquid Argon Time Projection Chambers (2020). URL <https://arxiv.org/abs/2007.03083>
- [154] N. Choma, F. Monti, L. Gerhardt, et al., in *2018 17th IEEE International Conference on Machine Learning and Applications (ICMLA)* (2018), pp. 386–391. DOI 10.1109/ICMLA.2018.00064. URL <https://arxiv.org/abs/1809.06166>
- [155] Z. Qian, et al., Nucl. Instrum. Meth. A **1010**, 165527 (2021). DOI 10.1016/j.nima.2021.165527. URL <https://arxiv.org/abs/2101.04839>
- [156] F. Drielsma, Q. Lin, P.C. de Soux, L. Dominé, R. Itay, D.H. Koh, B.J. Nelson, K. Terao, K.V. Tsang, T.L. Usher, Phys. Rev. D **104**(7), 072004 (2021). DOI 10.1103/PhysRevD.104.072004. URL <https://arxiv.org/abs/2007.01335>
- [157] S. Alonso-Monsalve, D. Douqa, C. Jesús-Valls, T. Lux, S. Pina-Otey, F. Sánchez, D. Sgalaberna, L.H. Whitehead, Phys. Rev. D **103**(3), 032005 (2021). DOI 10.1103/PhysRevD.103.032005. URL <https://doi.org/10.1103/PhysRevD.103.032005>
- [158] J. Hewes, et al., EPJ Web Conf. **251**, 03054 (2021). DOI 10.1051/epjconf/202125103054. URL <https://doi.org/10.1051/epjconf/202125103054>
- [159] C. Adams, K. Terao, T. Wongjirad. PILArNet: Public Dataset for Particle Imaging Liquid Argon Detectors in High Energy Physics (2020). URL <https://arxiv.org/abs/2006.01993>
- [160] J. Martín-Albo, et al., JHEP **05**, 159 (2016). DOI 10.1007/JHEP05(2016)159. URL [https://doi.org/10.1007/JHEP05\(2016\)159](https://doi.org/10.1007/JHEP05(2016)159)
- [161] P. Abratenko, et al., Phys. Rev. D **103**(5), 052012 (2021). DOI 10.1103/PhysRevD.103.052012. URL <https://arxiv.org/abs/2012.08513>
- [162] S.Y.C. Chen, T.C. Wei, C. Zhang, H. Yu, S. Yoo, Phys. Rev. Res. **4**(1), 013231 (2022). DOI 10.1103/PhysRevResearch.4.013231. URL <https://doi.org/10.1103/PhysRevResearch.4.013231>
- [163] B. Clerbaux, M.C. Molla, P.A. Petitjean, Y. Xu, Y. Yang, IEEE Trans. Nucl. Sci. **68**(8), 2187 (2021). DOI 10.1109/TNS.2021.3085428. URL <https://arxiv.org/abs/2011.08847>
- [164] R. Abbasi, et al., JINST **16**, P07041 (2021). DOI 10.1088/1748-0221/16/07/P07041. URL <https://arxiv.org/pdf/2101.11589.pdf>
- [165] R. Frühwirth, R.K. Bock, *Data analysis techniques for high-energy physics experiments*, vol. 11 (Cambridge University Press, 2000)
- [166] F. Ragusa, L. Rolandi, New J. Phys. **9**, 336 (2007). DOI 10.1088/1367-2630/9/9/336. URL <https://doi.org/10.1088/1367-2630/9/9/336>
- [167] R. Frühwirth, A. Strandlie. Pattern recognition and reconstruc-

- tion: Datasheet from landolt-börnstein - group i elementary particles, nuclei and atoms · volume 21b1: “detectors for particles and radiation. part 1: Principles and methods”. DOI 10.1007/978-3-642-03606-4_13. URL https://materials.springer.com/lb/docs/sm_lbs_978-3-642-03606-4_13. Part of SpringerMaterials
- [168] H. Kälviäinen, P. Hirvonen, L. Xu, E. Oja, *Image Vis. Comput.* **13**(4), 239 (1995). DOI 10.1016/0262-8856(95)99713-B. URL [https://doi.org/10.1016/0262-8856\(95\)99713-B](https://doi.org/10.1016/0262-8856(95)99713-B)
- [169] R.E. Kalman, *Journal of Basic Engineering* **82**(1), 35 (1960). DOI 10.1115/1.3662552. URL <https://doi.org/10.1115/1.3662552>
- [170] D.E. Catlin, *The Discrete Kalman Filter* (Springer New York, New York, NY, 1989). DOI 10.1007/978-1-4612-4528-5_7. URL https://doi.org/10.1007/978-1-4612-4528-5_7
- [171] R. Fruhwirth, *Nucl. Instrum. Meth. A* **262**, 444 (1987). DOI 10.1016/0168-9002(87)90887-4. URL [https://doi.org/10.1016/0168-9002\(87\)90887-4](https://doi.org/10.1016/0168-9002(87)90887-4)
- [172] R. Mankel, *Nucl. Instrum. Meth. A* **395**, 169 (1997). DOI 10.1016/S0168-9002(97)00705-5. URL <https://inspirehep.net/literature/443697>
- [173] B. Schmidt, *J. Phys. Conf. Ser.* **706**(2), 022002 (2016). DOI 10.1088/1742-6596/706/2/022002. URL <https://doi.org/10.1088/1742-6596/706/2/022002>
- [174] The HEP.TrkX Collaboration. Hep advanced tracking algorithms with cross-cutting applications (2016). URL <https://heptrkx.github.io>
- [175] S. Farrell, D. Anderson, P. Calafiura, G. Cerati, L. Gray, J. Kowalkowski, M. Mudigonda, Prabhat, P. Spentzouris, M. Spiropoulou, A. Tsaris, J.R. Vlimant, S. Zheng, *EPJ Web Conf.* **150**, 00003 (2017). DOI 10.1051/epjconf/201715000003. URL <https://doi.org/10.1051/epjconf/201715000003>
- [176] A. Tsaris, et al., *Journal of Physics: Conference Series* **1085**(4), 042023 (2018). DOI 10.1088/1742-6596/1085/4/042023. URL <https://dx.doi.org/10.1088/1742-6596/1085/4/042023>
- [177] S. Farrell, et al., in *4th International Workshop Connecting The Dots 2018* (2018). URL <https://arxiv.org/abs/1810.06111>
- [178] X. Ju, et al., *Eur. Phys. J. C* **81**(10), 876 (2021). DOI 10.1140/epjc/s10052-021-09675-8. URL <https://doi.org/10.1140/epjc/s10052-021-09675-8>
- [179] S.e.o. Amrouche, in *The NeurIPS '18 Competition*, ed. by S. Escalera, R. Herbrich (Springer International Publishing, Cham, 2020), pp. 231–264. URL <https://arxiv.org/abs/1904.06778>
- [180] The Exa.TrkX Collaboration. Hep advanced tracking algorithms at the exascale (2019). URL <https://exatrxx.github.io>
- [181] X. Ju, et al., in *33rd Annual Conference on Neural Information Processing Systems* (2020). URL <https://arxiv.org/abs/2003.11603>
- [182] N. Choma, et al., in *Proceedings of the 2020 Connecting The Dots Workshop* (2020). URL <https://arxiv.org/abs/2007.00149>

- [183] A. Elabd, et al., *Front. Big Data* **5**, 828666 (2022). DOI 10.3389/fdata.2022.828666. URL <https://doi.org/10.3389/fdata.2022.828666>
- [184] S. Carrazza, J.M. Cruz-Martinez, M. Rossi, *Comput. Phys. Commun.* **264**, 107995 (2021). DOI 10.1016/j.cpc.2021.107995. URL <https://arxiv.org/abs/2009.06635>
- [185] M. Rossi, S. Carrazza, J.M. Cruz-Martinez, in *Proceedings of 40th International Conference on High Energy physics — PoS(ICHEP2020)*, vol. 390 (2021), vol. 390, p. 921. DOI 10.22323/1.390.0921. URL <https://pos.sissa.it/390/921/>
- [186] L.A. Harland-Lang, A.D. Martin, P. Motylinski, R.S. Thorne, *Eur. Phys. J. C* **75**(5), 204 (2015). DOI 10.1140/epjc/s10052-015-3397-6. URL <https://doi.org/10.1140/epjc/s10052-015-3397-6>
- [187] R.D. Ball, et al., *Eur. Phys. J. C* **77**(10), 663 (20). DOI 10.1140/epjc/s10052-017-5199-5. URL <https://doi.org/10.1140/epjc/s10052-017-5199-5>
- [188] C.P. Yuan, et al., in *Proceedings of XXVII International Workshop on Deep-Inelastic Scattering and Related Subjects — PoS(DIS2019)*, vol. 352 (2019), vol. 352, p. 001. DOI 10.22323/1.352.0001. URL <https://pos.sissa.it/352/001>
- [189] H. Plothow-Besch, *Comput. Phys. Commun.* **75**, 396 (1993). DOI 10.1016/0010-4655(93)90051-D. URL <https://cds.cern.ch/record/239783>
- [190] M.R. Whalley, D. Bourilkov, R.C. Group, in *HERA and the LHC: A Workshop on the Implications of HERA and LHC Physics (Startup Meeting, CERN, 26-27 March 2004; Midterm Meeting, CERN, 11-13 October 2004)* (2005), pp. 575–581. URL <https://arxiv.org/abs/hep-ph/0508110>
- [191] D. Bourilkov, R.C. Group, M.R. Whalley. Lhapdf: Pdf use from the tevatron to the lhc (2006). DOI 10.48550/ARXIV.HEP-PH/0605240. URL <https://arxiv.org/abs/hep-ph/0605240>
- [192] A. Buckley, J. Ferrando, S. Lloyd, K. Nordström, B. Page, M. Rüfenacht, M. Schönherr, G. Watt, *Eur. Phys. J. C* **75**, 132 (2015). DOI 10.1140/epjc/s10052-015-3318-8. URL <https://doi.org/10.1140/epjc/s10052-015-3318-8>
- [193] S. Carrazza, J.M. Cruz-Martinez, *Comput. Phys. Commun.* **254**, 107376 (2020). DOI 10.1016/j.cpc.2020.107376. URL <https://arxiv.org/abs/2002.12921>
- [194] J.M. Cruz-Martinez, S. Carrazza. N3pdf/vegasflow: vegasflow v1.0 (2020). DOI 10.5281/zenodo.3691926. URL <https://doi.org/10.5281/zenodo.3691926>
- [195] M. Abadi, et al. TensorFlow: Large-scale machine learning on heterogeneous systems (2015). URL <https://www.tensorflow.org/>. Software available from tensorflow.org
- [196] Python package index - pypi. URL <https://pypi.org/>
- [197] C.R. Harris, et al., *Nature* **585**(7825), 357 (2020). DOI 10.1038/s41586-020-2649-2. URL <https://doi.org/10.1038/s41586-020-2649-2>

- [198] T. Gehrmann, et al., in *Proceedings, 13th International Symposium on Radiative Corrections: Application of Quantum Field Theory to Phenomenology (RADCOR2017): St. Gilgen, Austria, September 24-29, 2017*, vol. RADCOR2017 (2018), vol. RADCOR2017, p. 074. DOI 10.22323/1.290.0074. URL <https://doi.org/10.22323/1.290.0074>
- [199] J. Campbell, T. Neumann, JHEP **12**, 034 (2019). DOI 10.1007/JHEP12(2019)034. URL [https://doi.org/10.1007/JHEP12\(2019\)034](https://doi.org/10.1007/JHEP12(2019)034)
- [200] J. Cruz-Martinez, T. Gehrmann, E. Glover, A. Huss, Phys. Lett. B **781**, 672 (2018). DOI 10.1016/j.physletb.2018.04.046. URL <https://arxiv.org/abs/1802.02445>
- [201] A. Gehrmann-De Ridder, T. Gehrmann, E. Glover, JHEP **09**, 056 (2005). DOI 10.1088/1126-6708/2005/09/056. URL <https://doi.org/10.1088/1126-6708/2005/09/056>
- [202] J. Currie, E.W.N. Glover, S. Wells, JHEP **04**, 066 (2013). DOI 10.1007/JHEP04(2013)066. URL [https://doi.org/10.1007/JHEP04\(2013\)066](https://doi.org/10.1007/JHEP04(2013)066)
- [203] V. Bertone, S. Carrazza, N.P. Hartland, Comput. Phys. Commun. **212**, 205 (2017). DOI 10.1016/j.cpc.2016.10.006. URL <https://arxiv.org/abs/1605.02070>
- [204] S. Carrazza, J. Cruz-Martinez, Eur. Phys. J. **C79**(8), 676 (2019). DOI 10.1140/epjc/s10052-019-7197-2. URL <https://doi.org/10.1140/epjc/s10052-019-7197-2>
- [205] A. Valassi, S. Roiser, O. Mattelaer, S. Hageboeck, EPJ Web Conf. **251**, 03045 (2021). DOI 10.1051/epjconf/202125103045. URL <https://doi.org/10.1051/epjconf/202125103045>
- [206] A. Valassi, et al. madgraph5/madgraph4gpu: vchep2021 proceedings (2021). DOI 10.5281/zenodo.5087381. URL <https://doi.org/10.5281/zenodo.5087381>
- [207] NVIDIA, P. Vingelmann, F.H. Fitzek. Cuda, release: 10.2.89 (2020). URL <https://developer.nvidia.com/cuda-toolkit>
- [208] S. Carrazza, J. Cruz-Martinez, M. Rossi, M. Zaro, EPJ Web Conf. **251**, 03022 (2021). DOI 10.1051/epjconf/202125103022. URL <https://doi.org/10.1051/epjconf/202125103022>
- [209] S. Carrazza, J. Cruz-Martinez, M. Rossi, M. Zaro, Eur. Phys. J. C **81**(7), 656 (2021). DOI 10.1140/epjc/s10052-021-09443-8. URL <https://doi.org/10.1140/epjc/s10052-021-09443-8>
- [210] J.M. Cruz-Martinez, S. Carrazza, M. Rossi, M. Zaro. N3pdf/madflow: Beta release for madflow (2021). DOI 10.5281/zenodo.4958257. URL <https://doi.org/10.5281/zenodo.4958257>
- [211] N.D. Christensen, C. Duhr, Comput. Phys. Commun. **180**, 1614 (2009). DOI 10.1016/j.cpc.2009.02.018. URL <https://arxiv.org/abs/0806.4194>
- [212] C. Degrande, C. Duhr, B. Fuks, D. Grellscheid, O. Mattelaer, T. Reiter, Comput. Phys. Commun. **183**, 1201 (2012). DOI 10.1016/j.cpc.2012.01.022. URL <https://arxiv.org/abs/1108.2040>
- [213] J. Alwall, M. Herquet, F. Maltoni, O. Mattelaer, T. Stelzer, JHEP **06**, 128 (2011). DOI 10.1007/JHEP06(2011)128. URL [https://doi.org/10.1007/JHEP06\(2011\)128](https://doi.org/10.1007/JHEP06(2011)128)

- 1007/JHEP06(2011)128
- [214] H. Murayama, I. Watanabe, K. Hagiwara. HELAS: HELicity amplitude subroutines for Feynman diagram evaluations (1992). URL <https://inspirehep.net/literature/336604>
 - [215] F. Maltoni, K. Paul, T. Stelzer, S. Willenbrock, Phys. Rev. D **67**, 014026 (2003). DOI 10.1103/PhysRevD.67.014026. URL <https://arxiv.org/abs/hep-ph/0209271>
 - [216] P. de Aquino, W. Link, F. Maltoni, O. Mattelaer, T. Stelzer, Comput. Phys. Commun. **183**, 2254 (2012). DOI 10.1016/j.cpc.2012.05.004. URL <https://arxiv.org/abs/1108.2041>
 - [217] J.R. Andersen, et al. Les Houches 2013: Physics at TeV Colliders: Standard Model Working Group Report (2014). URL <https://arxiv.org/abs/1405.1067>
 - [218] F. Maltoni, T. Stelzer, JHEP **02**, 027 (2003). DOI 10.1088/1126-6708/2003/02/027. URL <https://doi.org/10.1088/1126-6708/2003/02/027>
 - [219] M. Rossi, S. Vallecorsa, Computing and Software for Big Science **6**(1) (2022). DOI 10.1007/s41781-021-00077-9. URL <https://doi.org/10.1007/s41781-021-00077-9>
 - [220] B. Abi, R. Acciarri, et al., JINST **15**(08), T08008 (2020). DOI 10.1088/1748-0221/15/08/T08008. URL <https://doi.org/10.1088/1748-0221/15/08/T08008>
 - [221] B. Abi, et al. Deep Underground Neutrino Experiment (DUNE), Far Detector Technical Design Report, Volume II: DUNE Physics (2020). URL <https://arxiv.org/abs/2002.03005>
 - [222] B. Abi, R. Acciarri, et al., JINST **15**(08), T08009 (2020). DOI 10.1088/1748-0221/15/08/T08009. URL <https://doi.org/10.1088/1748-0221/15/08/T08009>
 - [223] B. Abi, R. Acciarri, et al., JINST **15**(08), T08010 (2020). DOI 10.1088/1748-0221/15/08/T08010. URL <https://doi.org/10.1088/1748-0221/15/08/T08010>
 - [224] B. Abi, R. Acciarri, et al. The Single-Phase ProtoDUNE Technical Design Report (2017). URL <https://arxiv.org/abs/1706.07081>
 - [225] A.A. Abud, et al., JINST **17**(01), P01005 (2022). DOI 10.1088/1748-0221/17/01/P01005. URL <https://doi.org/10.1088/1748-0221/17/01/P01005>
 - [226] Y. Li, et al., Nuclear Instruments and Methods in Physics Research Section A: Accelerators, Spectrometers, Detectors and Associated Equipment **816**, 160 (2016). DOI <https://doi.org/10.1016/j.nima.2016.01.094>. URL <https://arxiv.org/abs/1508.07059>
 - [227] C. Adams, R. An, et al., Journal of Instrumentation **13**(07), P07006 (2018). DOI 10.1088/1748-0221/13/07/p07006. URL <https://arxiv.org/abs/1802.08709>
 - [228] R. Acciarri, et al., JINST **12**(02), P02017 (2017). DOI 10.1088/1748-0221/12/02/P02017. URL <https://arxiv.org/abs/1612.05824>
 - [229] S. Ramo, Proc. Ire. **27**, 584 (1939). DOI 10.1109/JRPROC.1939.228757. URL <https://doi.org/10.1109/JRPROC.1939.228757>
 - [230] G. Cavalleri, E. Gatti, G. Fabri, V. Svelto, Nucl. Instrum. Meth. **92**, 137

- (1971). DOI 10.1016/0029-554X(71)90235-7. URL [https://doi.org/10.1016/0029-554X\(71\)90235-7](https://doi.org/10.1016/0029-554X(71)90235-7)
- [231] L. Hamel, M. Julien, Nuclear Instruments and Methods in Physics Research Section A: Accelerators, Spectrometers, Detectors and Associated Equipment **597**(2), 207 (2008). URL <https://doi.org/10.1016/j.nima.2008.09.008>
- [232] R. Veenhof, Nucl. Instrum. Meth. A **419**, 726 (1998). DOI 10.1016/S0168-9002(98)00851-1. URL [https://doi.org/10.1016/S0168-9002\(98\)00851-1](https://doi.org/10.1016/S0168-9002(98)00851-1)
- [233] H. Nyquist, Phys. Rev. **32**, 110 (1928). DOI 10.1103/PhysRev.32.110. URL <https://link.aps.org/doi/10.1103/PhysRev.32.110>
- [234] R. Acciarri, C. Adams, et al., Journal of Instrumentation **12**(08), P08003 (2017). DOI 10.1088/1748-0221/12/08/p08003. URL <http://dx.doi.org/10.1088/1748-0221/12/08/P08003>
- [235] B. Baller, JINST **12**(07), P07010 (2017). DOI 10.1088/1748-0221/12/07/P07010. URL <https://arxiv.org/abs/1703.04024>
- [236] C. Adams, et al., JINST **13**(07), P07007 (2018). DOI 10.1088/1748-0221/13/07/P07007. URL <https://arxiv.org/abs/1804.02583>
- [237] N. Wiener, *Extrapolation, Interpolation, and Smoothing of Stationary Time Series* (The MIT Press, 1964)
- [238] D. Valsesia, G. Fracastoro, et al. Image denoising with graph-convolutional neural networks (2019). URL <https://arxiv.org/abs/1905.12281>
- [239] D. Valsesia, G. Fracastoro, et al. Deep graph-convolutional image denoising (2019). URL <https://arxiv.org/abs/1907.08448>
- [240] M. Simonovsky, N. Komodakis. Dynamic edge-conditioned filters in convolutional neural networks on graphs (2017). URL <https://arxiv.org/abs/1704.02901>
- [241] Q. Liu, M. Kampffmeyer, et al. Scg-net: Self-constructing graph neural networks for semantic segmentation (2020). URL <https://arxiv.org/abs/2009.01599>
- [242] T.N. Kipf, M. Welling, CoRR **abs/1609.02907** (2016). URL <http://arxiv.org/abs/1609.02907>
- [243] K. Xu, W. Hu, J. Leskovec, S. Jegelka, in *International Conference on Learning Representations* (2019). URL <https://openreview.net/forum?id=ryGs6iA5Km>
- [244] S. Xie, et al. Aggregated residual transformations for deep neural networks (2017). URL <https://arxiv.org/abs/1611.05431>
- [245] E.D. Church. Larsoft: A software package for liquid argon time projection drift chambers (2014). URL <https://arxiv.org/abs/1311.6774>
- [246] S.J. Reddi, S. Kale, et al., in *International Conference on Learning Representations* (2018). URL <https://openreview.net/forum?id=ryQu7f-RZ>
- [247] S.S. Channappayya, A.C. Bovik, et al., IEEE Transactions on Image Processing **17**(6), 857 (2008). DOI 10.1109/TIP.2008.921328. URL <https://doi.org/10.1109/TIP.2008.921328>
- [248] Z. Wang, A.C. Bovik, IEEE Signal Processing Magazine **26**(1), 98 (2009).

- DOI 10.1109/MSP.2008.930649. URL <https://doi.org/10.1109/MSP.2008.930649>
- [249] H. Zhao, O. Gallo, et al. Loss functions for neural networks for image processing (2018). URL <https://arxiv.org/abs/1511.08861>
- [250] M. Rossi. Slicing with dl models at protodune-sp (2021). URL <https://indico.cern.ch/event/855454/contributions/4596430/>
- [251] J.S. Marshall, M.A. Thomson, Eur. Phys. J. C **75**(9), 439 (2015). DOI 10.1140/epjc/s10052-015-3659-3. URL <https://doi.org/10.1140/epjc/s10052-015-3659-3>
- [252] M.A. Thomson, Nucl. Instrum. Meth. A **611**, 25 (2009). DOI 10.1016/j.nima.2009.09.009. URL <https://arxiv.org/abs/0907.3577>
- [253] J.S. Marshall, A. Münnich, M.A. Thomson, Nucl. Instrum. Meth. A **700**, 153 (2013). DOI 10.1016/j.nima.2012.10.038. URL <https://arxiv.org/abs/1209.4039>
- [254] R. Acciarri, C. Adams, et al., Eur. Phys. J. C **78**(1), 82 (2018). DOI 10.1140/epjc/s10052-017-5481-6. URL <https://doi.org/10.1140/epjc/s10052-017-5481-6>
- [255] M. Antonello, et al., Adv. High Energy Phys. **2013**, 260820 (2013). DOI 10.1155/2013/260820. URL <https://doi.org/10.1155/2013/260820>
- [256] A. Scarpelli, in *Proceedings of Neutrino Oscillation Workshop — PoS(NOW2018)*, vol. 337 (2019), vol. 337, p. 036. DOI 10.22323/1.337.0036. URL <https://pos.sissa.it/337/036/>
- [257] S. Ruder. An overview of gradient descent optimization algorithms (2017). URL <https://arxiv.org/abs/1609.04747>

List of Publications

As of February 8, 2023

Refereed publications

PDFFlow: parton distribution functions on GPU [184].

MadFlow: automating Monte Carlo simulation on GPU for particle physics processes [209].

Deep Learning Strategies for ProtoDUNE Raw Data Denoising [219].

Publications under review

Slicing with deep learning models at ProtoDUNE-SP [250]. Proceedings of 20th International Workshop on Advanced Computing and Analysis Techniques in Physics Research — ACAT 2021¹.

Publications in conference proceedings

PDFflow: hardware accelerating parton density access [185]. Proceedings of 40th International Conference on High Energy physics — PoS(ICHEP2020).

MadFlow: towards the automation of Monte Carlo simulation on GPU for particle physics processes [208]. Proceedings of 25th International Conference on Computing in High Energy and Nuclear Physics — CHEP 2021.

¹Article already accepted by the editor. The proceedings book has not been issued yet.

Acknowledgments

The thesis work has been done in cooperation with the University of Milan and CERN openlab groups.

The research has been funded and supported by the IBM Power Development group, that also provided hardware and intellectual contribution.

Several people contributed to the realization of the present work. A huge thank you to them who have made this possible.

To the supervisors Stefano Carrazza and Sofia Vallecorsa for their precious guidance during the whole journey.

To Eric Aquaronne, that has always been present to organize and sponsor the work throughout the IBM company.